

The Discovery Potential of Neutral Supersymmetric Higgs Bosons with Decay to Tau Pairs at the ATLAS Experiment

DISSERTATION

zur Erlangung des akademischen Grades
Doctor rerum naturalium
(Dr. rer. nat.)

vorgelegt
der Fakultät Mathematik und Naturwissenschaften
der Technischen Universität Dresden

von
Diplom-Physikerin Jana Schaarschmidt
geboren am 27. Februar 1983 in Annaberg-Buchholz

Gutachter : Prof. Dr. Michael Kobel
Dr. Louis Fayard

Tag der Einreichung: 05. Oktober 2010

Abstract

This work presents a study of the discovery potential for the neutral supersymmetric Higgs bosons $h/A/H$ decaying to τ -pairs with the ATLAS experiment at the LHC. The study is based on Monte Carlo samples which are scaled to state-of-the-art cross sections. The analyses are designed assuming an integrated luminosity of 30 fb^{-1} and a center-of-mass energy of $\sqrt{s} = 14 \text{ TeV}$. The results are interpreted in the m_h^{max} benchmark scenario.

Two final states are analyzed: The dileptonic channel where the two τ -leptons decay to electrons or muons and the lepton-hadron channel where one τ decays to an electron or muon and the other τ decays to hadrons. The study of the dilepton channel is based completely on the detailed ATLAS simulation, the analysis of the lepton-hadron channel is based on the fast simulation.

The collinear approximation is used to reconstruct the Higgs boson mass and its performance is studied. Cuts are optimized in order to discriminate the signal from background and to maximize the discovery potential given a certain Higgs boson mass hypothesis. In the lepton-hadron channel the selection is split into two analyses depending on the number of identified b-jets. Procedures to estimate the dominant backgrounds from data are studied. The shape and normalization of the $Z \rightarrow \tau\tau$ background are estimated from $Z \rightarrow \ell\ell$ control regions. The $t\bar{t}$ contributions to the signal regions are estimated from $t\bar{t}$ control regions.

The individual analyses are combined and sensitivity predictions are made depending on the Higgs boson mass m_A and the coupling parameter $\tan\beta$. The light neutral MSSM Higgs bosons with $m_A = 150 \text{ GeV}$ can be discovered when at least $\tan\beta = 11$ is realized in nature. The heavy neutral MSSM Higgs bosons with $m_A = 800 \text{ GeV}$ can be discovered for $\tan\beta \geq 44$. However, due to the large width of the reconstructed Higgs boson mass and the mass degeneration, only the sum of at least two of the three Higgs boson signals will be visible.

Kurzfassung

Mit dieser Arbeit wird eine Studie des Entdeckungspotentials neutraler supersymmetrischer Higgs-Bosonen $h/A/H$ und dem Zerfall in τ -Paare mit dem ATLAS Detektor am LHC vorgelegt. Die Studie basiert auf Monte Carlo Simulationen, die auf die neuesten Wirkungsquerschnitte normiert werden. Die Analysen wurden für eine Datenmenge entsprechend einer integrierten Luminosität von 30 fb^{-1} bei einer Schwerpunktsenergie von 14 TeV entwickelt. Die Ergebnisse werden für die Parameterwerte des m_h^{max} -Szenarios interpretiert.

Zwei Endzustände werden analysiert: Im voll-leptonischen Kanal zerfallen beide τ -Leptonen in Elektronen oder Myonen. Im semi-leptonischen Kanal zerfällt eines der beiden τ -Leptonen in ein Elektron oder Myon und das andere τ zerfällt in Hadronen. Die Studie des voll-leptonischen Kanals basiert vollständig auf der detaillierten ATLAS Simulation. Eine schnelle Detektorsimulation bildet die Grundlage für die Analyse des semi-leptonischen Kanals.

Die kollineare Näherung wird verwendet um die Masse der Higgs-Bosonen zu rekonstruieren. Die Leistungsfähigkeit dieser Näherung wird studiert. Selektionsschnitte werden optimiert um Signal- von Untergrundeignissen zu trennen, wobei das Entdeckungspotenzial in Abhängigkeit von gegebenen Massenhypothesen maximiert wird. Im semi-leptonischen Kanal wird die Selektion entsprechend der Anzahl der identifizierten b-Jets aufgeteilt in zwei Analysen. Es werden Methoden zur Abschätzung der dominanten Untergründe aus echten Daten studiert. Die Form und Normierung des $Z \rightarrow \tau\tau$ Untergrundes werden aus Kontrollregionen abgeschätzt die mit $Z \rightarrow \ell\ell$ Ereignissen angereichert sind. Der Anteil des $t\bar{t}$ Untergrundes in den Signalregionen wird aus $t\bar{t}$ -Kontrollregionen ermittelt.

Die einzelnen Analysen werden schließlich miteinander kombiniert und es werden Voraussagen zur Sensitivität in Abhängigkeit der Masse des Higgs-Bosons m_A und des Kopplungsparameters $\tan\beta$ getroffen. Die leichten neutralen MSSM Higgs-Bosonen mit einer Masse von $m_A = 150 \text{ GeV}$ können entdeckt werden gesetzt den Fall, dass in der Natur mindestens ein Wert von $\tan\beta = 11$ verwirklicht ist. Die schweren neutralen MSSM Higgs-Bosonen mit einer Masse von $m_A = 800 \text{ GeV}$ können für $\tan\beta \geq 44$ gefunden werden. Da jedoch die Breite der rekonstruierten Massenverteilung sehr groß ist und mindestens zwei der drei neutralen Higgs Bosonen beinahe massenentartet sind, wird nur die Summe der Signale der verschiedenen Higgs Bosonen sichtbar sein.

Table of Contents

1. Preamble	1
2. Theoretical Foundations	3
2.1. The Standard Model of Particle Physics	3
2.1.1. Introduction	3
2.1.2. Electromagnetic and Electroweak Gauge Theory	5
2.1.3. Higgs Mechanism	9
2.1.4. Considerations on the Higgs Boson Mass	12
2.1.5. Standard Model Higgs Bosons at the LHC	14
2.2. Beyond the Standard Model: Supersymmetry	16
2.2.1. The Concept of Supersymmetry	16
2.2.2. Motivation of Supersymmetry	17
2.2.3. The Minimal Supersymmetric Standard Model	19
2.2.4. Benchmark Scenarios	23
2.2.5. Production of Neutral MSSM Higgs Bosons at the LHC	23
2.2.6. Properties of the Neutral MSSM Higgs Boson in the m_h^{\max} scenario	24
3. Previous and Present Higgs Boson Searches	29
3.1. Higgs Boson Searches at LEP	29
3.1.1. Search for SM Higgs Bosons	29
3.1.2. Search for MSSM Higgs Bosons	29
3.2. Higgs Boson Searches at the Tevatron	31
3.2.1. Search for SM Higgs Bosons	32
3.2.2. Search for MSSM Higgs Bosons	32
4. Experimental Setup	35
4.1. The Large Hadron Collider	35
4.2. The ATLAS Detector	37
4.2.1. Coordinate System and Definition of Basic Quantities	37
4.2.2. Inner Detector	38
4.2.3. Calorimetry	41
4.2.4. Muon System	45
4.2.5. Luminosity Detectors	47
4.2.6. Trigger and Data Acquisition	48

5. Monte Carlo Event Generation	51
5.1. Monte Carlo Generators	51
5.1.1. Overview	51
5.1.2. Matrix Elements	52
5.1.3. Parton Showers	53
5.1.4. Matching of Matrix Elements and Parton Showers	53
5.2. Detector Simulation	54
5.2.1. Overview	54
5.2.2. Full Simulation	54
5.2.3. Fast Simulations	55
5.3. Datasets Used	56
5.3.1. The Signal Process and Cross Sections	56
5.3.2. Background Processes and Cross Sections	57
6. Object Identification	63
6.1. Electrons	63
6.1.1. Overview	63
6.1.2. Identification of High- p_T Electrons	63
6.1.3. Electron Identification Cuts	64
6.2. Muons	65
6.2.1. Overview	65
6.2.2. Muons in the STACO Collection	66
6.2.3. Muon Identification Cuts	68
6.3. Tau Leptons	69
6.3.1. Overview	69
6.3.2. Calorimeter Based Reconstruction Algorithm	70
6.3.3. Track Based Reconstruction Algorithm	71
6.3.4. Tau Identification Cuts in the Lepton-Hadron Analysis	71
6.4. Jets and B-Tagging	73
6.4.1. Overview	73
6.4.2. Cone Jets	74
6.4.3. B-Tagging	74
6.5. Missing E_T	77
6.5.1. Overview	77
6.5.2. Cell Based Missing E_T Reconstruction	77
6.6. Object Allocation Ambiguity	79
7. Higgs Boson Mass Reconstruction	81
7.1. Collinear Approximation	81
7.2. Performance of the Collinear Approximation	83
7.2.1. The $h/A/H \rightarrow \tau_\ell \tau_h$ Channel	83
7.2.2. The $h/A/H \rightarrow \tau_\ell \tau_\ell$ Channel	90
7.3. Performance of the Visible Mass	95
7.3.1. The $h/A/H \rightarrow \tau_\ell \tau_h$ Channel	95
7.3.2. The $h/A/H \rightarrow \tau_\ell \tau_\ell$ Channel	97

7.4. MET Performance	98
7.5. Summary	102
8. Analysis of the Fully Leptonic Channel	103
8.1. Event Selection	103
8.1.1. Baseline Selection	103
8.1.2. Higgs Boson Mass-Dependent Selection	115
8.1.3. Results of the Event Selection	126
8.2. Systematic Uncertainties	131
8.2.1. Detector Related Uncertainties	131
8.2.2. Theory Related Uncertainties	132
8.2.3. Systematic Uncertainties of $t\bar{t}$	132
8.2.4. Data-Driven $Z \rightarrow \tau\tau$ Background Estimation	134
8.2.5. Summary of Background Uncertainties	151
8.2.6. Systematic Uncertainties of the Signal Process	151
8.3. Discovery and Exclusion Potential in the Dilepton Channel	153
8.3.1. Discovery	153
8.3.2. Exclusion	156
8.3.3. Comparison to Published Analysis	157
8.3.4. Discussion	158
9. Analysis of the Lepton-Hadron Channel	161
9.1. Event Selection	161
9.1.1. Baseline Selection	161
9.1.2. Split into non b-tagged and b-tagged Analysis	165
9.1.3. Results of the Event Selection	174
9.2. Systematic Uncertainties	184
9.2.1. Sources of Systematic Uncertainties	184
9.2.2. Data-driven $t\bar{t}$ Background Estimation in the b-tagged Analysis	184
9.2.3. $Z \rightarrow \tau\tau$ Background Uncertainties	199
9.2.4. W+jets Background Uncertainties	201
9.2.5. Summary of Background Uncertainties	201
9.2.6. Systematic Uncertainties of the Signal Process	201
9.3. Discovery Potential	205
9.3.1. Profile Likelihood Method	205
9.3.2. Results for the Lepton-Hadron Channel	208
9.3.3. Combination with the Lepton-Lepton Channel	210
9.3.4. Discussion	213
9.3.5. Comparison to Other Publications	214
10. Conclusions	217
10.1. Status of LHC and ATLAS	217
10.2. Search for Supersymmetric Higgs Bosons	217
A. Comparison of the Collinear Mass between FULLSIM and ATLFast-II	223

B. B-Tagging Weight Corrections for Rel. 12 Samples	225
C. Visible Mass in the Dileptonic Channel	227
C.1. Visible Mass at Baseline Selection Level	227
C.2. Visible Mass after Optimized Cuts	230
D. Canceling of Systematic Uncertainties by $Z \rightarrow \tau\tau$ to $Z \rightarrow \ell\ell$ Ratios	233
E. Comparison of Significance Calculations	237
F. Lepton and τ Identification Weights for the Lepton-Hadron Analysis	239
G. Single Top Estimation from Monte Carlo in the Lepton-Hadron Analysis	243
G.1. Contributing Processes	243
G.2. Cut Factorisation and Correction Factors	243
G.3. Results	244
H. Systematic Uncertainties of $t\bar{t}$ Estimation Based on Jet Multiplicities	247
I. Combined Discovery Potential Assuming No $\Delta\sigma_{t\bar{t}}$ in the Dilepton Channel	253
Bibliography	257
List of Figures	267
List of Tables	271

1

Preamble

Particle physics explores the constitution of matter, particle properties and interactions between them. The current theoretical description - the Standard Model - was very successfully verified by past and present experiments. With the recent startup of the Large Hadron Collider (LHC) the fundamental bosons such as the W and Z and the heaviest known matter particle, the top quark, have been re-discovered at highest collision energies ever achieved in a collider experiment.

With the beginning of the LHC era, discoveries of new particles are eagerly anticipated. In fact, the design of the LHC and its experiments was mainly driven by the search for new phenomena [1], that is the Higgs boson and Supersymmetry. The discovery of the Higgs boson would be the ultimate proof of the current particle physics theory in explaining the origin of particle masses. Direct searches at the Large Electron Positron Collider (LEP) for the Higgs boson resulted in a limit for its mass of at least 114.4 GeV [2]. Still continuing searches at the Tevatron led to the exclusion of a Standard Model Higgs boson with a mass between 158 GeV and 175 GeV using an integrated luminosity of up to 6.7 fb^{-1} [3]. So far, no evidence has been found proving the existence of the Higgs particle.

The Standard Model was verified with incredible precision, yet it lacks to explain a variety of observations in nature. One such outstanding example is the dark matter problem, which was initiated by observed deviations of the galactic rotation curves from the Newtonian calculations [4]. Possible dark matter candidates can only be proposed in extensions of the Standard Model theory. One of these extensions arises from introducing a symmetry between bosons and fermions, Supersymmetry, leading to the prediction of new particles and also to the presence of more than one Higgs field.

In this thesis the discovery potential of the neutral Supersymmetric Higgs bosons produced in pp collisions and the subsequent decay to tau pairs is studied using Monte Carlo samples at an LHC energy of 14 TeV with the ATLAS experiment. Even though the current schedule of the LHC operation does not foresee 14 TeV collisions until 2013, assessing possible discovery limits with simulated data is an important preparatory study to prove the unprecedented sensitivity of the ATLAS experiment. New Monte Carlo generators, more precise cross sections, detailed detector descriptions and data-driven background estimation procedures have been used in the analyses presented. The fully leptonic and the semi leptonic $h/A/H \rightarrow \tau\tau$ final states have been separately studied and are combined for setting limits on a discovery region.

This thesis is organized as follows:

Chapter 2 summarizes the theoretical foundations of the Standard Model and the Minimal Supersymmetric extension with emphasis to the Higgs sector.

Chapter 3 gives an overview of the previous and current Higgs boson searches and limits from other experiments.

Chapter 4 contains the description of the experimental setup.

Chapter 5 describes the chain of tools used for simulating events.

Chapter 6 contains information about the particle identification procedures which are relevant in the analyses.

Chapter 7 explains the method used for the Higgs boson mass reconstruction and states its performance.

Chapter 8 presents the cut analysis in the fully leptonic channel including a data-driven estimation method for the $Z \rightarrow \tau\tau \rightarrow 2\ell + 4\nu$ background.

Chapter 9 contains the analysis of the semi leptonic channel. In particular, it includes a data-driven $t\bar{t}$ background estimation procedure.

Chapter 10 closes with the conclusions and an outlook.

Theoretical Foundations

2.1. The Standard Model of Particle Physics

2.1.1. Introduction

In the Standard Model of Particle Physics [5, 6], which is a relativistic quantum field theory, all known matter is constituted by point-like spin 1/2 fermions. Interactions between them are mediated by spin 1 bosons. The matter consists of electrically charged leptons ℓ , neutral leptons (neutrinos) ν and quarks q . They are grouped into three generations, whereby the stable matter, which forms the atoms and molecules, consists only of first-generation particles (electrons, up and down quarks forming protons and neutrons). Each higher generation is a copy of the first generation but with unstable and heavier particles.

The first generation particles are the electron e (electrical charge $Q_e = -1$), the electron neutrino ν_e ($Q_{\nu_e} = 0$), the up quark u ($Q_u = +2/3$) and the down quark d ($Q_d = -1/3$). The second generation contains the muon μ , the muon neutrino ν_μ , the charm quark c and strange quark s . The third generation particles are the tau lepton τ , the tau neutrino ν_τ , the top quark t and bottom quark b . In contrast to the masses of the charged leptons, the neutrinos masses are not well-defined, only quadratic mass differences.

Anti-particles are realized in nature as well. They have the same mass but carry the opposite charges as their corresponding partners. The fermions are subject to the Pauli exclusion principle. They are listed in Table 2.1.

Generation	First		Second		Third	
	Flavor	Mass	Flavor	Mass	Flavor	Mass
Leptons	ν_e	-	ν_μ	-	ν_τ	-
	e	0.5110 MeV	μ	105.658 MeV	τ	1.777 GeV
Quarks	u	(1.5-3) MeV	c	1.25 GeV	t	171.3 GeV
	d	(3-7) MeV	s	95 MeV	b	4.20 GeV

Table 2.1.: Leptons and quarks and their properties [7].

The leptons are subject to lepton universality, meaning that the coupling strength to the spin 1 bosons is independent of the lepton flavor and in the ultra relativistic limit the leptons behave identically. Minor differences in the partial decay widths of for example the leptonic Z boson decay follow from the mass difference between the leptons and resulting phase space effects.

The electromagnetic (EM) force acts on an infinite range and is mediated by massless photons, γ . All electrically charged particles participate in the EM force. The weak interaction couples to the weak charge and is mediated by massive gauge bosons (W, Z). All leptons and quarks participate in the weak interaction. According to the Yukawa hypothesis, massive gauge bosons lead to short range acting forces. The range R of a virtual particle with energy E can be estimated from the Heisenberg uncertainty relation $\Delta x \cdot \Delta p \approx \hbar/2$, resulting in $R = \frac{\hbar c}{2E}$, eg. $R(E = 100\text{GeV}) \approx 10^{-18}\text{m}$.

The W boson interactions violate parity to 100%. The W bosons couples only to left-handed particles and right-handed anti-particles (see also Section 2.1.2). Experimental proof for parity violation was first found by Wu in 1956, who studied electrons emitted by beta-decay from cobalt atoms polarized in a magnetic field [8]. Later in 1957 Goldhaber measured the helicity¹ of neutrinos to be $h = -1 \pm 0.3$ [9].

The electromagnetic and weak forces are unified within the electroweak interaction (see Section 2.1.2).

The gluons as gauge bosons of the strong interaction are massless and couple to the strong charge, named color. All quarks participate in the strong interaction. Gluons also carry color charge, each gluon carries a combination of color and anti-color. The combination of the color triplet (red, green and blue) with its anti-color triplet leads to 8 different gluon types.

All gauge bosons are listed in Table 2.2.

Gauge Boson	Mass	Electric Charge	Interaction	Range
γ	$< 10^{-17} \text{ eV}$	$< 10^{-30}$	electromagnetic	∞
Z^0	91.188 GeV	0	weak	10^{-18} m
W^\pm	80.399 GeV	± 1	weak	10^{-18} m
g	0	0	strong	10^{-15} m

Table 2.2.: Gauge bosons and their properties [7].

Hadrons are composite particles formed by quarks. They are always color neutral, which leads to an effective short range of the strong interaction. Color neutrality is achieved by either combining quark and anti-quark carrying color and anti-color to mesons, or by the combination of three quarks with different color each to baryons. The proton (formed by uud-quarks) is the lightest baryon and stable. Experimental upper limits on the proton lifetime are in the order of at least 10^{29} years [7]. Its stability can be explained by the conservation of the baryon quantum number, B . The non-existence of single colored objects on scales larger than $\sim 10^{-18} \text{ m}$ is called confinement and follows from the potential of the strong force and is the consequence of gluons carrying color. On very short distances (in the limit of $r \rightarrow 0$), however, gluons and quarks act as if they were unbound (asymptotically free) because the strong coupling constant, α_s , decreases with higher energy.

Gravity as infinite-range fourth force cannot be consistently described as a quantum field theory and is not included in the Standard Model, but it is completely negligible on microscopic scales.

¹The helicity h is defined as the projection of the spin direction \vec{s} onto the momentum direction \vec{p} , $h = \frac{\vec{s} \cdot \vec{p}}{s \cdot p}$. In the limit of zero masses the helicity is equal to the chirality (handedness).

In fact, the relative strength of the gravitational force compared to the electromagnetic force acting on the same distance is about 10^{-36} for protons.

Both electroweak and strong interactions are described by relativistic quantum field theories with special underlying (gauge) symmetries. In general conservation laws follow from symmetries [10], and especially in particle physics underlying symmetries lead to observable quantities. The basics of electroweak gauge theory will be introduced in the next section.

2.1.2. Electromagnetic and Electroweak Gauge Theory

In the following, the gauge theory of quantum electrodynamics (QED), based on the $U(1)_Q$ symmetry group, is developed. QED is the simplest form of a local gauge theory and provides a description of electromagnetism. Then the Standard Model theory is illustrated. The starting point is the principle of least action. This variation principle states that the evolution of a physical system between two states is determined by requiring the action to be minimal. The action in a quantum field theory is given as a functional S :

$$S = \int d^4x \mathcal{L} = \int dt d^3\vec{r} \mathcal{L}(\partial_\mu \Psi, \partial_\mu \bar{\Psi}, \Psi, \bar{\Psi}). \quad (2.1)$$

\mathcal{L} is the Lagrangian density describing the system. The Lagrangian \mathcal{L} of a free relativistic spin 1/2 particle with mass m is given by:

$$\mathcal{L}_0 = \bar{\Psi} (i\gamma^\mu \partial_\mu - m) \Psi. \quad (2.2)$$

The principle of least action leads to the extended Euler-Lagrange formalism:

$$\delta S = 0 \Rightarrow \frac{\delta S}{\delta \bar{\Psi}} = \frac{\partial \mathcal{L}_0}{\partial \bar{\Psi}} - \partial_\mu \frac{\partial \mathcal{L}_0}{\partial (\partial_\mu \bar{\Psi})} = 0. \quad (2.3)$$

Evaluating this last equation leads then to the Dirac equation:

$$(i\gamma^\mu \partial_\mu - m) \Psi = 0. \quad (2.4)$$

The Dirac equation describes a massive spin 1/2 fermion, for example the electron, and includes solutions for anti-particles as well.

\mathcal{L}_0 is invariant under a global gauge transformation which depends on an arbitrary phase α which is independent of space and time:

$$\begin{aligned} \Psi \rightarrow \Psi' &= e^{i\alpha} \Psi, \\ \mathcal{L}'_0 &= \mathcal{L}_0. \end{aligned} \quad (2.5)$$

Ψ is not an observable itself - only its absolute value squared - and a global gauge transformation does not change the physical behavior of $|\Psi|^2$:

$$|\Psi'|^2 = |\Psi|^2. \quad (2.6)$$

Another possible transformation is the local gauge transformation. In local gauge transformations the phase $\alpha(x)$ depends on the space-time coordinates:

$$\begin{aligned}\Psi \rightarrow \Psi' &= e^{i\alpha(x)}\Psi, \\ \mathcal{L}'_0 &\neq \mathcal{L}_0.\end{aligned}\tag{2.7}$$

\mathcal{L} is not a priori invariant under a local gauge transformation, but invariance is achieved by adding another term:

$$\mathcal{L} = \mathcal{L}_0 + \mathcal{L}_{loc}.\tag{2.8}$$

This extra term is obtained from the principle of minimal coupling:

$$\partial_\mu \rightarrow \partial_\mu - iQeA_\mu.\tag{2.9}$$

By implementing this principle of minimal coupling the Lagrangian takes the following form:

$$\mathcal{L} = \mathcal{L}_0 - e(\bar{\Psi}\gamma^\mu\Psi)A_\mu = \mathcal{L}_0 - e j^\mu A_\mu.\tag{2.10}$$

A_μ is a vector field changing the phase of Ψ , and j^μ is a current. Now the local gauge transformation

$$\begin{aligned}\Psi \rightarrow \Psi' &= e^{i\alpha(x)}\Psi, \\ A_\mu \rightarrow A'_\mu &= A_\mu - \frac{1}{e}\partial_\mu\alpha(x), \\ (\mathcal{L}_0 + \mathcal{L}_{loc})' &= \mathcal{L}_0 + \mathcal{L}_{loc}\end{aligned}\tag{2.11}$$

leaves the Lagrangian invariant. The A_μ field couples with the parameter e , the electrical charge, and it can be identified with the photon field. Hence, requiring local gauge symmetry leads to the gauge boson of the electromagnetic interaction.

Adding a kinetic term leads to the following complete form of \mathcal{L} for the QED:

$$\mathcal{L}_{QED} = \bar{\Psi}(i\gamma^\mu\partial_\mu - m)\Psi - e j^\mu A_\mu - \frac{1}{4}F_{\mu\nu}F^{\mu\nu}.\tag{2.12}$$

$F_{\mu\nu}$ is the electromagnetic field tensor, defined as:

$$F_{\mu\nu} = \partial_\mu A_\nu - \partial_\nu A_\mu.\tag{2.13}$$

An explicit mass term $\frac{1}{2}M_\gamma^2 A_\mu A^\mu$ would destroy the local gauge symmetry in the case that $M_\gamma^2 \neq 0$, but experiments show that indeed the photon is massless, with an experimental upper limit of $M_\gamma < 10^{-18}$ eV [7]. This Lagrangian cannot describe massive bosons without violating local gauge invariance. However, such an invariance is preferred since local gauge theories are renormalizable [11].

Glashow, Salam and Weinberg showed that an analogous gauge theory for the weak interaction does not work and instead combined the electromagnetic and the weak theory [5]. The parity vio-

lation of the weak force² has to be included which is achieved by differentiating between left- and right-handed fermion fields:

$$\Psi_L = \frac{1 - \gamma^5}{2} \Psi, \quad \Psi_R = \frac{1 + \gamma^5}{2} \Psi. \quad (2.14)$$

The weak force couples to a quantum number I called weak isospin. The fermions are grouped into left-handed isospin doublets and right-handed isospin singlets. Assuming massless neutrinos, there are no right-handed neutrinos. However, they may be added to the theory to account for experimental evidences like neutrino oscillations [12, 13]. The electroweak unification is based on a $SU(2)_L \times U(1)_Y$ symmetry group. The quantum number of the $U(1)$ group, Y , is the weak hypercharge and relates to the electrical charge via the Gell-Mann-Nishijima formula:

$$Q = \frac{Y}{2} + I_3. \quad (2.15)$$

The fermionic doublets and singlets and their assigned quantum numbers are listed in Table 2.3.

Particles			Q	Y	I_3
$\begin{pmatrix} \nu_e \\ e \end{pmatrix}_L$	$\begin{pmatrix} \nu_\mu \\ \mu \end{pmatrix}_L$	$\begin{pmatrix} \nu_\tau \\ \tau \end{pmatrix}_L$	0	-1	+1/2
$\begin{pmatrix} u \\ d \end{pmatrix}_L$	$\begin{pmatrix} c \\ s \end{pmatrix}_L$	$\begin{pmatrix} t \\ b \end{pmatrix}_L$	-1	-1	-1/2
e_R	μ_R	τ_R	+2/3	+1/3	+1/2
ν_{eR}	$\nu_{\mu R}$	$\nu_{\tau R}$	-1/3	+1/3	-1/2
u_R	c_R	t_R	-1	-2	0
d_R	s_R	b_R	0	0	0
			+2/3	+2/3	0
			-1/3	-2/3	0

Table 2.3.: Left and right chiral fermions and their assigned quantum numbers. Q denotes the electrical charge, Y is the weak hypercharge and I_3 is the third component of the weak isospin.

Assuming a model world with only first generation particles, the fermion fields are given as:

$$\Psi_L = \begin{pmatrix} \nu_e \\ e \end{pmatrix}_L, \quad e_R, \quad \nu_R. \quad (2.16)$$

The Lagrangian 2.2 without the mass term $-m\bar{\Psi}\Psi$ then takes the form:

$$\mathcal{L} = \bar{\Psi}_L i \gamma^\mu \partial_\mu \Psi_L + \bar{e}_R i \gamma^\mu \partial_\mu e_R + \bar{\nu}_R i \gamma^\mu \partial_\mu \nu_R. \quad (2.17)$$

²In other words, the W bosons couple to the difference of vector to axial vector currents (V-A coupling). Vectors $(\bar{\Psi}\gamma_\mu\Psi)$ and axial vectors $(\bar{\Psi}\gamma_\mu\gamma_5\Psi)$ transform differently under parity operation which implies parity violation.

The covariant derivative is defined as follows:

$$i\partial_\mu \rightarrow i\partial_\mu - \frac{g}{2} \vec{\tau} \cdot \vec{W}_\mu - \frac{g'}{2} Y B_\mu. \quad (2.18)$$

$\vec{\tau}$ are the three Pauli matrices (τ^1, τ^2, τ^3), \vec{W}_μ are three vector fields ($W_\mu^1, W_\mu^2, W_\mu^3$), g and g' describe the strength of the couplings. To assure the local gauge invariance of \mathcal{L}

$$\hat{U} = e^{\frac{i}{2} \vec{\alpha}(x) \cdot \vec{\tau} + \frac{i}{2} \alpha' Y}, \quad (2.19)$$

so that $\Psi_L \rightarrow \hat{U} \Psi_L$, the gauge transformations of the vector fields W^μ have to be defined as:

$$g W_\mu \rightarrow g \hat{U} W_\mu \hat{U}^\dagger - i \hat{U} \partial_\mu \hat{U}^\dagger. \quad (2.20)$$

The Lagrangian with these substitutions does not include a mass term to conserve the local gauge symmetry.

The electroweak mixing is now performed using Eq. 2.15 in operator form, so the electromagnetic current gets split:

$$e j_\mu^{EM} = e \bar{\Psi} \gamma^\mu \hat{Q} \Psi = e \bar{\Psi} \gamma^\mu \left(\hat{I}_3 + \frac{\hat{Y}}{2} \right) \Psi = e \left(j_\mu^3 + \frac{1}{2} j_\mu^Y \right). \quad (2.21)$$

This leads to an electromagnetic and weak interaction term in the Lagrangian:

$$\mathcal{L}_{EM,w} = -i g \left(j^k \right)^\mu W_\mu^k - \frac{i}{2} g' \left(j^Y \right)^\mu B_\mu. \quad (2.22)$$

k is an index. For $k=3$ Equation 2.22 describes the neutral current; for $k=1, 2$ the charged currents. The physical fields are linear combinations of the field W_μ^3 and B_μ and are obtained using the two-dimensional rotation matrix:

$$\begin{pmatrix} A_\mu \\ Z_\mu \end{pmatrix} = \begin{pmatrix} \cos \theta_W & \sin \theta_W \\ -\sin \theta_W & \cos \theta_W \end{pmatrix} \cdot \begin{pmatrix} B_\mu \\ W_\mu^3 \end{pmatrix}. \quad (2.23)$$

Similar to QED, A_μ can be identified with the photon, Z_μ with the Z^0 boson. The rotation angle θ_W is called weak mixing angle or sometimes Weinberg angle and its value was measured to be $\sin^2(\theta_W) \approx 0.23$ at the energy scale of the Z boson mass.

The charged bosons, W^\pm , correspond to the fields W_μ^\pm which are linear combinations of $W_\mu^{1,2}$:

$$W_\mu^\pm = \frac{1}{\sqrt{2}} (W_\mu^1 \mp i \cdot W_\mu^2). \quad (2.24)$$

In the depicted theory not only the W and Z bosons are massless but also the fermion masses are zero. In the next section the Higgs mechanism is introduced which gives rise to massive W and Z bosons (but massless photons) and massive fermions, allowing at the same time for the conservation of local gauge symmetry.

2.1.3. Higgs Mechanism

The Higgs mechanism [14] is based on the idea that once (at high temperatures) the lowest energy state (vacuum state) of the universe was symmetrical but unstable. Today the vacuum state is stable but asymmetrical and carries a nonzero expectation value. This mechanism is also called spontaneous symmetry breaking. The Lagrangian in the electroweak theory has the $SU(2) \times U(1)_Y$ symmetry whereas the ground state has only $U(1)_Y$ symmetry. This broken symmetry leads to massive weak gauge bosons and at the same time (but differently) provides a mechanism for the fermion masses. In general, the Higgs mechanism is a way to acquire nonzero masses in any gauge theory.

In the following model the Higgs mechanism of a spontaneously broken global gauge symmetry

$$\begin{aligned}\Phi &\rightarrow \Phi' = e^{i\alpha}\Phi, \\ \mathcal{L} &\rightarrow \mathcal{L}' = \mathcal{L}\end{aligned}\tag{2.25}$$

is exemplified. The Lagrangian \mathcal{L} has the form:

$$\begin{aligned}\mathcal{L} &= T - V \\ &= (\partial_\mu \Phi)^* (\partial^\mu \Phi) - \left(\mu^2 \Phi^* \Phi + \lambda (\Phi^* \Phi)^2 \right).\end{aligned}\tag{2.26}$$

\mathcal{L} consists of three terms: $T = (\partial_\mu \Phi)^* (\partial^\mu \Phi)$ is a kinetic term, the potential V contains a mass term $\mu^2 \Phi^* \Phi$ and the term $\lambda (\Phi^* \Phi)^2$ describing the self coupling of four Φ fields with the strength λ . λ will also be referred to as Higgs self-coupling parameter later. Φ is a complex field:

$$\Phi = \frac{1}{\sqrt{2}} (\Phi_1 + i\Phi_2).\tag{2.27}$$

If $\lambda = 0$, V is a harmonic potential, but for $\lambda \neq 0$ and $\mu^2 < 0$ and using Equation 2.27, V takes the form of a Mexican hat (as displayed in Figure 2.1):

$$V = \frac{1}{2} \mu^2 (\Phi_1^2 + \Phi_2^2) + \frac{1}{4} \lambda (\Phi_1^2 + \Phi_2^2)^2.\tag{2.28}$$

It can be shown that indeed the Mexican hat potential V is the only renormalizable model where a complex scalar field Φ acquires a nonzero vacuum state. V has one local but unstable maximum at $\Phi_1 = \Phi_2 = 0$. The minimum is a circle in the Φ_1 - Φ_2 plane and can be calculated as:

$$\frac{\partial V}{\partial \Phi} = 0 \Rightarrow \Phi_1^2 + \Phi_2^2 = \frac{-\mu^2}{2\lambda} \equiv v^2.\tag{2.29}$$

This can be solved when choosing (for example)

$$\Phi_1 = v, \quad \Phi_2 = 0.\tag{2.30}$$

Now one can apply a small perturbation around the minimum:

$$\Phi(x) \approx \frac{1}{\sqrt{2}} (v + \eta(x) + i \cdot \xi(x)).\tag{2.31}$$

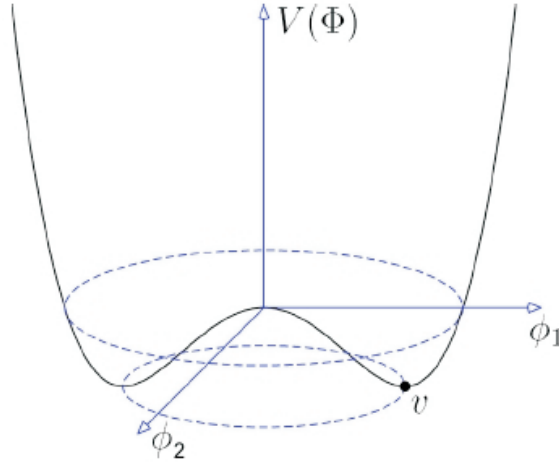


Figure 2.1.: The Higgs potential V as a function of Φ_1 and Φ_2 in the case of $\mu^2 < 0$ and $\lambda > 0$.

Substituting these terms into Equation 2.26 and neglecting terms with higher orders in the perturbation fields η and ξ leads to:

$$\mathcal{L}' = \frac{1}{2} (\partial_\mu \xi)^2 + \left(\frac{1}{2} (\partial^\mu \eta)^2 + \mu^2 \eta^2 \right) + \text{const.} \quad (2.32)$$

The term $\mu^2 \eta^2$ can be interpreted as a mass term for the field η . The mass m_η is then given as:

$$m_\eta = \sqrt{-2\mu^2}. \quad (2.33)$$

$\frac{1}{2} (\partial_\mu \xi)^2$ is the kinetic term for the field ξ . Because the potential V is flat in ξ direction and a mass term corresponding to ξ is missing, one can conclude that this Lagrangian leads to a massless boson, a Goldstone boson. It can be shown that every spontaneous breaking of a global symmetry leads to a massless boson (Goldstone theorem, 1961 [15]).

In the $SU(2) \times U(1)$ group of the Standard Model, the simplest representation of the Higgs field Φ is a complex isospin doublet with a hypercharge $Y = 1$ and given as:

$$\Phi = \begin{pmatrix} \Phi^+ \\ \Phi^0 \end{pmatrix} = \frac{1}{\sqrt{2}} \begin{pmatrix} \Phi_1 + i \cdot \Phi_2 \\ \Phi_3 + i \cdot \Phi_4 \end{pmatrix}. \quad (2.34)$$

Using the same ansatz for the Higgs potential V as in 2.26 leads to the degenerate minimum (a circle in the complex plane):

$$\frac{\partial V}{\partial \Phi} = 0 \Rightarrow \Phi_{min} = \sqrt{\Phi_1^2 + \Phi_2^2 + \Phi_3^2 + \Phi_4^2} = \sqrt{\frac{-\mu^2}{2\lambda}} e^{i\theta}. \quad (2.35)$$

Usually, $\theta = 0$ is used to fix one (arbitrary) vacuum state in the infinite number of states:

$$\Phi_{min}(\theta = 0) \equiv \Phi_{vacuum} = v. \quad (2.36)$$

v is called vacuum expectation value (vev). It can be measured by its relation to the Fermi constant G_F ³ as follows:

$$\frac{G_F}{\sqrt{2}} = \frac{1}{2v^2}. \quad (2.38)$$

G_F can be obtained with high precision by measuring the muon decay width. In this way the value of v was found to be $v = 246$ GeV. The short-range nature of the weak interaction and the direct observability of the non-zero vev of the weak gauge bosons are strong evidence for the mechanism of spontaneous electroweak symmetry breaking.

Fixing the Higgs field with the unitary gauge

$$\Phi_1 = \Phi_2 = \Phi_4 = 0 \quad (2.39)$$

removes the unphysical states $\Phi_{1,2,4}$ (which have to be interpreted as Goldstone bosons). The ground state is chosen to be:

$$\Phi_3 = v \Rightarrow \Phi_0 = \begin{pmatrix} 0 \\ v \end{pmatrix}. \quad (2.40)$$

Singling out Φ_3 as the component with non-zero vev further reflects the Gell-Mann-Nishijima formula 2.15 and the fact that the vacuum state has to be electrically neutral. Using the charge generator (2.15) \hat{Q} on Φ_0 and the properties of the Higgs field, this leads to:

$$\hat{Q}\Phi_0 = \left(\hat{I}_3 + \frac{\hat{Y}}{2} \right) \Phi_0 = \left(-\frac{1}{2} + \frac{1}{2} \right) \Phi_0 = 0. \quad (2.41)$$

Thus, the vacuum stays electrically neutral but it carries a hypercharge and an isospin so that it couples to the weak gauge bosons. The degrees of freedom (formerly represented by the Goldstone bosons) are absorbed by the vector particles W^\pm and Z^0 , giving them an additional degree of freedom, a longitudinal polarization. Only massive particles (with velocities below the speed of light) can carry a longitudinal degree of freedom. The photon remains massless and has only transverse polarization states.

The field $h(x)$ is used to introduce a small distortion around the minimum:

$$\Phi_0 = \begin{pmatrix} 0 \\ v + h(x) \end{pmatrix}. \quad (2.42)$$

$h(x)$ is a physical field, it is interpreted as being the scalar Higgs field of the universe.

The full Lagrangian contains now products of $h(x)$ with the gauge fields W_μ^k and B_μ . It can be

³The muon decay in leading order can be described by the propagation of a W boson. Enrico Fermi showed that this can be simplified to one vertex (a point-like interaction). By the electroweak theory, the coupling constant, G_F , is given as follows:

$$G_F = \frac{\sqrt{2}}{8} \cdot \left(\frac{g}{M_W} \right)^2. \quad (2.37)$$

with g being the weak coupling constant at the W scale.

shown that then the particle masses are given as follows:

$$\begin{aligned}
 m_{W^\pm} &= v \frac{g}{2}, \\
 m_{Z^0} &= v \frac{\sqrt{g^2 + g'^2}}{2}, \\
 m_f &= v \frac{\lambda_f}{\sqrt{2}}, \\
 m_{H^0} &= v \sqrt{2\lambda}.
 \end{aligned} \tag{2.43}$$

Fermions interact with the Higgs background field with a coupling λ_f proportional to their mass. However, these coupling terms must be added 'by hand' to the Lagrangian and their numerical values are inputs to the theory instead of results from it. The Standard Model has overall 19 non-predictable parameters assuming massless neutrinos: 9 fermion masses, 3 mixing angles and 1 CP violating phase in the quark sector, 3 coupling constants, 1 QCD vacuum angle and the Higgs boson self-energy coupling constant as well as the quadratic coupling constant.

2.1.4. Considerations on the Higgs Boson Mass

The Higgs boson H^0 is a neutral massive scalar (with spin 0) and the quantized excitation of the Higgs field. Its mass is a free parameter, but theoretical considerations lead to upper and lower constraints on its value. The Standard Model is a perturbative and unitary theory up to energies at the cut-off scale Λ . From partial wave analysis of elastic $WW \rightarrow WW$ scattering amplitudes, a limit of the Higgs boson mass can be set by requiring conservation of unitarity.

The tree-level scattering amplitude \mathcal{A} in the limit of high center-of-momentum energies $s \gg m_H^2$ is given as follows [16]:

$$\mathcal{A}(WW \rightarrow WW) \rightarrow -\frac{G_F m_H^2}{4\pi\sqrt{2}}. \tag{2.44}$$

Conservation of perturbative unitarity is ensured if

$$\frac{G_F m_H^2}{4\pi\sqrt{2}} \leq \frac{1}{2} \tag{2.45}$$

holds. This puts an upper limit on the Higgs boson mass as follows:

$$m_H \leq \sqrt{\frac{2\sqrt{2}}{G_F}} \approx 870 \text{ GeV}. \tag{2.46}$$

A lower limit (though with large uncertainties) can be gained by analyzing the Higgs self-coupling constant $\lambda = \frac{m_H^2}{2v^2}$ at the cut-off scale Λ (the energy scale at which new physics is supposed to supersede the Standard Model). Vacuum polarization by top quark loops leads to instabilities of

the vacuum ($\lambda < 0$) if the Higgs boson mass is not large enough to compensate λ [17]:

$$\begin{aligned} m_H &\geq 70 \text{ GeV} & \text{at } \Lambda &\approx \mathcal{O}(1 \text{ TeV}), \\ m_H &\geq 130 \text{ GeV} & \text{at } \Lambda &\approx \mathcal{O}(10^{19} \text{ GeV}). \end{aligned} \quad (2.47)$$

By using electroweak precision data from the Large Electron Positron Collider (LEP) and the Stanford Linear Collider (SLC) and comparison to theory predictions including loop corrections where the Higgs boson enters, a χ^2 value can be calculated as a function of the Higgs boson mass m_H . In Figure 2.2, the $\Delta\chi^2$ w.r.t. the χ^2 minimum from a global fit of all Standard Model parameters to the measured values of several observables is shown [18]. Very precisely measured quantities entering the fit as inputs are for example the W and Z boson masses and widths, the forward-backward asymmetry of $Z \rightarrow f\bar{f}$ ⁴ and the Weinberg angle measured in WW scattering or atomic parity violation. Free parameters next to m_H are for example the Z boson mass, the top quark mass and the EM and strong coupling constants. However, no results from direct searches for the Higgs particle are included in the fit shown in the image. The most probable value for m_H

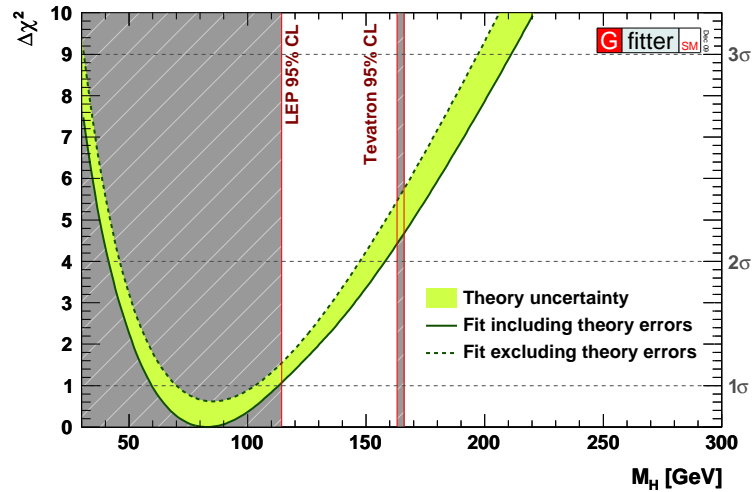


Figure 2.2.: $\Delta\chi^2$ value of fitting the Standard Model parameters to electroweak precision data being indirectly sensitive to Higgs boson contributions (from [18]). The solid line includes the theory errors, the dashed line does not. The $\Delta\chi^2$ minimum is found at $m_H = 83^{+30}_{-20}$ GeV. The grey areas depict experimentally excluded mass regions which, however, do not enter into the fit.

at $\Delta\chi^2 = 0$ is found at

$$m_H = 83^{+30}_{-20} \text{ GeV}. \quad (2.48)$$

Such a light Higgs boson is excluded experimentally, but the uncertainty on the mass is very large due to the logarithmic dependency of the radiative corrections on m_H that enter into the calcula-

⁴Forward-backward asymmetry, A_{FB} , is defined as $A_{FB} = \frac{\sigma_F - \sigma_B}{\sigma_F + \sigma_B}$, where σ_F (σ_B) denotes the cross section of fermions being emitted into the forward (backward) direction relative to the electron direction at LEP.

tions. The tendency of the theory to light Higgs boson masses is a valuable input to upcoming searches at the LHC but on the same time has an interesting theoretical side effect. As will be pointed out later, in the Minimal Supersymmetric scenario the lightest Higgs boson h is limited to a mass lighter than 140 GeV, while in the Standard Model there is no such intrinsic constraint. Higgs boson search results from previous and running experiments will be extensively discussed in Chapter 3.

2.1.5. Standard Model Higgs Bosons at the LHC

In proton-proton collisions at the LHC the Standard Model Higgs boson will be produced in the following processes (ordered by cross section):

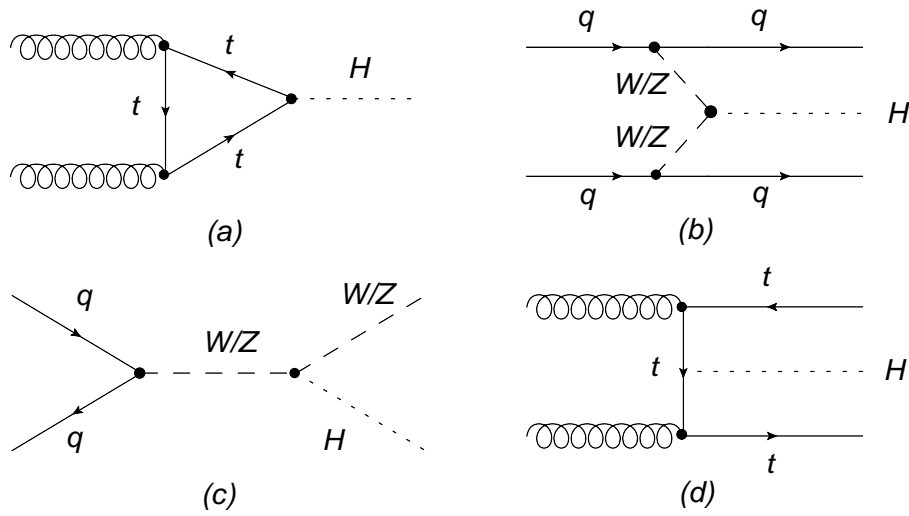


Figure 2.3.: Relevant Standard Model Higgs boson production processes in leading order. (a) gluon fusion, (b) vector boson fusion, (c) W/Z associated and (d) $t\bar{t}$ associated production.

- Gluon fusion (Figure 2.3a)

The Higgs boson is produced by the fusion of two gluons via a heavy-quark loop. This process is also called direct production and it has the largest cross section over the allowed mass range. As displayed in the leading order diagram, the loop is dominated by top quarks. Important higher order processes are for example $gg \rightarrow Hg$, $gq \rightarrow Hq$ and $g\bar{q} \rightarrow H\bar{q}$. The detection of a Higgs boson produced via gluon fusion, however, is challenging, because there are large background contributions from QCD multi-jet production which are hard to suppress if no other striking signal signatures are present. Only Higgs boson decays to two or more leptons (such as in $H \rightarrow ZZ$ or $H \rightarrow WW$) or the Higgs decay to two photons will provide sufficient discrimination against backgrounds.

- Vector boson fusion (VBF) (Figure 2.3b)

In this channel the Higgs boson is produced by the fusion of two weak vector bosons W or Z which are radiated off quarks. This process has the second largest cross section for $m_H < 800$ GeV.

This process leaves a special signature in the detector. The quarks hadronize to jets which will be detected in the forward region of the detector (close to the beam pipe). There is no color connection between the two quarks, hence between the two forward jets, little hadronic activity is expected in the signal process. This typical VBF signature is used to suppress QCD background.

- Associated production WH, ZH (Figure 2.3c)

In this process the Higgs boson is radiated off a weak vector boson (Higgsstrahlung). This process is important in the intermediate mass range $m_H < 2 \cdot m_Z$, but its cross section falls rapidly with an increasing value of m_H .

- Associated production $t\bar{t}H$ (Figure 2.3d)

The Higgs production in association with top-pairs is less important because the cross section is about five times smaller than the one for WH or ZH for $m_H < 200$ GeV.

Assuming a light Higgs boson ($m_H < 135$ GeV), the $t\bar{t}$ associated Higgs boson production with subsequent decay of the Higgs boson to a pair of bottom quarks might be observable. Although the Higgs boson decay to $b\bar{b}$ has the largest branching fraction (around 90%) this channel cannot be triggered without prescale⁵, because of large QCD backgrounds. However, in case of leptonic W decays the $t\bar{t}$ system can be used for triggering and further discrimination against backgrounds.

The branching ratios and cross sections of the Higgs boson production and decay channels are fixed by theory as soon as the Higgs boson mass is known (a comprehensive description of the Standard Model Higgs boson branching ratios, decay widths and cross section calculations is given in [17]). Figure 2.4 displays the branching ratios and the cross sections at a center-of-mass energy of 14 TeV of the most important channels.

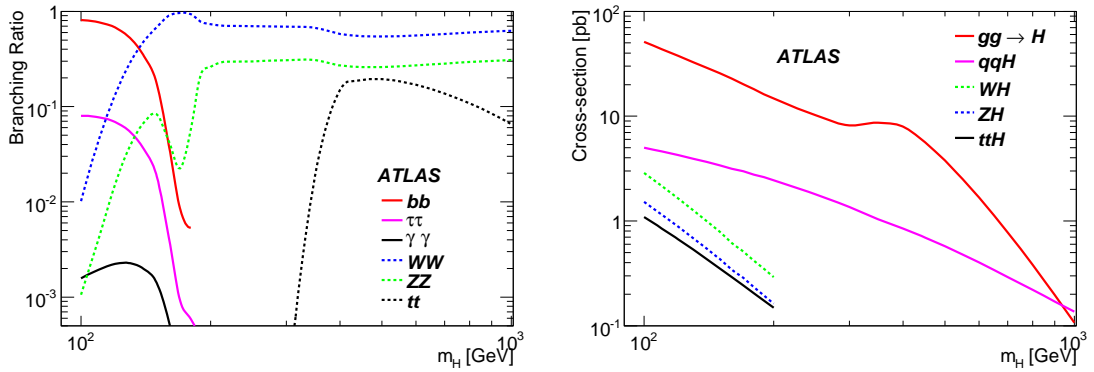


Figure 2.4.: Standard Model Higgs boson decay branching ratios as a function of m_H (left) and production cross sections at the LHC at 14 TeV (right) (both taken from [19]).

Figure 2.5 displays the expected discovery significance including systematic uncertainties in various channels for both the ATLAS and the CMS experiments. In the low mass region $m_H < 130$ GeV

⁵ A trigger prescale denotes the choice that only a random fraction of all triggered events is kept for further analysis, like for example on average every 100th or 1000th event, due to limitations of computing resources.

$H \rightarrow \tau\tau$ produced in VBF and $H \rightarrow \gamma\gamma$ produced in gluon fusion are the only relevant channels. In the intermediate mass region, $130 \text{ GeV} < m_H < 160 \text{ GeV}$, and at high masses above 200 GeV the Higgs boson decay to $ZZ \rightarrow 4\ell$ is dominant. The Higgs boson decay to ZZ and the subsequent decay to four muons is also called the *golden channel*, since the presence of four muons in one event is a very unique and therefore distinguishable signature at a hadron collider. At Higgs boson masses between 160 GeV and 180 GeV, the decay to WW is the most promising channel, because this decay has a branching ratio of close to 100% in this mass range.

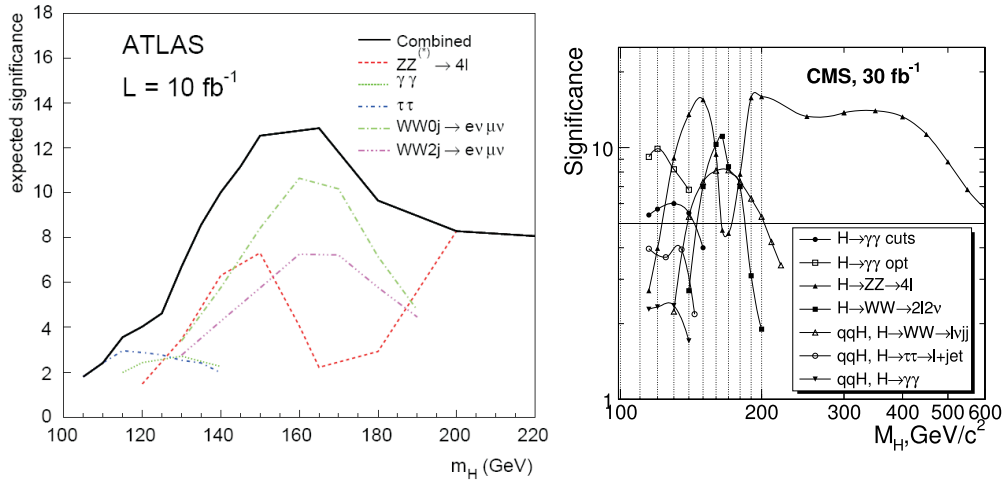


Figure 2.5.: Left plot: Expected significance of the ATLAS experiment of various Standard Model Higgs boson search channels with an integrated luminosity of 10 fb^{-1} for Higgs boson masses between 105 GeV and 220 GeV [19]. Right plot: Expected significance with 30 fb^{-1} at the CMS experiment [20]. In both experiments the high mass region is dominated completely by $H \rightarrow ZZ$. In the significance calculations systematic uncertainties are incorporated.

2.2. Beyond the Standard Model: Supersymmetry

2.2.1. The Concept of Supersymmetry

In Supersymmetry (SUSY) the spin-half matter particles and the integer spin force carriers are united into one concept. A SUSY transformation Q is an operation transforming fermionic into bosonic (or bosonic into fermionic) states (details can be found for example in [21]):

$$\begin{aligned}
 Q|Boson\rangle &\propto |Fermion\rangle \\
 Q|Fermion\rangle &\propto |Boson\rangle.
 \end{aligned} \tag{2.49}$$

The SUSY transformations do not change the $SU_c(3) \times SU_L(2) \times U(1)_Y$ quantum numbers, or in other words, SUSY partners carry the same quantum numbers. But, for example, no SUSY partner of the gluon can be identified with any SM fermion. Consequently, the particle content must be expanded, such that each SM particle has at least one corresponding SUSY partner. Considering for example the SUSY partner of the spin 1/2 electron, the selectron with spin 1, again no charged

bosonic particle at the electron mass $m_e = 511$ keV has been observed. This leads to the next assumption that SUSY cannot be an exact symmetry of nature but has to be a broken symmetry. The SUSY mass scale is expected to be in the order of 1 TeV (this will be motivated in the discussion on fine tuning in the next subsection).

2.2.2. Motivation of Supersymmetry

Despite the success of the Standard Model, many fundamental questions remain unsolved. This leads to the assumption that the Standard Model is only a part of a more fundamental theory. In the following two outstanding problems will be discussed and SUSY will be motivated as it proposes solutions to these questions.

- **Dark Matter Problem**

First evidence for the existence of dark matter was found by Zwicky by analyzing the motion of galaxies in clusters [22] and later by Rubin by measuring the rotation speed of spiral and elliptic galaxies [4]. They discovered that the translational and rotational velocities are too fast and unexplainable just by the gravitational force of the visible matter. Further proof was provided by gravitational lensing. According to general relativity, very massive objects like stars or galaxy clusters bend space and thus the path of light rays emitted by bright objects behind the gravitational source. Again, the mass of the objects is found to be too small to account for the measured deflection angles [23]. Also the distribution of hot gas in galaxies differs from the expectations. All these effects are explainable at once by the presence of massive particles which are invisible in the electromagnetic spectrum and are *cold* (massive w.r.t. keV and therefore slowly moving at the time of structure formation) but clumped to large structures.

The density of the universe was determined by WMAP by measuring the cosmic microwave background [24]. This was compared to the mass of visible stellar objects and consequently it was found that only 4.6% of the mass of the universe is made up by known Standard Model matter, 23% is dark matter and the rest is denoted as dark energy.

In the Standard Model theory there is no dark matter candidate. The neutrinos from the three Standard Model generations are too light and too fast to account for the discrepancies⁶. Uncertainties in the determination of the masses of exotic objects such as super-massive black holes and quasars are not sufficient either because the number of such objects is not large enough. However, supersymmetry provides a candidate with the lightest neutralino, χ^0 [26] (the SUSY particle content will be listed in the next section), under the assumption that R parity is conserved. R parity is a special symmetry which is included into the Lagrangian to ensure lepton and baryon number conservation and hence proton stability [27]. It is calculated as $R = (-1)^{2s+3B+L}$ with the spin s , the baryon number B and the lepton number L . SUSY particles have $R = -1$ while SM particles have $R = +1$. Assuming R parity conservation, SUSY particles can therefore only be produced in pairs. The lightest SUSY particle (LSP) is then stable.

⁶There are models suggesting that neutrinos contribute significantly to dark matter in a so-called hot dark matter scenario, which is, however, inconsistent with the Standard Model of Cosmology [25]. Neutrinos of a possible 4th generation in an extended Standard Model theory are much heavier with a mass of at least 45 GeV (half the Z boson mass), but so far there are no indications for a 4th generation.

- **Fine Tuning Problem**

Power-law divergences of the radiative corrections of the Higgs mass should in principle enlarge its value enormously up to the scale Λ where the Standard Model is superseded by new physics (this could be the scale of a unification of strong and electroweak forces $\mathcal{O}(10^{16} \text{ GeV})$ - the GUT scale - or at the latest the Planck scale) for each order of perturbation theory. This behavior is different for the fermions, where radiative corrections to the mass are protected by chiral symmetry and also different for the photon, where gauge symmetry protects it from acquiring a mass.

The observable Higgs mass m is calculated as follows:

$$m^2 = m_0^2 + (\delta m)^2, \quad (2.50)$$

with m_0 being the mass on tree level and $m_0 \sim \mathcal{O}(100 \text{ GeV})$. The correction term δm from fermion loops is of the form of (see eg. in [28])

$$(\delta m)^2 \sim g^2 m^2 / m_W^2 \left(\Lambda^2 - m^2 \ln \frac{\Lambda^2}{m^2} + \mathcal{O}\left(\frac{1}{\Lambda^2}\right) \right). \quad (2.51)$$

To keep m small, the loop-corrections have to be canceled by counterterms with an incredible precision of the order of

$$\mathcal{O}(\text{fine tuning}) \approx \frac{\mathcal{O}(EW^2)}{\mathcal{O}(\Lambda^2)} \approx 10^{-26}. \quad (2.52)$$

This is in principle allowed but a more natural solution is clearly preferred.

SUSY solves this problem⁷ because the SUSY partners of the fermions, sfermions \tilde{f} , cancel the divergent fermion loops. The sfermion loop correction to m^2 is given analog to Equation 2.51 but with a different sign of the Λ^2 term. The radiative Higgs boson mass correction remains to be of the order of the electroweak scale:

$$\delta m^2 \approx \mathcal{O}(\alpha) \cdot |m_{\tilde{f}}^2 - m_f^2| \approx \mathcal{O}(10^{-2}) \cdot m_{SUSY}^2. \quad (2.53)$$

Related to the fine tuning problem is the hierarchy problem, which is the question why the Higgs boson mass of $\mathcal{O}(100 \text{ GeV})$ is much smaller than the Planck mass $m_{Pl} = 10^{19} \text{ GeV}$. In SUSY the remaining question is where the hierarchy between the SUSY mass scale and the GUT scale comes from. This, however, might be answered by the SUSY breaking mechanism.

There are other non-understood issues such as the existence of gravity and its inconsistency with the Standard Model theory and the non-unification of the running SM coupling constants α , α_w and α_s at the GUT scale. Furthermore, there is the matter-antimatter asymmetry problem which cannot be explained completely by the strength of CP violation in the SM or the unpredictability of Standard Model parameters and the number of particle generations. Cosmological unknowns such as flatness of the universe (which is the reason for postulating dark energy in the first place), its accelerated expansion, the inflation period and finally the very beginning of the universe provide

⁷There is another possibility to solve the fine tuning problem by assuming that the Higgs particle is not an elementary scalar but a bound state of fermions, like in technicolor theory [29].

more motivation for developing further theories such as a great unified theory, (super)string theory and/or extra dimensions which are beyond the scope of this thesis. Most of these theories, however, contain Supersymmetry.

2.2.3. The Minimal Supersymmetric Standard Model

The Minimal Supersymmetric Standard Model (MSSM) is a direct supersymmetrization of the Standard Model. It is minimal in the sense that it contains the smallest number of new particle states and new interactions consistent with phenomenology. The MSSM field content is listed in Table 2.4.

SM Particles			R parity	Spin	SUSY Partners			R parity	Spin
ν_{eL}	$\nu_{\mu L}$	$\nu_{\tau L}$	+1	1/2	$\tilde{\nu}_{eL}$	$\tilde{\nu}_{\mu L}$	$\tilde{\nu}_{\tau L}$	-1	0
e_L	μ_L	τ_L	+1	1/2	\tilde{e}_L	$\tilde{\mu}_L$	$\tilde{\tau}_L$	-1	0
ν_R	$\nu_{\mu R}$	$\nu_{\tau R}$	+1	1/2	$\tilde{\nu}_{eR}$	$\tilde{\nu}_{\mu R}$	$\tilde{\nu}_{\tau R}$	-1	0
e_R	μ_R	τ_R	+1	1/2	\tilde{e}_R	$\tilde{\mu}_R$	$\tilde{\tau}_R$	-1	0
u_L	c_L	t_L	+1	1/2	\tilde{u}_L	\tilde{c}_L	\tilde{t}_L	-1	0
d_L	s_L	b_L	+1	1/2	\tilde{d}_L	\tilde{s}_L	\tilde{b}_L	-1	0
u_R	c_R	t_R	+1	1/2	\tilde{u}_R	\tilde{c}_R	\tilde{t}_R	-1	0
d_R	s_R	b_R	+1	1/2	\tilde{d}_R	\tilde{s}_R	\tilde{b}_R	-1	0
H_d^0	H_d^-		+1	0	\tilde{h}_d^0	\tilde{h}_d^-		-1	1/2
H_u^+	H_u^0		+1	0	\tilde{h}_u^+	\tilde{h}_u^0		-1	1/2
g			+1	1	\tilde{g}			-1	1/2
W^\pm	W_3^0	B^0	+1	1	\tilde{W}^\pm	\tilde{W}_3^0	\tilde{B}^0	-1	1/2

Table 2.4.: Field content of the MSSM, spin and R parity quantum numbers. The construction of the fields and its mixing to observable particles is described in the text.

To construct the MSSM, a vector superfield is assigned to each SM gauge field and a super chiral field is assigned to each SM matter field (details are given in [30] for instance). The superpartners of each superfield carry the same gauge and global quantum numbers and consequently they mix to the observable mass eigenstates.

The particle content of the vector superfields is one gauge boson and its partner a gaugino. It can be shown by transformation arguments that the gauginos cannot be identified with any SM matter particle. The four observable neutral SUSY particles are called neutralinos $\chi_{1,2,3,4}^0$ and are mixed states of the neutral gaugino fields, \tilde{B}^0 , \tilde{W}_3^0 , and the neutral Higgsinos, $h_{u,d}^0$ (see below). The four observable charged SUSY particles are called charginos, $\chi_{1,2}^\pm$, and are mixed states from the charged fields, \tilde{W}^\pm , and charged Higgsinos, h_u^+ and h_d^- .

The chiral superfields contain a fermion and a complex scalar partner. There is one superfield for each chirality of every SM fermion. The superpartners of the matter fermions are the spin zero sfermions (squarks and sleptons). For example, to the up-quark, u_R and u_L , the squarks, \tilde{u}_R

and \tilde{u}_L , are assigned. However, it should be noted that chirality cannot be defined for zero spin particles. The physically observable states, \tilde{u}_1 and \tilde{u}_2 , are mixtures from the chiral fields $\tilde{u}_{L,R}$ after electroweak symmetry breaking.

The SM Higgs doublet is promoted to two doublets of left-chiral superfields:

$$\Phi = \begin{pmatrix} \Phi^+ \\ \Phi^0 \end{pmatrix} \rightarrow H_u = \begin{pmatrix} h_u^+ \\ h_u^0 \end{pmatrix}, H_d = \begin{pmatrix} h_d^0 \\ h_d^- \end{pmatrix}. \quad (2.54)$$

The extension of the Higgs doublet to two SUSY Higgs doublets is not minimal but necessary to avoid anomalies as was pointed out by Alvarez-Gaume and Witten for instance, [31]. The H_u doublet carries hypercharge $Y = +1$ while H_d carries $Y = -1$. The vacuum expectation value v_u of the scalar component of h_u^0 gives mass to the up-type fermions and the vev v_d of h_d^0 gives mass to the down-type fermions. The ratio of both vev is called $\tan \beta$:

$$\tan \beta = \frac{v_u}{v_d}. \quad (2.55)$$

The couplings in the SM correspond to $\tan \beta = 1$. The Higgs boson phenomenology is very dependent on $\tan \beta$ as will be pointed out later. The two MSSM vev relate to the measured SM vev by $\sqrt{v_u^2 + v_d^2} = v_{SM} = 246 \text{ GeV}$.

The components of the two Higgs doublets represent 8 degrees of freedom. However, these weak eigenstates do not represent physical states. Those are obtained by transforming the Higgs fields from the weak eigenstate basis into a mass-eigenstate basis and by diagonalizing the Higgs boson mass-square matrix (this is explained in detail in [32]). The results of the mixing are given as follows, depending on the value of β (from the ratio of the vev) and the mixing angle α :

$$\begin{aligned} \begin{pmatrix} h^0 \\ H^0 \end{pmatrix} &= \sqrt{2} \begin{pmatrix} \cos \alpha & -\sin \alpha \\ \sin \alpha & \cos \alpha \end{pmatrix} \cdot \begin{pmatrix} \text{Re}(h_u^0) - v_u \\ \text{Re}(h_d^0) - v_d \end{pmatrix}, \\ \begin{pmatrix} G^- \\ H^- \end{pmatrix} &= \begin{pmatrix} \cos \beta & -\sin \beta \\ \sin \beta & \cos \beta \end{pmatrix} \cdot \begin{pmatrix} h_d^- \\ h_u^+ \end{pmatrix}, \\ \begin{pmatrix} G^0 \\ A^0 \end{pmatrix} &= \sqrt{2} \begin{pmatrix} \cos \beta & -\sin \beta \\ \sin \beta & \cos \beta \end{pmatrix} \cdot \begin{pmatrix} \text{Im}(h_d^0) \\ \text{Im}(h_u^0) \end{pmatrix}, \\ G^+ &= (G^-)^\dagger \\ H^+ &= (H^-)^\dagger. \end{aligned} \quad (2.56)$$

The G^0 and G^\pm can be identified as Goldstone bosons. The physically observable Higgs bosons are the CP-even h^0 and H^0 bosons, the CP-odd A^0 boson and the charged Higgs bosons H^\pm . The Goldstone bosons vanish by requiring unitary gauge as was done in the SM Higgs mechanism. Their degrees of freedom are absorbed as polarizations in the therefore massive Z and W bosons.

The values of β and α are unknown but related to each other and boson masses as follows⁸:

$$\begin{aligned}\sin 2\alpha &= -\sin 2\beta \cdot \left(\frac{m_{H^0}^2 + m_{h^0}^2}{m_{H^0}^2 - m_{h^0}^2} \right), \\ \cos 2\alpha &= -\cos 2\beta \cdot \left(\frac{m_{A^0}^2 + m_{Z^0}^2}{m_{H^0}^2 - m_{h^0}^2} \right).\end{aligned}\quad (2.57)$$

Furthermore, it can be shown that the couplings g to up-type fermions ($u\bar{u}$), down-type fermions ($d\bar{d}$) and vector bosons (VV) fulfill the following sum rules:

$$\begin{aligned}g_{h^0 d\bar{d}}^2 + g_{H^0 d\bar{d}}^2 &= \frac{1}{\cos^2 \beta}, \\ g_{h^0 u\bar{u}}^2 + g_{H^0 u\bar{u}}^2 &= \frac{1}{\sin^2 \beta}, \\ g_{h^0 VV}^2 + g_{H^0 VV}^2 &= 1.\end{aligned}\quad (2.58)$$

The couplings of the neutral MSSM Higgs bosons $\Phi = h^0, H^0, A^0$ in comparison to the SM Higgs boson H of equal mass are shown in Table 2.5. One can see that the coupling to down-type fermions is enhanced for the A^0 for large values of $\tan \beta$ (i.e. small values of $\cos \beta$) and either not too small values of $\sin \alpha$ for h^0 or not too small values of $\cos \alpha$ for H^0 . Especially the coupling of the A^0 boson to down-type fermions is proportional to $\tan \beta$, the cross section is therefore proportional to $\tan^2 \beta$ compared to the cross section of the SM Higgs boson.

Φ	$g_{\Phi u\bar{u}}/g_{Hu\bar{u}}$	$g_{\Phi d\bar{d}}/g_{Hd\bar{d}}$	$g_{\Phi VV}/g_{HV V}$
h^0	$\cos \alpha / \sin \beta$	$-\sin \alpha / \cos \beta$	$\sin(\beta - \alpha)$
H^0	$\sin \alpha / \sin \beta$	$\cos \alpha / \cos \beta$	$\cos(\beta - \alpha)$
A^0	$1 / \tan \beta$	$\tan \beta$	0

Table 2.5.: The couplings of the neutral MSSM Higgs bosons Φ to up- and down-type fermions and vector bosons compared to a SM Higgs boson H of equal mass. The coupling of the CP-odd A^0 to vector bosons is forbidden because of CP conservation.

A natural but yet to be confirmed value of $\tan \beta$ can be obtained by the following consideration (from [33]). In the SM the ratio of $t\bar{t}H$ to $b\bar{b}H$ coupling at tree level is given by:

$$\frac{g_{H t\bar{t}}^{SM}}{g_{H b\bar{b}}^{SM}} = \frac{m_t}{m_b} \approx 35. \quad (2.59)$$

⁸When including radiative corrections, the mixing angle α becomes an effective angle α_{eff} .

In contrast in the MSSM this ratio depends on the value of $\tan \beta$ (again in leading order):

$$\frac{g_{\Phi t\bar{t}}^{MSSM}}{g_{\Phi b\bar{b}}^{MSSM}} = f_{\Phi}(\alpha, \beta) \cdot \frac{1}{\tan(\beta)} \cdot \frac{m_t}{m_b}, \quad (2.60)$$

with $f_{\Phi}(\alpha)$ being given by (as compared to Table 2.5):

$$f_{\Phi}(\alpha, \beta) = \begin{cases} -\cot \alpha, & \Phi = h^0 \\ \tan \alpha, & \Phi = H^0 \\ \cot \beta, & \Phi = A^0. \end{cases} \quad (2.61)$$

Assuming that the ratio of the couplings and $f_{\Phi}(\alpha, \beta)$ to be in the order of one, values of $\tan \beta$ as large as 30-40 could be accommodated naturally in the MSSM.

Within the MSSM the masses of the CP-even neutral Higgs bosons are calculable in terms of the other MSSM parameters. In fact, on tree level only two parameters remain free which are commonly chosen to be $\tan \beta$ and m_A . One can find a constraint on m_{h^0} as follows:

$$\begin{aligned} m_{h^0} &\leq m_{A^0} \leq m_{H^0}, \\ m_{h^0} &\leq m_{Z^0} \leq m_{H^0}. \end{aligned} \quad (2.62)$$

Equation 2.62 in particular states that m_{h^0} is smaller than m_Z , which contradicts the LEP result of $m_H > 114$ GeV. However, radiative corrections raise this mass constraint up to values of $m_{h^0} \lesssim 135$ GeV [34]. Those corrections arise mainly from top and stop loops, and at high $\tan \beta$ values also bottom and sbottom loops, and therefore depend greatly on the top mass. This constraint on the Higgs boson mass is especially interesting since the electroweak precision fit (as was discussed before on Figure 2.2) indicates the preference of a light Higgs boson, although in the SM theory such a hard limit does not exist.

The full MSSM Lagrangian contains SUSY breaking operators (so-called soft SUSY breaking terms), leading to more than 100 new physical parameters. This is because the exact dynamics of the breaking mechanism are unknown. The soft SUSY breaking terms in the MSSM Lagrangian do not lead to quadratic divergences, which means they do not destroy the delicate cancelation introduced in the discussion on fine tuning. The underlying idea behind this is that at much higher energy scales than the weak scale (~ 100 GeV) there is a *hidden sector* which breaks SUSY spontaneously. This is communicated to the weak scale in some yet unknown mechanism resulting, however, in the soft breaking terms [35]. The introduction of these various new parameters seems to be counterproductive compared to the 19 free parameters of the SM. The parameter space, however, can be truncated to solutions not including unacceptable phenomenology such as flavor changing neutral currents for instance. Another way to constrain the SUSY parameter space is to require coupling constant unification at the GUT scale. It is common to fix almost all of these parameters in the so-called constrained MSSM and to study only a few different points of the remaining 7 free parameters to exemplify the sensitivity reach of experiments (details follow in the next subsection). The actual parameter values which are realized in nature can either be measured in the case of observables like SUSY particle masses, or they must be extracted by fitting experimental data to the theoretical models using high dimensional fitting programs such as Fittino [36] or Gfitter [18] in case of non-observables.

2.2.4. Benchmark Scenarios

On tree level the MSSM Higgs sector is fully described by the A^0 boson mass and the value of $\tan\beta$. By higher order corrections the Higgs boson properties become sensitive to the SUSY breaking mechanism and therefore all other parameters. The largest impact stems from the $t - \tilde{t}$ and $b - \tilde{b}$ sectors. As mentioned above, the SUSY parameter space is usually constrained and only the following 5 quantities are left free:

M_{SUSY}	Energy scale of the SUSY breaking
M_2	Gaugino mass at the electroweak scale
μ	Mass parameter in the supersymmetric Higgs potential
$m_{\tilde{g}}$	Gluino mass
X_t	Stop mixing parameter (usually studied in different renormalization schemes)

It is still difficult to explore and to visualize the entire 7 dimensional parameter space, therefore the five enumerated parameters - except for m_A and $\tan\beta$ - are fixed in benchmark scenarios representing different SUSY phenomenology aspects. The benchmark scenarios were formerly developed for the Higgs boson search at LEP (Ref. [37]) and have later been adjusted to hadron collider physics (details in [38]).

The scenarios mainly influence the upper mass constraint on m_h . In the m_h^{\max} scenario the parameters are chosen such that the value of m_h for a given value of $\tan\beta$ is maximized leading to conservative limits on $\tan\beta$. The *minimal mixing* scenario is constructed similar to the m_h^{\max} but with vanishing mixing in the stop sector. This decreases the theoretical m_h limit to $m_h < 116$ GeV which is still slightly above the LEP sensitivity limit. The *large μ* scenario yields relative small Higgs boson masses compared to the m_h^{\max} scenario and suppressed decays to b and τ pairs. LEP was able to cover the complete $m_A - \tan\beta$ plane of the *large μ* scenario and consequently this scenario is ruled out already and will not be considered anymore. In the *gluophobic Higgs* scenario the direct Higgs boson production (gluon fusion) is strongly suppressed for not too large values of m_A . Furthermore, the decay of h to photon pairs is suppressed here. In the *small α_{eff}* scenario the decay modes $h \rightarrow b\bar{b}$ and $h \rightarrow \tau^+\tau^-$ are suppressed, especially for large values of $\tan\beta$. However, in this scenario the decay $h \rightarrow \gamma\gamma$ is not suppressed in comparison to the SM for large parts of the $m_A - \tan\beta$ plane.

The discussed scenarios do conserve CP, but CP violation in the Higgs sector cannot be a priori excluded [39]. CP violation could be realized by introducing a complex phase in the soft SUSY breaking terms (analog to the complex phase in the quark mixing matrix). The *CPX* scenario is such a realization and was explored at LEP but it will not be considered here.

The values of the SUSY parameters as fixed by the benchmark scenarios are listed in Table 2.6. The m_h^{\max} scenario is the bases for the presented Monte Carlo studies. The properties of the neutral MSSM Higgs bosons in the m_h^{\max} scenario are discussed in the next subsection.

2.2.5. Production of Neutral MSSM Higgs Bosons at the LHC

In the MSSM other production channels gain importance in comparison to the SM, depending on the benchmark scenario. In the m_h^{\max} -scenario the coupling to down-type fermions is enhanced. Consequently, the bottom quark associated production channel $pp \rightarrow b\bar{b}\Phi$ (with $\Phi \in (h, H, A)$) becomes relevant and in the gluon fusion process $pp \rightarrow gg\Phi$ the contributions from bottom quark

Parameters	m_h^{\max}	min. mixing	gluophobic	small α_{eff}	large μ
M_{SUSY}	1000	2000	350	800	400
M_2	200	200	300	500	400
μ	200	200	300	2000	1000
$M_{\tilde{g}}$	800	8000	500	500	200
X_t^{OS}	2000	0	-750	-1100	-300
$X_t^{\overline{MS}}$	2450	0	-770	-1200	-300
max. value of m_h	133	116	119	123	107

Table 2.6.: Parameters of the CP conserving benchmark scenarios and their numerical values given in GeV. The stop mixing parameter X_t is given in the on-shell and the \overline{MS} renormalization schemes. The maximum allowed value of m_h is not a free parameter and only given for information assuming a top mass of $m_t = 174.3$ GeV.

loops next to top loops have to be considered. A discussion on the cross sections of these processes follows in the next subsection. Figure 2.6 depicts a few Feynman diagrams for the b-associated production and the gluon fusion.

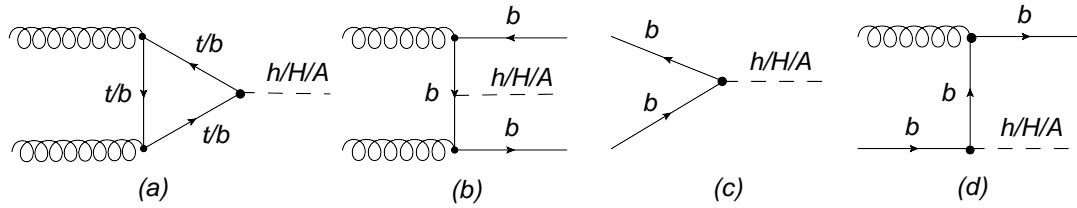


Figure 2.6.: Lowest order Feynman diagrams for the gluon fusion (a) and b-associated production (b,c,d).

2.2.6. Properties of the Neutral MSSM Higgs Boson in the m_h^{\max} scenario

The masses, widths, branching fractions and cross sections of the neutral MSSM Higgs bosons in the m_h^{\max} benchmark scenario are calculated using the program FEYNHIGGS 2.6.5⁹. FeynHiggs is a Fortran code for the diagrammatic calculation of the masses, mixings and other properties of the Higgs bosons in the MSSM at the two-loop level [40–43].

Figure 2.7 illustrates the Higgs boson masses as a function of m_A . The h and A bosons are almost degenerate in mass for $m_A \lesssim 130$ GeV, the H and the A are approximately degenerate in mass if $m_A \gtrsim 130$ GeV. The remaining mass difference depends on $\tan\beta$ and becomes smaller for an increasing value of $\tan\beta$. At $m_A \approx 130$ GeV, in the intense coupling region, all three neutral Higgs bosons come close in mass and a separation will be very difficult. As will be pointed out later, the mass resolution in the $\tau\tau$ decay channel is not sufficient for a separation. In the decay channel $h/H/A \rightarrow \mu\mu$ a separation could be possible depending on the amount of accumulated

⁹A top mass of $m_t = 172.5$ GeV was used as input to FEYNHIGGS.

data, detector understanding and the value of $\tan\beta$ [44]. A higher value of $\tan\beta$ leads to a larger cross section, but then the mass difference between the Higgs bosons becomes smaller.

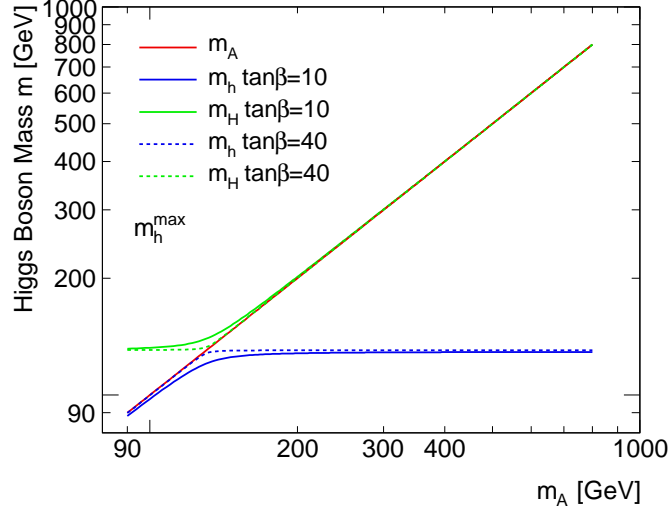


Figure 2.7.: Masses of the neutral MSSM Higgs bosons in the m_h^{\max} scenario as function of m_A for a low (dashed lines) and a high (solid lines) value of $\tan\beta$. The h and A (H and A) are almost degenerate in mass for $m_A \lesssim 130$ GeV ($m_A \gtrsim 130$ GeV). The mass difference depends on $\tan\beta$ and becomes smaller for an increasing value of $\tan\beta$.

The total widths of the neutral Higgs bosons are depicted in Figure 2.8 as a function of m_A . They become larger with increasing values of $\tan\beta$. The widths of H and A are of the order of a few GeV for not too large values of $\tan\beta$ and m_A . The detector resolution in the $\tau\tau$ channel is limited, hence the reconstructed widths is larger than the natural width by approximately one order of magnitude.

The branching ratio (BR) of the Higgs bosons to τ -pairs are shown in Figure 2.9 together with the value for a SM Higgs boson with a mass equal to m_A . In the SM the $H \rightarrow \tau\tau$ mode is only relevant for a light Higgs boson mass up to $m_H \approx 160$ GeV, where the decays to ZZ and WW start to dominate. In the MSSM the decay to vector bosons is suppressed and the $\tau\tau$ channel is relevant in the whole allowed mass region up to 1 TeV. The branching ratio depends on $\tan\beta$ and is larger for increased values of $\tan\beta$. In the high $\tan\beta$ region the decay probability to tau pairs is stable about 10%. The decay to bottom pairs has a branching fraction of approximately 90%, however, this channel is almost impossible to trigger and therefore indistinguishable from QCD background.

The cross section for b-associated production is shown in Figure 2.10. The SM cross section value is also depicted, it is several orders of magnitude smaller than the MSSM value, depending on the value of $\tan\beta$. The b-associated production is a completely negligible process in the SM. For very large values of m_A (depending on $\tan\beta$) the cross section of the lightest CP even boson h becomes larger than the cross section for H and A . This is also called the decoupling region. In fact, if a small value of $\tan\beta$ is realized in nature, the h will be the only visible MSSM Higgs over a large range of m_A . It will then be indistinguishable from the SM Higgs. In the intense coupling region

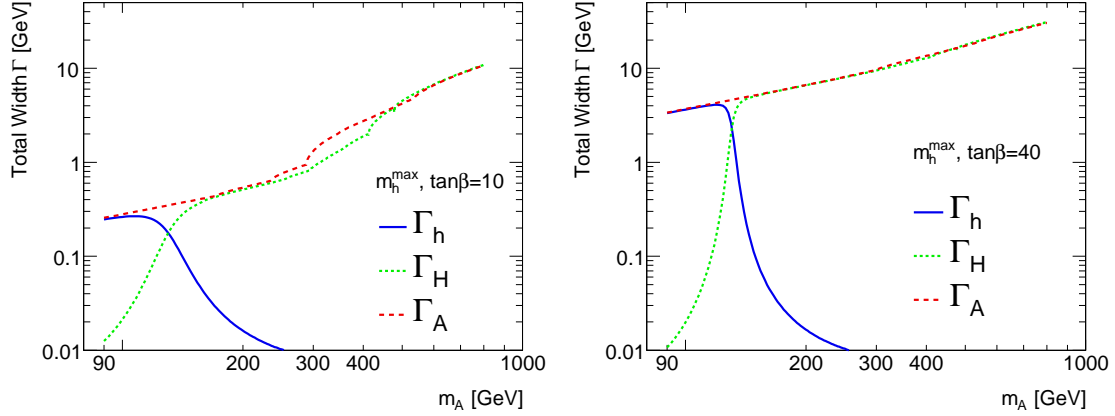


Figure 2.8.: Total width of the neutral MSSM Higgs Bosons as function of m_A for two values of $\tan\beta$. The left plot shows the widths for $\tan\beta = 10$, the right plot illustrates them for $\tan\beta = 40$.

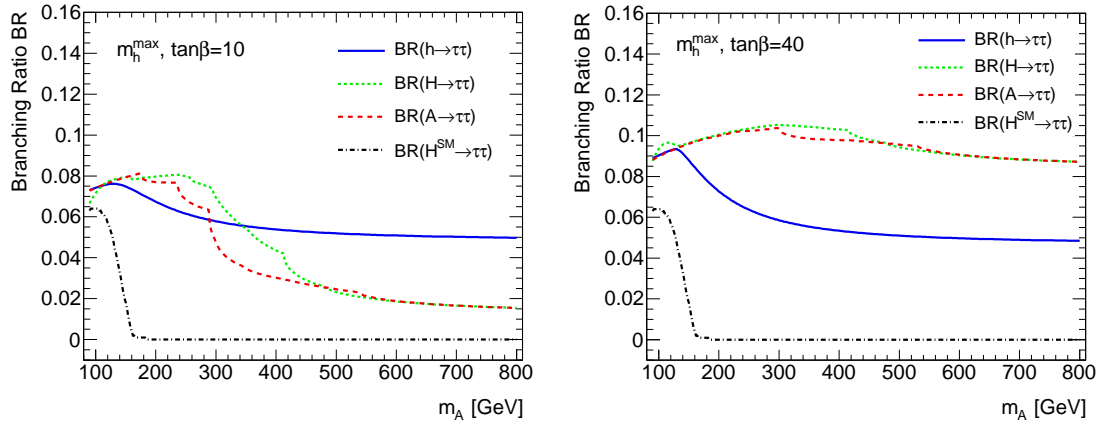


Figure 2.9.: Branching ratio of the Higgs bosons to tau pairs as function of m_A , left for $\tan\beta = 10$ and right for $\tan\beta = 40$. The branching ratio of the SM Higgs boson with a mass of m_A is also illustrated. The enhancement of the coupling to down-type fermions is visible.

the cross sections of h , H and A are approximately equal. Below $m_A \approx 130$ GeV the cross section of H and above $m_A = 130$ GeV the cross section of h is much smaller than the ones of the mass degenerate bosons. Consequently, when analyzing this channel, only one signal sample needs to be simulated: One Higgs boson signal with mass equal m_A and the cross section equal the sum of the cross sections of the degenerate bosons.

The cross sections of the direct production (gluon fusion) are displayed in Figure 2.11 together with the value for a SM Higgs boson with mass equal m_A . The SM cross section is larger than the MSSM values for $m_A \gtrsim 200$ GeV. The MSSM cross section of gluon fusion compared to b -associated production is smaller except for small values of m_A . The h boson has the dominant cross section over a larger region of m_A compared to the b -associated channel, the H and the A

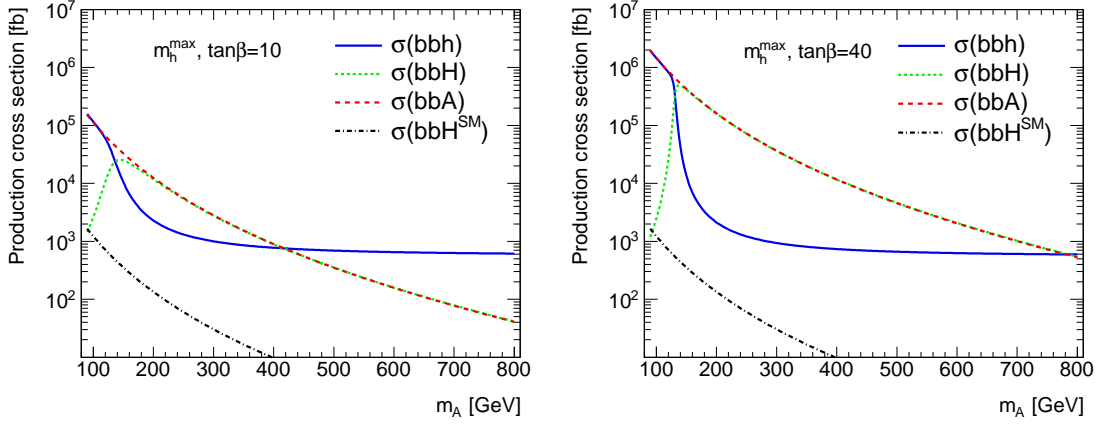


Figure 2.10.: Production cross section for bottom associated MSSM Higgs bosons as function of m_A for $\tan\beta = 10$ (left plot) and $\tan\beta = 40$ (right plot). The value of a SM Higgs with the mass equal to m_A is also shown. The SM cross section is several orders of magnitude smaller than the MSSM cross section.

will not be detectable in this region. For a light A boson, however, and large values of $\tan\beta$ the gluon fusion channel is a valuable addition to the b -associated production, especially in the case of an analysis approach without identifying b -jets (for instance in case of problems with the tracking system).

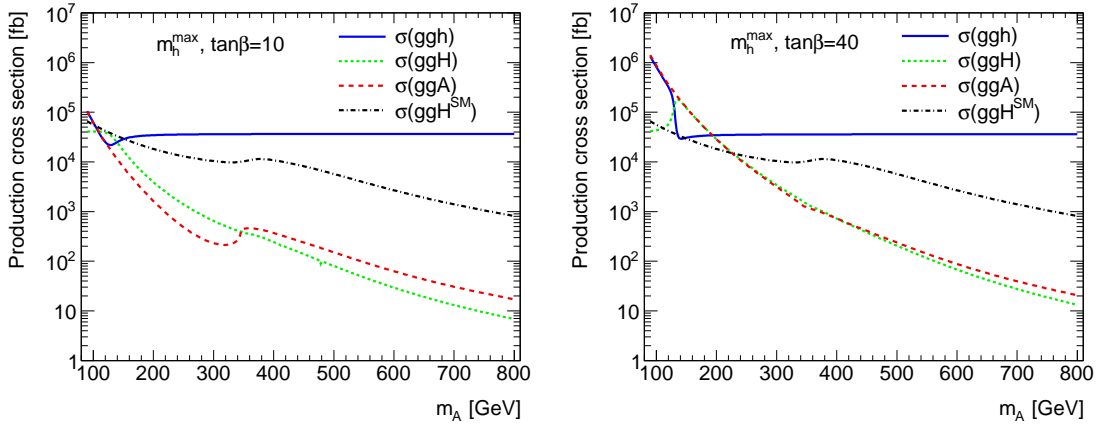


Figure 2.11.: Gluon fusion production cross sections of the neutral MSSM Higgs bosons as function of m_A . The left plot is given for $\tan\beta = 10$ and the right plot for $\tan\beta = 40$. The SM cross section value is also displayed for a mass equal to m_A .

The dependence of the cross sections for direct and b -associated production on the value of $\tan\beta$ is shown in Figure 2.12. The cross sections of bbH and bbA show a quadratic dependence on $\tan\beta$, while σ_h is almost constant over the considered $\tan\beta$ range. The same behavior for σ_h is visible in the gluon fusion process. The cross sections of H and A in direct production show a dip for small values of $\tan\beta$ but increase for larger values.

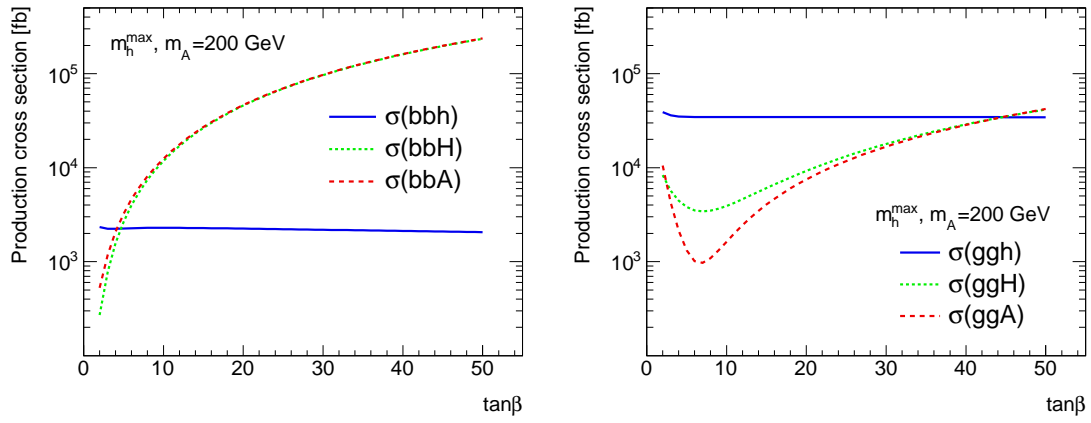


Figure 2.12.: The dependence of the cross sections on $\tan\beta$ in b-associated production (left plot) and gluon fusion (right plot) for $m_A = 200$ GeV. The cross sections of bbH and bbA show a quadratic dependence, for gluon fusion the dependence is more complicated. The cross sections for the h boson in both production modes are fairly independent of $\tan\beta$.

Previous and Present Higgs Boson Searches

3.1. Higgs Boson Searches at LEP

LEP was an electron positron collider located at the CERN laboratory operating from 1989 until 2000 at a variable center of mass energy \sqrt{s} of up to 209 GeV. Its associated main experiments were ALEPH [45], DELPHI [46], L3 [47] and OPAL [48].

3.1.1. Search for SM Higgs Bosons

At LEP a potential SM Higgs boson would have been produced mainly in the Z-associated Higgsstrahlung process $e^+e^- \rightarrow ZH$. Small additional contributions were expected from W and Z boson fusion. One main Higgs boson decay channel was the decay to $b\bar{b}$ and the decay of the associated Z bosons to $q\bar{q}$. Hence, the analyzed signatures were primarily four jet events. Unlike a hadron collider, the e^+e^- initial state at LEP is well defined and non-hadronic, thus it is possible to reconstruct a fully hadronic final state. Other signatures studied at LEP were the missing energy final state ($H \rightarrow b\bar{b}$, $Z \rightarrow \nu\bar{\nu}$), the leptonic final state ($H \rightarrow b\bar{b}$, $Z \rightarrow \ell^+\ell^-$) and the tau final states ($H \rightarrow b\bar{b}$, $Z \rightarrow \tau^+\tau^-$ and $H \rightarrow \tau^+\tau^-$, $Z \rightarrow b\bar{b}$).

The maximal kinematic range for a direct Higgs boson search in the ZH channel accessible at LEP was $m_H \leq 118$ GeV. In early analyses using data with $\sqrt{s} < 202$ GeV a SM Higgs boson with $m_H < 107.9$ GeV was excluded at 95% CL. [49]. At higher energies very close to the kinematic limit ($\sqrt{s} = 189$ GeV – 209 GeV), the experiments came to different conclusions. ALEPH reported an excess consistent with a SM Higgs boson hypothesis with $m_H = 115$ GeV [45]. The results of L3 [47] and OPAL [48] were consistent with a background only hypothesis. DELPHI measured a slight deficit of observed background events [46]. The results were combined in a global limit of $m_H < 114.4$ GeV at 95% CL. [2].

Figure 3.1 displays the globally combined test statistic $-2\ln Q$ as a function of the test mass m_H . Q is the ratio of the likelihoods of the signal plus background hypothesis, \mathcal{L}_{s+b} , and of the background only hypothesis, \mathcal{L}_b . In the mass range of $m_H > 115$ GeV the negative values of $-2\ln Q$ indicate a slight preference of the signal+background hypothesis albeit at low significance.

3.1.2. Search for MSSM Higgs Bosons

The main production channels for MSSM Higgs bosons at LEP were the Higgsstrahlung processes $e^+e^- \rightarrow Zh$ and $e^+e^- \rightarrow ZH$ for the CP-even Higgs bosons and the pair production processes $e^+e^- \rightarrow hA$ and $e^+e^- \rightarrow HA$ for the CP-odd bosons. Minor contributions were expected from W and Z fusion. The h boson decays mainly to fermion pairs and a small fraction to W and Z boson pairs, resulting from the fact that the mass of the h is well below the pair-production threshold.

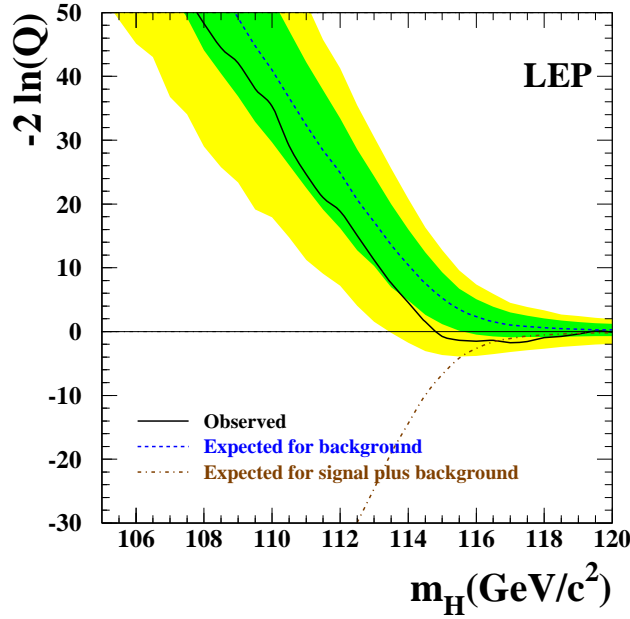


Figure 3.1.: LEP wide combination of the test statistic $-2\ln Q$ in the search for a SM Higgs boson (taken from Ref. [2]). For the background only hypothesis the 95% (green or dark shaded area) and 68% (yellow or light shaded) probability bands are also shown. The negative values of the test statistic at $m_H > 115$ GeV indicate that the signal + background hypothesis is slightly more favored than the background only hypothesis.

The A boson decays to fermions, mostly $b\bar{b}$ and $\tau^+\tau^-$, because the coupling to vector bosons is zero, as was mentioned before in Chapter 2. In the benchmark scenarios developed for LEP the SUSY mass scale is large and the decay to SUSY particles is therefore absent. A CP-violating scenario was also considered, indeed the same search channels were used as in the CP-conserving case and significant differences were expected in angular distributions due to spin correlations of the decay products.

For Higgs bosons produced via Higgsstrahlung the event signatures studied were the same as in the search for a SM Higgs boson (the four jet, missing energy, leptonic and tauonic signatures). In the case where the Higgs boson decay to b-quark pairs was suppressed, complementary flavor independent studies were conducted and no b-jet identification was required. Interesting final states for Higgs boson pair production were the four b-jet signature, mixed final states where one Higgs bosons decays to $b\bar{b}$ and the other to $\tau^+\tau^-$ and the four τ -lepton final state. If a Higgs boson produced in pair production decayed further into two Higgs bosons, thus three Higgs bosons were produced, final states ranging from six b-jets to six τ -leptons were studied and complemented by flavor-independent searches.

By scaling the excluded cross section of a SM Higgs boson to the MSSM cross section value and by studying the deviation of the Z boson width from the SM expectation, further points in the $m_A - \tan\beta$ plane were excluded.

LEP explored several CP-conserving and CP-violating benchmark scenarios and set limits in each

of them. The large μ scenario was ruled out. Limits were set on topological cross sections for Higgs-like signals. More details are given in Ref. [50]. As was done in the search for the SM Higgs boson, a likelihood ratio Q was used as test statistic to distinguish a background-only from a signal plus background hypothesis. For an exclusion, the ratio $\frac{L_{s+b}}{L_b}$ had to be less than 0.05. The top mass was either fixed to $m_t = 174.3$ GeV or varied. Using the fixed top mass and the m_h^{\max} scenario at high values of $\tan\beta$, the h is excluded for $m_h < 92.8$ GeV and the A boson is excluded for $m_A < 93.4$ GeV at 95% CL. Figure 3.2 illustrates the excluded regions in the $m_A - \tan\beta$ plane. It also displays the exclusion of $\tan\beta$ as a function of the top mass. For $m_t = 172.5$ GeV a value of $0.6 < \tan\beta < 2.5$ is excluded.

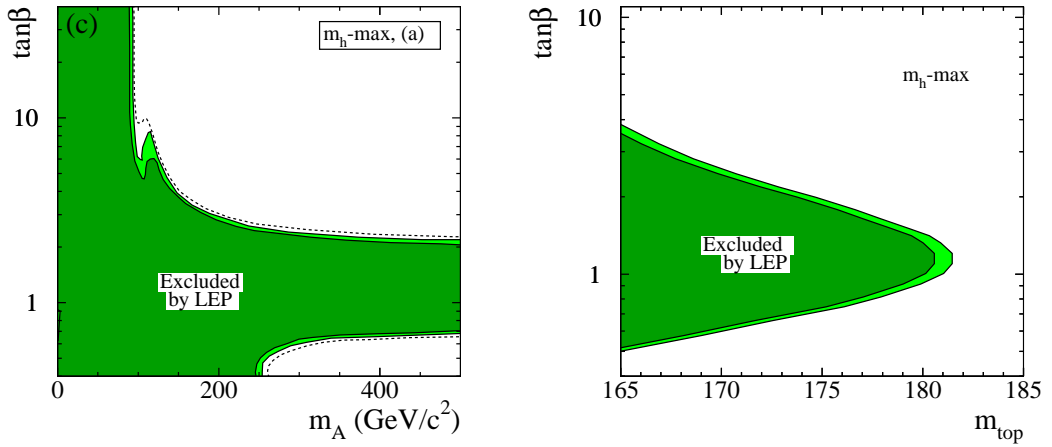


Figure 3.2.: Combined LEP search results for the neutral MSSM Higgs bosons in the m_h^{\max} benchmark scenario (from Ref [50]). The left plot shows the exclusion areas in the $m_A - \tan\beta$ plane, the right plot as function of m_t and $\tan\beta$. The light shaded (light green) area shows the 95% CL., the dark shaded are (dark green) the 99.7% CL. exclusion region. The dashed line display the expected exclusion based on Monte Carlo studies.

Two variations of the m_h^{\max} scenario have been studied. When inverting the sign of μ , the exclusion of $\tan\beta$ at $m_t = 172.5$ GeV decreases to $0.6 < \tan\beta < 2.1$. If the signs of μ and X_t are inverted, the limit on $\tan\beta$ at the same top mass changes to $0.55 < \tan\beta < 2.7$.

3.2. Higgs Boson Searches at the Tevatron

The Tevatron is a proton-antiproton collider located near Fermilab in the USA operating at a center of mass energy of $\sqrt{s} = 1.96$ TeV. The CDF and DØ experiments take data since 1987 and will continue operation for a couple of years. Not all available data has been analyzed so far, hence future updates on the analyses will yield improvements of the current results. Until the writing of this thesis no significant signal excess has been found.

3.2.1. Search for SM Higgs Bosons

The Tevatron experiments published several papers on Higgs boson searches, each one corresponding to the most recent accumulated luminosity, the latest one in July 2010 with an integrated luminosity of up to 6.7 fb^{-1} [3]. The sensitivity from these new combinations exceed those of previous combinations significantly [51, 52].

The combination includes overall 129 exclusive final states from both experiments. The analyses contain multi-variate techniques, such as boosted decision trees and neural networks. Production channels studied are the W- and Z-associated production, vector boson fusion and gluon fusion. Decay modes analyzed are $H \rightarrow b\bar{b}$, $H \rightarrow WW$, $H \rightarrow \tau\tau$ and $H \rightarrow \gamma\gamma$. In addition, an analysis of $t\bar{t}H \rightarrow t\bar{t}b\bar{b}$ was performed.

The $H \rightarrow WW$ channel has the highest sensitivity especially for Higgs bosons with masses above 150 GeV where the branching ratio is almost 100%. In the $H \rightarrow WW$ analysis signal events are characterized by large MET and two oppositely charged and isolated leptons. The dileptonic final states ee , $\mu\mu$ and $e\mu$ are considered since they provide a clear signature. However, also the case where one W boson decays into two jets was considered in one sub-analysis. The events are classified by the number of jets (0, 1 and 2 or more jets) and these channels are then combined.

In the low mass region, the W/Z associated production and the subsequent decay of the Higgs boson to b-quark pairs are the most sensitive channels. Independent sub-analyses have been performed requiring one or two b-tags and different jet multiplicities. In the case of ZH production the Z boson decay to two leptons or two neutrinos was analyzed. In the case of WH production the decay studied was $W \rightarrow \ell\nu$.

Figure 3.3 displays the observed and expected limits on the SM Higgs boson. The limits are expressed as a multiple of the SM cross section prediction as a function of the Higgs boson test mass. Given the signal-plus-background hypothesis and $m_H = 115 \text{ GeV}$ ($m_H = 165 \text{ GeV}$), a factor of 1.56 (0.68) times the SM cross section is the current upper limit on the Higgs boson production. Light SM Higgs boson with masses up to 109 GeV and heavier Higgs boson with masses between 158 GeV and 175 GeV are excluded with 95% CL.

3.2.2. Search for MSSM Higgs Bosons

The Tevatron experiments conducted searches for the neutral MSSM Higgs bosons in gluon fusion and b-associated production in inclusive modes without b-tagging information or by requiring identified b-jets. The inclusive production mode yielded larger cross sections but was only useable in the $\tau\tau$ final states due to overwhelming QCD backgrounds, whereas in the associated production $\tau\tau$ and $b\bar{b}$ decays were analyzed. Upper limits on production cross sections were then interpreted as exclusion regions in the $m_A - \tan\beta$ plane. Searches for charged Higgs bosons lighter than the top quark were done by analyzing events expected from $t\bar{t}$ decays and limits were set as well¹.

In March 2010 an update on the $\tau\tau$ final state analyses was released resulting in better exclusion limits than ever before. The fully and semi-leptonic final states were investigated using integrated luminosities of 1.8 fb^{-1} up to 2.2 fb^{-1} and improved theoretical calculations. The treatment of correlations between systematic uncertainties arising from background estimates based on Monte Carlo was revisited. The W background, which is a very important background in the semi-leptonic final states, was estimated by the use of a control data sample. Tau identification was

¹Details on those studies can be found in [53].

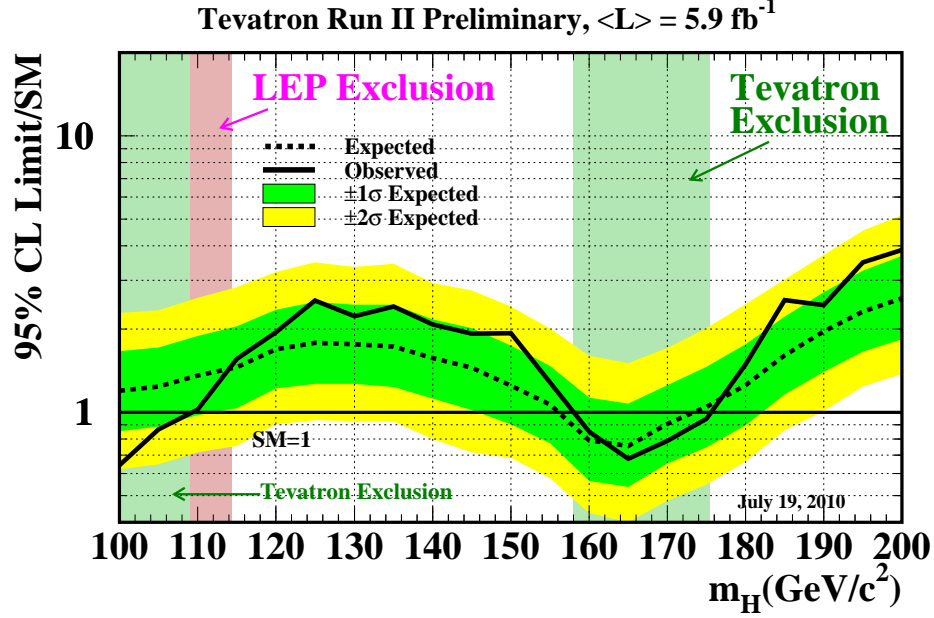


Figure 3.3.: Combined results for the SM Higgs boson search at CDF and D0 (from [3]). The solid (dashed) line shows the observed (expected) 95% CL. exclusion contour in multiples of SM Higgs boson cross sections for the background only hypothesis. The green and yellow (dark and light shaded) areas indicate the 1σ and 2σ uncertainty bands on the expected limit, respectively. Tevatron excluded SM Higgs bosons with masses of up to 109 GeV and between 158 GeV and 175 GeV mostly based on the $H \rightarrow WW$ decay channel.

based on neural networks. The statistical combination of the subsequent tau decay channels was cross checked by using Bayesian and frequentistic approaches which gave similar results within 10%. Limits on the cross sections times BR for neutral MSSM Higgs bosons range from 13.6 pb to 0.65 pb for masses between 90 GeV up to 200 GeV, as shown in Figure 3.4. These limits are interpreted in the benchmark scenarios. The right plot of Figure 3.4 displays the exclusions in the $m_A - \tan\beta$ plane for the m_h^{\max} scenario. Inverting the sign of μ had only very little effect on the results. These updated results significantly shift the upper limit on $\tan\beta$ in comparison to former publications.

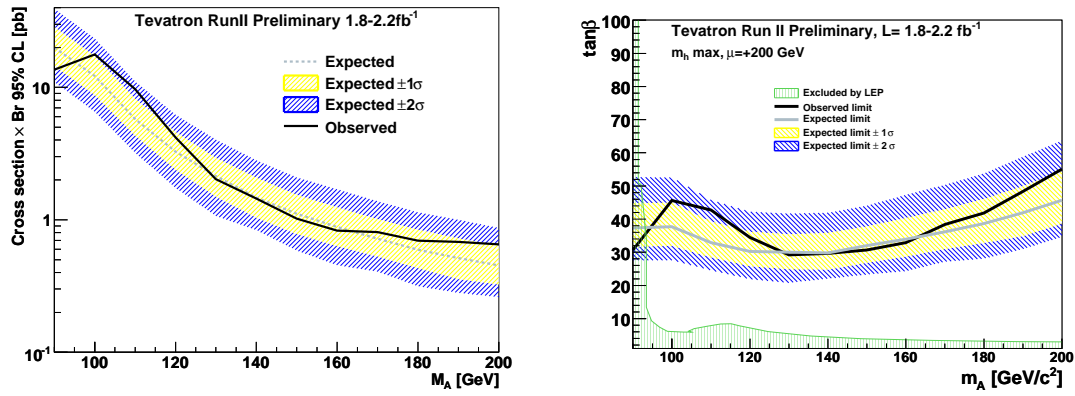


Figure 3.4.: Combined Tevatron results from neutral MSSM Higgs boson searches (from Ref. [54]). In the left plot the solid (dashed) line displays the 95% CL. limit on the observed (expected) cross section times branching ratio of $H \rightarrow \tau\tau$ for the background only hypothesis. The yellow (light shaded) and blue (medium dark shaded) areas correspond to the 1σ and 2σ uncertainty bands. The right plot shows the exclusions in the $m_A - \tan\beta$ plane of the m_h^{\max} scenario. The color code is the same as for the left plot, the dark shaded region shows the LEP limits. No theoretical uncertainties were considered and minor effects from the Higgs boson width dependence on $\tan\beta$ were neglected.

4.1. The Large Hadron Collider

The Large Hadron Collider (LHC) is a proton-proton (and also lead-lead nuclei) collider machine located 50 m - 170 m underground near Geneva at the south-west border between Switzerland and France. The LHC design is reported in detail in Ref. [55]. It is operated by the CERN¹ laboratory. It was build into the same 27 km circumference tunnel that hosted the former LEP accelerator and its construction was basically completed in 2008, followed by one year of repairs after a quench incident². Since fall 2009 the LHC is operational again.

The LHC is based on the synchrotron principle with two separated beam pipes within one cryostat system (*two-in-one design*). The two proton beams run in opposite directions and are brought to collision at several points along the ring by crossing each other. 1 232 dipole magnets with a field strength of 8.3 T are used to force the beam onto its circular path, and 392 quadrupole magnets focus the beam. The magnets are cooled to 1.9 K with super fluid liquid helium to allow for super conductivity. The anticipated beam energy is 7 TeV, however, pending commissioning tasks such as the training of the super-conducting magnets lead to a reduction of the beam energy to 3.5 TeV during the 2010 and 2011 operation.

The ring consists of eight about 500 m long straight elements, four of them having beam intersection points. Between the straight elements there are 23 regular lattice periods containing quadrupoles, beam pick-up monitors and cryogenic connection systems. The multi-purpose detectors ATLAS [58] and CMS [20] are located vis-à-vis at Point 1 and Point 5 respectively. The ATLAS and CMS collaborations both will do electroweak precision physics and search for the Higgs boson, Supersymmetry and other physics beyond the SM. At Point 2 the ALICE experiment is located. ALICE will explore the quark-gluon plasma, a state of matter μs after the big-bang, by analyzing lead-lead collisions [59]. At Point 8 the LHCb detector is situated. LHCb is an asymmetric experiment which will mainly measure B hadrons and help to understand CP violation [60].

¹CERN - Conseil Européen pour la Recherche Nucléaire.

²The quench, which led to one year of repairs, happened on 19th of September in 2008, 9 days after LHC first became operational [56]. The source of the quench was a fault in the electrical connection between two dipoles during a ramping test. A resistive zone developed and triggered the quench protection system. An electrical arc, however, punctured the helium enclosure which lead to the release of large amounts of helium into the vacuum system. The valves could not handle the enormous pressure of more than 0.15 MPa which resulted into releasing helium into the beam pipes, the neighboring sectors and finally the tunnel itself. During this sudden pressure release many magnets became misaligned or were even misplaced by several tens of cm. As a consequence of this incident, the magnetic system had to be warmed up, 14 broken quadrupoles and 39 dipoles had to be brought to the surface for repairs and the beam pipe had to be cleaned on a length of 4 km. New safety systems were installed, above all a new quench protection system with special detectors, better valves and stronger magnet anchoring. Another shutdown has to take place before the magnets will be ramped up to the nominal field strength allowing for operation with $E = 7$ TeV per beam. This update will contain mainly a substitution of all the superconducting cable interconnections (*splices*) [57].

Point 3 and Point 7 are *cleaning insertions* and used for the collimation of the beam halo to minimize background and luminosity losses. At Point 4 the Radio-Frequency (RF) accelerator system is hosted. The field frequency is 400.8 MHz providing an accelerator gradient of 5 MV/m. The two beams are accelerated by separate cavities to alleviate losses due to transient beam loading and damping. Point 6 contains the beam dump system. In case of a beam abort first the beams are slowed down by special magnets and steered to transfer lines and finally dumped into massive absorbers. This system is important in case of hardware failures and for safety reasons (for example in case of an access during runs).

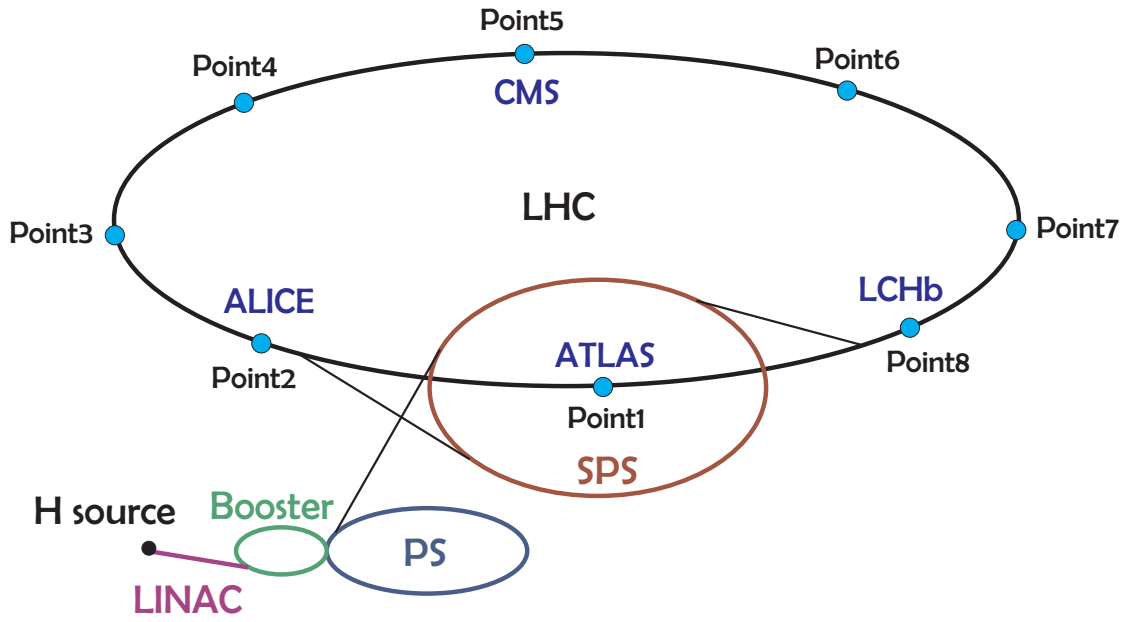


Figure 4.1.: Schematic and simplified view of the LHC and pre-accelerators (not to scale).

The protons are grouped into bunches, each bunch contains a maximum of $1.1 \cdot 10^{11}$ protons, and up to 2880 bunches will be filled into the ring. The LHC is designed for a bunch crossing rate of 40 MHz. The actual bunch crossing rate as well as the number of protons per bunch are variable and define the instantaneous luminosity, \mathcal{L} . The instantaneous luminosity is calculated from machine parameters as follows:

$$\mathcal{L} = \frac{N_b^2 \cdot n_b \cdot f \cdot \gamma \cdot F}{4\pi \cdot \varepsilon \cdot \beta^*}, \quad (4.1)$$

where N_b is the number of particles per bunch, n_b the number of bunches, f the revolution frequency, γ the relativistic gamma factor, ε the emittance, β^* the beta function at the interaction point and F a geometric factor. The design luminosity is $10^{34} \text{cm}^{-2} \text{s}^{-1}$, which will be reached after a few years of successful operation at lower luminosities. At high luminosities many proton-proton interactions (*pile-up*) will occur during one bunch crossing, for example at $10^{34} \text{cm}^{-2} \text{s}^{-1}$, 23 simultaneous collisions are expected. Lead ion collisions are foreseen at a luminosity of $10^{27} \text{cm}^{-2} \text{s}^{-1}$. The protons are taken from a hydrogen source. The hydrogen gets ionized and the protons are separated from the electrons by electromagnetic fields. The protons are then filled into the *linear*

particle accelerator (Linac-2) where they are pre-accelerated to 50 MeV. The next accelerator chain elements are the *Booster* and the *Proton Synchrotron* (PS) where the protons gain an energy of 1.4 GeV and 26 GeV, respectively. Then the protons are injected into the *Super Proton Synchrotron* (SPS) and accelerated to 450 GeV, from where they are injected into the LHC ring. Figure 4.1 displays the general concept of the accelerator complex and indicates the location of the 8 LHC access points.

4.2. The ATLAS Detector

The ATLAS³ detector is the largest of the main experiments with a size of 44 m in length, 22 m in diameter and a weight of 7000 t. In the following the main detector parts are briefly described. A full description is given in Ref. [61] and [58]. Figure 4.2 displays an image of the ATLAS detector.

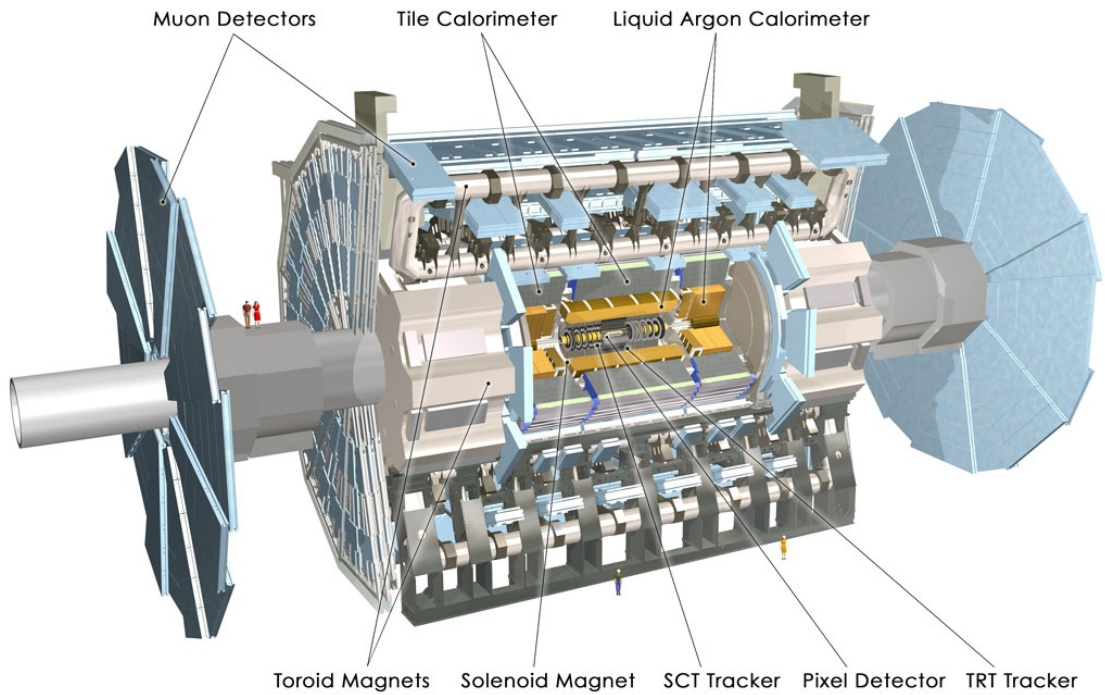


Figure 4.2.: The ATLAS detector in a cut-away view. The main systems are marked and labeled.

4.2.1. Coordinate System and Definition of Basic Quantities

The space coordinates x , y and z form a right-handed system defined as follows: The coordinate origin is the interaction point, the beam direction corresponds to the z axis, the x - y plane is the plane transverse to the beam direction, the positive x -axis points from the interaction point of the

³ATLAS - A Toroidal LHC Apparatus.

two proton beams to the center of the LHC ring, the y axis points upwards to the ground. Cylindrical coordinates are used in practise, formed by the radius R , the z coordinate and the azimuthal angle ϕ given by

$$\tan \phi = p_y / p_x. \quad (4.2)$$

The pseudorapidity η is defined as

$$\eta = -\ln \tan \theta / 2. \quad (4.3)$$

This variable is useful in data analysis since the number of particles produced in QCD processes is approximately flat in η in the fiducial detector volume. The polar angle θ is calculated from

$$\cot \theta = p_z / p_T, \quad (4.4)$$

where p_T is the transverse momentum, given by

$$p_T = \sqrt{p_x^2 + p_y^2}. \quad (4.5)$$

The distance ΔR is defined as follows:

$$\Delta R = \sqrt{(\Delta \eta)^2 + (\Delta \phi)^2}. \quad (4.6)$$

A sketch with the coordinates and angles as well as η as a function of θ is displayed in Figure 4.3. Trajectories of charged particles in an ideal uniform magnetic field are described by measuring the following five parameters: $1/p_T$, ϕ , d_0 (transverse track parameter, the transverse distance to the beam axis at the point of closest approach), $\cot \theta$ and z_0 (longitudinal impact parameter, z position of the track at the point of closest approach).

In hadron collisions, the transverse momentum, p_T , and transverse energy, E_T , are more reliable kinematic variables than \vec{p} or E , because the interacting partons carry an unknown fraction of the protons momentum in longitudinal direction. Using momentum conservation in the transverse plane, the components of the missing transverse momentum, $p_{T,\text{miss}}$, are defined as:

$$\begin{aligned} p_{x,\text{miss}} &= - \sum_{\text{particles}} p_x, \\ p_{y,\text{miss}} &= - \sum_{\text{particles}} p_y. \end{aligned} \quad (4.7)$$

In the ultra relativistic limit the missing transverse energy (MET) $E_{T,\text{miss}}$ is equal to $p_{T,\text{miss}}$.

The ATLAS detector is symmetrical with respect to the y axis. The side with negative values of z is called C side, the opposite one is the A side.

4.2.2. Inner Detector

The inner detector (ID) is installed closest to the interaction point. The high-radiation environment puts stringent conditions on detector technology, electronics and services like cooling. The purpose of the ID is to reconstruct the primary vertex and possible secondary vertices, to measure

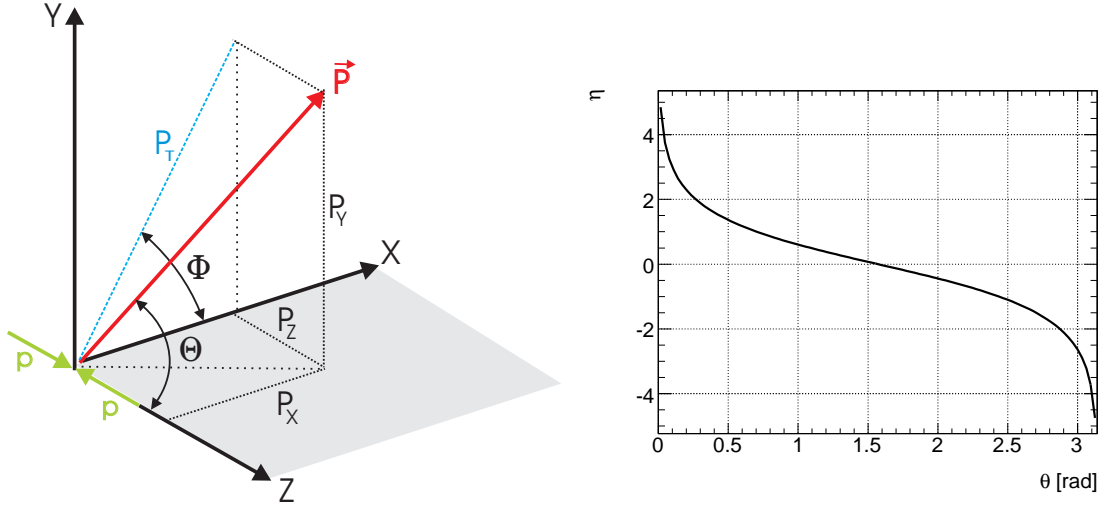


Figure 4.3.: Left: Coordinates and angles as used within ATLAS. Right: The dependence of the pseudorapidity η on the angle θ .

tracks from charged particles with $p_T > 0.5$ GeV (in initial data taking even $p_T > 0.1$ GeV) and to identify short-lived particles. It covers pseudorapidities of $|\eta| < 2.5$, extends 7 m in length and 1.15 m in radius and is located within a 2 T solenoid field. It consists of three independent but complementary sub-detectors: The pixel detector, the semi conductor tracker (SCT) and the transition radiation tracker (TRT). The TRT extends to $|\eta| < 2.0$ and allows to identify electrons and to suppress background from pions. The TRT is operated at room temperature, but the silicon sensors of the other two sub-detectors have to be cooled to -25 °C. In Figure 4.4 a drawing of the ID is illustrated. Two example tracks crossing the ID are shown as well.

The expected resolution of the impact parameters z_0 and d_0 are given as follows [58]:

$$\sigma(d_0) = 11 \oplus \frac{73}{p_T/\text{GeV}\sqrt{\sin\theta}} \quad (\mu\text{m}), \quad (4.8)$$

$$\sigma(z_0) = 87 \oplus \frac{115}{p_T/\text{GeV}\sqrt{\sin^3\theta}} \quad (\mu\text{m}). \quad (4.9)$$

The momentum resolution of a muon is stated as [58]:

$$\sigma\left(\frac{1}{p_T}\right) = 3.6 \cdot 10^{-4} \oplus \frac{1.3 \cdot 10^{-2}}{p_T/\text{GeV}\sqrt{\sin\theta}} \quad (\text{GeV}^{-1}). \quad (4.10)$$

The Pixel Detector

With a total of 140 million detector elements, the pixel detector has the highest granularity of all the ATLAS detectors. This granularity is needed to compensate for the high track density and to allow for good pattern recognition. One purpose of the pixel detector is to identify b-jets and τ -leptons by reconstructing their decay vertices.

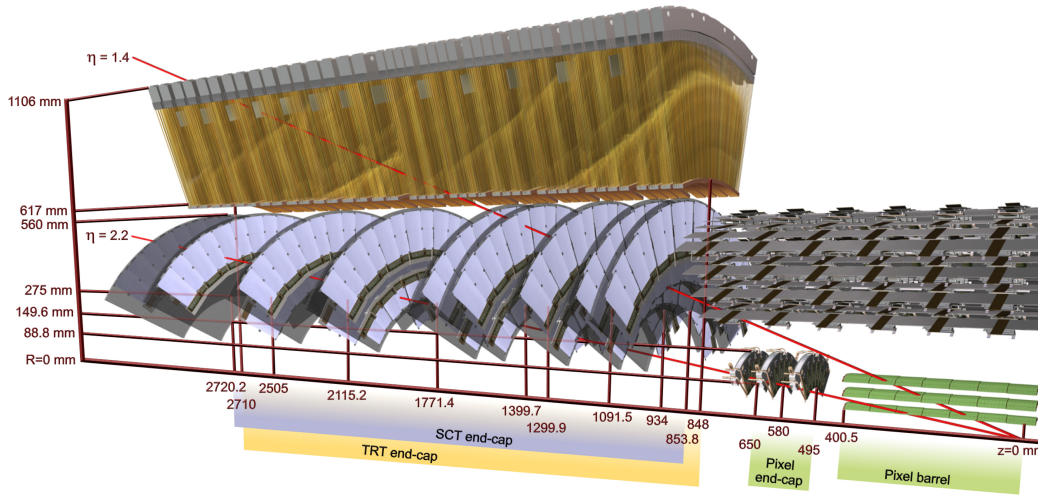


Figure 4.4.: Drawing of the inner detector components. Two tracks with $p_T = 10$ GeV arising from the interaction point cross the detector. The track with $\eta = 1.4$ traverses the three pixel layers, four of the SCT disks and circa 40 straws from the TRT. The track with $\eta = 2.2$ hits the innermost pixel layer, two of the pixel disks and the last four SCT disks. It misses the TRT completely.

The central part consists of three layers with 1456 modules. The layers are located alongside the z axis at radii of 5.05 cm, 8.85 cm and 12.25 cm and extend 801 mm in length. The innermost layer (also called B layer) of the pixel detector will be damaged by radiation after three years of operation at nominal luminosity. A new innermost layer will be inserted between the beam pipe and the B layer, probably in the year 2016. At larger z values, at $z = \pm 49.5$, $z = \pm 58.0$ and $z = \pm 65.0$ cm, there are pixel disks, three disks on each detector side. The disks are oriented transversal to the beam pipe and comprise 48 modules each. Each module contains 46080 pixels, and most of the pixels have a nominal size of $50 \times 400 \mu\text{m}^2$, the rest have a size of $50 \times 600 \mu\text{m}^2$. The modules overlap to provide a hermetic coverage.

The pixel sensors are semiconductor diodes in reverse-biasing mode. Charged particles crossing the high voltage field between the sensor electrodes lead to the production of electron-hole pairs. These excitons become separated and accumulate at the electrodes. This signal is measured and directed to the readout electronics.

The Semi Conductor Tracker

The SCT has a coarser granularity because it is further away from the interaction point than the pixel detector, where the highest track densities occur. It covers the region within $|\eta| < 2.5$. It was designed to provide eight precision measurements per track in the intermediate radial range. The SCT modules are arranged in the central region in four barrel layers at radii between 30 cm and 53 cm. In the forward direction there are 9 disks on each detector side between $z = 853$ mm and $z = 2710$ mm. Each disk has a radius of 56 cm. Each SCT module consists of four single sided p-on-n silicon detectors, and each detector has 768 readout channels. On each side of the module two single detectors are wire-bounded to form strips. In the barrel these strips are 12.8 cm in size and in the end-caps they are between 6 cm (at innermost radii) to 12 cm (at outer radii) in

length. Two of such wire-bonded detector pairs are then glued together at a 40 mrad angle, which allows the precise measurement of the z coordinate.

The SCT has a total of 61 m^2 of detector area and 6.2 million readout channels. The spatial resolution is $16 \text{ }\mu\text{m}$ in $R\phi$ and $580 \text{ }\mu\text{m}$ in z direction. Single tracks can be distinguished if they are separated by at least $200 \text{ }\mu\text{m}$.

The Transition Radiation Tracker

The outer tracker system is a combined straw tube tracker and transition radiation tracker. It is designed to provide 36 measurements along a track and covers the region within $|\eta| < 2.0$. The spacial track resolution is less than 0.15 mm for charged particles tracks of $p_T > 0.5 \text{ GeV}$.

The straw tubes have a diameter of 4 mm , a maximum length of 144 cm and are filled with a gas mixture of 70% Xe, 20% CO_2 and 10% CF_4 . In the center of each straw tube there is a $50 \text{ }\mu\text{m}$ thick gold-plated tungsten wire. A high voltage field is applied between the tubes and the wires. Charged particles which pass the tubes ionize the gas atoms in the tubes. The separated electrons drift toward the electrodes and ionize other gas atoms on their way. This leads to a pulse which is then recorded by the readout electronics.

The space between the straws is filled with Xenon gas and foils of polyethylene and polypropylene. Fast moving charged particles passing through those foils radiate photons as a function of the speed of the particle due to the different di-electrical constants of the materials used. These photons are then absorbed by the gas atoms in the tubes which then emit electrons. These electrons again ionize other atoms which lead to another signal pulse. The TRT allows to discriminate between electrons and charged particles of higher mass, like pions, for the same momentum.

The TRT barrel within $|\eta| < 0.7$ consists of 52544 straw tubes, which are arranged in three rings between radii of 56 cm to 107 cm parallel to the beam pipe. In forward direction until $|\eta| < 2.0$ 18 disks form one TRT end-cap on each detector side and here the tubes are oriented radially. The total number of TRT channels is about 351 000.

4.2.3. Calorimetry

A view of the ATLAS calorimeters is presented in Figure 4.5. The calorimeter system is partially based on Liquid Argon or on scintillator technology. The Liquid Argon calorimeter consists of an electromagnetic calorimeter (ECAL) with high granularity covering the pseudorapidity region $|\eta| < 2.5$, a hadronic calorimeter (HCAL) covering $|\eta| < 3.2$ and forward calorimeters (FCAL) covering $3.1 < |\eta| < 4.9$. The scintillator based calorimeter parts are the Tile barrel covering $|\eta| < 1.0$ and the extended Tile barrel in the range between $0.8 < |\eta| < 1.7$.

At larger values of η special calorimeters are used to measure the luminosity. They will be described later.

The calorimeters are designed to absorb the particles and measure their energies except for muons and only weakly interacting particles such as neutrinos or potential neutral sparticles. Particles enter the calorimeter, interact with the material and initiate a particle shower which is then detected. By separating the calorimeter in small segments both longitudinally and transversally, the particle track and its identity can be detected. The EM calorimeter is more sensitive to EM interacting particles especially electrons and photons, in hadronic calorimeters strongly interacting particles (jets) are measured. The hadronic calorimeter is located at outer radii and is supposed to absorb as many particles as possible in order to inhibit a punch-through into the muon system.

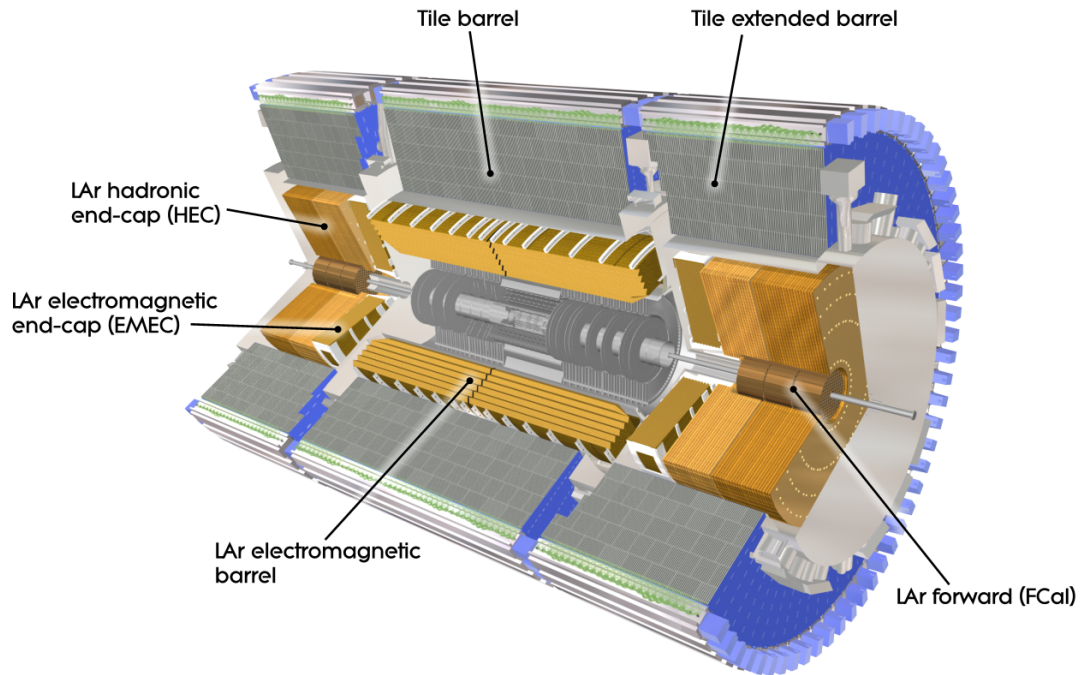


Figure 4.5.: Cut-away view of the ATLAS calorimeters. The golden parts are the Liquid Argon calorimeters, the greyish detectors are the hadronic Tile calorimeters. The calorimeters and the central solenoid are encapsulated in a threepart cryostat (one barrel and two end-cap vessels).

The missing energy is measured by summing over all calorimeter cells and correcting for noise and inactive (*dead*) material for example from the cryostats, support structure or non-functional cells. The cell energy has to be calibrated according to the object type measured. Details on the MET measurement are given in Ref. [19].

The Electromagnetic Calorimeter

The ECAL is a sampling calorimeter using lead as passive absorber and liquid argon (LAr) as active material. Electrons and photons interact with the absorber and emit photons via Compton scattering and bremsstrahlung, the photons convert into electron-positron pairs. These processes are repeated as long as the particles' energy is large enough, this way creating an EM shower. The electrons ionize the liquid argon atoms in the drift gaps and are driven to the electrodes by the high-voltage field, leading to secondary ionization and forming a pulse which is recorded by the readout electronics. The ECAL has about 190 000 channels.

The Kapton⁴ electrodes and absorbers are arranged in an accordion shape. This geometry provides for a full ϕ coverage and a fast readout. The folding angle is varied to allow for a constant drift gap size of 2.1 mm in the barrel. In the end-caps the gap size increases with radius from 0.8 mm to 3.1 mm.

⁴Kapton is the trade name for a high-end polyamide thermoplastic.

The ECAL is divided into a barrel part with $|\eta| < 1.475$ and an end-cap part (EMEC) covering a range of $1.375 < |\eta| < 3.2$ on each detector side. The barrel is divided into two identical parts which are separated by a 6 mm gap at $z = 0$. Each barrel half has a weight of 57 tons, a length of 3.2 m and consists of 16 modules each covering an azimuthal region of $\Delta\phi = 22.5^\circ$. Each barrel module contains 3424 cells. Each end-cap is divided into two wheels with 27 tons each, one inner wheel with $1.375 < |\eta| < 2.5$ and one outer wheel at $2.5 < |\eta| < 3.2$. The total thickness in terms of radiation lengths, X_0 , in the barrel is at least 24 and at least 26 in the end-caps.

The ECAL consist of three layers and a pre-sampler in the central region. The pre-sampler is 11 mm (5 mm) thick in the barrel (end-cap) and covers the region $|\eta| < 1.8$. It measures the early phase of the EM shower process to identify the material and therefore energy loss in front of the ECAL. The cells in the first sampling are of strip form with a pitch of 4.7 mm in η direction and a thickness of $4.3 X_0$. It has a high granularity of $\Delta\eta \times \Delta\phi = 0.003 \times 0.1$ to provide especially good separation of photons from π^0 decays. The second layer is divided into square towers of a size of $\Delta\eta \times \Delta\phi = 0.025 \times 0.025$ and extends up to $24 X_0$. This sampling collects the bulk of the EM showers. The third layer collects the tail of the shower and prohibits a recoil of the hadronic showers from the hadronic calorimeters into the first two layers. It has a granularity of $\Delta\eta \times \Delta\phi = 0.05 \times 0.025$ and a thickness between $2 X_0$ and $12 X_0$. The inner wheel of the end-cap is, however, only segmented into two layers at a coarser granularity of $\Delta\eta \times \Delta\phi = 0.1 \times 0.1$. A sketch of the sampling structure is presented in Figure 4.6.

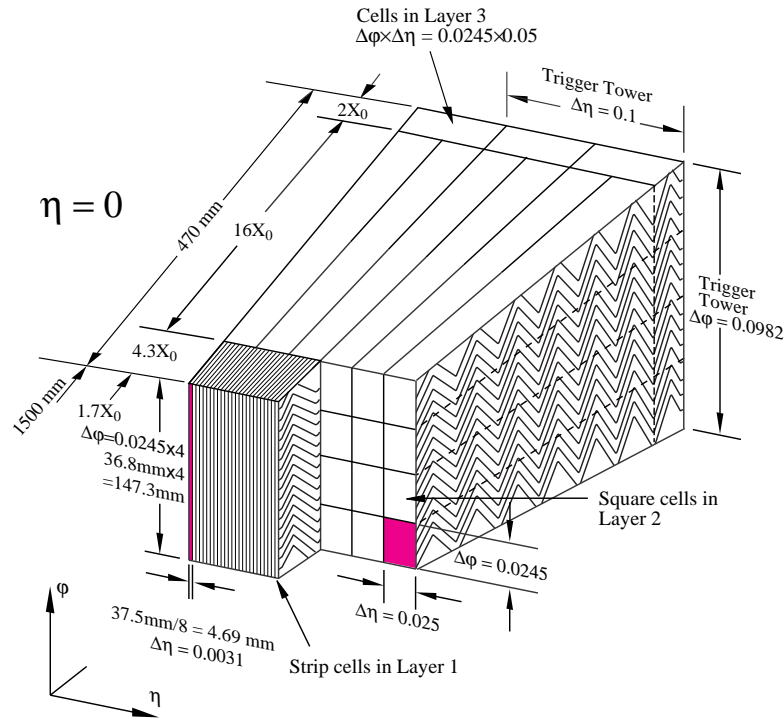


Figure 4.6.: Sketch of the three main samplings of the ECAL presented in a view from inside to outside. The pre-sampler is not drawn. The granularity in eta and phi of the cells of each of the three layers is also shown.

The barrel and each end-cap are encapsuled in a three-part cryostat. Between the barrel and the

end-cap cryostat vessel there is a physical gap, which is equipped with the minimum bias trigger scintillator (MBTS). The amount of inactive material in this transition region is $7 X_0$ large, which leads to a significant deterioration of the precision of the energy measurement within $1.37 < |\eta| < 1.52$.

The signal traverses the so-called feedthroughs to pass through the cryostat wall. The triangular signal gets shaped, sampled (one sample every 25 ns) and digitized in the front-end boards mounted on top of the cryostats. The signal information gets stored in 144 so-called pipeline cells to cope with the L1 trigger latency time of $2.5 \mu s$. From the amplitude and shape of the digitized signal pulse the energy and timing information is calculated. The trigger towers are built and sent to the central trigger processor (CTP). The back-end electronics located in the service hall outside the ATLAS cavern calculate the transverse energy which is needed as input to the next trigger levels. First data quality checks are performed before the information is finally processed by the reconstruction algorithms.

The expected energy resolution of the ECAL is stated as follows [58]:

$$\frac{\sigma(E)}{E} = \frac{a \cdot \sqrt{\text{GeV}}}{\sqrt{E/\text{GeV}}} \oplus b \oplus \frac{c}{E}, \quad (4.11)$$

with $a = 10\%$, $b = 0.7\%$ and $c = 300 \text{ MeV}$. The first term is denoted as sampling term and describes fluctuations of the number of particles n in the samplings $\sim \sqrt{n} \sim \sqrt{E}$. The second term is the linear term $\sim E$ and describes factors like leakage or ϕ modulation. The third term is the constant term arising from electronics noise and pile-up effects which depends on the luminosity but not on the energy.

The Hadronic Calorimeter

There are several subsystems which compose the HCAL. In the range $|\eta| < 1.7$ there is the Tile calorimeter (TileCAL), based on steel and scintillator material. LAr technology was used for the forward calorimeters in the range $3.1 < |\eta| < 4.9$, and also for the hadronic end-caps (HEC) in the region of $1.5 < |\eta| < 3.2$. The HEC and the FCAL are included in the same cryostat vessels which house the EMEC.

The TileCAL is a periodic sampling calorimeter using steel as absorber and scintillating tiles as active material. It extends from an inner radius of 2.28 m to an outer radius of 4.25 m. Particles entering the TileCAL initiate showers, the scintillator material becomes excited and emits light when it relaxes to the ground state. The tiles are 3 mm thick and connected to photo multipliers by optical fibres which shift the scintillator light to the visible part of the EM spectrum. Similar to the ECAL, the TileCAL has three samplings with thicknesses $1.4 X_0$, $4.0 X_0$ and $8.0 X_0$ at $\eta = 0$. The Tile barrel extends to $|\eta| < 1.0$, in the range $0.8 < |\eta| < 1.7$ there is an extended tile barrel on each detector side. The TileCAL has about 10000 channels.

The HEC is a LAr-based calorimeter using copper as absorber material. It consists of two wheels on each detector side, with an outer radius of 2.03 m. The granularity of the front wheel is given as $\Delta\eta \times \Delta\phi = 0.2 \times 2\pi/64$, the rear wheel has half the granularity in ϕ . Each wheel is built from 32 identical modules, overall the HEC contains 5632 channels. Three electrodes are mounted in the LAr gap of 8.5 mm splitting the gap into 4 drift spaces of 1.8 mm. The plates are flat and not accordion shaped.

The FCAL is also based on LAr as active material, but with much smaller gap sizes because of its

exposure to high radiation fluxes. It is divided into three parts on each detector side. The first part has copper as absorber material, because copper conducts heat very fast. The other two parts use tungsten absorbers. The gap size in the first part is only $250 \mu\text{m}$, the tungsten parts have a gap of $375 \mu\text{m}$. The thin gap is achieved by not using plates but rods and tubes which are arranged in a honey comb matrix. The rods are at a positive high voltage while the tubes and the matrix are grounded, between them is the LAr gap. The coverage of large η values by the FCAL assures especially a reliable MET measurement. It is also important for process involving jets emitted into forward direction, as for example the VBF signatures. The FCAL has 3542 channels.

The jet energy resolution of the HCAL has the same contributing terms as the energy resolution in the ECAL and is stated as follows [58]:

$$\frac{\sigma(E)}{E} = \frac{(50 - 60)\% \cdot \sqrt{\text{GeV}}}{\sqrt{E/\text{GeV}}} \oplus 1.7\% \oplus \frac{3 \text{ GeV}}{E}. \quad (4.12)$$

4.2.4. Muon System

The muon spectrometer is the outermost detector component. A view on the muon system is presented in Figure 4.7. Muons are relatively long living particles with lifetimes of $\tau = 2.2 \cdot 10^{-6} \text{ s}$. They pass through the inner detector and the calorimeters and are hardly affected by energy loss due to bremsstrahlung compared to electrons, since they are 207 times heavier. The muon detector consists of four different sub-systems: The monitored drift tubes (MDT) provide precision measurements as well as the cathode strip chambers (CSC) which cover large values of η . The resistive plate chambers (RPC) and the thin gap chambers (TGC) form the muon trigger system. Over a muon p_T range from about 10 GeV up to 100 GeV the muon momentum resolution is in the order of 2%.

A strong magnetic field is provided by super-conducting air-core toroids. The magnetic field, \vec{B} , is configured such that it is mostly orthogonal to the muon trajectories. The muon tracks get bent in the \vec{B} field with a curvature depending on the muon momentum. The \vec{B} field is continuously monitored by almost 1800 Hall sensors distributed within the muon system. In the range $|\eta| < 1.4$ the field is created by eight large toroids (each toroid in its own cryostat) providing a bending power of 1.5 to 5.5 Tm. In the region $1.6 < |\eta| < 2.7$ the field stems from the smaller end-cap toroids providing for 1 to 7.5 Tm. In the transition region $1.4 < |\eta| < 1.6$ both fields superimpose, leading to a smaller bending power capability.

Precision Chambers

The MDT and the CSC detectors are both designed to provide precise measurements of the muon track segments and thus the sagitta. The alignment of the muon chambers is essential for the precision and is monitored by an optical system. The relative positioning as well as the internal deformations are checked by 12000 sensors.

The MDT are aluminum tubes of 30 mm diameter, 70 - 630 cm length and $400 \mu\text{m}$ wall thickness, a $50 \mu\text{m}$ thick W-Re wire is located in its center. They are filled with a gas mixture of 93% Ar and 7% CO_2 . The MDT cover a range of $|\eta| < 2.0$, consist of 1088 chambers giving a total of 339000 channels. The position resolution is $80 \mu\text{m}$.

The CSC are located on the small muon wheels within the barrel close to the beam pipe. They are multiwire proportional chambers filled with 30% Ar, 50% CO_2 , 20% CF_4 with cathodes seg-

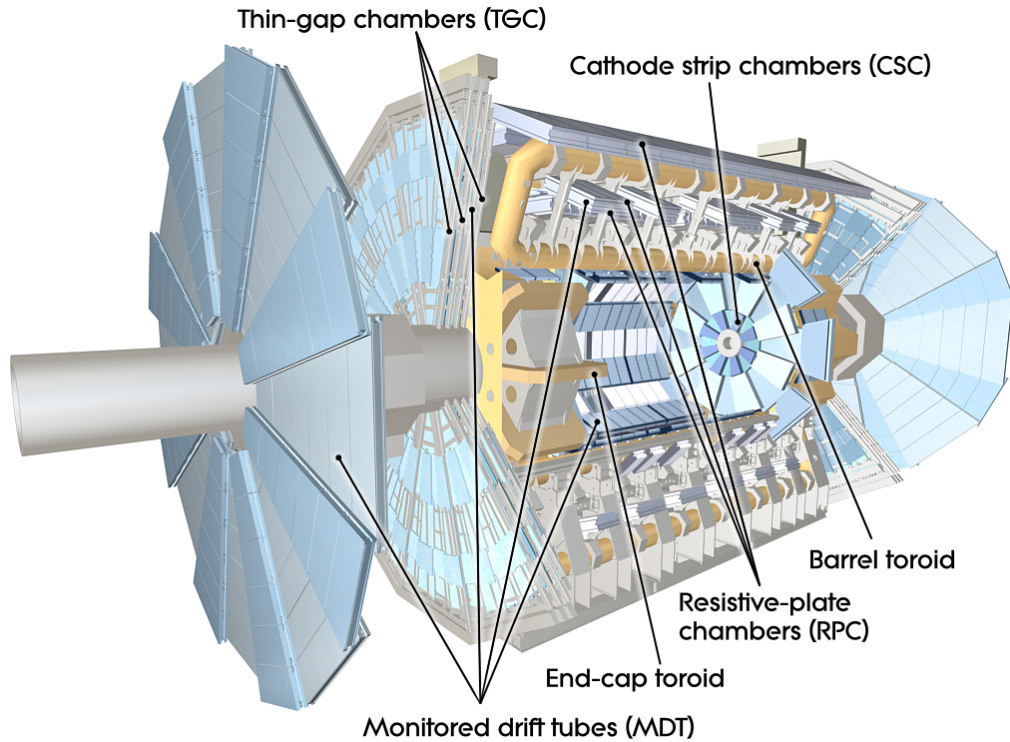


Figure 4.7.: Cut-away view of the ATLAS muon system.

mented into strips with large granularity. The precision coordinate is obtained by measuring the charge induced on the segmented cathode by the avalanche formed around the anode wire. They cover the range $2.0 < |\eta| < 2.7$ and thus increase the muon reconstruction efficiency which is essential for many interesting signatures as for example the Higgs boson decay to four muons. There are 32 CSC chambers and 31 000 channels. The position resolution achieved is about $60 \mu\text{m}$.

Trigger Chambers

The RPC and TGC form the muon trigger system. The trigger requires a good resolution not only in space but also in time to keep the latency time small. Both systems also contribute to the muon track measurement.

The RPC chambers are located on both sides of the MDT middle layer in the barrel. The RPC is a gaseous detector providing a space-time resolution of 1 cm and 1 ns. The basic RPC unit is a narrow gas gap formed by two parallel resistive plates, separated by insulating spacers made of polycarbonate. The primary ionization electrons are multiplied into avalanches by a high voltage field of typically 4.5 kV/mm. The gas is a mixture of $\text{C}_2\text{H}_2\text{F}_4$ and SF_6 . The readout strips have a pitch of 30 - 40 mm and are specifically optimized for good signal transmission.

The TGC are multiwire chambers located in the end-caps filled with a saturated gas mixture of 55% CO_2 and 45% C_5H_{12} to provide a quick response. Signals from the anode wires, arranged parallel to the MDT wires, provide the trigger information together with readout strips arranged

orthogonal to the wires. To form a trigger signal, several anode wires are grouped together and fed to a common readout channel. The number of wires per group varies between 4 and 20 depending on η . The track position is also read out in order to be combined with the information from the precision chambers.

4.2.5. Luminosity Detectors

Several smaller systems are installed in the very forward region of the ATLAS detector which measure the delivered luminosity. The luminosity can be calculated either directly from machine parameters or indirectly by measuring well defined and well understood processes. The three systems are LUCID⁵, ALFA⁶ and ZDC⁷.

In a possible upgrade additional proton-tagging detectors are foreseen at distances of ± 420 m from the IP and special radiation hard systems at ± 220 m.

LUCID

At distances of ± 17 m from the IP the LUCID detectors are located, detecting particles from inelastic p-p scattering. The number of detected particles is proportional to the number of protons per bunch, even if most of the particles are produced by secondary processes. The initial precision on the relative luminosity reached by LUCID will be 1% at a luminosity of $10^{33} \text{ cm}^{-2}\text{s}^{-1}$, in comparison the precision of the luminosity calculated from beam parameters is 11% and will probably be 5%.

LUCID contains twenty aluminum tubes which surround the beam pipe at a radius of 10 cm ($|\eta| = 5.8$) and point toward the IP. The tubes are 1.5 m long and have a diameter of 15 mm. They are filled with C_4F_{10} providing a Cerenkov threshold of 2.8 GeV for pions and 10 MeV for electrons for instance. If particles traverse the gas with a velocity which is larger than the speed of light in the material, Cerenkov radiation (photons) is emitted in a cone around the particle with an opening angle depending on the particles identity. LUCID has to withstand highest radiation levels. It has a time resolution of less than the bunch crossing rate of 25 ns.

ALFA

At ± 240 m the ALFA systems can be found. ALFA is measuring the absolute luminosity from elastic proton-proton scattering at small angles of $3 \mu\text{rad}$. The optical theorem connects the scattering amplitude to the total cross section from which the integrated luminosity is calculated. Since the extremely small angle is smaller than the nominal beam divergence, special beam conditions are needed for ALFA, meaning a low instantaneous luminosity and a reduced beam emittance. Therefore the Roman pot concept was used for the ALFA detector. The Roman pot is a volume which is separated from the beam pipe vacuum by a window but connected to it by bellows. It can then be moved up and down to bring it to a distance of 1 mm to the beam inside the beam pipe. On each side there are two Roman pots separated by 4 m.

ALFA is based on scintillating-fibre trackers allowing for a spatial resolution of less than $30 \mu\text{m}$ and minimal noise sensitivity. Each fibre has a width of 0.5 mm, the total detector area is only

⁵LUCID - LUMinosity measurement Using Cerenkov Integrating Detector.

⁶ALFA - Absolute Luminosity For Atlas.

⁷ZDC - Zero-Degree Calorimeter.

$32 \times 32 \text{ mm}^2$. Readout is provided by multi-anode phototubes. The expected precision of ALFA is 5% on the correction factor of the other detectors for the absolute luminosity measurement.

ZDC

The third system is the ZDC, foreseen to be located at $\pm 140 \text{ m}$ from the IP. It measures particles in the pseudorapidity range of $|\eta| > 8.2$. The ZDC was designed mainly for detecting forward neutrons from heavy ion collisions and it plays a key role in determining the centrality of these processes. The ZDC also provides an additional minimum bias trigger for the very initial data taking. By requiring a coincidence in the ZDC background from beam gas and beam halo effects are strongly reduced. The time resolution of the ZDC is 100 ps, allowing for vertex information without relying on the inner detector.

The ZDC consists of four modules per arm, one EM and three hadronic modules. Each module consists of tungsten and steel plates and quartz strips in between. The absorbers initiate a shower and its particles emit Cerenkov light which is detected by the quartz rods and transmitted to multi-anode photomultipliers (PMT) at the top of each module. The PMT gain will be monitored with a precision of 1%. To avoid radiation damage the ZDC will be removed in periods of proton-proton collisions.

4.2.6. Trigger and Data Acquisition

The trigger is the most crucial component needed to reduce the incoming data rate from 10^9 Hz at a luminosity of $10^{34} \text{ cm}^{-2}\text{s}^{-1}$ to 200 Hz for permanent storage by separating very rare interesting events from the minimum bias events with a very high efficiency. Interesting events in a hadron collider environment do mostly involve electroweak processes and contain leptons or large values of MET.

The first trigger element is the Level 1 (L1), which makes an initial selection based on the RPC and TGC and a reduced granularity information from all the calorimeter parts. The L1 reduces the data rate to 75 kHz (or 100 kHz after a possible upgrade). While the muon chambers select high p_T muons, the calorimeter objects searched for are high p_T electrons, photons and also hadronically decaying τ -leptons or large missing E_T and sum of E_T . The exact p_T thresholds (the trigger menu) for each object depend on the luminosity. Combinations of different objects (multi-object triggers) are also possible. The η and ϕ positions of the triggered muons and calorimeter towers together with the energy and signature information form the so-called regions of interest (RoI) and are used for the further selection. The L1 trigger needs also to identify the bunch crossing of interest (the so called L1 Accept - L1A). This is done by the Central Trigger Processor (CTP). The L1 is designed to do this initial selection within a latency time of $2.5 \mu\text{s}$ after the L1A, including a 500 ns contingency. Since this latency time is larger than the bunch crossing rate, the signals are stored in pipeline memories until they are processed. The L1 signals are received by the front-end electronics located on the detector which transmit the data to the read-out drivers (ROD) and then held in the read-out buffers (ROB) for the next selection steps. A sketch of the L1 system is presented in Figure 9.1.

The second trigger chain component is the Level 2 (L2). The L2 takes only the data in the RoI but now uses the full detector granularity to reduce the data rate to approximately 3.5 kHz. In case of the muons, the L2 measures the p_T more precisely and may increase the p_T threshold. It also applies isolation requirements to the objects. In case of electrons and taus, the L2 requires a match

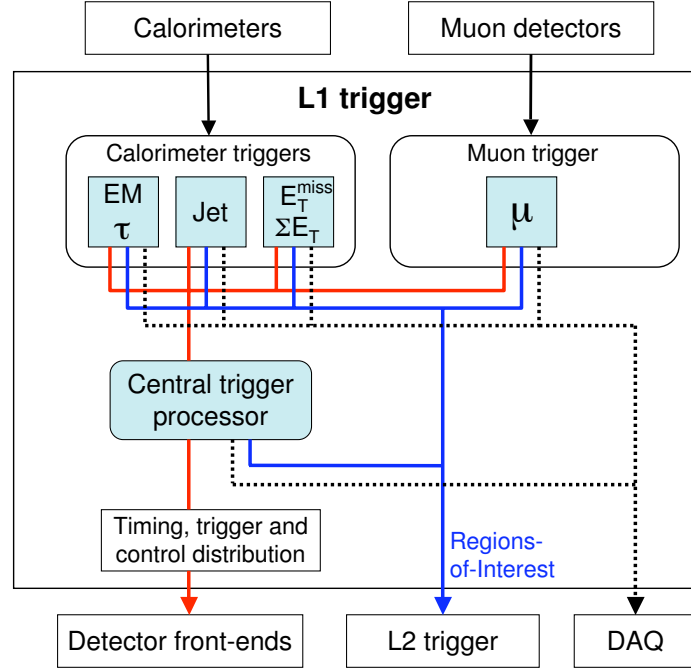


Figure 4.8.: Block diagram of the L1 trigger components. The L1 gathers information from the muon chambers and calorimeters and sends this to the CTP unit which will decide about the L1 accept. Then the information is passed on to the HLT and the DAQ.

of the calorimeter cluster with the inner detector track (in case of electrons especially by using TRT information) and also isolation. Photons do not have a track and hence less rejection power is gained here. Jets have even less rejection power since these objects are primarily produced in hadron colliders. The L2 sharpens and raises the p_T threshold for jets. For the energy sum triggers the RoI mechanisms can only be exploited to include corrections due to muons or recalculate the sum of the energy within the RoIs. The L2 latency depends on the event signature but is expected to be in the range of (10-40) ms.

The final step is the Event Filter (EF). L2 and EF together are also called High Level Trigger (HLT). The EF is based on offline selection algorithms and applies calibration, alignment and magnetic field configuration information to the L2 objects. First, the EF confirms the L2 decision and, if applicable, tightens p_T thresholds. Eventually the EF applies more complex algorithms such as vertex and track fitting. The EF is supposed to reduce the data rate to the final 200 Hz within an average time of 4 seconds. However, the actual trigger rates and menus are configurable and may differ from run to run if necessary. Once the EF has accepted the event, the Data Acquisition System (DAQ) transmits the data from the ROB to the disk storage for offline processing. The Detector Control System (DCS) provides the configuration, control and monitoring of the ATLAS detector during operation. It also supervises the hardware (gas pressures, voltages, temperatures) and provides a human interface to be operated from the ATLAS control room. The data amounts from the main LHC experiments even after passing the tight trigger selection will be extraordinary large (about 15 Pbytes per year). The LHC Computing Grid Project (LCG)

was developed to distribute the data (and also the simulated data) to different world-wide computing systems (Tiers). The Tier-0 site is localized at the CERN side and does the primary reconstruction and a back-up of the raw data. It distributes its data then to the Tier-1 sites which are large international computing centers (such as the GridKa in Karlsruhe for example). The Tier-2 sites are smaller national computer centers where also large parts of the central MC production take place. Tier-3 sites are usually clusters from institutes, the Tier-4 is the final element and denotes the personal desktops.

5

Monte Carlo Event Generation

To assess the discovery potential of new physics processes it is inevitable to do studies with simulated data first. The Monte Carlo (MC) event generator basically takes the role of the accelerator, the detector simulation program substitutes the detector output. The simulated data is then compared to the measured distributions to check the detector performance, validate the MC methods and to look for discrepancies between the SM expectation and the measurement.

5.1. Monte Carlo Generators

5.1.1. Overview

The basis of the MC description of a collider event is the factorization theorem. It divides the event into multiple, perturbative and non-perturbative, stages.

A MC event is in principle built from the following steps [62]:

- In the initial state the two protons come to collision. Each proton contains gluons and quarks and their momentum distribution is modeled by parton density functions (PDF).
- The hard interaction between a parton from each proton is defined. This is the interaction of interest. If the energy of this interaction is large, it can be described at a fixed order in α_s in perturbation theory.
- Short-living resonances (such as the Z boson for instance) are formed and decay. They have to be included in the process description. Spin and other correlations are transferred from the production to the decay subprocess.
- Initial state radiation by bremsstrahlung is added to the process. In case of QED interactions photons are emitted. In case of QCD interactions gluons and quarks are emitted, leading to a parton shower. The same applies to the outgoing particles (final state radiation).
- Interactions of the other partons are added to the hard interaction. These interactions are by definition softer but also lead to detectable particles in the final state. This process is also called underlying event. Each of these multiple interactions are then associated with initial and final state radiation.
- The beam remnant continues to travel along the beam axis. It is connected to the rest of the proton-proton system via color charge, since the complete proton is color neutral. These color connections have to be taken into account in the calculations.

- On softer energy scales the confinement becomes effective, this cannot be described by perturbation theory because α_s is large at this energy scale. Instead, this needs to be modeled based on various assumptions. One common approach is to assume an infinite number of colors ($N_c \rightarrow \infty$) such that each separate confinement field is stretched between color and anti-color. On a defined energy scale (factorization scale) the confinement fields break up and new quark-antiquark and diquark-antidiquark pairs are produced. Then color-connected quark-antiquark pairs are transformed into mesons, while color connected quark-diquark pairs form baryons. The phenomenological models describing the hadronization are fitted and tuned on real data.
- The decay of long-lived particles has to be modeled, as for example the decay of τ -leptons and hadrons. At this stage the MC description has to be matched to the detector simulation.
- In case of high instantaneous luminosities several proton-proton collision superimpose (pile-up), the additional collisions have to be modeled like the primary collision.

An event generator will consider these steps sequentially and iteratively to build up a very complex final state system with many particles. Each particle contains several degrees of freedom like for example mass, charge, momentum and lifetime, leading to a very large phase-space. To shrink the parameter space appropriate cuts are applied, as for example on p_T and η or on invariant masses of the final state particles.

5.1.2. Matrix Elements

From the Lagrangian of a quantum field theory its Feynman rules can be derived. These are used to construct the matrix element (ME) for a given process up to a chosen order in α_s . The cross sections of given processes are calculated from the ME. There are specialized ME libraries for low multiplicity final states and up to NNLO, as well as automated codes for larger multiplicity final states at tree level accuracy.

The basic steps of a ME calculation relevant to describe the hard interaction are the following [63]:

1. Find all possible Feynman diagrams.
2. Compute them to get the amplitude.
3. Sum over all color and helicity configurations.
4. Square the amplitude.
5. Integrate over the phase space.

Since the amplitude peaks in complicated ways in the phase space, a flat integration of the phase space is impractical. Commonly used approaches therefore are for instance *importance sampling*, *stratified sampling* and *multichannel sampling* [64].

It can be shown that in many QCD processes the partonic cross section is divergent for $p_T \rightarrow 0$. To avoid such unphysical singularities a p_T cut is applied. Also the PDF of gluons and sea quarks peak at small momentum fractions x , leading to rising cross sections for small p_T values.

To obtain the hadronic cross section the partonic cross sections σ_{ij} have to be convoluted with the flux of incoming partons i and j of the protons A and B :

$$\sigma = \sum_{i,j} \int \int dx_1 dx_2 \cdot f_i^A(x_1, \mu_F^2) \cdot f_j^B(x_2, \mu_F^2) \cdot \sigma_{ij}\left(x_1 p_1, x_2 p_2, \alpha_s(\mu_R^2), \frac{Q^2}{\mu^2}\right). \quad (5.1)$$

Q^2 denotes the momentum transfer between the two partons. μ_R and μ_F are the renormalization and factorization scales respectively. The long distance (hadronic) physics is factorized out and absorbed into the PDF f . The short distance (partonic) physics occurs at much larger energy scales.

5.1.3. Parton Showers

A parton shower (PS) is an iterative procedure that allows simplified expressions for QCD emissions such as $q \rightarrow qg$, $g \rightarrow gg$ and $g \rightarrow q\bar{q}$, using soft and collinear emission approximations without explicit ME calculations. Instead, these branchings are calculated at the leading log level and are solutions to the DGLAP¹ equations [65]. The DGLAP evolution calculations are universal, applicable to QCD and QED, and describe the behavior of partons at a given momentum scale.

In a parton shower a complex (for example) $2 \rightarrow n$ process is factorized into n simple $2 \rightarrow 2$ (or $2 \rightarrow 1$) processes and multiple soft and collinear emissions. Each parton emission is a stochastic Markov process in which values for Q , momentum fractions and azimuthal angles are generated. The cross section of the whole $2 \rightarrow n$ graph is associated to the cross section of the core $2 \rightarrow 2$ hard process, in the limit that the factorized emissions are soft and collinear.

To avoid the confinement effects in the non-perturbative region, usually a cut-off at energy scales of 1 GeV is applied. Below this scale no more soft or collinear branchings are simulated. Divergences and their cancelations are handled by *Sudakov* form factors [66]. This form factor expands the DGLAP equations and assures that the probability for a parton to branch never exceeds unity.

5.1.4. Matching of Matrix Elements and Parton Showers

The ME and the PS are complementary approaches, each one having advantages and disadvantages. While ME calculations are exact at a fixed order over the whole phase space, they are computationally laborious and therefore limited to a few particles. The PS resums the dominant contributions of soft and collinear emissions to all orders but cannot describe wide angle hard emissions. A unification of both concepts is clearly desirable. The goal of such a combination is a correct description of all the jet emissions at tree and leading log level, and to correctly resume the soft emissions into the parton shower. However, a jet might appear both from relatively hard emission during shower evolution and from the inclusion of higher orders in the ME calculation. This is also called *double counting* and needs to be avoided.

One matching algorithm is the CKKW² matching [67, 68]. This is implemented in the SHERPA MC generator [69, 70], which is used to generate the signal process of b-associated Higgs bosons decaying to tau pairs in this thesis. The simplified principle of the CKKW matching is to divide the multi-jet phase space into two regimes by choosing a cut-off scale μ , which is also called

¹DGLAP - Dokshitzer, Gribov, Lipatov, Altarelli, Parisi.

²CKKW - Catani, Krauss, Kuhn, Webber.

resolution scale. One regime then corresponds to the jet production by the ME, the other regime contains the jet evolution down to the fragmentation scale by the PS. The ME for all parton multiplicities are then reweighted with the ratio of α_s at the branching scales and with the appropriate Sudakov form factors to match what the PS would have done for this special kinematics. The PS is allowed to produce additional emissions vetoing those emissions which lead to resolved partons to avoid the double counting [71].

5.2. Detector Simulation

5.2.1. Overview

The MC generators create four-vectors of all the detectable and undetectable particles. These are used as input to the detector simulation program within the ATLAS software framework ATHENA [72]. All potential interactions of the final state particles with the detector material are evaluated and also the secondary interactions of decay products or shower particles as they propagate through the detector. Since the ATLAS detector has a very high granularity and complexity (see Chapter 4), this is generally a very time-consuming procedure (several minutes per event, depending on the CPU). Therefore various fast simulation packages were developed which use parameterizations to describe the detector response instead of the full detector description.

5.2.2. Full Simulation

The full detector simulation is based on the GEANT4 package [73, 74]. GEANT4 is a general toolkit for the simulation of the passage of particles through matter. The full simulation consists of three steps: Core simulation, digitization and reconstruction. An up-to-date write-up of the ATLAS software is given in Ref. [75].

In the core simulation all ATLAS subdetectors are simulated in detail [76], the output format are hits. The detector response is tuned on testbeam results³. The calorimeter simulation is very detailed for each component, this step in the simulation takes about 80% of the CPU time. Optimization procedures have been investigated and applied for reducing the memory consumption at runtime.

After running the core simulation the digitization step is performed, transforming the hits into digits. Typically a digit is produced when the voltage or current on a particular readout channel rises above a pre-configured threshold within a particular time-window. Some subdetector digit formats include the signal shape in detail over this time, while others simply record that the threshold has been exceeded within the relevant time window. Pile-up is simulated at the digitization step as overlay of several predefined events to save CPU time during simulation. Detector noise is added as well as cross-talk effects. The output is the raw data format (RDO), and at this stage the simulation output matches the real data detector output format, except for the presence of *truth information* in the simulation, containing generator information of particles.

The last step is the reconstruction of the digitized simulated or real data events before the final analysis follows. Here the digits from the raw data format are transformed back to particle collec-

³The testbeam facility was used to study the performance or do calibration of some ATLAS detector parts before they were installed in the ATLAS cavern and before any combined cosmic run took place [77–79]. The testbeam particles were provided by the SPS accelerator.

tions and their properties using various (more than 80) reconstruction and clustering algorithms. Often there are competing or complementing algorithms for the same particle types. The output formats are the event summary data format (ESD), the analysis object data format (AOD) or the derived physics data format (DPD). The reconstruction of one event takes on average 6 seconds. The ATLAS detector geometry used for simulation, digitization, and reconstruction is built from databases containing the information describing the physical construction and conditions data. The ATLAS geometry database stores all fundamental constants from the detector construction: Volume dimensions, rotations, and positions, element and material properties including densities. The magnetic field map is linked to the geometry database. The ATLAS Conditions database contains all the information needed to emulate a single data-taking run of the real detector (e.g. detector misalignments, dead channels or temperatures).

5.2.3. Fast Simulations

Many physics processes have very large cross sections, above all QCD processes like dijet events for example, but also the production of W and Z bosons. To evaluate their contributions in the Higgs boson analysis large MC samples have to be produced, which is, due to computing time issues, not feasible with full simulation. Several fast simulation programs have been developed in order to speed up the slowest parts of the full simulation or to replace the stochastic detector response completely by parameterizations.

ATLFAST-I has been developed for physics parameter space scans and studies that do not require the level of detail contained in the full simulation [80]. A factor of 1000 speed increase over full simulation is achieved with sufficient detail for many general studies. Truth objects are smeared by detector resolutions to provide physics objects similar to those of the reconstruction. Object four-vectors are written out, without any detailed simulation of efficiencies and fakes, with two exceptions: Because jet-flavor tagging efficiencies are applied, fake b-jets and taus are simulated. ATLFAST-I is the least detailed simulation method. There is no realistic detector description, so studies of detector-based quantities, such as calorimeter sampling energies and track hit positions, are not possible. Also, by default no reconstruction efficiencies are applied for photons, electrons, jets and tracks.

ATLFAST-II is another fast simulation, with the aim to simulate events as fast as possible while still being able to run the standard ATLAS reconstruction. ATLFAST-II is made up from two components: The Fast ATLAS Tracking Simulation (Fstras) [81] for the inner detector and muon system simulation and the Fast calorimeter Simulation (FastCaloSim) [82] for the calorimeter simulation. Optionally, any subdetector can be simulated with GEANT4 to provide the higher level of accuracy saving CPU time compared to the full simulation of the entire detector. An improvement in simulation time of a factor of 10 is achieved with full GEANT4 inner detector and muon simulation and FastCaloSim. A factor of 100 is achieved with Fstras and FastCaloSim. The ATLFAST-II output includes all the properties associated with a reconstructed object. In the case of Fstras these include the hits in the inner detector and muon system, and for FastCaloSim these include the energies in the calorimeter cells.

In this thesis both ATLFAST-I and II have been used as well as full simulation samples. There is another fast simulation package, the FAST-G4 simulation [83] which, however, was not used.

5.3. Datasets Used

In the following the datasets used for signal and background processes of the Higgs boson analyses are listed. The cross sections and cross section uncertainties are also given.

Any dataset used for the two main analysis was either produced in the central production system or privately produced and then validated against central production.

5.3.1. The Signal Process and Cross Sections

The cross sections for the b-associated Higgs boson production have been obtained by using the FEYNHIGGS program (see also Section 2.2.6). The underlying calculations are based on Ref. [33]. The cross sections for the gluon fusion are based on Ref. [84]. Cross section uncertainties on the b-associated Higgs production were obtained in Ref. [85] by this procedure:

- PDF uncertainties:
The PDF MRST2004nnlo [86] was replaced by the PDF MRST2002nnlo [87]. Half of the change observed when switching between those PDF was assigned as systematic uncertainty.
- Scale uncertainties:
Variations of the factorization scale μ_F and renormalization scale μ_R were performed as follows: $0.1 < \frac{\mu_{F/R}}{m_H} < 0.7$, their central value were chosen to be $\frac{\mu_{F/R}}{m_H} = 0.25$. The effect from the renormalization scale variation was found to be negligible.

The gluon fusion cross section uncertainties were obtained in Ref. [85] by these steps:

- PDF uncertainties:
The error PDFs from MRST2001 have been used and half of each change was summed up quadratically.
- Scale uncertainties:
The factorization and renormalization scales were each varied between $0.5 < \frac{\mu_{F/R}}{m_H} < 2.0$, and their central value were chosen to be $\frac{\mu_{F/R}}{m_H} = 1.0$.

Figure 5.1 shows the cross section uncertainties for the two signal production modes. While the uncertainties in the b-associated production are quite large (30%) for Higgs boson masses of 100 GeV, the uncertainties decrease for larger masses (eg. 5.5% for $m_A = 800$ GeV). The total uncertainty on the cross section in gluon fusion processes is nearly constant over the Higgs boson mass range considered here (approximately 10-15%).

Table 5.1 lists the 14 TeV signal points for b-associated Higgs boson production used for the analysis of the lepton-lepton final state. These samples were produced with SHERPA 1.0.8 [69,70] and reconstructed with Athena Release 12.6.5. They contain a dilepton particle filter. The filter efficiency is denoted as ϵ . The following tables also give the scale factor which is applied to scale the luminosity of the available MC sample to the anticipated luminosity of 30 fb^{-1} .

Tables 5.2 and 5.3 lists the 14 TeV signal samples used for the study of the lepton-hadron channel. Here both b-associated and gluon fusion processes were considered. The b-associated signal was produced using SHERPA 1.1.3, the gluon fusion samples were generated by PYTHIA [88].

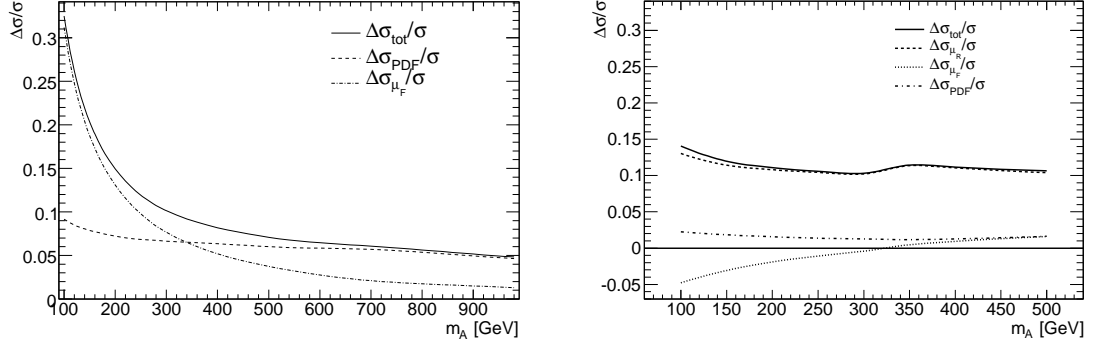


Figure 5.1.: Signal cross section uncertainties, left for b-associated and right for gluon fusion production (taken from Ref. [85]). While the gluon fusion uncertainty remains almost constant as a function of m_A , the uncertainties on the b-associated production decrease for larger A boson masses.

DS ID	m_A [GeV]	Events	$\sigma \cdot BR$ [pb]	L [fb^{-1}]	Scale factor	Filter
9084	110	13 250	3.25	4.07	7.37	$2 e/\mu, p_T > 5 \text{ GeV}$
5358	130	10 000	2.29	4.37	6.87	$2 e/\mu, p_T > 5 \text{ GeV}$
9085	160	15 500	1.27	13.01	2.3	$2 e/\mu, p_T > 5 \text{ GeV}$
9086	200	18 000	0.63	26.77	1.12	$2 e/\mu, p_T > 5 \text{ GeV}$
9087	300	20 000	0.16	125.6	0.24	$2 e/\mu, p_T > 5 \text{ GeV}$
9060	450	15 750	0.027	583.3	0.05	$2 e/\mu, p_T > 5 \text{ GeV}$

Table 5.1.: Samples of b-associated Higgs bosons decaying to tau pairs used for the lepton-lepton analysis at 14 TeV, the numbers given here correspond to $\tan\beta = 20$. Those samples were processed using the full simulation.

5.3.2. Background Processes and Cross Sections

Relevant background processes produce a signal-like event signature containing the following objects:

- Two leptons (electrons or muons) in the lepton-lepton analysis, or one lepton and one hadronic τ candidate in the lepton-hadron analysis.
- Missing E_T due to the presence of neutrinos stemming from the tau decays.
- One or more b-jets if the signal was produced in association with b-quarks.

While many background processes result in exactly the same signature as the signal, other backgrounds might fake this signature due to object misidentification of leptons or jets. Relevant background processes and cross sections at 14 TeV are described in the following. Examples of Feynman diagrams for the listed backgrounds are presented in Figures 5.2 and 5.3.

DS ID	m_A [GeV]	Events	$\sigma \cdot BR \cdot \varepsilon$ [pb]	L [fb^{-1}]	Scale factor	Filter
209500	150	600 000	18.61	32.2	0.93	-
209221	200	300 000	7.60	39.5	0.76	-
209123	300	60 000	1.61	37.3	0.80	-
209501	450	30 000	0.22	136.3	0.22	-
209502	600	30 000	0.048	625.0	0.048	-
209503	800	30 000	0.011	2727.0	0.011	-

Table 5.2.: Samples of b-associated Higgs bosons decaying to tau pairs used for the lepton-hadron analysis at 14 TeV, the numbers given here correspond to $\tan\beta = 20$. These samples were simulated using ATLFast-II.

DS ID	m_A [GeV]	Events	$\sigma \cdot BR$ [pb]	L [fb^{-1}]	Scale factor	Filter
209510	150	300 000	7.27	41.3	0.73	-
209511	200	150 000	1.73	86.7	0.34	-
209512	300	30 000	0.19	157.9	0.19	-
209513	450	30 000	0.018	1666.7	0.018	-

Table 5.3.: Samples of Higgs bosons produced in gluon fusion and decaying to tau pairs used for the lepton-hadron analysis at 14 TeV, the numbers given here correspond to $\tan\beta = 20$. Those samples were simulated using ATLFast-II.

$Z(\rightarrow e\bar{e}/\mu\bar{\mu}/\tau\bar{\tau}) + \text{jets}$

The Z decay to a pair of taus (and subsequent tau decays to electron, muon or pions) yields exactly the same signature as the $H \rightarrow \tau\tau$ process, especially if the Higgs boson mass is close to the Z boson mass.

The production of Z bosons decaying to pairs of electrons or muons has a large cross section. These backgrounds need to be evaluated and are of relevance especially in the lepton-lepton analysis. Its contribution to the final spectrum will depend mainly on the MET resolution, since this process does not contain true MET.

The cross section for the $Z(\rightarrow \ell\bar{\ell}) + \text{jets}$ process was calculated at NNLO accuracy and its value is $\sigma_{Z \rightarrow \ell\bar{\ell}} = (2036 \pm 60)$ pb [89, 90]. This calculation contains a cut on the invariant lepton-lepton mass of $m_{\ell\bar{\ell}} > 60$ GeV. This background is produced either using SHERPA or PYTHIA.

$W(\rightarrow e\nu/\mu\nu/\tau\nu) + \text{jets}$

This background is of special relevance in the lepton-hadron analysis, where a jet might fake a hadronic tau. The cross section for this process was obtained at NNLO accuracy. The value used here is $\sigma_{W+\text{jets}} = (20460 \pm 615)$ pb [89]. This background is produced either using SHERPA, JIMMY [91] or PYTHIA.

$$t\bar{t} \rightarrow b\bar{b} WW \rightarrow b\bar{b}\ell\ell\nu\nu/\ell\nu q\bar{q}$$

The semi- or fully leptonic decay of top-pairs is of special relevance in an analysis where the presence of a b-jet is required, because $t\bar{t}$ events contain two real b-jets in the hard process. The $t\bar{t}$ cross section was calculated to NLO+NLL accuracy and found to be $\sigma_{t\bar{t}\text{bar}} = (833 \pm 100)$ pb [92]. Using this value follows the ATLAS recommendation for cross sections [19], even though a new reference quotes a cross section at NLO+NNLL accuracy of 873 pb [93]. $t\bar{t}$ was produced with MC@NLO [94].

QCD Dijets

Dijet production will be the dominant final state at the LHC. The QCD process is usually divided into several sub-samples, corresponding to different virtualities and therefore different cross sections. The dijet cross section ranges over many orders of magnitude from 10^{-2} to 10^{10} pb [19]. The virtualities of the QCD sub-samples are given in Table 5.4. In this thesis contributions from J2-J6 are considered in the dilepton analysis and contributions from J1-J6 in the lepton-hadron analysis. As will be shown, the other contributions are negligible.

QCD Sub-Sample	Virtuality [GeV]
J0	8-17
J1	17-35
J2	35-70
J3	70-140
J4	140-280
J5	280-560
J6	560-1120
J7	1120-2240
J8	>2240

Table 5.4.: The QCD sub-samples and corresponding virtualities. The contributions from the J1-J6 samples are considered in this thesis.

A 50% uncertainty was assumed on the dijet cross section. In this thesis special dijet samples were used containing a filter which required a pair of b-quarks or one lepton (electron or muon) on generator level. Dijet backgrounds were produced using PYTHIA MC.

Single Top

Single top production occurs in t-channel, s-channel or in association with W bosons. The cross sections are calculated at NLO accuracy and given as $\sigma_{t\text{-channel}} = (246.6 \pm 12)$ pb, $\sigma_{s\text{-channel}} = (10.6 \pm 1)$ pb and $\sigma_{Wt} = (66 \pm 2)$ pb [95, 96]. The s-channel contribution was neglected in this thesis. Single top MC was produced by ACERMC [97].

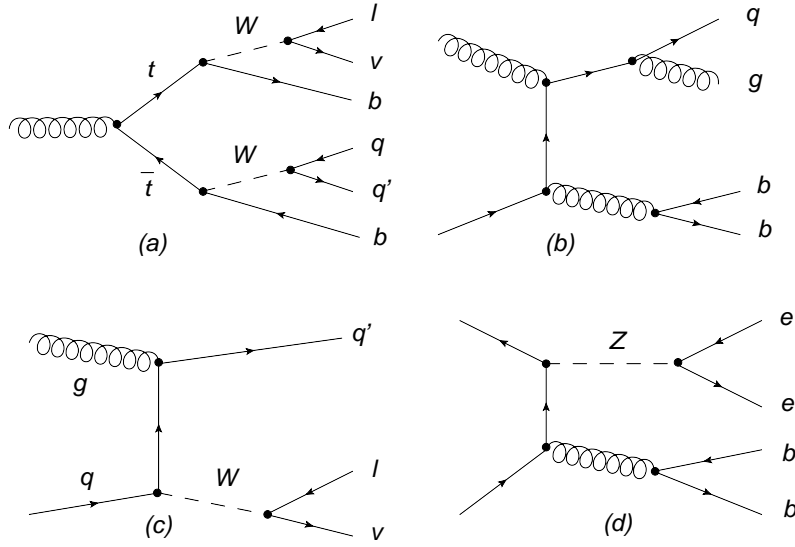


Figure 5.2.: Examples of Feynman diagrams for $t\bar{t}$ (a), QCD dijets (b), W+jets (c) and Z+jets (d) processes. The Z boson in this example is produced in association with a pair of b-quarks.

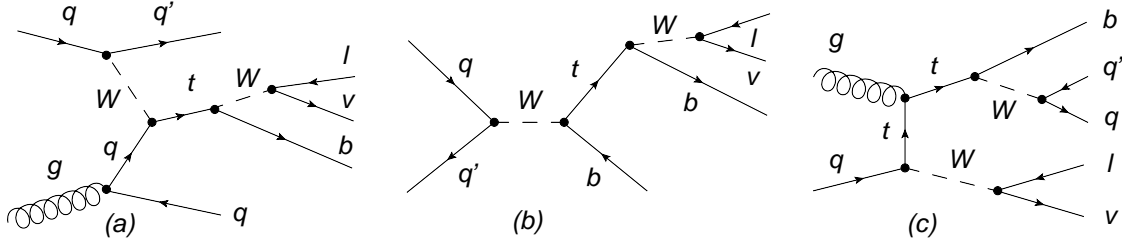


Figure 5.3.: Feynman graphs for the single top production in the t-channel (a), s-channel (b) and W-associated (c).

Details on the Datasets Used

Table 5.5 lists the background samples studied and some details on them for the lepton-lepton analysis at 14 TeV. Those samples were processed with full simulation in Athena Release 12. No single top samples were included in this study, which will be discussed later on.

Table 5.6 lists the background samples used for the lepton-hadron final state analysis. These samples were simulated in Athena Release 14 using ATLFast-II, except for the single top samples which are fully simulated samples in Athena Release 12.

DS ID	Process	Events	$\sigma \cdot BR \cdot \varepsilon$ [pb]	L [fb ⁻¹]	Scale factor	Filter
5200	$t\bar{t}$	422 208	461.0	0.92	32.76	$\ell\ell, \ell h$
5145	$Z \rightarrow \mu\mu$	443 450	1 812	0.25	122.59	$m > 60$ GeV
5146	$Z \rightarrow \tau\tau$	170 500	101.80	1.67	17.912	$m > 60$ GeV
9061	$Z \rightarrow \tau\tau$	99 000	19.16	5.16	5.81	$m > 60$ GeV, 2μ
5144	$Z \rightarrow ee$	376 200	1 751	0.22	139.63	$m > 60$ GeV
5100	$W \rightarrow e\nu$	519 850	13 029 200	0.040	751.9	e/μ
5101	$W \rightarrow \mu\mu$	192 799	13 831 000	0.014	2151.2	e/μ
5106	$W \rightarrow \tau\nu$	23 000	2 378 940	0.0097	3103.0	e/μ
5011	QCD J2	380 050	$9.6 \cdot 10^7$	$3.9 \cdot 10^{-6}$	$7.6 \cdot 10^6$	-
5012	QCD J3	365 050	$6.1 \cdot 10^6$	$5.9 \cdot 10^{-5}$	$5.01 \cdot 10^5$	-
5013	QCD J4	372 150	$3.2 \cdot 10^5$	0.001	25 796	-
5014	QCD J5	273 950	$1.2 \cdot 10^4$	0.022	1 314	-
5015	QCD J6	370 800	$3.4 \cdot 10^2$	1.1	27.5	-

Table 5.5.: Background samples used in the analysis of the lepton-lepton final state. These samples were simulated with the FULL SIMULATION. ε denotes the filter efficiency.

DS ID	Process	Events	$\sigma \cdot BR \cdot \varepsilon$ [pb]	L [fb ⁻¹]	Scale factor	Filter
209520	$Z \rightarrow ee$	1 993 486	1 609	1.22	24.5	$e/\mu, m > 60 \text{ GeV}$
209521	$Z \rightarrow \mu\mu$	1 988 773	1 590	1.24	24.2	$e/\mu, m > 60 \text{ GeV}$
209522	$Z \rightarrow \tau\tau$	1 995 857	306.3	6.4	4.7	$e/\mu, m > 60 \text{ GeV}$
209530	$W \rightarrow e\nu$	4 499 841	12 439	0.36	82.6	e/μ
209531	$W \rightarrow \mu\nu$	4 499 209	12 417	0.36	82.6	e/μ
209532	$W \rightarrow \tau\nu$	4 021 603	1 374	2.9	10.2	e/μ
209550	$t\bar{t}$	5 935 480	410.3	12.3	2.4	$\ell\ell, \ell h$
5500	Wt	51 100	25.5	2.0	15.0	no $WW \rightarrow 2\ell 2\nu$
5502	t-channel	79 600	81.5	0.98	30.6	$W \rightarrow \ell\nu$
209641	J1	99 750	87 655	0.001	26362.4	$e/\mu, b\bar{b}$
209642	J2	994 500	94 022	0.011	2836.3	$e/\mu, b\bar{b}$
209643	J3	263 750	31 083	0.008	3734.2	$e/\mu, b\bar{b}$
209644	J4	100 000	4 279	0.024	1253.8	$e/\mu, b\bar{b}$
209645	J5	100 000	296.8	0.34	89.0	$e/\mu, b\bar{b}$
209646	J6	100 000	11.9	8.37	3.6	$e/\mu, b\bar{b}$
209542	J2	396 500	231 456	0.0017	175 512	e/μ
209543	J3	200 000	68 384	0.003	10 258	e/μ
209544	J4	200 000	9 269	0.022	1 390	e/μ
209545	J5	199 500	653.4	0.031	98.3	e/μ
209546	J6	196 241	28.5	6.9	4.36	e/μ

Table 5.6.: Background samples used in the analysis of the lepton-hadron final state. ε denotes the efficiency of the lepton filter. All these samples were simulated with ATLFAST-II in the Athena Release 14, except for the single top samples which were fully simulated with Athena Release 12.

6

Object Identification

In the following the reconstruction and identification of objects relevant for the analyses are briefly discussed. A more comprehensive report is given in Ref. [19]. The object selection cuts used in both the lepton-lepton and lepton-hadron analysis are described. Differences between objects used in both analyses arise from the fact that different ATHENA release versions were used for the studies or different recommendations for the object ID were given at the time the studies were performed.

6.1. Electrons

6.1.1. Overview

At the LHC the rate of isolated electrons in the p_T range of 20 – 50 GeV compared to the rate of QCD jets is $\mathcal{O}(10^{-5})$. The correct ID of electrons is therefore crucial. The detector components most involved in the electron ID are the inner detector and the EM calorimeter. Three reconstruction algorithms are established in ATLAS:

- Standard reconstruction for high- p_T electrons:
This algorithm was optimized for the reconstruction of isolated electrons for example from $Z \rightarrow ee$ events. In this thesis only electrons reconstructed by this algorithm were used.
- Soft electron reconstruction for low- p_T electrons:
This algorithm is used for studies of electrons from J/Ψ decays or within b-jets with energies of a few GeV. Here the reconstruction is seeded by an inner detector track which is then extrapolated to the calorimeter.
- Reconstruction of forward electrons with $|\eta| > 2.5$:
This is a relatively new algorithm and uses only calorimeter information. This algorithm is needed for example to increase the reconstruction efficiency of a multi-electron channel like $H \rightarrow ZZ \rightarrow eeee$.

6.1.2. Identification of High- p_T Electrons

The seed for this algorithm is an EM tower with E_T above 3 GeV found in the EM calorimeter. A matching track is searched for among all reconstructed tracks which do not belong to a photon-conversion pair reconstructed in the inner detector. The track is required to match the tower within a window of $\Delta\eta \times \Delta\phi = 0.05 \times 0.1$.

Various corrections are applied to the cluster position and energy to take into account η - and

ϕ -dependent effects in the calorimeter and dead material. This is especially important for the transition region ($1.37 < |\eta| < 1.52$).

Shower shape variables are calculated and combined with track quality criteria and TRT information to discriminate real electrons from jets and pions. The ratio of the cluster energy to the track momentum, E/p , is required to be lower than 10. The hadronic leakage (energy deposit in the HCAL) is larger for jets than for electrons which can be used for separation. Track and calorimeter based isolation can be required for the electron candidates. The combined information is conveniently coded into the ISEM flag allowing to choose between various sets of cuts on the electron ID:

- **LOOSE:**
This includes very loose track-cluster matching, a cut on the hadronic leakage and on the shower shapes calculated in the second sampling of the ECAL.
- **MEDIUM:**
In addition to the LOOSE cuts, tighter cuts on the track-cluster matching are applied and shower shape information calculated in the first sampling. The MEDIUMNOISO flag does not include a cluster isolation requirement.
- **TIGHT:**
This included the same cuts as for the MEDIUM flag and additionally requires a hit in the B-layer of the pixel detector, TRT information and calorimeter isolation. The TIGHTNOISO flag excludes the isolation requirement.

To separate electrons produced in a hard process from electrons produced in semi-leptonic B decays for example, it is useful to require the electron to be isolated from other detector activity. Two kinds of isolation procedures are available: The track isolation applies a cut on the number of tracks in a ΔR cone around the track of the lepton. The calorimeter isolation is based on measuring the energy deposited in a ΔR cone around the lepton (more exact the energy between an outer and an inner cone around the lepton).

6.1.3. Electron Identification Cuts

Electrons in the Lepton-Lepton Analysis

The following requirements were imposed on the electrons for the dilepton analysis:

- Standard high p_T reconstruction algorithm (ONLYEGAMMA flag),
- ISEM::MEDIUM,
- $|\eta| < 2.5$,
- $E_T > 10$ GeV,
- Calorimeter isolation: $E_T^{\Delta R < 0.2} / p_T < 0.08$.

The impact of these cuts on the signal samples with $m_A = 130$ GeV and $m_A = 450$ GeV was evaluated and is listed in Table 6.1. The efficiency of the isolation cut will be discussed in Chapter 8.

m_A [GeV]	130	450	130	450	130	450
Cut	Relative Efficiency		Efficiency		Electrons	
no cut	100.0%	100%	100%	100.0%	37 676	67 882
$E_T > 10$ GeV	28.2%	35.6%	28.2%	35.6%	10 602	22 647
onlyEgamma	81.2%	75.5%	22.8%	26.9%	8 608	18 255
MEDIUM	79.8%	74.5%	18.3%	20.0%	6 868	13 622
$ \eta < 2.5$	100.0%	100.0%	18.3%	20.0%	6 868	13 622

Table 6.1.: Number of electrons and efficiencies of each of the electron ID cuts for the lepton-lepton analysis. The numbers are not normalized but reflect the available MC statistics.

Electrons in the Lepton-Hadron Analysis

The following cuts were applied to the electron candidates in the lepton-hadron analysis. The cuts are divided into a loose and a tight selection, because, as will be discussed later, for some backgrounds the tight selection is factorized. When the tight selection is factorized, loose objects are used for the analysis and the tight ID efficiency with respect to the loose selection is applied as an event weight.

- Loose selection:
 - Standard high p_T reconstruction algorithm,
 - $p_T > 24$ GeV,
 - $|\eta| < 2.5$,
 - isEM::MediumNoIso.
- Tight selection:
 - isEM::Tight,
 - Track isolation: $\#tracks(\Delta R < 0.3) < 2$,
 - Calorimeter isolation: $E_T^{\Delta R < 0.2}/p_T < 0.1$.

In Table 6.2 the number of electrons and the efficiency of each of the loose cut criteria are listed.

6.2. Muons

6.2.1. Overview

Muons are minimum ionizing particles, they traverse the calorimeters without getting absorbed. The detector components involved in muon reconstruction are the muon spectrometer and the inner detector. However, muons also deposit some energy in the ECAL. The muon system allows the identification of muons with a p_T above 3 GeV. Very low momentum muons are difficult to reconstruct since they do not reach the spectrometer, lose too much energy in the calorimeter

m_A [GeV]	150	800	150	800	150	800
Cut	Rel. Efficiency		Efficiency		# Electrons	
No cut	100%	100%	100%	100%	1.93975e+06	159623
$p_T > 24\text{GeV}$	18.3%	37.7%	18.3%	37.7%	354846	60149
High p_T Alg.	59.4%	55.8%	15%	27.1%	291523	43191
MEDIUMNoISO	9.7%	7.5%	3.1%	5.3%	60311	8488
$ \eta < 2.5$	99.7%	99.6%	3.1%	5.3%	60311	8488
TIGHT	6.7%	5.3%	2.6%	4.3%	51166	6849
Track isolation	99.4%	99.3%	2.5%	4%	49261	6375
Calo isolation	12.6%	10.6%	2.5%	3.9%	48299	6272

Table 6.2.: Number of electrons and efficiencies for each of the electron ID cuts for the lepton-hadron analysis. The numbers were obtained from two signal samples where the Higgs boson is produced in association with b-quarks. The numbers are not normalized but reflect the available MC statistic. The efficiency of the calorimeter isolation cut is strongly correlated with the isEM::MediumNoIso and isEM::Tight requirements.

and/or do not leave a significant signal over the noise in the muon spectrometer. ATLAS employs a variety of muon reconstruction algorithms:

- Stand-alone muons:
This algorithm finds tracks in the muon spectrometer and extrapolates them back to the beam line. Using this approach muons within $|\eta| < 2.7$ can be reconstructed.
- Combined muons:
The combined muon reconstruction algorithm takes the stand-alone muons and matches them to inner detector tracks. Muons within $|\eta| < 2.5$ can be reconstructed in this way.
- Tagged muons:
Tagged muons are found by extrapolating inner detector tracks to the muon spectrometer. Furthermore, calorimeter signals can be used to tag inner detector tracks stemming from muons.

Two muon collections are in use, the MUID [98] and the STACO [99] collection. STACO stems from 'statistical combination' and the algorithm merges the muon tracks with the muon spectrometer signals. The MUID algorithm globally fits all hits associated to muon tracks. In this thesis only STACO muons have been used to reconstruct the event, since this is the current default for most analyses.

6.2.2. Muons in the STACO Collection

Stand-alone muons in the STACO collection were reconstructed from the Muonboy algorithm [98]. Muonboy finds the muon spectrometer tracks and extrapolates them to the beam line. This extrapolation accounts for multiple scattering and energy loss in the calorimeters. Muons produced in the HCAL by kaon and pion decays are likely to be found in the stand-alone reconstruction. They

therefore form a background to physics analysis involving muons from the hard process. To avoid this background it is useful to use combined muons, as was done in this thesis. For the ID of a muon track space points are required in the pixel detector and the 4 innermost SCT layers. These seeds are then extended by adding measurements from the outer SCT layers. The match between both subsystems is verified by a χ^2 defined as difference between outer and inner track vector weighted by their combined covariance matrix.

In Figure 6.1 the χ^2 distributions of all combined STACO muon candidates is shown. The muons are required to have unit charge and to pass a cut of $p_T > 5$ GeV. These plots were created from the ATHENA Rel. 14 ATLFast-II samples used in the lepton-hadron analysis. The single top process includes the contributions from Wt and t-channel production, QCD denotes the sum of the contributions from J1-J6.

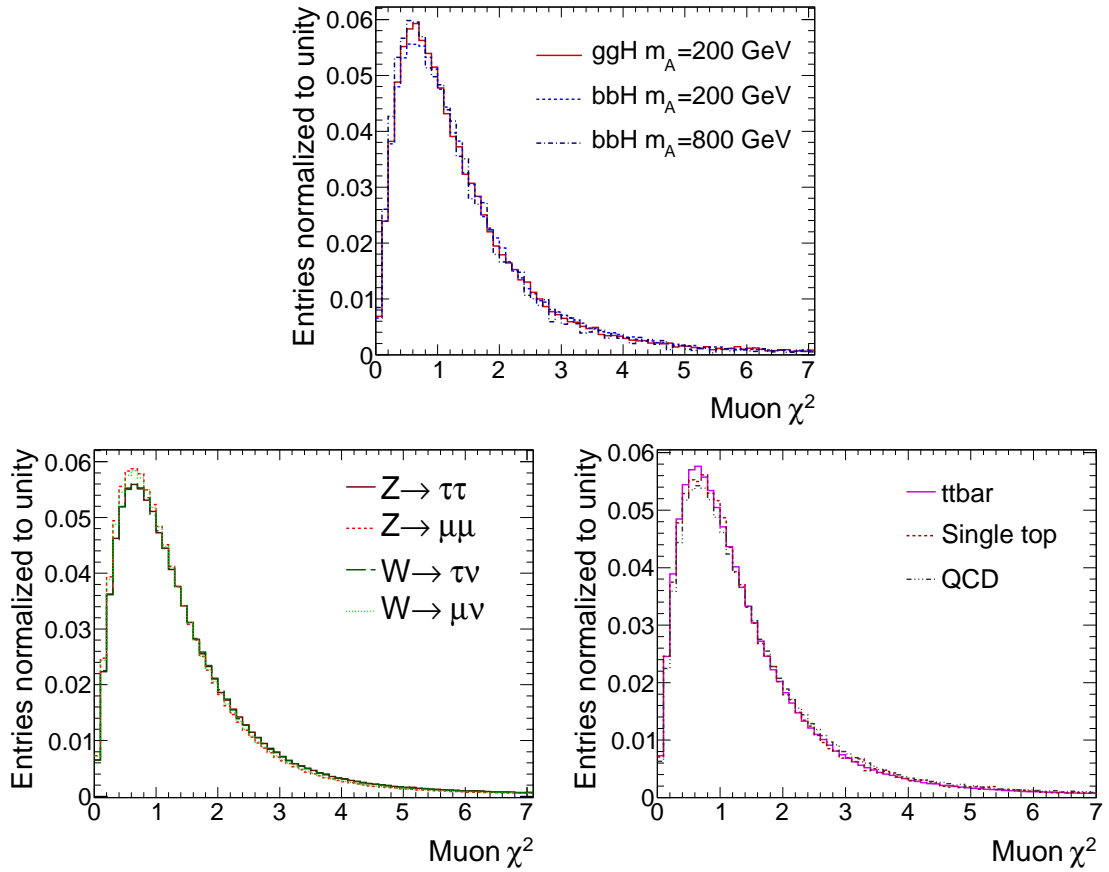


Figure 6.1.: χ^2 of combined muon candidates, for signal (upper plot) and backgrounds (lower plots). No significant process-dependent differences are observed.

6.2.3. Muon Identification Cuts

Muons in the Lepton-Lepton Analysis

The following requirements were imposed on the muons for the dilepton analysis:

- STACO high p_T muons (OnlyHighPt flag),
- Combined and best match muons,
- $|\eta| < 2.5$,
- $p_T > 10$ GeV,
- Calorimeter isolation: $E_T^{\Delta R < 0.2} / p_T < 0.07$.

The impact of these cuts on the signal samples with $m_A = 130$ GeV and $m_A = 450$ GeV was evaluated and is listed in Table 6.3. The efficiency of the isolation cut will be discussed in Chapter 8.

m_A [GeV]	130	450	130	450	130	450
Cut	Relative Efficiency		Efficiency		Muons	
no cut	100.0%	100%	100%	100.0%	11 574	18 565
$p_T > 10$ GeV	69.1%	79.9 %	69.1%	79.9%	7 999	14 826
onlyHighPt	99.1%	99.0%	68.5%	79.0%	7 933	12 750
$ \eta < 2.5$	97.0%	98.1%	66.5%	77.6%	7 697	10 752
Combined, best match	98.0%	98.1%	65.2%	76.1%	7 543	10 548

Table 6.3.: Number of muons and efficiencies for each cut of the muon ID cuts for the lepton-lepton analysis. The numbers reflect the MC statistics. Only muons from the STACO muon collection have been used in the thesis.

Muons in the Lepton-Hadron Analysis

For the lepton-hadron analysis, the muon ID cuts are separated into loose and tight cuts. For some processes the tight ID is factorized and loose objects are used in the analysis.

- Loose selection:
 - Combined STACO muons,
 - $p_T > 24$ GeV,
 - $|\eta| < 2.5$,
 - track match $\chi^2/\text{dof} < 8$.
- Tight selection:
 - Track isolation: $\# \text{tracks}(\Delta R < 0.3) < 2$,

– Calorimeter isolation: $E_T^{\Delta R < 0.2}/p_T < 0.1$.

In Table 6.4 the number of muons and the efficiency of each of the ID criteria are summarized.

m_A [GeV]	150	800	150	800	150	800
Cut	Rel. Efficiency		Efficiency		# Muons	
No cut	100%	100%	100%	100%	268617	16339
$p_T > 24\text{GeV}$	27.3%	54.9%	27.3%	54.9%	73410	8969
High p_T Alg.	87.7%	89.3%	26.7%	53.3%	71596	8705
$ \eta < 2.5$	94.9%	95.8%	25.8%	52.5%	69383	8580
combined, best match	81.5%	83.8%	25.7%	52%	68925	8494
$\chi^2/\text{dof} < 8$	98%	98.2%	25.1%	51.1%	67349	8344
Track isolation	82.8%	74.2%	22.5%	43.4%	60480	7086
Calo isolation	62%	62.4%	22.1%	42.2%	59347	6900

Table 6.4.: Number of muons and efficiencies for each of the muon ID cuts for the lepton-hadron analysis. The numbers were obtained from two signal samples where the Higgs boson is produced in association with b-quarks. The numbers are not normalized but reflect the available MC statistic.

6.3. Tau Leptons

6.3.1. Overview

The tau lifetime of $\tau \cdot c = 87 \mu\text{m}$ is too small for detecting taus directly. Instead, they are identified via their decay products. About 64.8% of the tau leptons decay into hadrons (mostly pions), 17.8% (17.4%) decay to electrons (muons). The latter case will be referred to as leptonic decays. At least one neutrino is involved in the tau decay resulting as missing E_T in the detector.

In case of a leptonic decay, τ_{lep} , the resulting electrons and muons are hard to separate from prompt leptons. Differences occur in the p_T distribution, which is usually harder for prompt leptons.

In the case of a hadronic decay, τ_{had} , the tau manifests itself in a jet visible in the inner detector and the calorimeter. The hadronic decays are classified via the number of primary charged hadrons. The decays $\tau^\pm \rightarrow \pi^\pm + \nu_\tau$ ($+n\pi^0$) or $\tau^\pm \rightarrow K^0 \pi^\pm \nu_\tau$ are called 1-prong, the decay $\tau^\pm \rightarrow 3\pi^\pm + \nu_\tau$ ($+n\pi^0$) is called 3-prong. Only in 0.1% of the tau decays five or more charged hadrons are produced. Relevant tau decay modes are listed in Table 6.5. Since QCD jets might fake the signature of a tau jet, identifying taus correctly is a crucial ingredient to the analysis. A tau jet is usually collimated, isolated, has a low track multiplicity and a characteristic shower shape. These differences are exploited in either cut-based or multivariate approaches.

Two tau algorithms are established in ATLAS:

- Calorimeter based (TauRec):

This algorithm is seeded by a cluster which is reconstructed in the hadronic and EM calorimeters. The ID variables are built from information from the tracker and the calorimeters.

Decay	Fraction
$\tau \rightarrow e + 2\nu$	17.8%
$\tau \rightarrow \mu + 2\nu$	17.4%
$\tau \rightarrow \pi^\pm + \nu$	11.1%
$\tau \rightarrow \pi^\pm + \nu + n\pi^0$	38.4%
$\tau \rightarrow 3\pi^\pm + \nu$	9.0%
$\tau \rightarrow 3\pi^\pm + \nu + n\pi^0$	5.6%

Table 6.5.: Tau decay modes and branching fractions [7].

- Track based (Tau1p3p):

The seed is built from a few high quality tracks collimated around the leading one. The energy is calculated from an energy-flow algorithm based on tracks and calorimeter information.

In this thesis only (hadronic) tau candidates have been used which were reconstructed by both algorithms.

6.3.2. Calorimeter Based Reconstruction Algorithm

This reconstruction method starts from *TopoJets* with an $E_T > 10$ GeV. *TopoJets* are jets where a cone algorithm¹ with $\Delta R = 0.4$ is run over topological clusters². Then, tracks within a cone radius of $\Delta R < 0.3$ are associated to the calo-seeded τ candidate. The energy of calo-based τ candidates is obtained by summing up the cells associated to the *TopoJet*. The cell energies are calibrated with a *local-hadronic* calibration [19]. These cell weights are a function of the cell energy density, the η and the calorimeter region of the *TopoJet*. Calibration of hadronic energy deposits is needed due to the non-compensating nature of the ATLAS calorimeters, which give the correct energy only for electromagnetic objects but underestimate the jet energy.

Several quantities are combined into a likelihood function to distinguish taus from jets: Electromagnetic radius R_{em} ³, isolation in the calorimeter, tau candidate charge, number of associate tracks, number of hits and E_T in the first ECAL layer, lifetime signed impact parameter of the leading track and the E_T over p_T ratio of the leading track. An one-dimensional likelihood ratio is constructed from these variables, where the ratios are either taken from simulated reference histograms or are obtained by fits of appropriate functions to each variable in five bins of E_T : (10-25) GeV, (25-45) GeV, (45-70) GeV, (70-100) GeV and >100 GeV. The tau ID efficiency is therefore E_T dependent and a fixed cut on the likelihood ratio will lead to a non-constant tau ID efficiency as a function of E_T .

¹A description of the cone jet finder algorithm is given in the Section 6.4.2 on jet reconstruction.

²Topological clusters (*TopoClusters*) will be discussed further in Section 6.5.2 on missing E_T reconstruction.

³The electromagnetic radius, R_{em} , and other quantities, are defined in Ref. [100].

6.3.3. Track Based Reconstruction Algorithm

A complete description of this algorithm is given in Ref. [101]. The idea of this approach is to start from a high- p_T and well collimated track (stemming from the charged pion) which is assumed to reproduce well the direction of the tau. The τ candidate is required to have a low track multiplicity of mostly 6 associated tracks (in most cases either 1 or 3 tracks) and has to be well isolated. A tau charge calculated from the sum of the track charges of either ± 1 or 0 is required.

The energy of the tau candidate is calculated using the energy flow approach in a ΔR cone of 0.2 around the seed track. The energy deposit is divided into three categories: The pure electromagnetic energy (cluster has no hadronic leakage and is isolated from tracks), the charged EM energy (cluster seeded by the impact point of a track), the neutral EM energy (energy from not yet used cells closest to the impact point of the track). First the energy scale of the τ is defined by the sum of the charged track momentum and then corrected by the various energy terms. As for the calorimeter based algorithm, different tracking and calorimetric quantities are combined into a likelihood ratio.

6.3.4. Tau Identification Cuts in the Lepton-Hadron Analysis

The cuts on the τ candidates in the lepton-hadron analysis are classified into loose and tight. For some of the background processes the tight ID efficiency is applied as a weight and loose objects are used in the analysis.

- Loose selection:
 - Calorimeter and track seeded tau candidates,
 - $p_T > 24$ GeV,
 - $|\eta| < 2.5$,
 - Pass the ELECTRONVETO and MUONVETO⁴.
- Tight selection:
 - 1 or 3 prong taus,
 - Likelihood ratio $LLH > 3.0$.
- Event selection:
 - E_T binned likelihood ratio cut (LLH):

$24 \text{ GeV} < p_T < 45 \text{ GeV}$	$LLH > 5.5$,
$45 \text{ GeV} < p_T < 70 \text{ GeV}$	$LLH > 6.7$,
$80 \text{ GeV} < p_T < 100 \text{ GeV}$	$LLH > 6.0$,
$100 \text{ GeV} < p_T$	$LLH > 7.5$.

In Figure 6.2 the number of tau candidates identified from the two algorithms is shown for signal and background processes. All tau candidates with integer charge passing a cut of $p_T > 5$ GeV have been used, hence not even the loose criteria are applied. The plots were created from ATHENA

⁴The ELECTRONVETO and MUONVETO flags include cuts on tracks in the TRT and the energy of the calorimeter cluster to suppress tau fakes from electrons and muons.

Rel. 14 ATLFast-II samples. The single top includes the contributions from Wt and t -channel, QCD denotes the sum of the contributions from J1-J6.

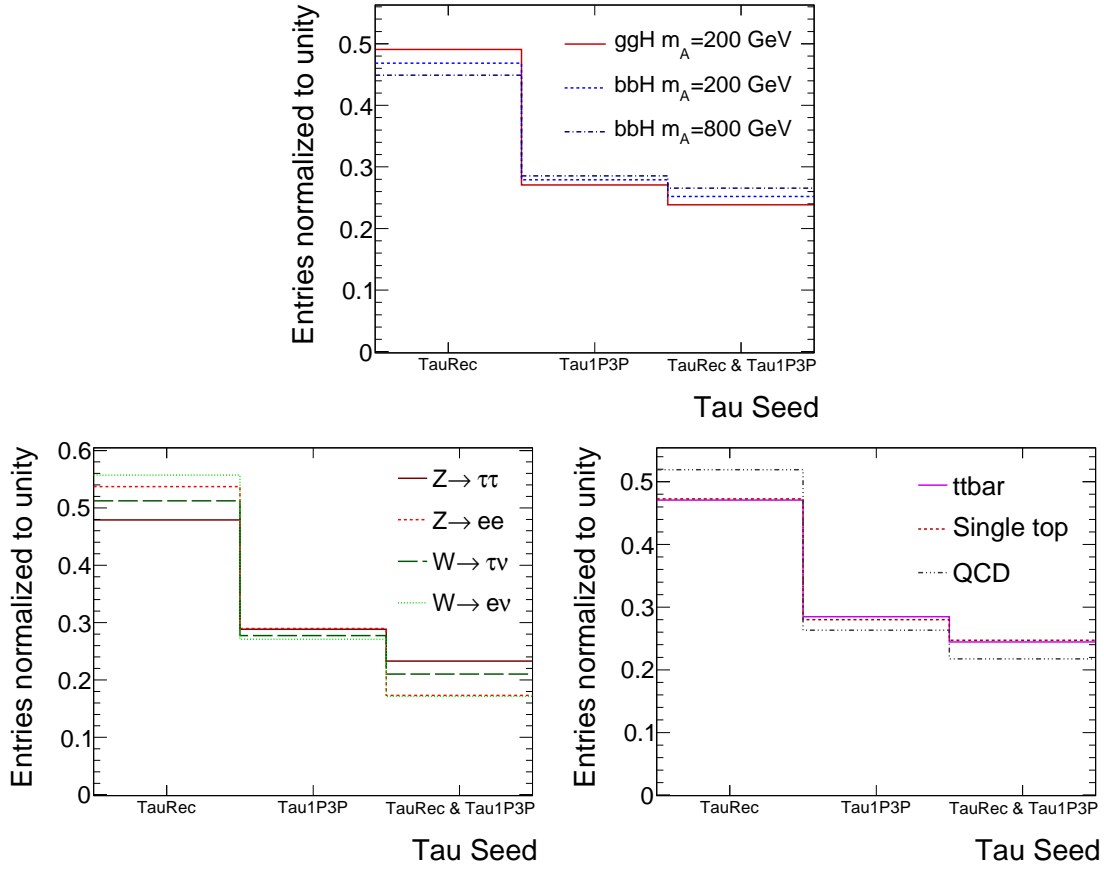


Figure 6.2.: Tau seeds for signal (upper plot) and backgrounds (lower plots). 'TauRec' ('Tau1P3P') denotes that the τ candidate is reconstructed by the TauRec (Tau1P3P) algorithm, but it does not mean a veto on the other algorithm. For 'TauRec & Tau1P3P' both seeds were required for each τ candidate.

In Table 6.6 the number of τ candidates and the corresponding efficiencies for each τ ID cut are listed.

m_A [GeV]	150	800	150	800	150	800
Cut	Rel. Efficiency		Efficiency		# Taus	
No cut	100%	100%	100%	100%	1.63748e+06	110982
Algorithm	48.5%	56.6%	48.5%	56.6%	793606	62830
Electron veto	46%	51.4%	40.2%	47.4%	659050	52621
Muon veto	94.5%	98%	39.4%	46.9%	645133	52065
Charge	68.7%	67%	33%	37%	539865	41016
$ \eta < 2.5$	99.9%	99.9%	33%	37%	539865	41016
$p_T > 24\text{GeV}$	50.2%	67.7%	26.7%	34.8%	437984	38616
1 or 3 prong	66.9%	62.3%	25.7%	31.8%	420209	35300
LLH > 3	34.5%	36.1%	19.7%	23.9%	322074	26539
tight LLH cut	26.7%	29.3%	16%	20.3%	262036	22564

Table 6.6.: Number of τ candidates and efficiencies for each of the hadronic τ ID cuts in the lepton-hadron analysis. The numbers are not normalized but reflect the available MC statistic.

6.4. Jets and B-Tagging

6.4.1. Overview

Jet reconstruction is provided within $|\eta| < 4.9$. The detector part essential for the jet reconstruction is the calorimeter. The inner detector is needed for the b-tagging.

A jet denotes the collimated bundle of objects arising from the hadronization of partons. Jets occur in almost any event at a hadron collider, either produced in the hard process or by secondary QCD emission. Especially the jet energy scale is needed to be known with high precision since it is strongly correlated to the missing E_T resolution, which is an important aspect in the presented analyses. The jet multiplicity offers discrimination of signal events against processes with high jet activity, as for instance the $t\bar{t}$ background. The correct flavor tagging of the original quark is important since true b-jets are present if the Higgs boson is produced in association with b-quarks. Various jet finder algorithms are available in ATLAS. There is no universal jet finder suited for every analysis and the algorithms are in permanent development. Well established are fixed cone algorithms [102] as well as the seedless infrared-safe (SIS) cone algorithm, the k_T [103, 104] and anti- k_T algorithm [105, 106]. Cone algorithms bundle particles to jets which are close in angle, while k_T algorithms combines particles which are close in momentum. In this thesis, following the ATLAS recommendation, only jets reconstructed by the fixed cone algorithm have been used. In new studies cone jets are superseded by anti- k_T jets, which are preferred since they are collinear and infrared safe⁵. This theoretical safety is not given for the seeded cone algorithm.

⁵Collinear safety denotes the independence of the jet reconstruction from splitting one particle into two collinear particles. Infrared safety is conserved if additional soft particles (or their absence) between two particles belonging to the same jet does not affect the recombination of the jet.

6.4.2. Cone Jets

Jets manifest themselves as clusters in the calorimeter projected onto the $\eta - \phi$ plane to an area of πR^2 , where R denotes the radius of the circle around the cluster center. Extrapolating the cluster position to the primary vertex gives a 3-dimensional cone. The standard cone algorithm requires a seed for the jet. A seed is a cell within a cluster with an E_T larger than a threshold value (the current threshold is $E_T > 1$ GeV). All seeds passing the cut are ordered according to descending E_T . The highest E_T seed is then combined with all objects within the cone radius R around the seed cell at η_c and ϕ_c . Then a new cone center is calculated from the four-momenta of the combined objects. All objects within the new cone are combined. If, however, the new cone center is close enough to η_c and ϕ_c , the jet is considered stable and the algorithm is successfully finished. Otherwise the recombination procedure is repeated with the next highest seed until the jet is finally stable or it is removed after a certain number of iterations. The jet finder algorithm loops over all seeds repeating the above procedure.

Since this algorithm is not infrared safe by design, a dedicated *split-and-merge* algorithm is applied for recovering partly the infrared safety. Jets, which share constituents with more than a certain fraction $f = 0.5$ of the E_T of the less energetic jet, are merged. Jets are split if the amount of shared E_T is below that threshold fraction f .

Several cone radii are used in ATLAS. In this thesis relatively narrow cone sizes of $R = 0.4$ have been applied.

6.4.3. B-Tagging

Overview

B-tagging denotes the labeling of a jet as originating from a b-quark. A jet is called mis-tagged if it was labeled as a b-jet but is in reality stemming from a light- or a c-quark. Since processes as for example $Zb\bar{b}$ or $Wb\bar{b}$ have a much smaller cross section than the inclusive Z+jets or W+jets production, these latter background processes can be efficiently reduced by a reliable b-tagging procedure. $t\bar{t}$ on the other hand is a background with true b-jets in the final state and cannot be suppressed by b-tagging.

B-tagging is based on the identification of B-hadrons in a jet. The lifetime of a B-hadron is 1.6 ps ($c \cdot \tau \approx 450 \mu m$) and the mass of approximately 5 GeV is larger than for other hadrons. A flight length of typically 3 mm (for a B-hadron with $p = 35$ GeV) results in a displaced secondary vertex. In general, tracks in b-jets have a larger signed impact parameter d_0 with respect to the primary vertex. B-jets have a higher track multiplicity, they are wider than light-jets and can contain (non-isolated) soft electrons or muons. The sign of the impact parameter is positive if the angle between the jet direction and the line joining the primary vertex to the point of closest approach is less than 90° . Also, the fragmentation of b-quarks is harder than that of light-jets and about 70% of the b-quark momentum is retained in the B-hadron.

In ATLAS a variety of b-tagging algorithms is available. They are either based on the tracks' impact parameters in one or more dimensions, a reconstructed secondary vertex, a combination of both or on soft-lepton tagging. The default ATLAS b-tagger is the IP3D+SV1 algorithm, which was used in the studies of this thesis.

In the IP3D algorithm for each track a transverse impact parameter significance, S_{d_0} , is defined by $S_{d_0} = \frac{d_0}{\sigma_{d_0}}$, where σ_{d_0} is the uncertainty on d_0 . A second significance, S_{z_0} is calculated from

the longitudinal impact parameter $|z_0| = |\Delta z| \cdot \sin \theta$. For each track a track weight is calculated from a probability ratio $w_{\text{track}} = \frac{b(S_{d_0}, S_{z_0})}{u(S_{d_0}, S_{z_0})}$. b and u are the predefined, smoothed and normalized distributions for the two hypothesis (b-jet b or light-jet u) which are obtained from reference histograms. The IP3D jet weight, w_{IP3D} , is calculated from the track weights as follows:

$$w_{\text{IP3D}} = \sum_{\text{track}} \ln(w_{\text{track}}). \quad (6.1)$$

The SV1 tagger fits a secondary vertex (SV) by using tracks which survive some preselection cuts. The distance between primary and secondary vertex is not used for discriminating light-jets from b-jets due to its correlation with d_0 and z_0 . Instead, 3-dimensional reference histograms are filled and used as discriminating variables u and b , containing the SV mass, the energy fraction of tracks in the SV and the number of good 2-track vertices. In case a SV is found, the SV1 jet weight is then defined as follows:

$$w_{\text{SV1}} = \ln \left(\frac{\varepsilon_b \cdot b}{\varepsilon_u \cdot u} \right). \quad (6.2)$$

$\varepsilon_b \approx 65\%$ denotes the efficiency to fit a SV in a b-jet, $\varepsilon_u \approx 3\%$ is the efficiency to find a SV in a light-jet. ε_b and ε_u were obtained from MC simulations. If no SV is fitted, the SV1 weight is given as:

$$w_{\text{SV1}} = \ln \left(\frac{1 - \varepsilon_b}{1 - \varepsilon_u} \right). \quad (6.3)$$

The total jet weight of the standard b-tagger is then calculated as:

$$w_{\text{jet}} = w_{\text{IP3D}} + w_{\text{SV1}}. \quad (6.4)$$

In this thesis, a cut on the total jet weight was applied to impose the b-tagging requirement. In the lepton-lepton analysis a weight cut of 3 was chosen. For the lepton-hadron analysis a cut on the weight of larger than 4 was applied.

Correction of the Light Jet Rejection Rate in Rel. 12

In ATHENA Rel. 12, the light-jet⁶ rejection rate was over-estimated and needed to be corrected for each MC sample. The light-jet rejection rate is defined as the inverse of the mistag rate:

$$\text{rejection rate} = \frac{1}{\text{mistag rate}}. \quad (6.5)$$

⁶In this context light-jets denotes only jets originating from u, d or s quarks.

The mistag rate is defined as the number of true⁷ light-jets passing the b-tagging weight cut divided by the number of all true light-jets:

$$\text{mistag rate} = \frac{\text{light-jets passing b-tagging weight cut}}{\text{all light-jets}}. \quad (6.6)$$

A reduction of the rejection rate to 70% of the original Rel. 12 value was commonly chosen [19], based on recommendations from b-tagging experts. This was realized by shifting the b-tagging weight of every true light-jet to a higher value, so that the overall light-jet rejection rate was decreased to 70%. The obtained weight corrections are listed in Appendix B.

Performance

To give an impression of the performance of the used SV1+IP3D tagger, the b-tagging efficiency and the light-jet rejection rate are displayed in Figure 6.3. The performances in ATHENA Rel. 12 and 14 are directly compared. The light-jet correction was applied for the Rel. 12 signal samples. The b-tagging efficiency is larger in Rel. 12 by 5%. A weight cut of 3 or 4 corresponds to a working point between 50% and 60% b-tagging efficiency. The light-jet rejection is shown as a function of the b-tagging efficiency. It is comparable between the two releases at the region of the working points.

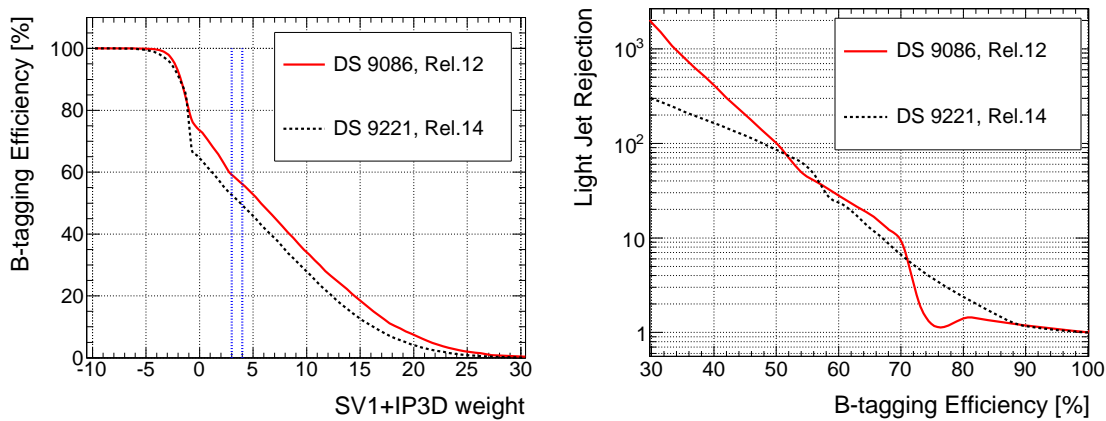


Figure 6.3.: Left: The efficiency that a jet originating from a b-quark is correctly tagged as a b-jet as a function of the flavor tagging weight obtained from Higgs boson samples which were processed in two different ATHENA software releases. The Higgs boson is produced in association with b-quarks and a mass of 200 GeV is assumed. The working points at weight 3 (weight 4) for the dilepton (lepton-hadron) analysis are marked by vertical lines. Right: The light-jet rejection rate as a function of the b-tagging efficiency obtained from the same signal samples. The Rel. 12 sample contains a factor of 17 less statistics compared to the Rel. 14 sample, which explains the unphysical structure at b-tagging efficiencies between 70% and 80%.

⁷A true light-jet (true b-jet) is a reconstructed jet resulting from a u/d/s-quark (b-quark) according to the MC event record. The reconstructed flavor might be different.

6.5. Missing E_T

6.5.1. Overview

Due to the presence of neutrinos in the signal final state, the reconstruction and resolution of the missing E_T (also called MET) is a crucial ingredient to the analysis. In principle, the x and y components of the MET are calculated from the negative signed sum of the $E_{x,y}$ of all other objects (Equation 4.7). However, several corrections need to be applied. The energy deposits need to be classified into various types and calibrated accordingly. Further challenges in the MET reconstruction arise from limited detector coverage, finite detector resolution, dead detector regions and noise, because all these effects produce fake MET.

In ATLAS two algorithms are established for the MET reconstruction:

- **Cell-based:**
This algorithm starts from selecting the energy deposits in calorimeter cells which pass a certain noise cut. The cells are then globally calibrated by weights which depend on the energy density and which were obtained from MC simulations. In a second step the cells are calibrated according to the reconstructed objects assigned to the calorimeter clusters. Corrections are applied for energy losses in the cryostats and for energy carried away by muons. This algorithm is described in detail below.
- **Object-based:**
This algorithm starts from the reconstructed, calibrated and classified objects to calculate the MET. Then this MET term is corrected for energy deposits which could not be assigned to objects. This method is especially used in analyses looking for low- p_T objects such as pions or soft jets.

In this thesis MET reconstructed by the cell-based algorithm was used exclusively, since this follows the ATLAS recommendation.

6.5.2. Cell Based Missing E_T Reconstruction

The first step for the MET reconstruction is the noise suppression procedure. The electronic noise of all calorimeter channels would contribute to the total MET resolution with roughly 13 GeV. Therefore, only cells with an energy deposit exceeding a noise cut are used. However, a noise cut which is too hard will reduce the reconstruction efficiency of events with only little MET, such as the light Higgs boson decay to τ -pairs for example. In ATLAS the noise suppression is implemented by using only cells within 3-dimensional topological calorimeter clusters. A TopoCluster is reconstructed starting from a seed cell with $|E_{cell}| > 4\sigma_{noise}$, where σ_{noise} denotes the width of the noise distribution. Neighbors with $|E_{cell}| > 2\sigma_{noise}$ are associated to the seed cell. Finally, all the cells at the boundary surrounding the cluster are included ($|E_{cell}| > 0\sigma_{noise}$). This algorithm is also called the 4/2/0 configuration approach.

The next step is the calculation of the MET (also called *final* MET). This includes contributions from the following terms:

$$\vec{E}_{x,y}^{Final} = \vec{E}_{x,y}^{calo} + \vec{E}_{x,y}^{muon} + \vec{E}_{x,y}^{cryo}. \quad (6.7)$$

The three contributing terms are explained in the following:

- $\cancel{E}_T^{\text{calo}}$
The $\cancel{E}_T^{\text{calo}}$ is calculated by summing over the E_T of all cells in identified TopoClusters. The energy measured in the cells is at the electromagnetic scale. This is the correct scale for objects like electrons or photons, but the energy of jets is underestimated. Therefore, this MET yields in a 30% shift of the E_T scale with respect to the true MET. To account for this the energy deposits are classified into EM and hadronic deposits. The classification is based on the energy density and shower shape which is different in EM and in hadronic showers. The hadronic deposits of all cells are then globally weighted using the *local-hadronic* calibration [19].
- $\cancel{E}_T^{\text{muon}}$
The muon term is calculated by the negative sum of the x and y components momenta of all identified muons. Muons within $|\eta| < 2.5$ are combined with their tracks from the ID. Standalone muons are used with a range of $2.5 < |\eta| < 2.7$. No p_T cut is applied to the muon candidates at this stage.
- $\cancel{E}_T^{\text{cryo}}$
Hadronic showers extend across the EM calorimeters via the cryostat walls into the HCAL system. The cryostat thickness is about half an interaction length and the energy loss there needs to be accounted for. This term also enters the jet energy calibration. The energy loss in the cryostat is calculated by the energy difference between the last layer in the ECAL and the first layer of the Tile calorimeter. This energy difference is then corrected by a calibration weight. The cryostat term contributes to a level of 5% to jets with $p_T > 15$ GeV.

The last step in the MET calculation is the refined calibration of cells associated to objects. The objects are identified and are then associated by navigating back to the clusters and then back to the cells. The association follows a defined order: Electrons, photons, muons, τ_{had} , b-jets and light-jets⁸, hence if cells belong to more than one objects only the highest-ranking object is associated. The idea hereby is that these identified objects are calibrated with better accuracy than the hadronic energy deposits. The local-hadronic calibration weights are replaced by the object calibration weights. Energy deposits in cells which could not be associated (denoted as $\cancel{E}^{\text{RefOut}}$) are also included in the refined calculation and here the global calibration weights are used.

The refined MET term replaces the $\cancel{E}_T^{\text{calo}}$ term in Equation 6.7 and is given as follows:

$$\cancel{E}_{x,y}^{\text{RefFinal,calib}} = - \left(\cancel{E}_{x,y}^{\text{Ref,El}} + \cancel{E}_{x,y}^{\text{Ref,Tau}} + \cancel{E}_{x,y}^{\text{RefBjets}} + \cancel{E}_{x,y}^{\text{RefMuon}} + \cancel{E}_{x,y}^{\text{RefJets}} + \cancel{E}_{x,y}^{\text{RefOut}} \right), \quad (6.8)$$

where each term is calculated from the negative of the sum of the energy of calibrated cells inside a specific object plus the globally calibrated energy from non-associated cells. The refined final MET is then calculated according to Equation 6.7 as follows:

$$\cancel{E}_{x,y}^{\text{RefFinal}} = \cancel{E}_{x,y}^{\text{RefFinal,calib}} + \cancel{E}_{x,y}^{\text{muon}} + \cancel{E}_{x,y}^{\text{cryo}}. \quad (6.9)$$

The refined final MET is used for the event reconstruction within this thesis, unless marked otherwise. For shortness it will be referred to just as MET.

Figure 6.4 shows the MET distribution for selected signal samples and all background processes.

⁸Here, light-jets denotes jets originating from u , d , s or c quarks.

These figures were created from the ATHENA Rel. 14 ATLFast-II samples used in the lepton-hadron analysis. As before, the single top process includes the contributions from Wt and t -channel production, QCD denotes the sum of the contributions from J1-J6.

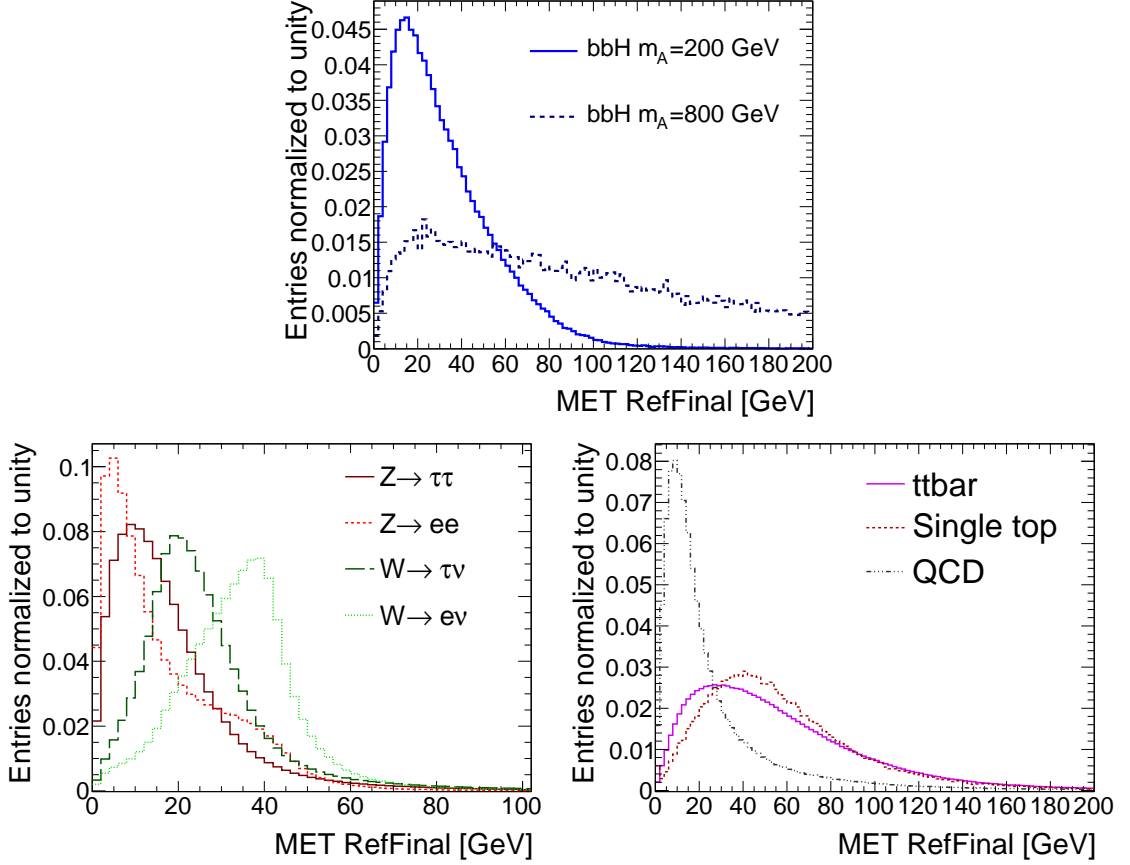


Figure 6.4.: Refined final MET for signal (upper plot) and backgrounds (lower plots). The average MET becomes larger with increasing Higgs boson masses. In $Z \rightarrow ee$ and $Z \rightarrow \mu\mu$ no real MET is present. Large MET values are expected in the $W \rightarrow e/\mu\nu$, $t\bar{t}$ and single top processes. In $W \rightarrow \tau\nu$ the average MET is smaller because the momentum of the prompt neutrino partially cancels the momentum of the neutrino from the τ decay.

6.6. Object Allocation Ambiguity

When the objects are reconstructed by the relevant ATHENA algorithms, it can happen that one object is reconstructed by several different algorithms. An electron object for example can be found in the electron container but also in the muon container if it was (wrongly) reconstructed and identified by the muon reconstruction algorithms. To avoid this *overlap*, a dedicated object priority list is applied. The object will then only be classified by the highest priority type if it is reconstructed by different algorithms. The priority list used for this thesis is chosen as follows:

Muons \Rightarrow Electrons \Rightarrow Taus \Rightarrow Jets.

If two objects are closer to each other than $\Delta R = 0.2$, the object with the lower priority is removed from the allocation list of identified objects. This will also be referred to as *overlap removal*.

Higgs Boson Mass Reconstruction

7.1. Collinear Approximation

Due to the presence of neutrinos in the $h/A/H \rightarrow \tau\tau$ decay channel, the mass of the Higgs particle cannot be reconstructed completely from its decay products. Neutrinos escape the direct detection in the ATLAS detector but result in MET, as they take away a considerable amount of the transverse momentum in the event.

Since the Higgs boson mass is large compared to the tau mass, the two τ -leptons from the Higgs boson decay experience a strong Lorentz boost, i.e. they have a large relativistic γ -factor. Their decay products (electrons/muons or pions/kaons and neutrinos) are then also boosted and emitted collinear to the τ direction of flight. This is illustrated in Figure 7.1. This behavior is exploited by the applied mass reconstruction method, the collinear approximation [107].

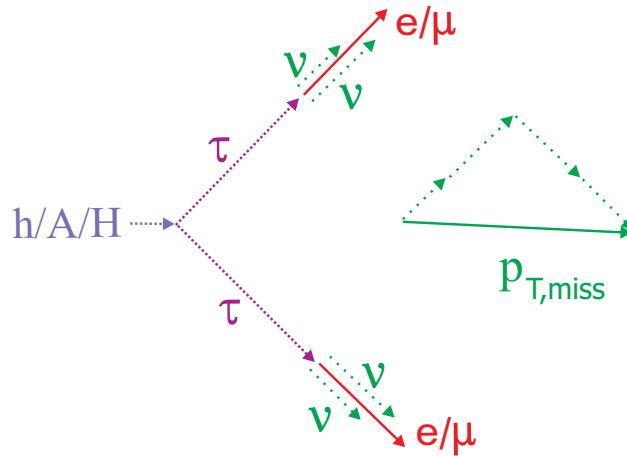


Figure 7.1.: Scheme of the Higgs boson decay, here for the case that both τ -leptons decay leptonically. The τ decay products are emitted collinear to the τ direction of flight. The MET vector is the sum of the p_T of the neutrinos.

In Figure 7.2 the distribution of the angle between the true electron (or muon) and the true τ is shown. The objects have been matched to reconstructed objects by requiring a $\Delta R < 0.3$ and a cut of $p_T > 20$ GeV is applied to all objects involved. A clear peak at zero rad is visible. The same behavior was found for the angle between the electron (or muon) and the neutrinos [108]. The plot is made from the Rel. 14 ATLFast-II samples for a Higgs boson mass of 300 GeV.

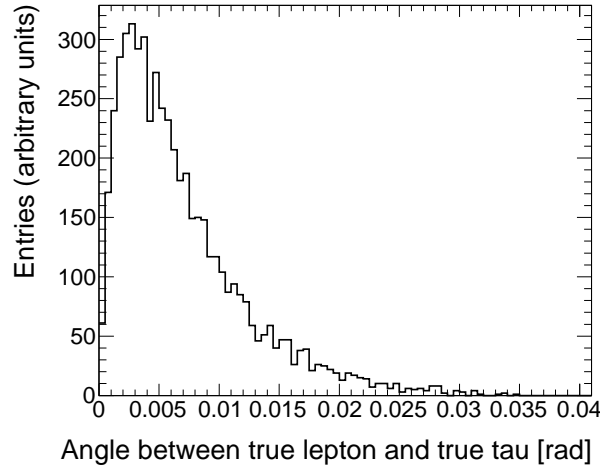


Figure 7.2.: Distribution of the angle between true tau and true electron/muon of the same charge for a Higgs boson signal sample of $m_A = 300$ GeV. The tau and the electron/muon have been matched to reconstructed objects by requiring a $\Delta R < 0.3$. The angle strongly peaks at approximately zero, which proves the collinearity.

When the two τ -leptons decay, the total transverse momentum is conserved:

$$\vec{p}_{T,1}^\tau + \vec{p}_{T,2}^\tau = \vec{p}_{T,1}^{\ell/h} + \vec{p}_{T,2}^{\ell/h} + \vec{p}_{T,\text{miss}}. \quad (7.1)$$

Since the τ -lepton and its decay products are emitted collinearly, the τ momenta ($i = 1, 2$) can be substituted by the momenta of the visible decay products scaled with a factor x :

$$\vec{p}_{T,i}^\tau = \frac{\vec{p}_{T,i}^{\ell/h}}{x_i}. \quad (7.2)$$

The factor x describes the fraction of the tau p_T carried away by its visible decay product. Only values in the range $0 < x < 1$ are physically meaningful. x_1 and x_2 are calculated from the momentum conservation (Equation 7.1) in the x and y components:

$$\begin{aligned} x_1 &= \frac{p_{x,1}^{\ell/h} \cdot p_{y,2}^{\ell/h} - p_{y,1}^{\ell/h} \cdot p_{x,2}^{\ell/h}}{p_{y,2}^{\ell/h} \cdot p_{x,\text{miss}} - p_{x,2}^{\ell/h} \cdot p_{y,\text{miss}} + p_{x,1}^{\ell/h} \cdot p_{y,2}^{\ell/h} - p_{y,1}^{\ell/h} \cdot p_{x,2}^{\ell/h}}, \\ x_2 &= \frac{p_{x,1}^{\ell/h} \cdot p_{y,2}^{\ell/h} - p_{y,1}^{\ell/h} \cdot p_{x,2}^{\ell/h}}{p_{x,1}^{\ell/h} \cdot p_{y,\text{miss}} - p_{y,1}^{\ell/h} \cdot p_{x,\text{miss}} + p_{x,1}^{\ell/h} \cdot p_{y,2}^{\ell/h} - p_{y,1}^{\ell/h} \cdot p_{x,2}^{\ell/h}}. \end{aligned} \quad (7.3)$$

The invariant $\tau\tau$ -mass is given as follows:

$$m_{\tau\tau}^2 = (p_1^\tau + p_2^\tau)^2. \quad (7.4)$$

Here $p_\tau = (E_\tau, \vec{p}_\tau)$ labels the relativistic four-momentum. Using $p_\tau^2 = m_\tau^2$ one obtains:

$$m_{\tau\tau}^2 = 2 \cdot (m_\tau^2 + p_1^\tau \cdot p_2^\tau). \quad (7.5)$$

Neglecting the τ mass and using the collinear approximation Equation 7.2 leads to:

$$m_{\tau\tau}^2 = 2 \cdot \left(\frac{p_1^{\ell/h} \cdot p_2^{\ell/h}}{x_1 \cdot x_2} \right). \quad (7.6)$$

This leads to the final equation for the reconstructed Higgs boson mass:

$$m_{\tau\tau} = \frac{m_{\ell/h, \ell/h}}{\sqrt{x_1 \cdot x_2}}, \quad (7.7)$$

where the invariant di-lepton (or lepton-pion/lepton-kaon) mass is given by

$$m_{\ell/h, \ell/h}^2 \approx 2 \cdot p_1^{\ell/h} \cdot p_2^{\ell/h}, \quad (7.8)$$

when the e , μ and pion or kaon masses are neglected. There are two conditions which need to be fulfilled in order for this approximation to give correct results:

- The MET of the event needs to be equal to the vector sum of the \vec{p}_T from the neutrinos stemming from the Higgs boson decay. This cannot be fulfilled exactly, since a measurement is always limited by the detector capabilities. The MET resolution therefore directly influences the mass resolution.
- The Higgs particle needs to have a non-zero p_T , otherwise the two tau leptons are emitted with a difference in the azimuthal angle of $\Delta\Phi = 180^\circ$. In this case no physical solution to the collinear approximation can be found. This can be suppressed by cutting either on a minimal p_T of the Higgs boson

$$|\vec{p}_{T, \text{Higgs}}| = \left| \begin{pmatrix} p_{x,1}^\tau + p_{x,2}^\tau \\ p_{y,1}^\tau + p_{y,2}^\tau \end{pmatrix} \right| = \left| \begin{pmatrix} p_{x, \text{miss}} + p_{x,1}^{\ell/h} + p_{x,2}^{\ell/h} \\ p_{y, \text{miss}} + p_{y,1}^{\ell/h} + p_{y,2}^{\ell/h} \end{pmatrix} \right|, \quad (7.9)$$

or a maximal $\Delta\Phi$ of the two visible tau decay products, which is strongly correlated.

In the following different performance issues for the collinear mass will be discussed. A loose object and event selection was applied to both the Rel. 14 ATLFast-II samples for the lepton-hadron mode and the FULLSIM samples from Rel. 12 for the dilepton analysis. An alternative variable, the visible mass, is studied as well and is compared to the collinear mass. A discussion of the MET performance and a summary conclude the chapter.

7.2. Performance of the Collinear Approximation

7.2.1. The $h/A/H \rightarrow \tau_\ell \tau_h$ Channel

The electrons, muons and τ -leptons used in the performance studies are selected based on the LOOSE object selection as described in Chapter 6. No MET cut and no requirement on jets were

applied to the events. If one tau and one electron or muon fulfilling the object selection were found, the event was kept in the analysis. The tau and electron/muon with the highest p_T were used for the studies. No cut on $\Delta\Phi_{\ell h}$ was applied. x_1 and x_2 were required to have values between 0 and 1, unless stated otherwise.

Figure 7.3 displays the reconstructed $\tau\tau$ masses for all considered Higgs mass hypotheses produced in association with b-quarks or by gluon fusion. Normalization to unity reveals a dependence of the reconstructed width on the Higgs boson mass. This, however, is not correlated to the natural Higgs boson width as displayed in Fig. 2.8. Depending on the value of $\tan\beta$, the natural width is at least one order of magnitude smaller than the reconstructed width.

A shift of the mass peak to lower values than the input Higgs boson mass value is observed. The central part of the reconstructed mass distributions was fitted by a simple Gaussian to quantify the peak position and the width. In Figure 7.4 the collinear mass is displayed and fitted separately for the $\tau_e\tau_h$ and the $\tau_\mu\tau_h$ channels. A slight shift to lower mass values in the $\tau_\mu\tau_h$ channel of 1-2 GeV compared to the $\tau_e\tau_h$ channel is visible. This shift, however, is not significant compared to the mass resolution and will not be considered further.

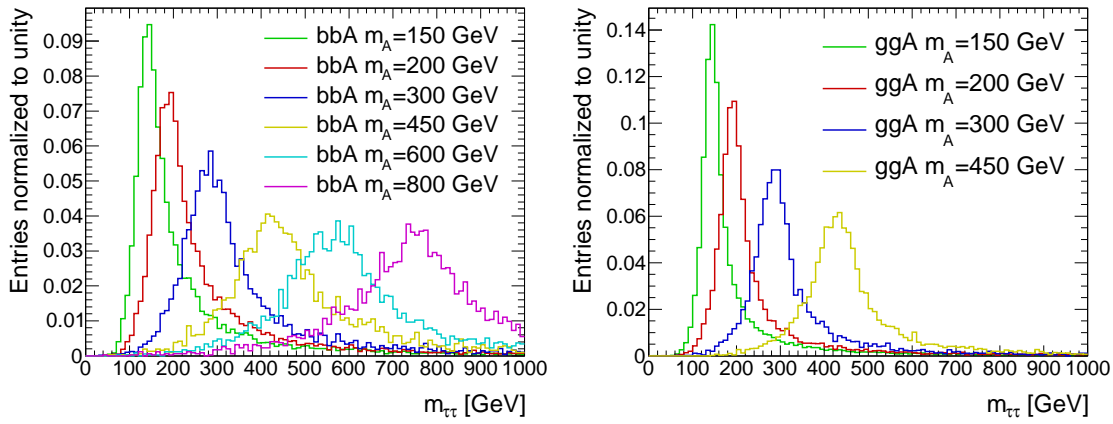


Figure 7.3.: Reconstructed collinear mass in the lepton-hadron channel for various Higgs boson mass hypotheses, left for b-associated and right for direct production. The distributions are normalized to unity. The mass resolution becomes worse with an increasing m_A .

The fitted peak position and its difference to the input mass value as function of m_A is shown in Figure 7.5. The fitted width as well as the relative mass resolution as function of m_A are presented in Figure 7.6. The signal events produced in gluon fusion show exactly the same mass shift as in b-associated production. However, their width and relative mass resolution in gluon fusion is significantly smaller than when the Higgs boson was produced in association with b-quarks. One reason for the better performance of the collinear mass for gluon fusion signal events is found in the different distributions of $p_{T,Higgs}$. When the Higgs boson is produced in gluon fusion, it carries on average more p_T than in production with b-quarks. This was also noticed in previous studies of the lepton-hadron channel [109]. Other studies showed, that a Higgs boson produced in VBF has a larger p_T than the b-associated signal [110]. This leads to differences in the distribution of $x_1 \cdot x_2$ and $\Delta\Phi_{\ell h}$, but not to differences in the invariant lepton-pion mass. The relevant figures are

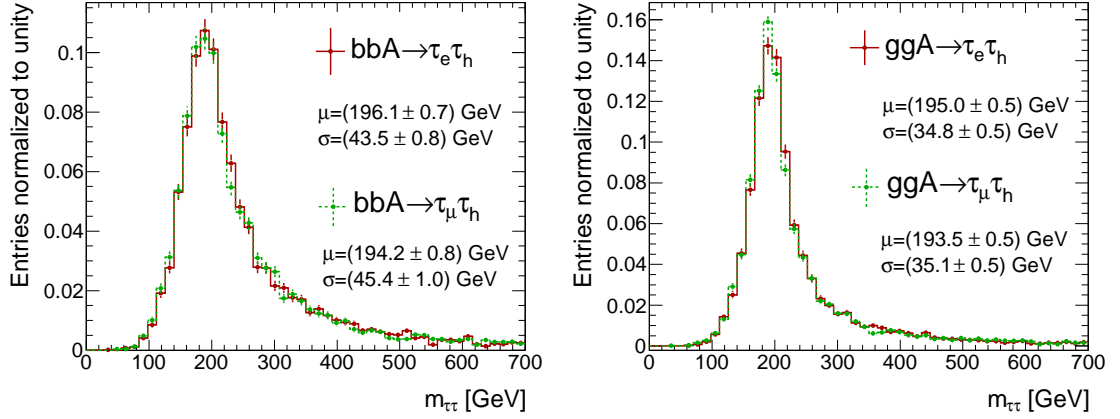


Figure 7.4.: Reconstructed collinear mass, separated for the $\tau_h \tau_e$ (dashed green line) and $\tau_h \tau_\mu$ (solid red line) channels. Left for b-associated and right for direct production. A Higgs boson mass of 200 GeV was chosen. The central parts of the peak were fitted with a Gaussian. Compared to the $\tau_h \tau_e$, the mass peak in the $\tau_h \tau_\mu$ channel is slightly shifted to lower values.

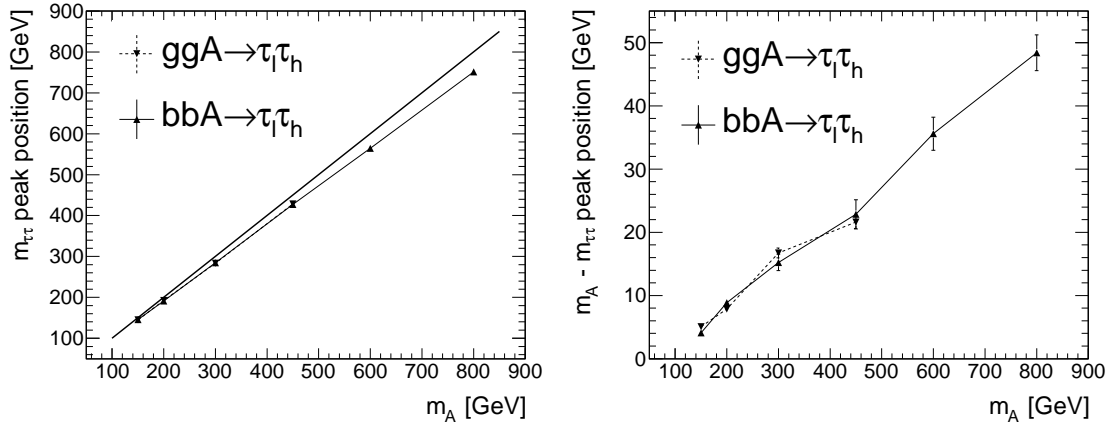


Figure 7.5.: Left: The peak position of the collinear mass in the lepton-hadron channel as a function of m_A . The line with $m_{\tau\tau} = m_A$ is also drawn. Right: The difference of the peak position to the input mass, also as function of m_A . The shift of the mass peak to lower values is similar for both production modes.

given in Figures 7.7-7.9 for Higgs boson masses of 200 GeV and 450 GeV. There is an expected difference between x_1 and x_2 according to the different denominators in Equation 7.3¹.

¹The pions/kaons from the τ decay carry on average more p_T than the electrons or muons. Considering Equation 7.3, there the hadronic system of the τ decay is labeled with index 2 (ie. $p_{x,2}^{\ell/h} \equiv p_x^h$) and the electron/muon is labeled with index 1 (ie. $p_{x,1}^{\ell/h} \equiv p_x^\ell$). Consequently, the values of x_1 are larger than x_2 on average.

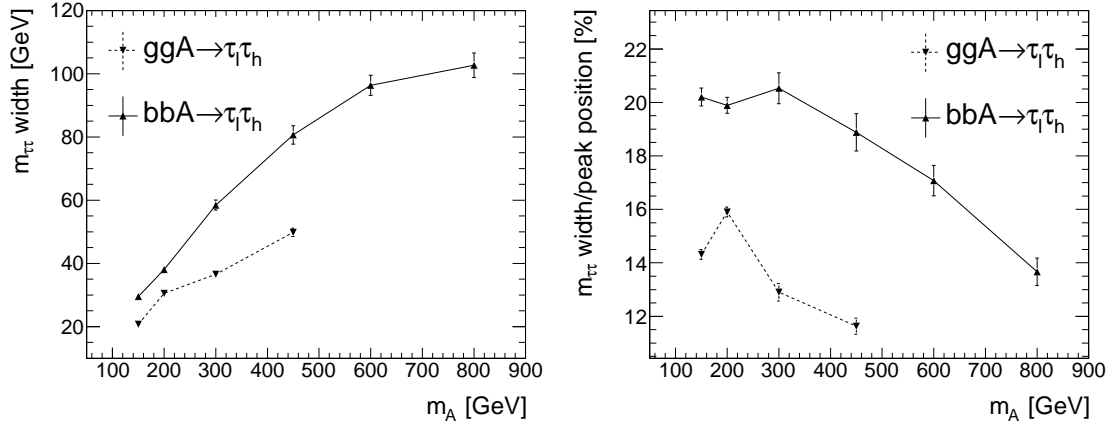


Figure 7.6.: Left: The width of the central part of the mass peak as a function of m_A for the lepton-hadron channel. Right: The width of the mass peak divided by the peak position. The relative mass resolution improves for larger A masses. The mass from the Higgs boson in direct production (dashed line) has a better resolution than if produced in association with b-quarks (solid line).

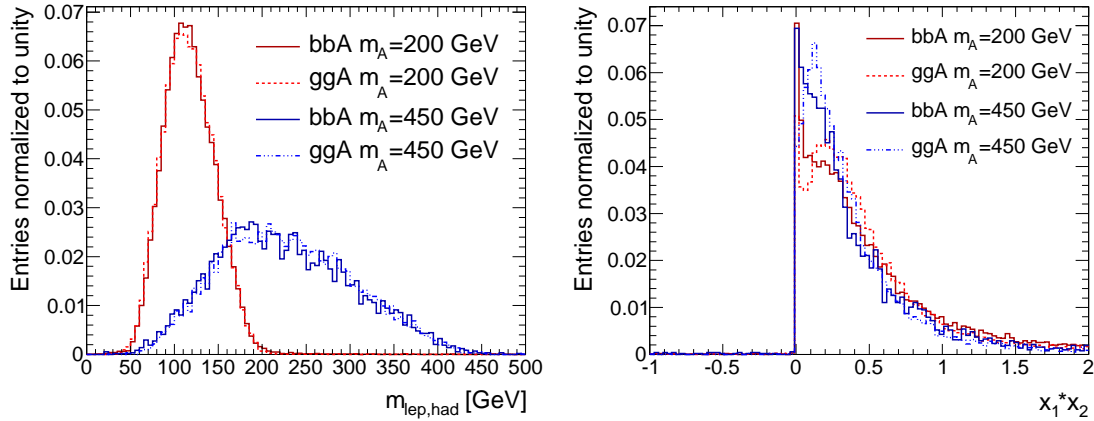


Figure 7.7.: Left: The invariant mass of the electron/muon and the hadronic τ for two Higgs boson mass hypotheses. The gluon fusion signal is marked by dashed lines, the b-associated signal by solid lines. There is no significant difference between the two production modes in this distribution. Right: The distribution of the product of the scaling fractions, $x_1 \cdot x_2$. Due to kinematics, the distributions are slightly different in the two production modes. For these two plots no cuts on x_1 and x_2 are applied.

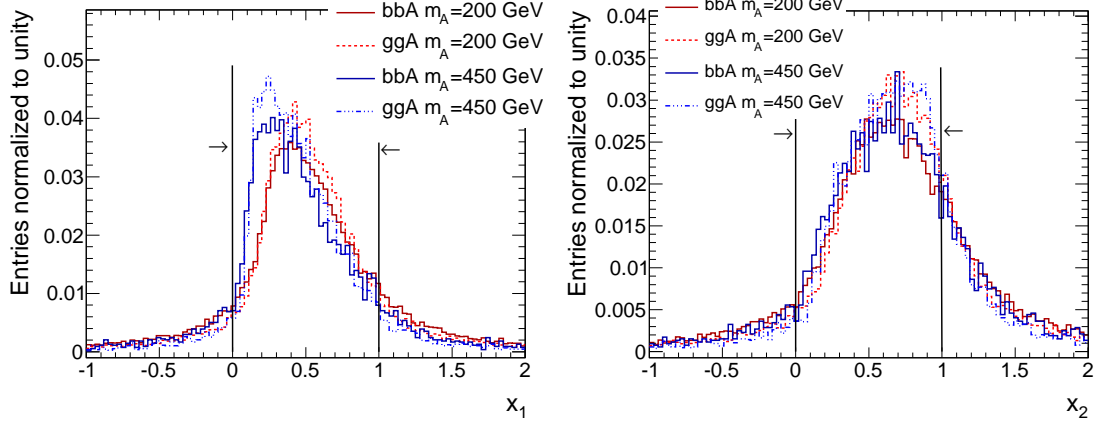


Figure 7.8.: The distributions of x_1 (left) and x_2 (right) for Higgs boson events produced via gluon fusion (blue lines) or in association with b-quarks (red lines), for a Higgs boson mass of 200 GeV (solid lines) and 450 GeV (dashed lines). The differences between x_1 and x_2 are due to the p_T difference between the electron/muon and the hadronic system in τ decays. The cuts applied are marked with black lines, the arrows indicate the events which are kept in the analysis.

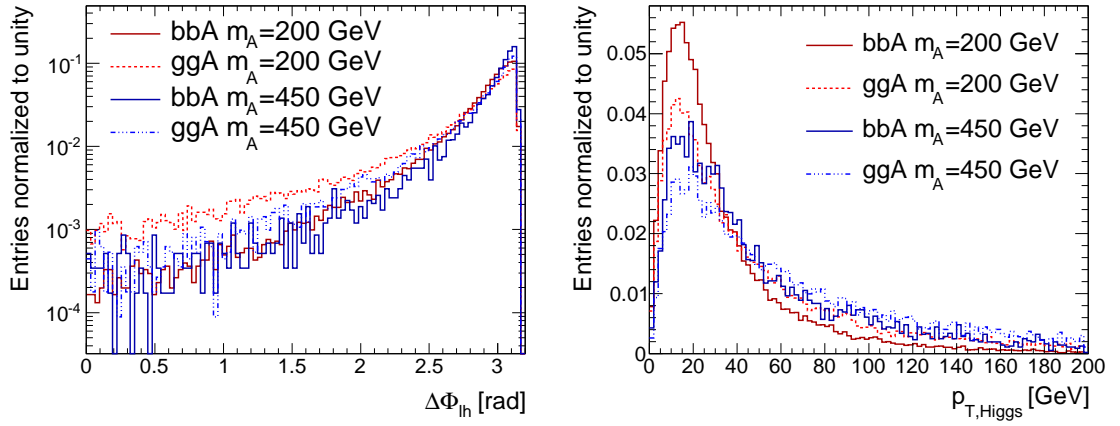


Figure 7.9.: Left: The $\Delta\Phi_{\ell h}$ angle between the electron/muon and the hadronic τ . A distinct peak at $\Delta\Phi_{\ell h} = \pi$ is visible. The events from the b-associated production (solid lines) have a steeper distribution than the events from the gluon fusion (dashed lines). Also, the distribution gets steeper for larger A masses. Right: The distribution of $p_{T,\text{Higgs}}$. The events produced in direct production have a larger $p_{T,\text{Higgs}}$ than the events from the b-associated production. This corresponds to the differences seen in the $\Delta\Phi_{\ell h}$ and $x_1 \cdot x_2$ distribution.

The correlations of the $m_{\tau\tau}$ peak position and resolution with several quantities for signal events produced either in association with b-quarks or in gluon fusion is presented in the following Figures 7.10 through 7.13 for a Higgs boson mass hypothesis of $m_A = 200$ GeV. The correlation of the peak position to various observables is small. However, the correlation of the $m_{\tau\tau}$ resolution with other variables is very apparent. Considering for example the dependence of the $m_{\tau\tau}$ resolution with $p_{T,\text{Higgs}}$, the b-associated signal events accumulate at lower values of $p_{T,\text{Higgs}}$. This behavior is visible in all the presented 2-dimensional plots.

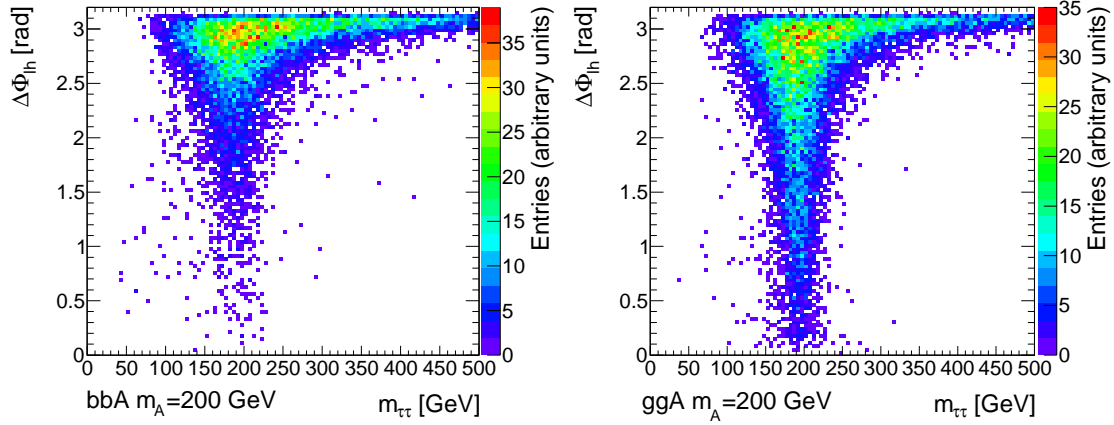


Figure 7.10.: The correlation of the collinear mass resolution with $\Delta\Phi_{\ell h}$, here for a Higgs boson mass of 200 GeV. The left plot displays the events produced in association with b-quarks, the right plot the events produced in gluon fusion. Both distributions show a clear deterioration of the collinear mass for values of $\Delta\Phi_{\ell h} \approx \pi$.

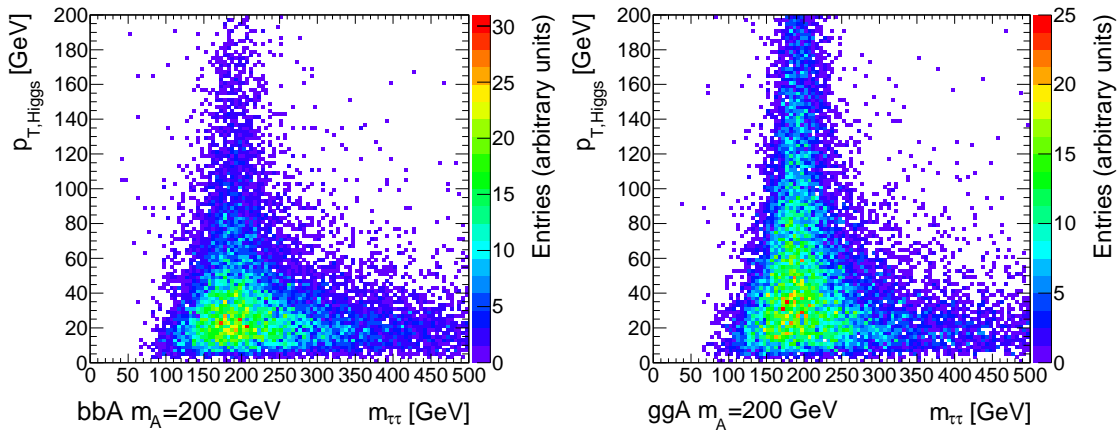


Figure 7.11.: The correlation of the $m_{\tau\tau}$ resolution with $p_{T,\text{Higgs}}$ for $m_A = 200$ GeV, left for b-associated and right for gluon fusion signal events. For larger values of $p_{T,\text{Higgs}}$, the mass resolution improves.

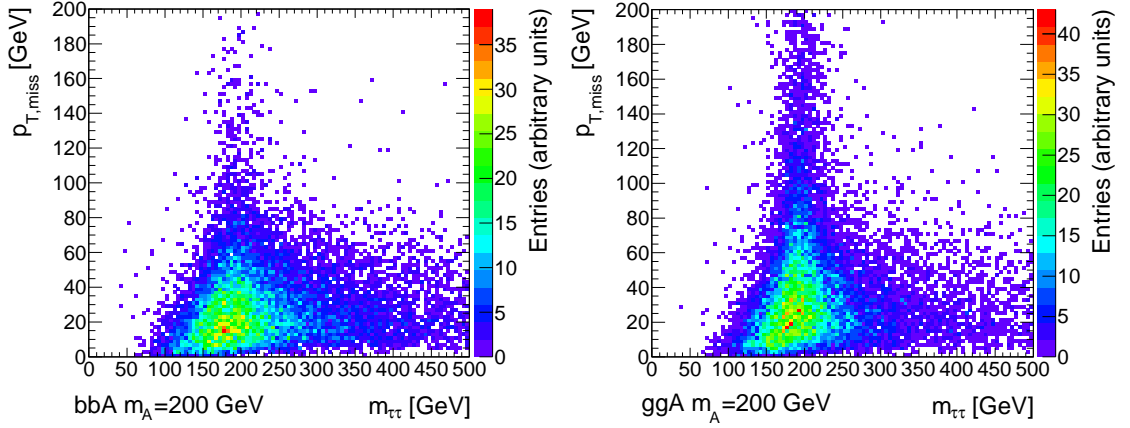


Figure 7.12.: The correlation of the collinear mass resolution with $p_{T,\text{miss}}$ for $m_A = 200$ GeV, left for b-associated and right for gluon fusion signal events. The correlation is not as pronounced as for $p_{T,\text{Higgs}}$ or $\Delta\Phi_{\ell h}$, however, an improvement of the mass resolution is observed for large values of $p_{T,\text{miss}}$.

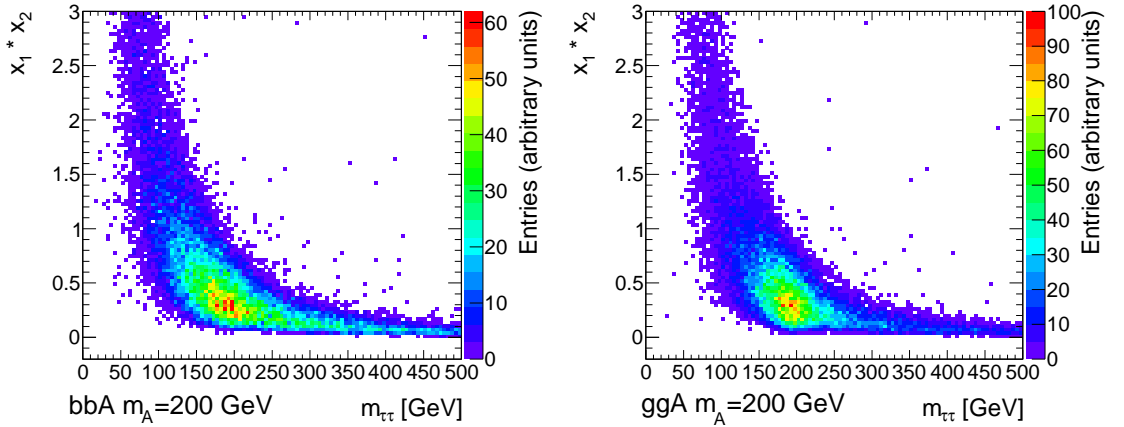


Figure 7.13.: The correlation of the collinear mass with $x_1 \cdot x_2$ for $m_A = 200$ GeV, left for b-associated and right for gluon fusion signal events. The stronger peak of the b-associated signal events at $x_1 \cdot x_2 \approx 0$ (compare to Fig. 7.7) results in a worse mass resolution for these events than for the gluon fusion events.

To obtain physically meaningful values for the collinear approximation, the scaling factors x_1 and x_2 are required to have values between 0 and 1. This cut decreases the mass reconstruction efficiency, but also significantly reduces background contributions, as will be discussed later. The efficiency of the collinear approximation in the lepton-hadron channel is presented in Figure 7.14. To improve the mass resolution, usually also cuts on $\Delta\Phi_{\ell h}$ are applied. This, however, decreases the signal efficiency strongly especially for large A boson masses. The efficiency is much larger for gluon fusion signal events than for b-associated signal events, due to the reasons mentioned above. The impact of different $\Delta\Phi_{\ell h}$ cuts on the discovery significance will be addressed later.

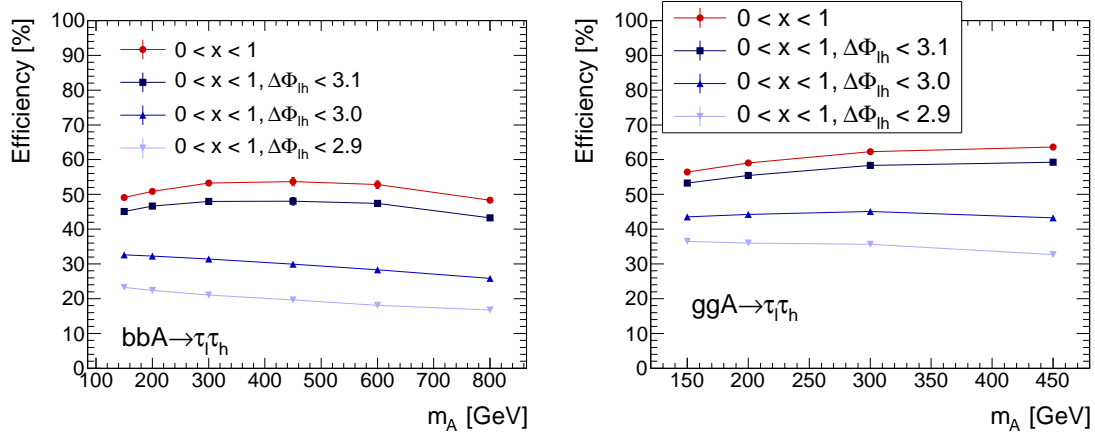


Figure 7.14.: The relative efficiency of the collinear approximation as a function of m_A for signal produced with b-quarks (left) and in gluon fusion (right). An efficiency of 100% corresponds to the reference point in the cutflow where neither a cut on $\Delta\Phi_{\ell h}$ nor on x_1 or x_2 is applied. Due to differences in the $\Delta\Phi_{\ell h}$ distribution (compare to Fig. 7.9), the efficiency for the gluon fusion is considerably larger than for the b-associated signal events.

7.2.2. The $h/A/H \rightarrow \tau_\ell \tau_\ell$ Channel

For evaluating the performance of the collinear mass in the dilepton channel, the object selection criteria as listed in Chapter 6 were applied to the Rel. 12 FULLSIM samples. Only b-associated signal events were considered. No MET cut and no jet requirements were applied in this study. The leptons (electrons/muon) used for the mass reconstruction were selected by choosing the pair with opposite sign with the highest p_T sum. No trigger cuts were imposed for this particular study. The reconstructed invariant $\tau\tau$ -mass for all considered mass points are displayed in Figure 7.15 (left). As was observed in the lepton-hadron channel, the width increases with rising m_A and the peak is shifted to lower values. In Figure 7.15 (right) the collinear mass is plotted separately for the $\tau_e \tau_e$, $\tau_\mu \tau_\mu$ and $\tau_e \tau_\mu$ channels. Within the uncertainties, the performance of the collinear mass is similar in all three channels.

The central part of the mass peak was fitted by a Gaussian. The mass peak positions and their difference to the input mass as function of m_A are shown in Figure 7.16. The $m_{\tau\tau}$ distribution peaks always below the input mass m_A . In fact, the left-shift was already observed in former studies of the dileptonic channel in Rel. 11 with ATLFAS-I [108]. The width of the Gaussian and the relative mass resolution are presented in Figure 7.17.

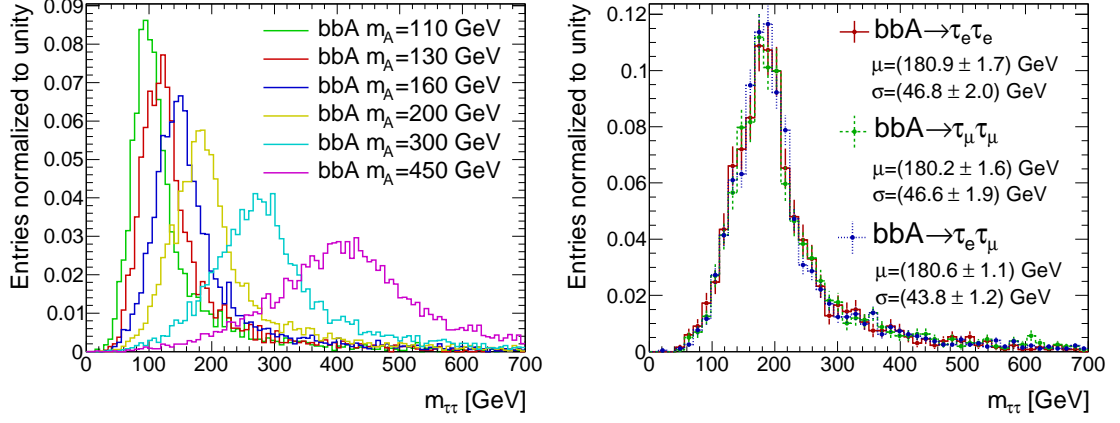


Figure 7.15.: Left: Reconstructed invariant $\tau\tau$ -mass for various Higgs boson mass hypotheses. The distributions are normalized to unity. The widths increase with rising m_A . Right: Reconstructed collinear mass broken down to the dileptonic subchannels: $\tau_e \tau_e$ (solid red line), $\tau_\mu \tau_\mu$ (dashed green line) and $\tau_e \tau_\mu$ (dotted blue line) for an input Higgs boson mass of 200 GeV. The mass distributions are very similar for all three channels. The fitted values of mean and width of a Gaussian are noted in the plot.

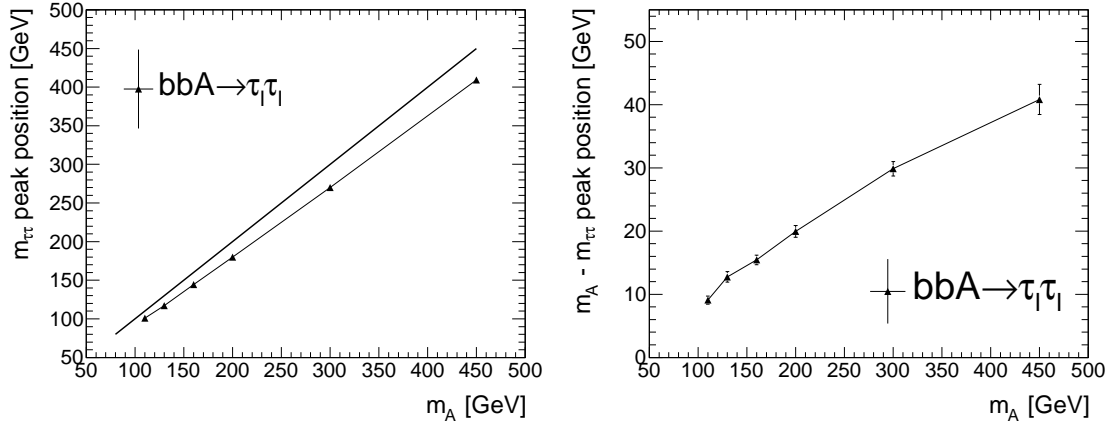


Figure 7.16.: Left: Peak position of the fitted collinear mass as a function of m_A . The error bars are too small to be seen. The line with $m_{\tau\tau} = m_A$ is also drawn. Right: The difference of the peak position to the input A mass. As was observed in the lepton-hadron channel (Fig. 7.5), the left-shift increases with a rising A mass. Compared to the lepton-hadron channel, the left-shift is roughly a factor two larger in the dilepton channel.

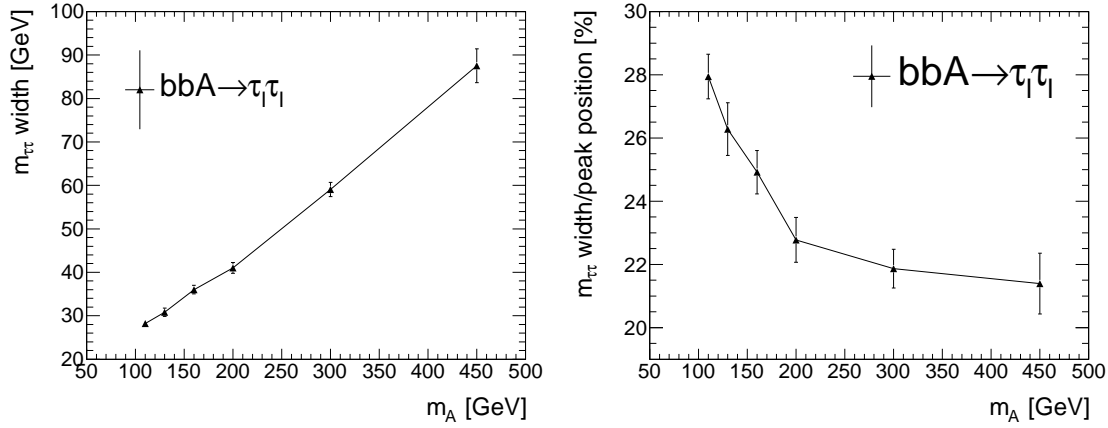


Figure 7.17.: Left: The width of the central part of the reconstructed $m_{\tau\tau}$ as a function of m_A . Right: Relative mass resolution as a function of m_A . Compared to the lepton-hadron channel (Fig. 7.6), the width, σ , is similar in the dilepton channel. Due to the larger left-shift, however, the relative mass resolution (σ/m_A) is worse in the dileptonic case.

The invariant dilepton mass, the distribution of $x_1 \cdot x_2$, the $\Delta\Phi_{\ell\ell}$ and the $p_{T,\text{Higgs}}$ are displayed in Figures 7.18 and 7.19 for two Higgs boson masses. The larger the Higgs boson mass, the more back-to-back the leptons are emitted. The p_T of the Higgs boson is small and hardly increases with rising m_A . The distributions of x_1 and x_2 are displayed in Figure 7.20. Differences between x_1 and x_2 arise from the fact that the leptons are ordered in p_T . Analog to the lepton-hadron channel, the denominators in Equation 7.3 lead to differences between x_1 and x_2 , if there are differences in p_T between the leptons. In this case, the lepton labeled with index 1 carries a larger p_T , which on average leads to larger values of x_2 (compare also to Fig. 7.8, where the case is reversed). If the

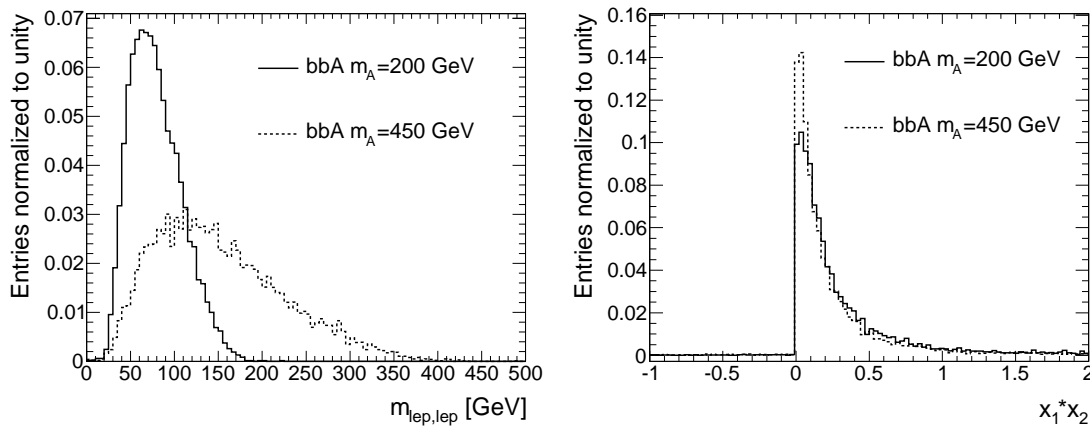


Figure 7.18.: Left: The invariant dilepton mass for $m_A = 200$ GeV (solid line) and $m_A = 450$ GeV (dashed line). Right: The distribution of $x_1 \cdot x_2$ for the same Higgs boson mass hypotheses. No cut on $0 < x_i < 1$ ($i = 1, 2$) was applied for these two plots.

leptons were chosen completely random, the differences between x_1 and x_2 would vanish.

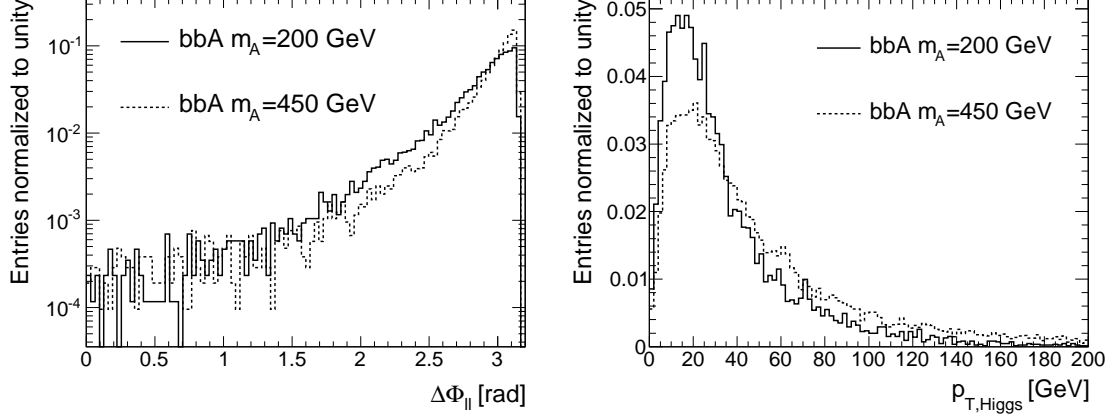


Figure 7.19.: The distribution of the $\Delta\Phi_{\ell\ell}$ of the two leptons (left) and the $p_{T,Higgs}$ (right) for $m_A = 200$ GeV (solid line) and $m_A = 450$ GeV (dashed line). A larger Higgs boson mass leads to a steeper rise in the $\Delta\Phi_{\ell\ell}$ distribution and a slightly larger $p_{T,Higgs}$.

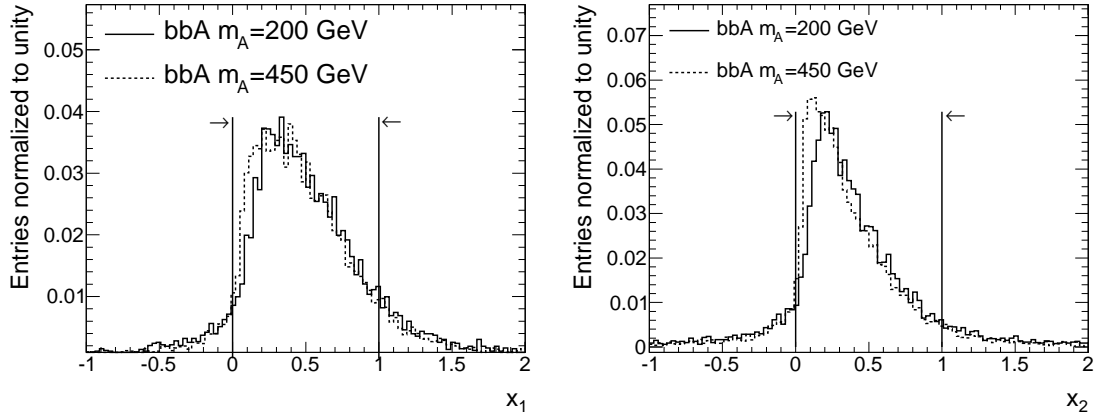


Figure 7.20.: The distribution of x_1 (left) and x_2 (right) for $m_A = 200$ GeV (solid line) and $m_A = 450$ GeV (dashed line). The differences between x_1 and x_2 are due to the p_T -sorting of the electrons and muons. The cuts applied are marked with black lines, the arrows indicate the events which are kept in the analysis.

The correlations of the $m_{\tau\tau}$ resolutions to $\Delta\Phi_{\ell\ell}$, $p_{T,Higgs}$, $p_{T,miss}$ and $x_1 \cdot x_2$ are displayed in Figures 7.21 and 7.22, showing the same behavior as found in the lepton-hadron channel.

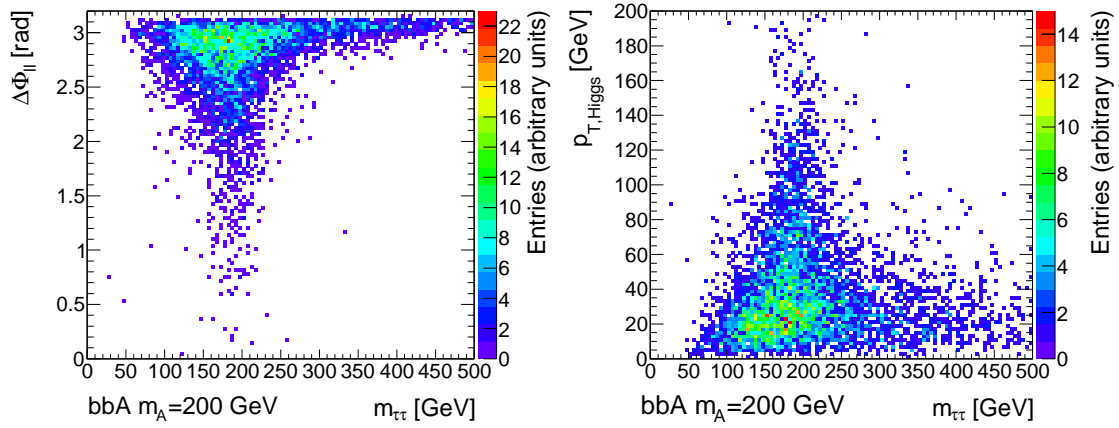


Figure 7.21.: The correlation of the collinear mass resolution with $\Delta\Phi_{\ell\ell}$ (left) and $p_{T,\text{Higgs}}$ (right) for $m_A = 200$ GeV. As was observed in the lepton-hadron channel, the deterioration of the mass resolution for $\Delta\Phi_{\ell\ell} \approx \pi$ and small values of $p_{T,\text{Higgs}}$ is clearly visible.

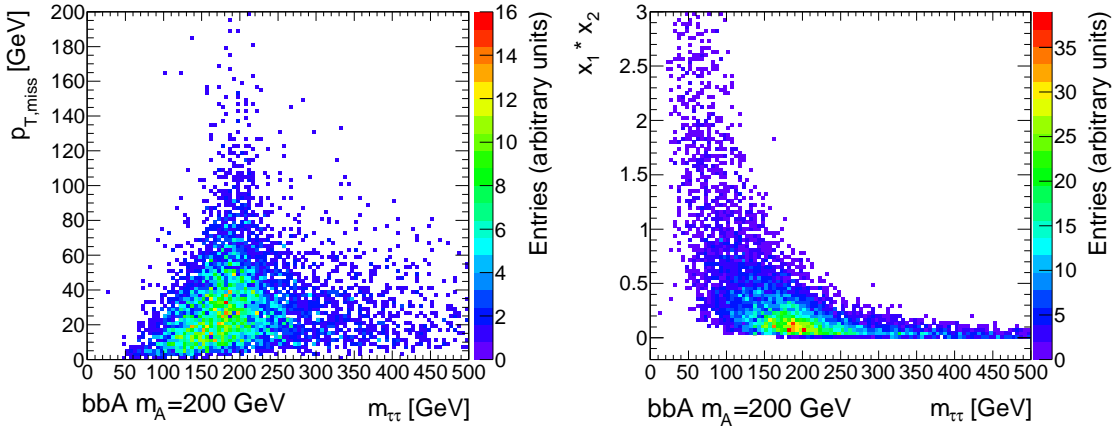


Figure 7.22.: The correlation of the collinear mass resolution with $p_{T,\text{miss}}$ (left) and $x_1 \cdot x_2$ (right) for $m_A = 200$ GeV. The mass resolution clearly worsens for low values of $p_{T,\text{miss}}$ and $x_1 \cdot x_2 \approx 0$.

The efficiency of the collinear mass is shown in Figure 7.23. The efficiency of the cuts on x and $\Delta\Phi_{\ell\ell}$ is slightly higher than in the $\tau_\ell \tau_h$ channel. The dependence of the $\Delta\Phi_{\ell\ell}$ cut efficiency on the Higgs boson mass is visible.

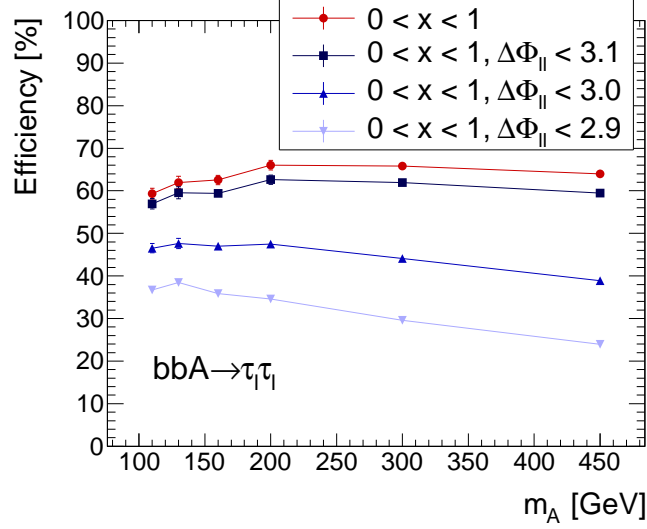


Figure 7.23.: The efficiency of the collinear approximation as a function of m_A in the dileptonic channel. The cut efficiency of $\Delta\Phi_{\ell\ell}$ depends on m_A , while it is almost flat for the cut on x_1 and x_2 . The efficiency greatly drops for cuts below 3.0 when imposing a cut on $\Delta\Phi_{\ell\ell}$ (compare to Fig. 7.19).

7.3. Performance of the Visible Mass

The visible mass was used in searches for the MSSM Higgs bosons for example at CDF [111]. In this thesis the same definition as in CDF is taken to calculate the visible mass. It is constructed as the invariant mass of a pseudo MET four-vector and the four-vectors of the visible $\tau\tau$ -decay products (either electrons/muons or pions/kaons). The pseudo MET vector, p_{miss} , is defined as follows:

$$p_{\text{miss}} = (p_{T,\text{miss}}, p_{x,\text{miss}}, p_{y,\text{miss}}, 0). \quad (7.10)$$

The visible mass, m_{visible} , is then given by:

$$m_{\text{visible}}^2 = \left(E_1^{\ell/h} + E_2^{\ell/h} + p_{T,\text{miss}} \right)^2 - \left(p_{x,1}^{\ell/h} + p_{x,2}^{\ell/h} + p_{x,\text{miss}} \right)^2 - \left(p_{y,1}^{\ell/h} + p_{y,2}^{\ell/h} + p_{y,\text{miss}} \right)^2 - \left(p_{z,1}^{\ell/h} + p_{z,2}^{\ell/h} \right)^2. \quad (7.11)$$

When reconstructing the visible mass, no cuts need to be applied. Its reconstruction efficiency is therefore 100%. However, it will not peak at the Higgs boson mass since information is missing. In the following, the same cuts are applied as were used for the performance studies of the collinear mass.

7.3.1. The $h/A/H \rightarrow \tau_\ell \tau_h$ Channel

The visible mass was reconstructed for both the b-associated and gluon fusion signal events, for all available Higgs boson mass points. The mass distributions are displayed in Figure 7.24. The

mass resolution strongly decreases with rising m_A . The visible mass peaks well below the input Higgs boson mass.

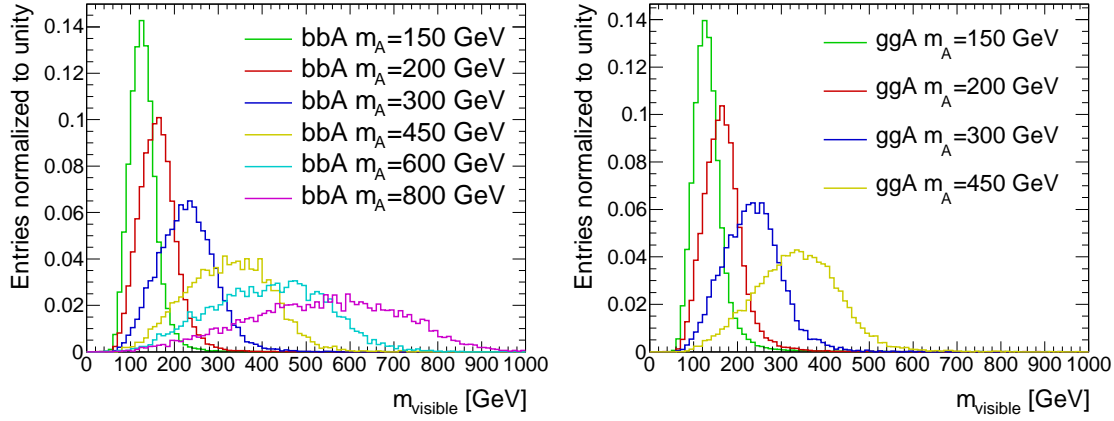


Figure 7.24.: The visible mass in the lepton-hadron channel for b-associated (left) and direct production (right). The width greatly increases with rising m_A . The mass peaks below the Higgs boson mass.

As for the collinear mass, the central part of the mass peaks was fitted with a simple Gaussian to extract the width and the peak position. The peak position and its difference to the input Higgs boson mass are displayed in Figure 7.25. The left shift of the visible mass peak is the same for gluon fusion and b-associated signal events. The width and the relative mass resolution are shown in Figure 7.26. Unlike the collinear mass, where the relative mass resolution improves with an increasing m_A , the resolution of m_{visible} deteriorates for larger values of m_A .

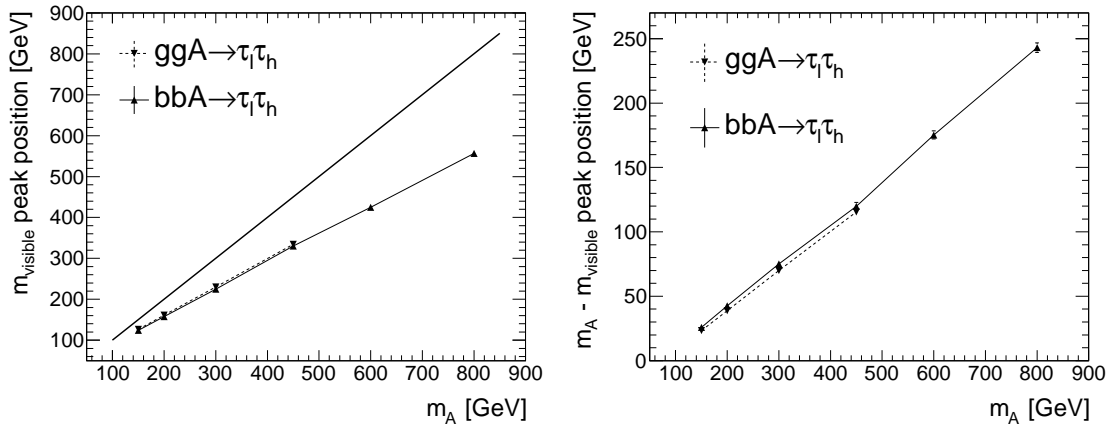


Figure 7.25.: Left: The peak position of the visible mass as a function of m_A . The line with $m_{\text{visible}} = m_A$ is also drawn. Right: The difference of the m_{visible} peak and the input A mass. The ggA events (dashed line) and bbA events (solid line) show the same behavior.

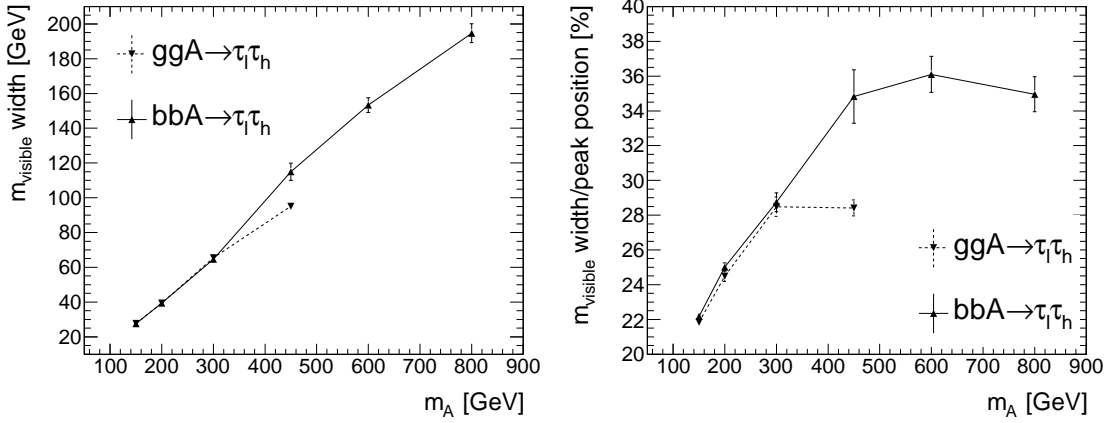


Figure 7.26.: Left: The width of the visible mass as function of m_A for b-associated production (solid line) and gluon fusion (dashed line). Right: The relative mass resolution over m_A . Compared to the collinear mass, the relative mass resolution worsens for increasing m_A .

7.3.2. The $h/A/H \rightarrow \tau_\ell \tau_\ell$ Channel

The performance of the visible mass was also evaluated using the FULLSIM samples for the dilepton analysis, where the Higgs boson was produced in association with b-quarks. The same selection as for the study of the collinear mass performance was applied. The reconstructed m_{visible} for all mass hypotheses are shown in Figure 7.27. A deterioration of the mass resolution with rising m_A and the left-shift of the peak is observed.

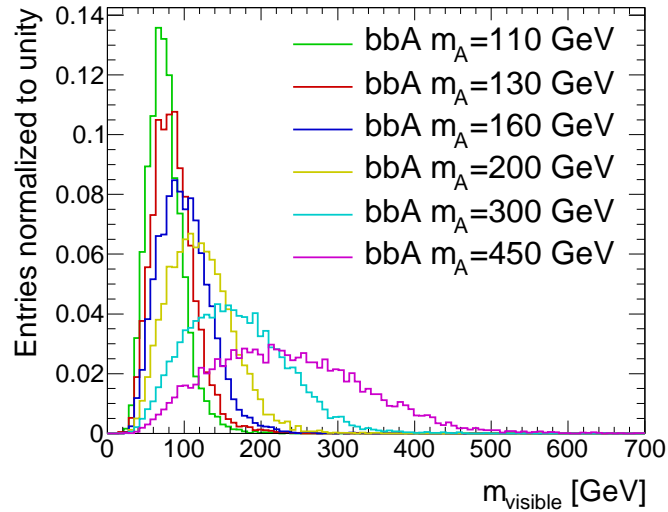


Figure 7.27.: The reconstructed visible mass in the dileptonic channel for various Higgs boson mass hypotheses. All distributions are normalized to unity. The width deteriorates greatly with increasing m_A . This behavior is more pronounced in the dilepton than in the lepton-hadron channel.

The mass peak was fitted with a Gaussian. The peak position is significantly shifted to lower mass values. The fitted mean and the difference to the input Higgs boson mass are displayed in Figure 7.28. The width and the relative mass resolution are shown in Figure 7.29. Similar to the lepton-hadron channel, the performance of m_{visible} deteriorates with increasing m_A .

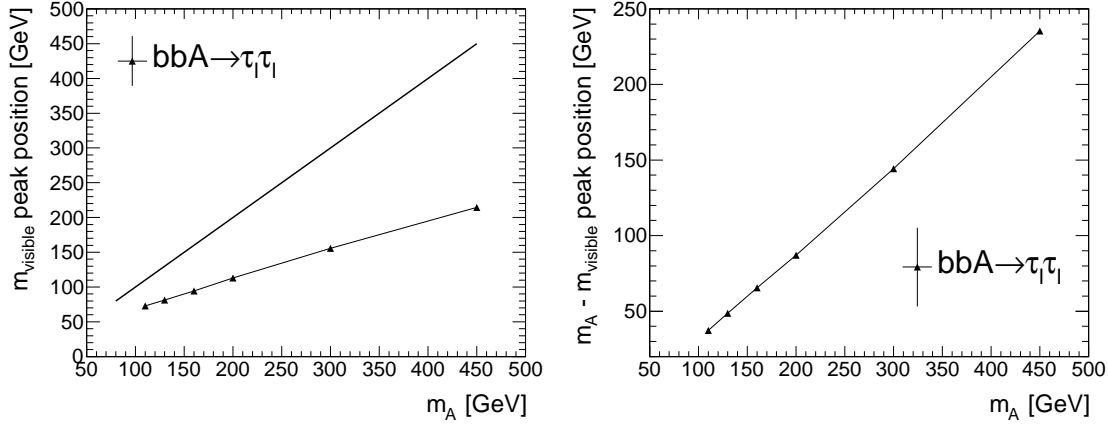


Figure 7.28.: The peak position of m_{visible} (left) and its difference to the input mass (right) as function of m_A . The left-shift of the peak position is a factor two larger than observed in the lepton-hadron channel (compare to Fig. 7.25).

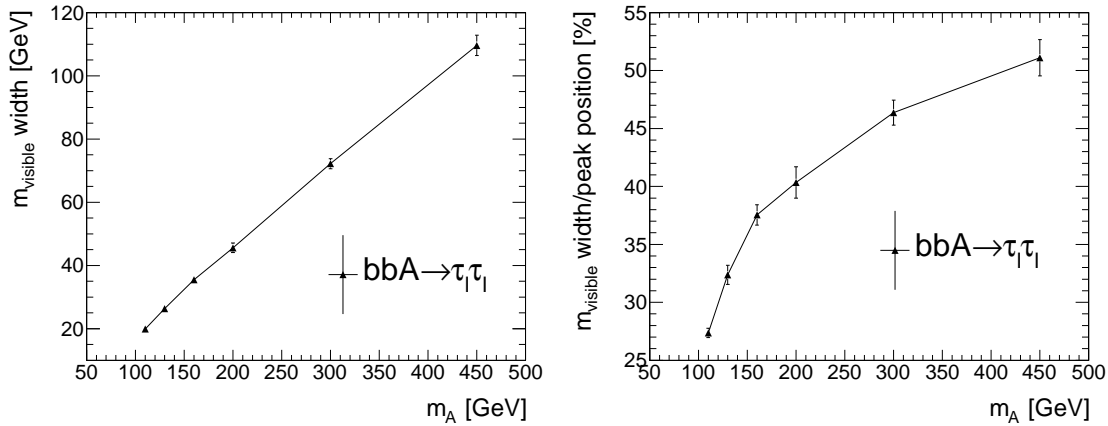


Figure 7.29.: The width of m_{visible} (left) and the relative mass resolution (right) as a function of the input A mass. While the widths of m_{visible} in the dileptonic and semi-leptonic channels are similar, the relative mass resolution in the dilepton mode is worse because of the larger left-shift of the peak position.

7.4. MET Performance

The accurate measurement of MET in ATLAS is a crucial input to the mass reconstruction. The MET resolution is quantified as the width of the distribution of the difference between truth MET

and the reconstructed MET. The truth MET is the negative sum of the E_T of all non-interacting particles. The MET resolution is then typically given as a function of ΣE_T , which is the scalar sum of the E_T of all objects within one event. Asymmetric tails and shifts of the difference of truth and reconstructed MET indicate the presence of fake MET.

For the following plots, the same object and event selection was applied as was used for the study of the performance of the collinear mass. Figure 7.30 shows the ΣE_T and the integrated MET resolution in the lepton-hadron channel using the Rel. 14 samples. A Higgs boson mass of $m_A = 300$ GeV was used for this plot, both in b-associated and gluon fusion production. The gluon fusion events yield slightly more ΣE_T than the events produced with b-quarks. A small shift of the MET resolution of 1.6 ± 0.1 GeV is visible for the gluon fusion process, which, however, has no impact on the mass resolution. The MET resolution is the relevant quantity for the mass reconstruction performance.

Figure 7.31 displays the ΣE_T and the MET resolution in the lepton-lepton channel using the fully simulated samples. The ΣE_T is smaller than in the lepton-hadron channel. This is a result from the fact that the neutrinos carry away a large fraction of the E_T .

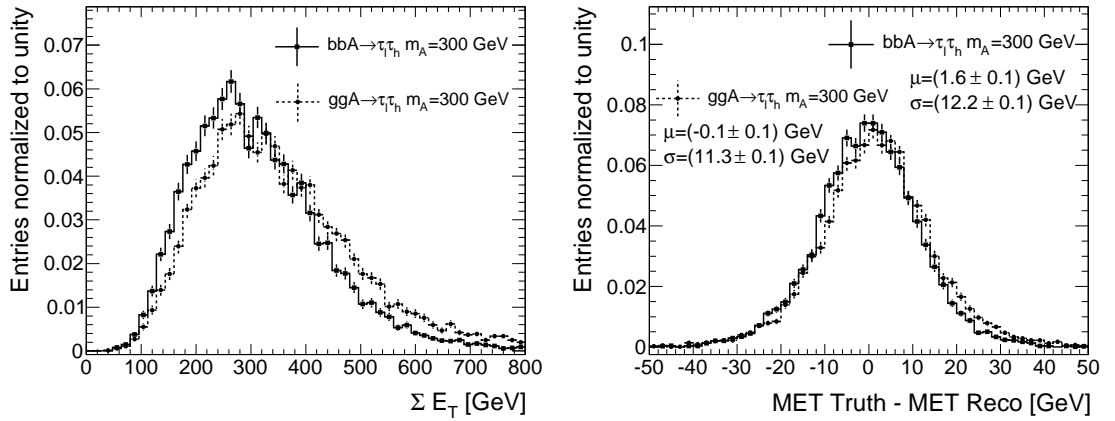


Figure 7.30.: Left: The distribution of ΣE_T for $m_A = 300$ GeV in the **lepton-hadron channel**. The events from b-associated production (solid line) have less ΣE_T than the events from gluon fusion (dashed line). Right: The difference of truth and reconstructed MET. This distribution is fitted with a simple Gaussian for the two different production modes. A slight shift between the two distributions is observed. The MET resolution, however, is comparable.

The MET resolution binned in ΣE_T is presented in Figure 7.32. The graphs were fitted by a function of the form $\sigma_{\text{MET}} = a + b * \sqrt{\Sigma E_T}$, which describes the MET resolution fairly well. The fitted parameters are found to be:

Mode	Decay	a [GeV]	Δa [GeV]	b [$\sqrt{\text{GeV}}$]	Δb [$\sqrt{\text{GeV}}$]
bbA	$\tau_h \tau_\ell$	2.37	1.03	0.49	0.06
ggA	$\tau_h \tau_\ell$	3.01	0.96	0.46	0.05
bbA	$\tau_\ell \tau_\ell$	3.59	0.67	0.33	0.04

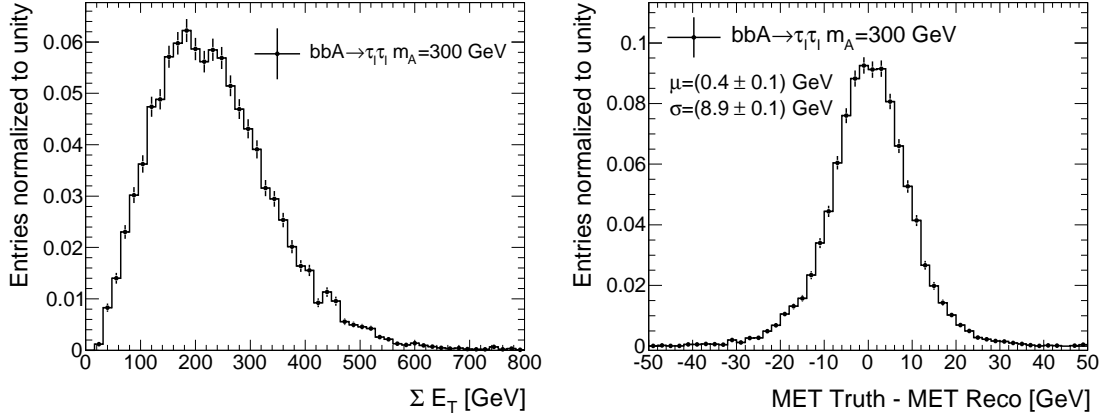


Figure 7.31.: Left: The ΣE_T in the **lepton-lepton channel** for $m_A = 300$ GeV. Right: The difference of truth and reconstructed MET, for all events passing the selection. The MET resolution is the width of the Gaussian, σ .

As expected, the MET resolution is similar for the two different signal production processes in the lepton-hadron analysis. The MET resolution in the lepton-lepton analysis is better by a few GeV, especially for larger values of ΣE_T , if compared to the performance in Rel. 14. A more detailed comparison of the collinear approximation when using the full simulation or ATLFAST-II is presented in Appendix A.

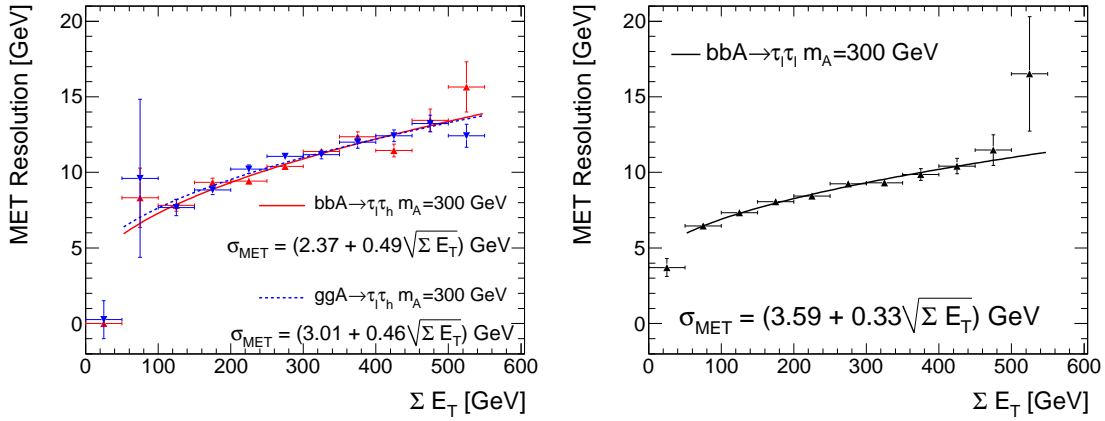


Figure 7.32.: The MET resolution binned in ΣE_T , left for the lepton-hadron channel and right for the dilepton channel. The resolution graphs follow a function proportional to $\sqrt{\Sigma E_T}$.

In the following the impact of the MET resolution on the collinear mass was studied. This was achieved by substituting the reconstructed MET by the true MET in the mass reconstruction algorithm. The central part of the $m_{\tau\tau}$ distribution then approximately follows the form of a Breit-Wigner function, and not a Gaussian, like when using the reconstructed MET. The Breit-Wigner

function, $p(E)$, for a particle having a width Γ and a mass M , is defined as follows:

$$p(E) = \frac{1}{2\pi} \cdot \frac{\Gamma^2}{(E - M)^2 + \Gamma^2/4}. \quad (7.12)$$

The results for the lepton-hadron channel and the dilepton channel are displayed in Figure 7.33. In all cases a clear improvement of the mass resolution is visible when using the true MET. Also, the left-shift of the peak position is much smaller. It should be noted, however, that a slight left-shift is still present which must be understood as an inherent feature of the collinear approximation.

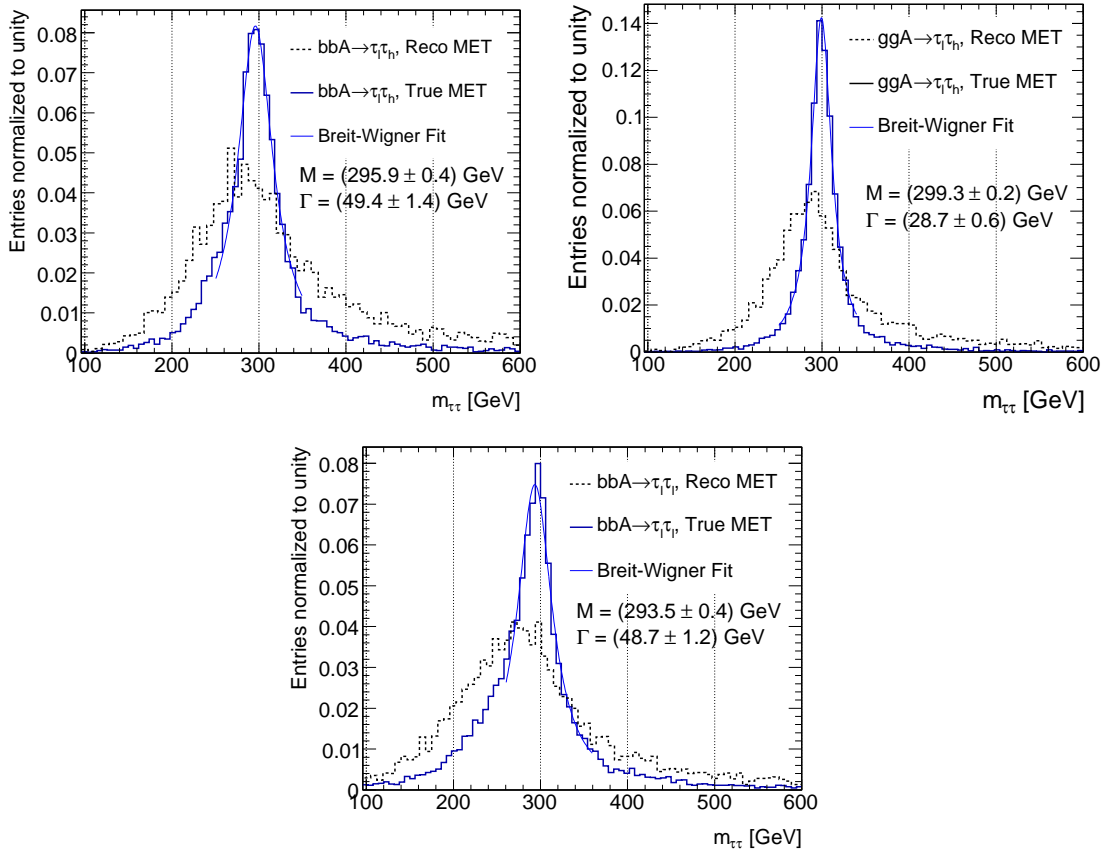


Figure 7.33.: The reconstructed collinear mass in the lepton-hadron channel (upper plots) and the lepton-lepton channel (lower plot), with the reconstructed MET (dashed lines) and the true MET (solid lines), all for $m_A = 300$ GeV. The mass distributions with the true MET have been fitted with a Breit-Wigner function. The left plot shows the results for the b-associated production, the right plot for gluon fusion. The mass performance largely depends on the MET resolution.

7.5. Summary

In this chapter the reconstruction of the Higgs particle was discussed using either the collinear approximation or the visible mass. An exact mass reconstruction is not possible due to the presence of neutrinos in the final state. The definition of the collinear mass exploits the collinearity of the τ -leptons and its decay products to calculate the scale factors x_1 and x_2 , which are used to correct the invariant mass of the visible τ decay products to reproduce the $m_{\tau\tau}$ distribution. The visible mass is calculated from the four vectors of the visible τ decay products and a pseudo four-vector constructed from the measured MET, but the loss of information is not completely recovered.

The collinear mass involves kinematic cuts in order to result in physically meaningful mass values, which significantly decreases the reconstruction efficiency. These cuts are powerful in order to reduce backgrounds as will be discussed further on. The visible mass does not involve further cuts, but is strongly shifted to lower mass values. The collinear mass is less shifted to lower $m_{\tau\tau}$ values. In both cases the difference to the input mass is a function of m_A and therefore of the kinematics. In both mass calculations the mass resolution deteriorates for larger values of m_A . The relative mass resolution of the collinear mass, however, is better compared to the visible mass.

Higgs boson events produced in gluon fusion result in a smaller reconstructed width of the $m_{\tau\tau}$ peak than the events produced in association with b-quarks. This can be explained by differences between the p_T spectra of the reconstructed Higgs bosons between both production types. Events produced in gluon fusion yield on average in a larger value of $p_{T,\text{Higgs}}$ than the b-associated signal events. Other strong correlations have been found between the $m_{\tau\tau}$ resolution and quantities such as $\Delta\Phi_{\ell\ell/\ell,h}$, $p_{T,\text{miss}}$ and $x_1 \cdot x_2$.

The mass resolution is completely dominated by the MET resolution, while the natural width is negligible. The precise measurement of the MET in real data is a crucial input to this search channel and will directly influence the significance of a potential discovery.

Analysis of the Fully Leptonic Channel

This analysis of the dileptonic final state is strongly based on the analysis by the author of this thesis published in [112], as a part of [19], where the discovery potential of this channel was evaluated in detail for the first time. Several improvements of the published analysis have been implemented in this thesis which will be discussed in the relevant sections. The analysis presented is completely based on FULLSIM samples. The technical details of those samples were listed in Chapter 5. The object identification algorithms and cuts were already discussed in Chapter 6. Higgs boson masses between 110 GeV and 450 GeV have been considered. The analysis aims at an integrated luminosity of 30 fb^{-1} at a center-of-mass energy of 14 TeV.

This chapter is organized as follows: At first the event selection is discussed. The selection is divided into a baseline selection independent of the Higgs boson mass, and a mass-dependent selection. Afterwards, the systematic uncertainties are computed. A method for the data-driven estimation of the $Z \rightarrow \tau\tau$ background is especially emphasized. Finally, the discovery potential is presented and discussed.

8.1. Event Selection

8.1.1. Baseline Selection

Based on the signal signature, a baseline selection independent of the Higgs mass was applied to all samples. This already removes the majority of the background events and simplifies the following mass-dependent optimization.

Trigger

As in former studies [108], four different trigger items were chosen. Those items are not prescaled¹ and correspond to the trigger menu for an instantaneous luminosity of $10^{33} \text{ cm}^{-2} \text{ s}^{-1}$ which is typical expected in the first years of data-taking at $\sqrt{s} = 14 \text{ TeV}$.

- mu20 (Chain: L1_MU20, L2_mu20, EF_mu20)
The event is triggered if at least one muon with a p_T of at least 20 GeV is found.
- e25i (Chain: L1_EM25i, L2_e25i, EF_e25i)
The event is triggered if at least one electron with a p_T of at least 25 GeV is found.
- 2e15i (Chain: L1_2EM15i, L2_e15iL2_e15i, EF_e15iEF_e15i)
The event is triggered if at least two electrons with a p_T of at least 15 GeV are found.

¹Trigger prescaling is used to reduce the event recording rate, by selecting on average only every 10th, 100th or xth event which was triggered by the particular item.

- mu10+e15i (Chain: L1_MU10+L1_EM15, L2_mu10+L2_e15i, EF_mu10+EF_e15i)
The event is triggered if at least one muon with a p_T of at least 10 GeV and one isolated electron with a $p_T > 15$ GeV are found.

The event is kept in the analysis, if at least one of the four trigger item requirements were satisfied (the trigger *fired*). Due to the unavailability of some trigger items in some of the FullSim samples used, for consistency all four triggers have been implemented offline by imposing p_T cuts on the electrons and muons. Hence, for example, the mu20 trigger fired, when among all reconstructed muons at least one has $p_T > 20$ GeV. This corresponds to a 100% trigger efficiency with respect to reconstructed leptons which slightly over-estimates the selection efficiency.

Table 8.1 lists the relative trigger efficiency for each item and the overall trigger efficiency. The QCD background is efficiently reduced by the leptonic triggers. The overall trigger efficiency for the signal increases with rising m_A , because then the average p_T of the leptons becomes larger and the trigger thresholds are passed more often.

Process	mu20	e25i	2e15i	mu10+e15i	Any trigger
h/A/H (110 GeV)	36.9	22.5	6.1	17.2	59.6
h/A/H (130 GeV)	41.2	29.7	7.5	21.8	68.1
h/A/H (160 GeV)	47.2	35	9	24.7	74.9
h/A/H (200 GeV)	52	41.5	11.1	27.6	81.1
h/A/H (300 GeV)	58.7	51.2	14.2	32.6	89.1
h/A/H (450 GeV)	63.4	56.9	16.3	36.1	92.9
$t\bar{t}$	35.2	29.4	3.9	10.1	60.3
$Z \rightarrow \tau\tau$	28.9	15.9	4.2	13.7	47.4
$Z \rightarrow ee$	0.1	70.8	40.1	0.3	72.1
$Z \rightarrow \mu\mu$	86.2	0.5	0	1	86.3
$W \rightarrow \tau\nu$	13.9	5.9	0.1	0.3	19.9
$W \rightarrow e\nu$	0	56	0.3	0.1	56.1
$W \rightarrow \mu\nu$	77.3	0.2	0	0.5	77.5
QCD	12.2	14.1	0.5	1.4	25.6

Table 8.1.: Percentage of events triggered by the different items. The column *Any trigger* denotes the percentage of the events triggered by any of the four items (*or* condition).

Lepton Isolation

A relative isolation cut was applied on all leptons in order to reduce QCD dijet events, where leptons can be found within the jet cones. Figure 8.1 displays the E_T in a $\Delta R = 0.2$ cone divided by the p_T of the leptons. The plot contains all electrons/muons passing the object ID and overlap removal (Chapter 6). The isolation cuts chosen are the following:

- Electrons: $E_T/p_T < 0.08$,
- Muons: $E_T/p_T < 0.07$.

The cut on the relative isolation is very powerful against QCD dijet events because in this process leptons stem from semi-leptonic hadron decays mostly. The impact of different A masses has

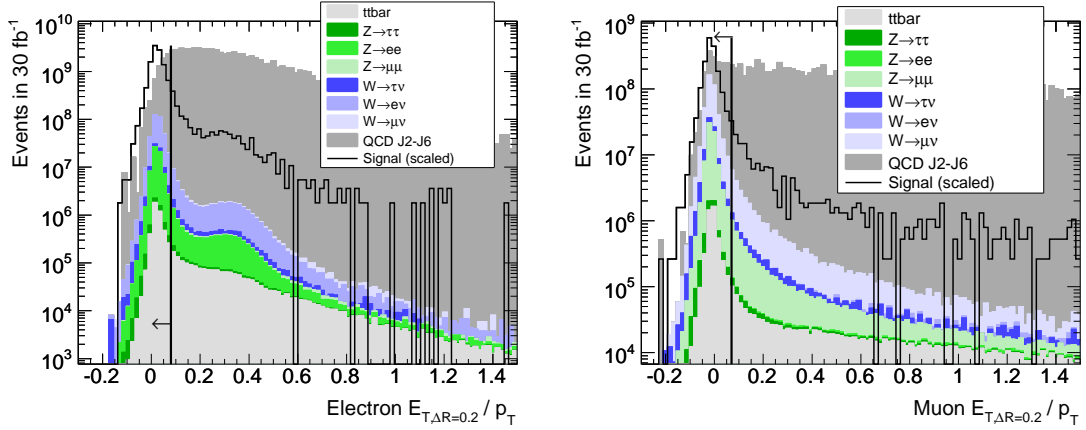


Figure 8.1.: The E_T in a cone with size $\Delta R = 0.2$ divided by the p_T of the electrons (left) and muons (right). The signal is scaled to the area of the sum of all backgrounds for better visibility. The lines indicate the chosen cut values, the arrows point at the events which are kept in the analysis. A Higgs mass of 130 GeV has been assumed. The background processes are normalized to cross section.

been checked, the best cut value is independent from the Higgs boson mass. Table 8.2 lists the relative cut efficiencies for each of the different processes for electrons and muons. The QCD background is efficiently suppressed by the isolation cuts, while there is hardly any impact on the signal contribution.

Since these cuts remove most of the QCD events, the lepton isolation was not applied for the QCD samples but the cut efficiency was applied as a weight. The factorization of the isolation cut allows to evaluate the efficiencies of the following cuts and to give a more reliable estimate of the remaining QCD contribution, which would be impossible given the limited MC statistics.

The lepton isolation was not applied in the published analysis and the QCD contribution was not evaluated.

Process	Electrons	Muons
h/A/H (110 GeV)	90	93.8
h/A/H (130 GeV)	89.5	92.8
h/A/H (160 GeV)	90.3	93.7
h/A/H (200 GeV)	90	92.9
h/A/H (300 GeV)	90.7	92.9
h/A/H (450 GeV)	91.1	92.1
$t\bar{t}$	70.4	78.6
$Z \rightarrow \tau\tau$	88.3	93.4
$Z \rightarrow ee$	91.5	21.2
$Z \rightarrow \mu\mu$	39	95.5
$W \rightarrow \tau\nu$	87.3	94.1
$W \rightarrow e\nu$	91.1	14.8
$W \rightarrow \mu\nu$	30.7	95.5
QCD	7.9	7.2

Table 8.2.: Fraction of leptons which pass the isolation criteria, in percent. The numbers are calculated with respect to the number of all reconstructed electrons or muons passing the object ID cuts and the overlap removal.

Lepton Selection

Two high- p_T leptons are chosen for the analysis. The two leptons can either be two electrons, two muons, or one electron and one muon. The leptons which pass the object ID criteria and the overlap removal are ordered in p_T and combined with each other. In case more than two leptons are found in the event, the pair with the largest scalar p_T sum and opposite charge is passed on to the analysis.

B-Tagging

In this analysis only the process of Higgs boson production in association with b-quarks was considered. Hence, a b-tag is applied already at baseline selection level to reduce backgrounds containing no true b-jets², such as the majority of Z and W decays. An IP3D+SV1 b-tagging weight cut value of 3 was chosen. If at least one b-tagged jet with $p_T > 15$ GeV is found, the event is kept in the analysis.

Figure 8.2 displays the b-tagging weight for a signal sample and the $Z(\rightarrow \mu\mu) + \text{jets}$ sample broken down to the true flavors. The flavor tagging weight of the light-jets needed to be shifted for each sample to correct for the over-estimated light-jet rejection rate (see Section 6.4.3 and Appendix B).

²A true b-jet (true light-jet) is a reconstructed jet resulting from a b-quark (u/d/s-quark) according to the MC event record. The reconstructed flavor might be different.

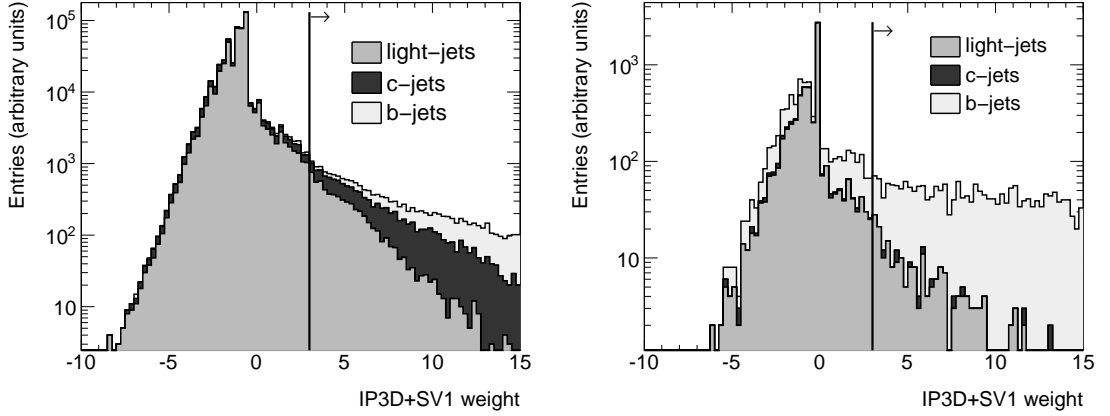


Figure 8.2.: The corrected b-tagging weight for $Z(\rightarrow \mu\mu) + \text{jets}$ (left) and for a Higgs boson signal with $m_A = 130$ GeV (right), broken down into the true flavor of each jet. The excess of b-jets in the signal is obvious. The weight cut at 3 is marked, the arrows indicate the entries which pass the cut.

Cut on the Number of Jets

A cut on the number of high- p_T jets with $p_T > 15$ GeV was applied in order to reduce the backgrounds further, in particular the $t\bar{t}$ contribution.

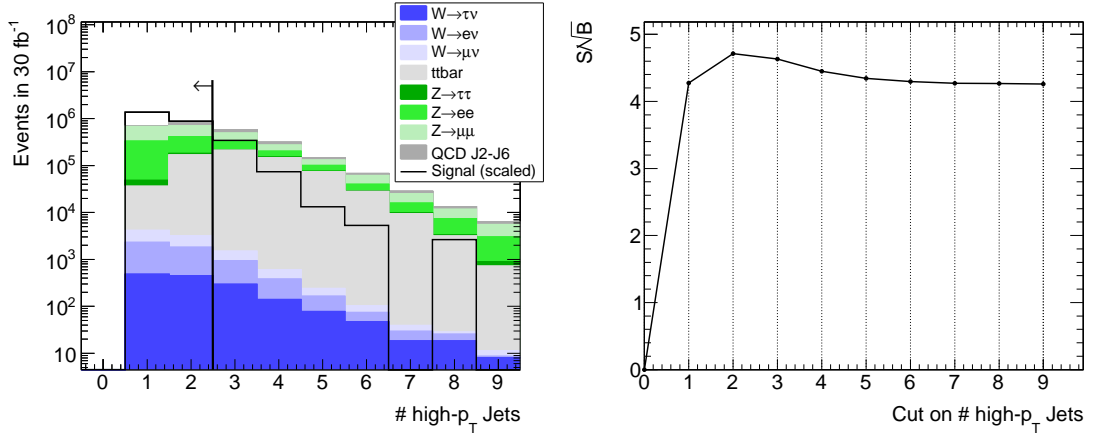


Figure 8.3.: Left: The number of high- p_T jets is plotted for a signal hypothesis of $m_A = 130$ GeV and various background processes. The signal is scaled to the number of background events for better visibility. Right: The statistical significance S/\sqrt{B} , also for $m_A = 130$ GeV, is given as a function of the cut value.

The cut value was optimized such that the statistical significance, Z , becomes maximal. The statistical significance for a large number of background events B and signal events S is given as:

$$Z = \frac{S}{\sqrt{B}}. \quad (8.1)$$

Figure 8.3 displays the number of high- p_T jets after the trigger, lepton selection and at least one b-tag were applied. The statistical significance as a function of the cut value is also shown. The cut value chosen is to keep only events having less than three jets with $p_T > 15$ GeV. Combined with the requirement of at least one b-tag this leaves only events with one or two jets in the analysis.

Missing E_T Cut

In order to suppress the QCD background contributions and $Z \rightarrow ee/\mu\mu$, a cut on a minimal $E_{T,\text{miss}}$ is applied. In these events the missing E_T is usually small and mostly fake MET. Furthermore, a cut on the MET is usually applied in order to not include events with poorly reconstructed jets and other particle leading to fake MET. The baseline cut on MET is chosen such that a Higgs boson signal with a low m_A is not reduced significantly. To further suppress background processes, the MET cut will be tuned in the Higgs boson mass-dependent analyses.

The cut value applied at baseline selection level is:

- $E_{T,\text{miss}} > 15$ GeV.

Figure 8.4 displays the MET distribution of various processes and indicates the cut value. It also shows the MET distribution broken down to the different QCD samples. The plots were prepared for all events, no selection was applied.

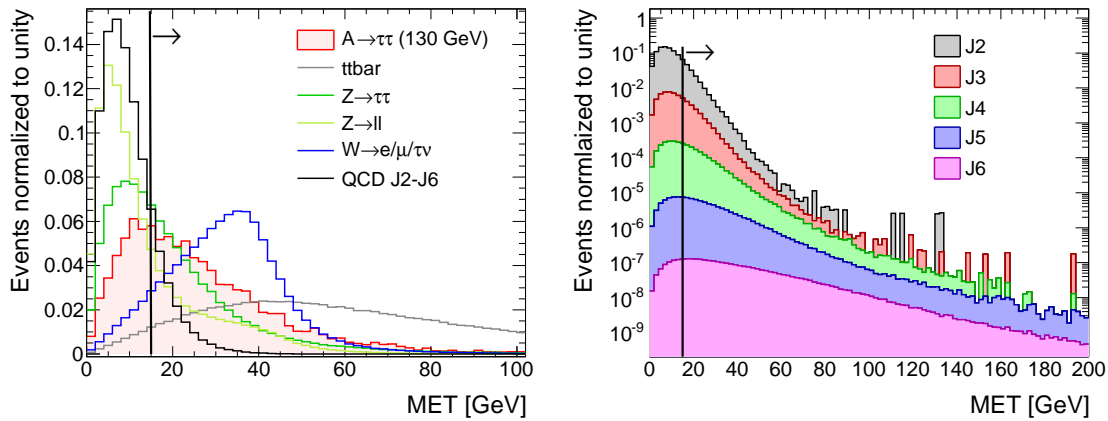


Figure 8.4.: Left: MET distributions for various processes and a signal hypothesis of $m_A = 130$ GeV. All distributions are normalized to unity for better visibility. Right: The MET broken down into various QCD samples. Each samples is normalized to cross section, the sum is normalized to unity. The cut value is indicated, the arrows point to the events kept in the analysis.

Cut on Lepton p_T

QCD background can be reduced further by cutting on a minimal p_T of the electrons and muons. At the object selection level leptons with $p_T > 10$ GeV were passed on to the analysis. This might not be sufficient enough for the QCD suppression. The evaluation of the QCD background, however, is difficult and afflicted with large uncertainties due to the extremely large cross sections for

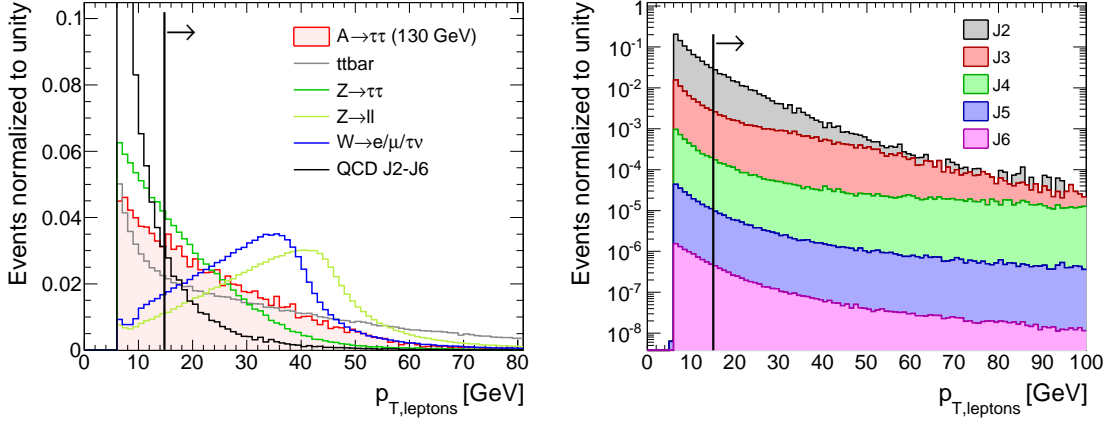


Figure 8.5.: Left: p_T distributions of the leptons for various processes and a signal hypothesis of $m_A = 130$ GeV. All distributions are normalized to unity for better visibility. Right: The $p_{T,\ell}$ broken down into various QCD samples. Each samples is normalized to cross section, the sum is normalized to unity. The cut value is indicated, the arrows point to the events kept in the analysis.

the samples with a low virtuality. This will be discussed further at the end of the baseline selection subsection.

The cut value is chosen as follows:

- $p_{T,\text{leptons}} > 15$ GeV.

Figure 8.5 displays the p_T distribution of various processes and indicates the cut value. The right plot displays the dependence of the distribution on the QCD sample. The smaller the virtuality, the more the p_T is peaking at lower values. The plot was prepared for all electron and muon candidates passing the overlap removal.

In the published analysis, the minimal MET cut and p_T cut were chosen to be only 10 GeV.

Cut on Dilepton Mass

In case the two selected leptons are either two electrons or two muons, a cut on the invariant dilepton mass, $m_{\ell\ell}$, is applied to suppress $Z \rightarrow ee$ and $Z \rightarrow \mu\mu$ events. The cut is chosen such that the reconstructed Z boson peak is cut out from the mass spectrum:

$$m_{\ell\ell} < 80.0 \text{ GeV or } m_{\ell\ell} > 100.0 \text{ GeV}.$$

In the case when one electron and one muon are selected, no cut on the dilepton mass is applied in the baseline analysis.

Figure 8.6 displays the $m_{\ell\ell}$ distribution before this cut is applied in both the $ee/\mu\mu$ and the $e\mu$ channel. In the published analysis, this cut was not applied at baseline selection level, but it entered in the optimized m_A -dependent cut analysis. Applying this cut already at baseline level, however, leads to less differences between the $ee/\mu\mu$ and $e\mu$ final states and therefore simpler, less final state-dependent cuts in the further analysis.

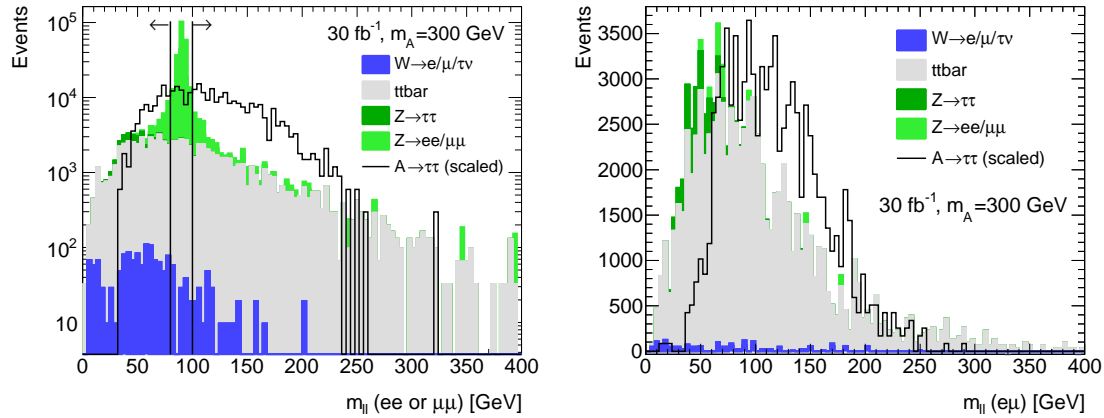


Figure 8.6.: The distribution of the invariant dilepton mass, left in the $ee/\mu\mu$ channel and right for the $e\mu$ final state. The mass window cut is indicated by lines, the arrows point to the events which are kept in the analysis. The cut is only applied in the dielectron and dimuon final states.

Collinear Approximation

For reconstructing the collinear mass (details in Chapter 7), only events which pass the following cuts are kept in the analysis:

- $0 < x_1 < 1$,
- $0 < x_2 < 1$.

x_1 and x_2 are the scaling fractions to correct the p_T values of the electron or muon from the τ decay to the value of the initial τ (see Equation 7.3). These cuts are not applied in the case when the visible mass is reconstructed.

Baseline Selection Cut Flow

The cut flow for the baseline cuts is given in Table 8.3. The results are given as numbers of events normalized to an integrated luminosity of 30 fb^{-1} at $\sqrt{s} = 14 \text{ TeV}$.

The numbers for the W +jets and the QCD processes are obtained by using cut factorization. Cut factorization is used to increase the available MC statistics by not applying independent cuts at the same time but one-by-one or in independent groups and multiplying the individual efficiencies. The factorization was performed as follows:

- The trigger and the lepton selection were grouped together since these cuts are not independent, this will be referred to as first group.
- The efficiency of an event to pass the b-tagging requirement was obtained independent from the first group. In Table 8.3 the number of events after the b-tag is then given as number of events containing at least one b-jet times the efficiency of the first group.

- The cut on the number of jets and the b-tag are not independent, hence these cuts form the second group. In Table 8.3, the number of events after the cut on the number of jets is the number of events passing the second group times the efficiency of the first group.
- The MET cut efficiency was obtained independently from all other cuts, this will be referred to as third group to be consistent with the notation. In Table 8.3, the number of events after the MET cut is the number of events passing the cut on the number of jets (as obtained by the factorization as described above) times the efficiency of the third group, ie. it is the product of the efficiencies of first group, second group and third group.
- The number of events passing the remaining baseline selection cuts are not independent from trigger and lepton selection and not independent from each other, but independent from the second and third group. In Table 8.3, the number of events after the $p_{T,\ell}$ cut is given by the number of events passing the first group and the cut on $p_{T,\ell}$ times the efficiency of the second group and the third group. The number of events passing the $m_{\ell\ell}$ cut is given as number of events passing the first group and the cuts on $p_{T,\ell}$ and $m_{\ell\ell}$ times the efficiency of the second group times efficiency of the third group. The number of events passing the collinear approximation was obtained in the same way.

At baseline selection level the majority of background events is removed. The remaining events have a signal-like topology. The baseline selection is sufficient for a Higgs boson mass independent search but does not reflect the full potential.

Discussion of QCD Background

After the baseline analysis is performed, the contributions from QCD processes are very small compared to the other backgrounds and signal for small m_A . QCD events are significantly suppressed by cutting on MET and the p_T of the electrons and muons. The smaller the virtualities of the QCD sub-samples, the more efficient these cuts are. However, it should be noted that the contributions from QCD events with virtualities smaller than 35 GeV have not been evaluated, due to the limited MC statistics. Furthermore, the uncertainties from the cut factorization are not accounted for, because they can only be evaluated by studying samples containing several orders of magnitude more events.

The signal efficiency for the low Higgs boson mass hypothesis is reduced strongly by the cuts on MET and p_T of the leptons. In the future, better lepton isolation and lepton identification procedures might be developed. In this case, the cuts on MET and $p_{T,\ell}$ should be lowered if a search for Higgs bosons with low mass is conducted.

In the analysis published in [19], the QCD contribution was not evaluated but assumed to be negligible. The studies in this thesis indicate that indeed QCD is negligible if lepton isolation and a sufficiently large minimal MET and lepton p_T cut are applied; the collinear approximation also strongly suppresses QCD (see baseline selection cutflow Table 8.3). After the baseline selection less than 140 QCD events remain. QCD background will therefore not be considered anymore in the further study of the dilepton channel.

Process	Trigger	Lepton Selection	> 0 b-tags	1 or 2 jets	MET Cut	$p_{T,\ell}$ Cut	$m_{\ell\ell}$ Cut	Coll. Appr.
h/A/H (110 GeV)	130105	77935	15304	13887	10032	6177	6079	4497
h/A/H (130 GeV)	104641	60717	15579	13028	10155	6775	6330	4886
h/A/H (160 GeV)	64294	37787	9306	8244	6870	4903	4346	3326
h/A/H (200 GeV)	36876	21728	5685	5026	4318	3315	2931	2340
h/A/H (300 GeV)	10345	6321	1935	1663	1507	1277	1163	916
h/A/H (450 GeV)	2245	1427	452	373	352	319	306	250
$t\bar{t}$	8.34242e+06	827098	681201	201255	194507	170464	157493	34656
$Z \rightarrow \tau\tau$	1.44756e+06	830236	34977	24171	16880	9031	8944	6821
$Z \rightarrow ee$	3.78672e+07	1.78605e+07	730544	510348	103605	99696	14382	2234
$Z \rightarrow \mu\mu$	4.71522e+07	2.28066e+07	945636	645175	159240	150169	19859	3065
$W \rightarrow \tau\nu$	1.41902e+07	40397	1335	819	576	346	346	154
$W \rightarrow e\nu$	2.19191e+08	243617	4160	3158	2930	1528	1384	118
$W \rightarrow \mu\nu$	3.21586e+08	264714	4079	3177	2823	1354	1354	138
QCD J2	1.31023e+10	3.41325e+06	299689	153675	30993	1073	1073	125
QCD J3	4.94433e+09	94314	15421	4134	1369	84	84	11
QCD J4	5.05964e+08	1871	485	80	40.3	7.9	7.6	0.9
QCD J5	2.9737e+07	42.5	15.8	2	1.38	0.35	0.35	0.05
QCD J6	1.23869e+06	1.15	0.58	0.07	0.06	0.02	0.02	0.01

Table 8.3.: Cut flow for the baseline selection. Shown are numbers of events normalized to an integrated luminosity of 30 fb^{-1} at $\sqrt{s} = 14 \text{ TeV}$. The signal cross sections were evaluated for $\tan\beta = 30$.

Statistical Significance after the Baseline Cuts

The statistical significance S/\sqrt{B} was calculated at baseline selection level both when reconstructing the collinear mass and the visible mass. The results using the visible mass are given in Appendix C. The $\tau\tau$ mass distributions for signal and background processes after all baseline cuts are displayed in Figure 8.7 for a signal hypothesis of $\tan\beta = 45$. A signal peak will be visible on top of the SM background for large values of $\tan\beta$ and a low m_A ($m_A \lesssim 200$ GeV). Even if the baseline analysis does not reflect the full discovery potential, it can be applied to search for an Higgs boson-like excess in the $m_{\tau\tau}$ spectrum. The reconstructed visible mass distributions after the baseline cuts are given in Figure C.1.

For evaluating the statistical significance a mass window cut is applied based on the expected mass resolutions, σ , for the signal:

$$\begin{aligned} m_0 - 1.5 \cdot \sigma < m_{\tau\tau} < m_0 + 2.0 \cdot \sigma, \\ m_0 - 1.5 \cdot \sigma < m_{\text{visible}} < m_0 + 2.0 \cdot \sigma. \end{aligned} \quad (8.2)$$

Here, m_0 denotes the fitted mass peak position for each assumed true m_A mass, as determined from the MC (see Section 7.2.1). The window is chosen asymmetrical to fit the mass shape, as was discussed in the previous chapter in Figures 7.16, 7.17, 7.25 and 7.26. The numerical values for the collinear mass analysis are listed in Table 8.4. The corresponding values for the visible mass analysis are given in Appendix C, Table C.1.

m_A [GeV]	m_0 [GeV]	σ [GeV]	$m_{\tau\tau}^{\text{low}}$	$m_{\tau\tau}^{\text{high}}$
110	101	28	59	157
130	117	31	71	179
160	145	36	91	217
200	179	43	116	265
300	270	59	182	388
450	409	88	278	584

Table 8.4.: The $m_{\tau\tau}$ mass window cut chosen for the baseline selection. Here, $m_{\tau\tau}^{\text{low}}$ and $m_{\tau\tau}^{\text{high}}$ denote the lower (upper) edge of the mass window, m_0 is the position where the signal peaks and σ is the mass resolution.

The results for an integrated luminosity of 30 fb^{-1} and $\tan\beta = 45$ are summarized in Table 8.5 for the collinear mass analysis and in Table C.2 for the visible mass analysis. Although the signal efficiency of the collinear mass reconstruction is approximately 25% smaller than when reconstructing the visible mass, the statistical significance is larger.

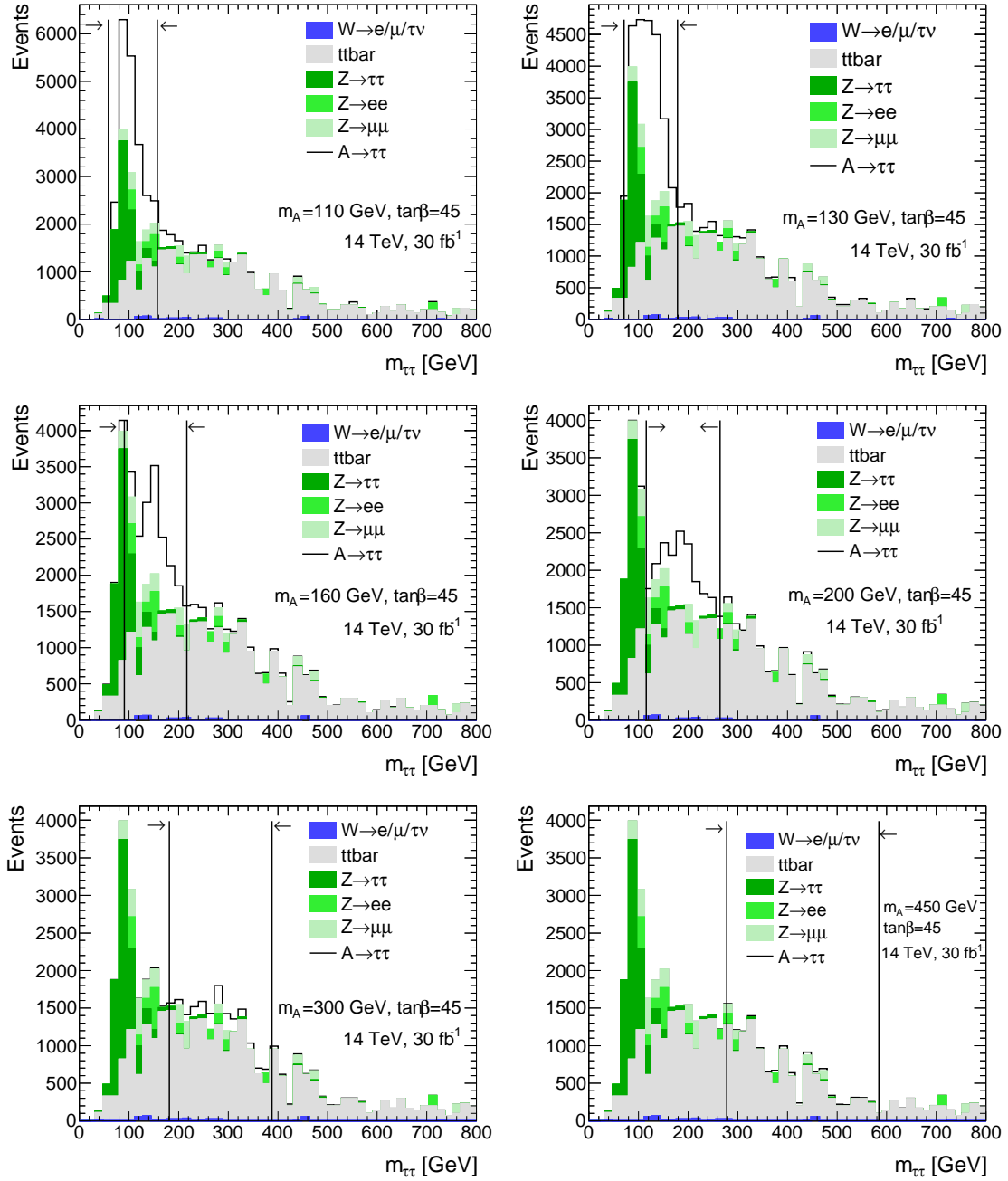


Figure 8.7.: Reconstructed collinear mass after baseline cuts for Higgs boson mass hypotheses as indicated in the plots, all for $\tan\beta = 45$. The lines and arrows indicate the chosen mass window cuts. The corresponding plots for the visible mass are given in Figure C.1.

m_A	S	B	S/\sqrt{B}
110 GeV	1697	14814	13.9
130 GeV	1911	16726	14.8
160 GeV	1315	16321	10.3
200 GeV	831	15157	6.7
300 GeV	315	16136	2.5
450 GeV	69	12943	0.6

Table 8.5.: Number of signal events, S , background events, B , and statistical significance, S/\sqrt{B} , in the mass window for $\tan\beta = 45$ and 30 fb^{-1} at $\sqrt{s} = 14 \text{ TeV}$, when reconstructing the collinear mass at baseline selection level. The corresponding values for the visible mass analysis are given in Table C.2.

8.1.2. Higgs Boson Mass-Dependent Selection

Based on the results from the baseline analysis, Higgs boson mass-dependent cuts are optimized in order to suppress the remaining background processes, namely $Z(\rightarrow \tau\tau)$ +jets and $t\bar{t}$. Since reconstructing the collinear mass yields a higher significance than the visible mass, the final significance will be extracted from the $m_{\tau\tau}$ spectrum and not the m_{vis} distribution, hence all cuts have been optimized with cuts on x_1 and x_2 applied.

For each of the variables, the cuts were optimized in an iterative procedure in order to maximize the statistical significance S/\sqrt{B} . The following observables were chosen for the cut analysis:

- MET,
- $\Delta\Phi_{\ell\ell}$,
- $m_{\ell\ell}$,
- $p_{T,\text{Higgs}}$ (as defined by Equation 7.9),
- $p_{T,\text{leading b-jet}}$.

Other variables such as the p_T of the leading lepton, the p_T of the dilepton system, or $x_1 \cdot x_2$ have been checked but were found to be strongly correlated to the five observables listed above and were, in contrary to the published analysis, not used here.

The starting point for the optimization are the distributions of these variables after the baseline selection. Then, for each variable the best cut is found at the value when the statistical significance shows a distinct maximum. However, not the best cut values are applied for the next iteration, but looser cuts. Then, in the second iteration, again the best cut is found for each of the variables by maximizing the statistical significance. If the best cut value does not change, the optimization procedure is done, otherwise more iterations are performed.

It should be noted, however, that the sizes of the MC samples used are limited. Such an optimization might end up in bins where the signal fluctuated up and the background fluctuated down or is even absent given the available MC statistics. These effects were avoided by limiting the number of iterations and by comparing the cut values for each signal mass hypothesis with each other.

The cuts chosen in this thesis are in general looser than these in the published analysis, to avoid statistical fluctuations.

Since there is no $Z \rightarrow e\mu$ decay, different background contributions are found in the $ee/\mu\mu$ and the $e\mu$ channels. Therefore, the difference of the cut values between those two final states types have been checked. However, due to the cut on the dilepton mass applied in the baseline selection, almost no significant differences are left. Only the cut on the MET distribution was chosen differently between the $ee/\mu\mu$ and the $e\mu$ channel when an improvement of the statistical significance could be obtained.

When the cuts are applied, the background composition changes with an increasing Higgs boson mass. Hence, for a Higgs boson mass close to the Z boson mass the $Z \rightarrow \tau\tau$ background will be dominant, while for large A masses the $Z \rightarrow \tau\tau$ contribution is negligible compared to that from the $t\bar{t}$ events.

In the following Figures 8.8-8.13, the distributions of the cut variables are displayed and the cut values are indicated. If different cuts between the $ee/\mu\mu$ and $e\mu$ channel are chosen, both distributions are shown. All these plots have been prepared after the baseline cuts were applied.

The cut values for each Higgs boson mass hypothesis are summarized in Table 8.6.

m_A	MET	$m_{\ell\ell}$	$\Delta\Phi_{\ell\ell}$	$p_{T,b-jet}$	$p_{T,Higgs}$
110 GeV	< 80 GeV	< 75 GeV	> 1.7 rad	< 60 GeV	< 80 GeV
130 GeV	< 80 GeV	(35...75) GeV	> 1.8 rad	< 70 GeV	< 80 GeV
160 GeV	< 80 GeV	(40...80) GeV	> 1.9 rad	< 70 GeV	< 80 GeV
(only $ee/\mu\mu$)	> 20 GeV				
200 GeV	< 100 GeV	(40...140) GeV	> 2.0 rad	< 70 GeV	< 70 GeV
(only $ee/\mu\mu$)	> 25 GeV				
300 GeV	> 25 GeV	(50...200) GeV	> 2.5 rad	< 60 GeV	< 60 GeV
450 GeV	> 30 GeV	> 100 GeV	> 2.7 rad	< 60 GeV	< 60 GeV

Table 8.6.: m_A -dependent cut values in the lepton-lepton analysis.

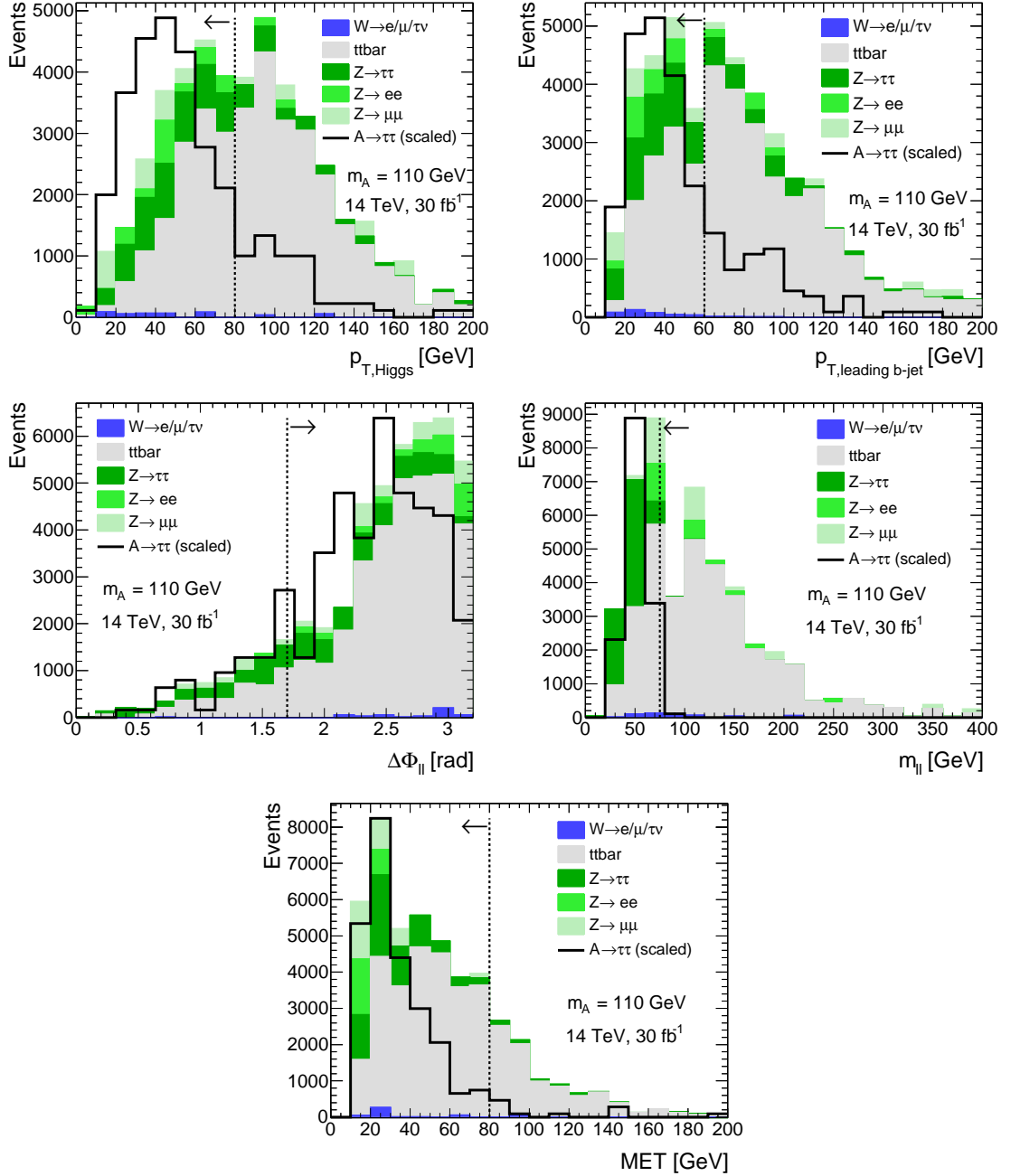


Figure 8.8.: The distributions of the variables for the Higgs boson mass-dependent cuts after the baseline cuts have been applied, for a mass hypothesis of $m_A = 110$ GeV. The signal is scaled to the largest background bin for better visibility. The cuts are indicated.

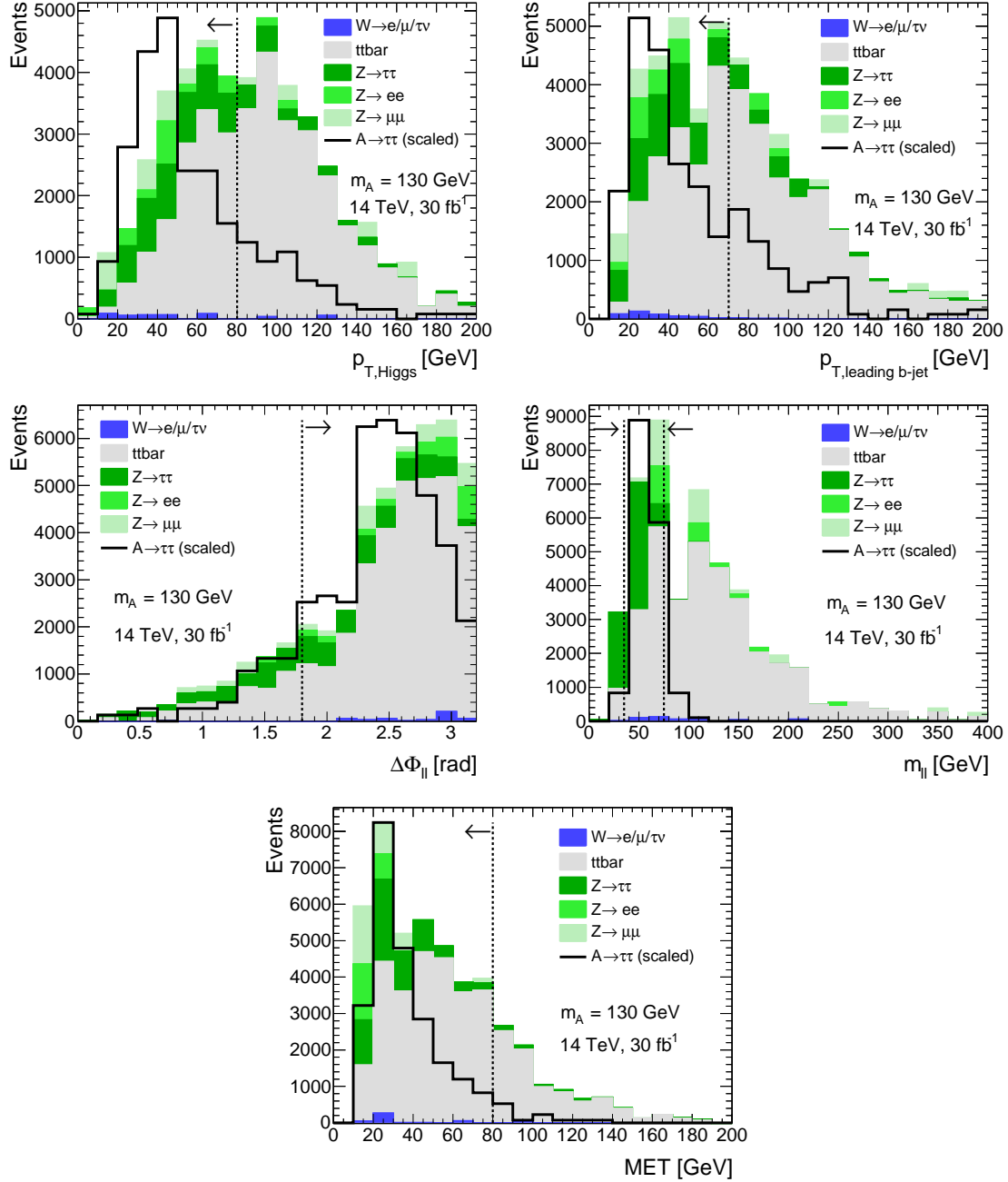


Figure 8.9.: The distributions of the variables for the Higgs boson mass-dependent cuts after the baseline cuts have been applied, for a mass hypothesis of $m_A = 130$ GeV. The signal is scaled to the largest background bin for better visibility. The cuts are indicated.

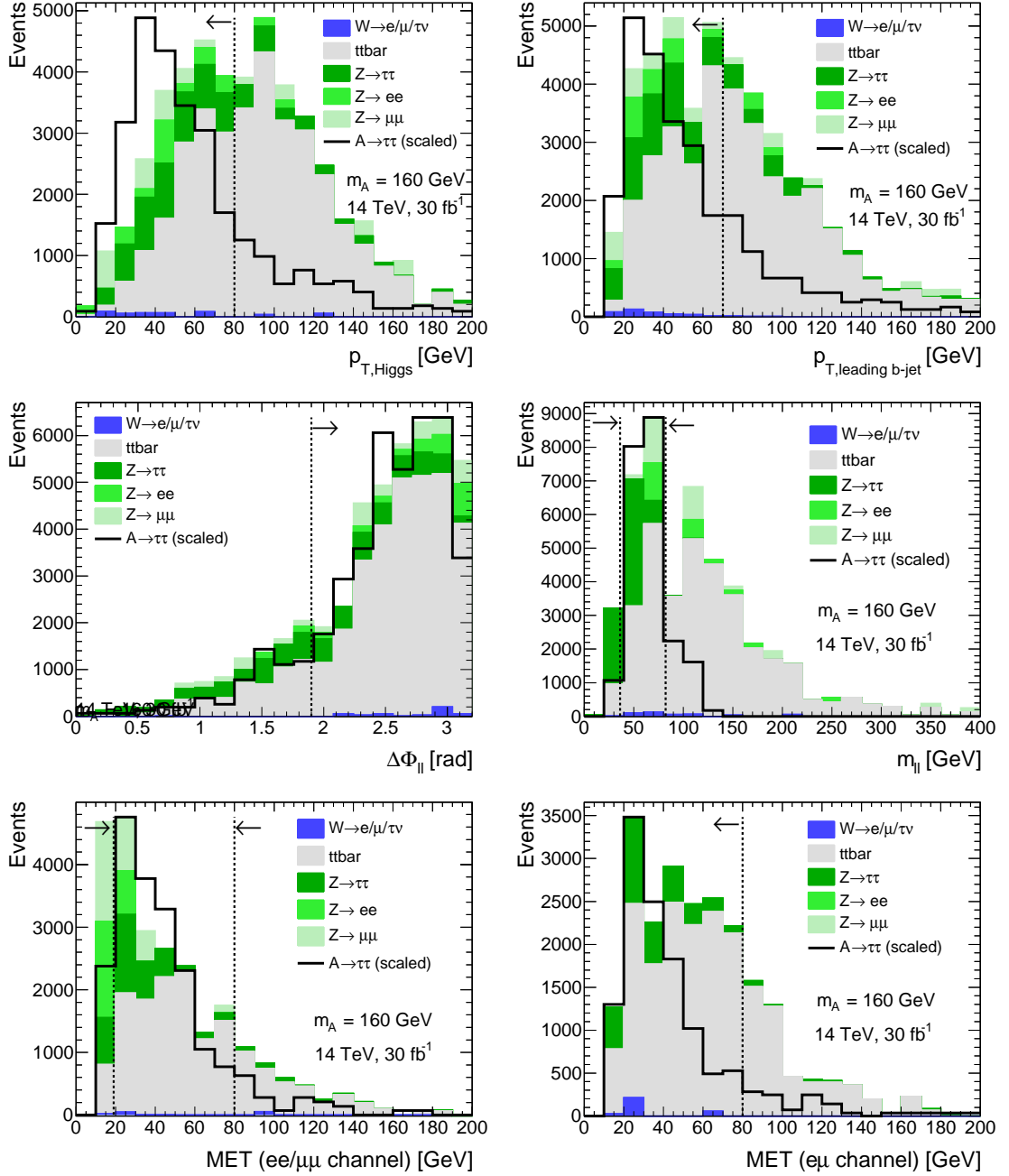


Figure 8.10.: The distributions of the variables for the Higgs boson mass-dependent cuts after the baseline cuts have been applied, for a mass hypothesis of $m_A = 160$ GeV. The signal is scaled to the largest background bin for better visibility. The cuts are indicated.

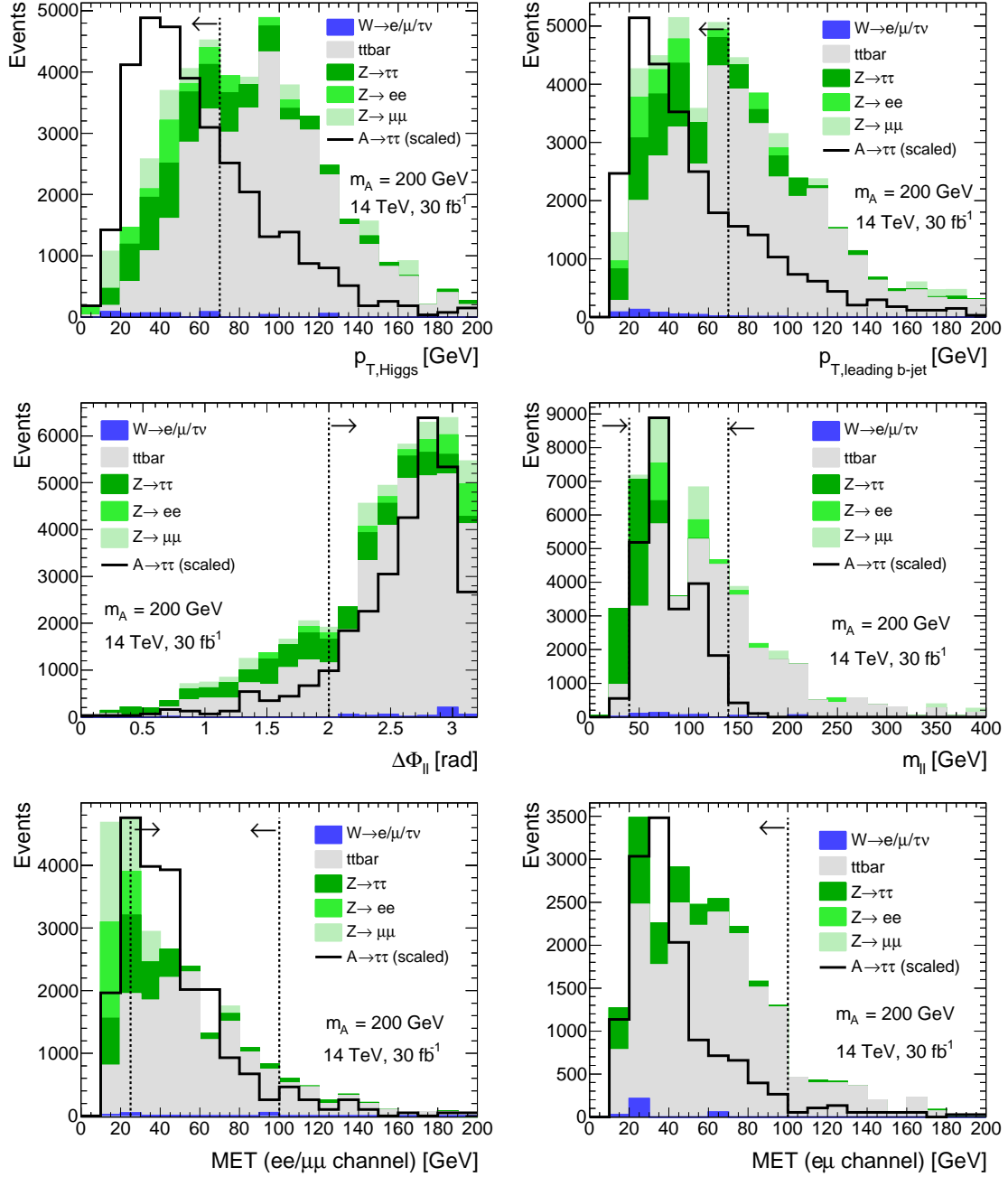


Figure 8.11.: The distributions of the variables for the Higgs boson mass-dependent cuts after the baseline cuts have been applied, for a mass hypothesis of $m_A = 200$ GeV. The signal is scaled to the largest background bin for better visibility. The cuts are indicated.

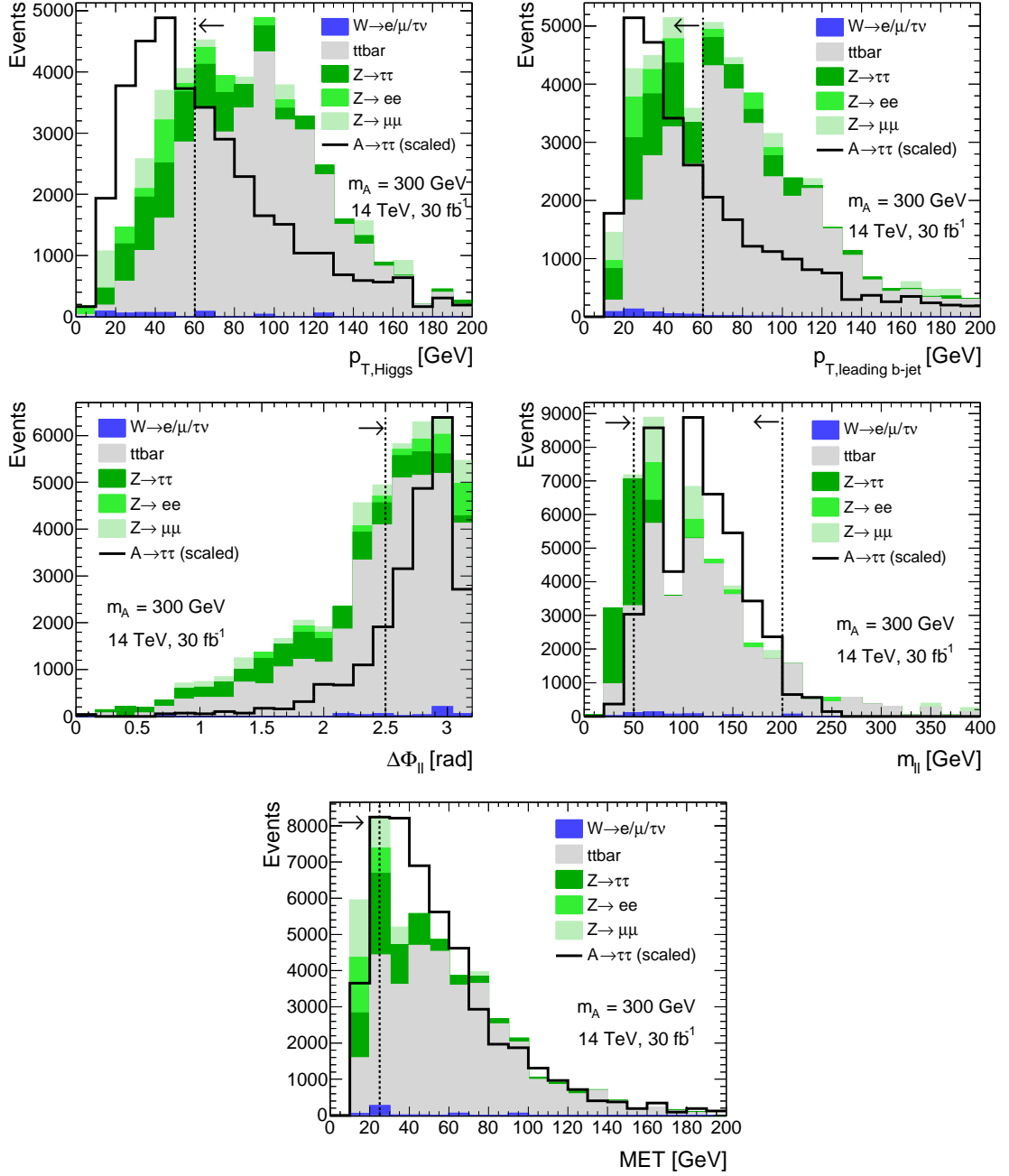


Figure 8.12.: The distributions of the variables for the Higgs boson mass-dependent cuts after the baseline cuts have been applied, for a mass hypothesis of $m_A = 300$ GeV. The signal is scaled to the largest background bin for better visibility. The cuts are indicated.

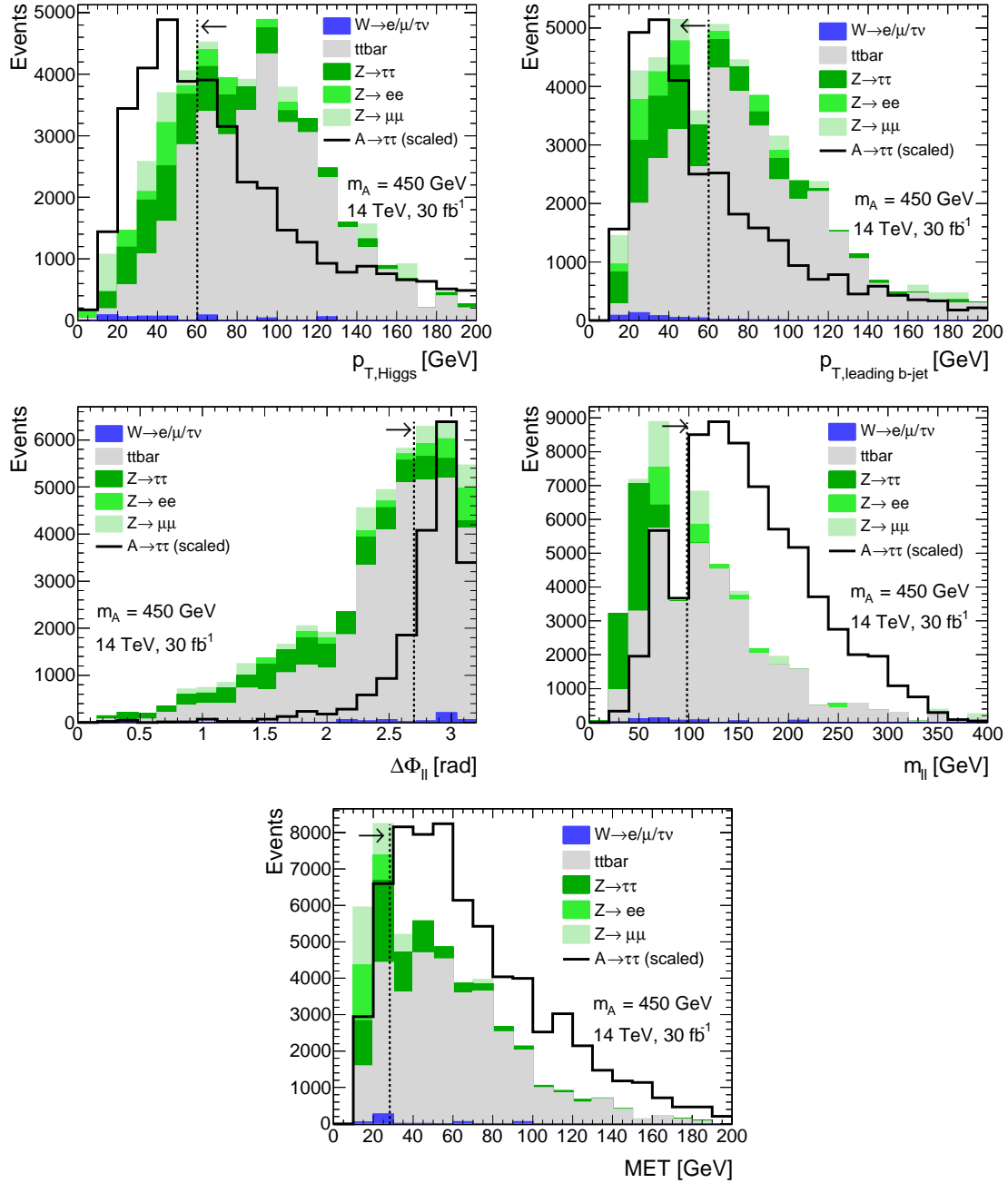


Figure 8.13.: The distributions of the variables for the Higgs boson mass-dependent cuts after the baseline cuts have been applied, for a mass hypothesis of $m_A = 450$ GeV. The signal is scaled to the largest background bin for better visibility. The cuts are indicated.

A few observations are discussed in the following:

- The MET of the signal processes for $m_A \leq 200$ is rather low, therefore an upper MET cut is applied in order to suppress especially $t\bar{t}$. The MET distribution of heavier Higgs bosons is comparable to the MET for $t\bar{t}$ events, an upper cut is therefore not useful. A minimal MET cut of 15 GeV was already applied in the baseline analysis to suppress backgrounds without real MET (QCD and $Z \rightarrow \ell\ell$).
- The heavier the Higgs bosons, the more the distribution of $\Delta\Phi_{\ell\ell}$ peaks at $\Delta\Phi_{\ell\ell} \approx \pi$, because the taus and their decay products have a large Lorentz boost. The varying cuts on a minimal $\Delta\Phi_{\ell\ell}$ reflect that.
- While the distributions of $m_{\ell\ell}$, MET and $\Delta\Phi_{\ell\ell}$ depend a lot on the Higgs boson mass, the p_T of the leading b-jet and the $p_{T,\text{Higgs}}$ do not show such a strong mass dependence.
- For low m_A , the $Z \rightarrow \tau\tau$ is hard to suppress. Requiring at least one b-jet is basically the only chance to reduce it significantly.

The cut flows for all six Higgs boson mass hypotheses are given in Tables 8.7-8.12. Given are numbers of events scaled to an integrated luminosity of 30 fb^{-1} . The numbers of signal events are scaled to cross sections according to $\tan\beta = 30$.

The contributions from $W \rightarrow e/\mu/\tau + \nu$ and $Z \rightarrow ee/\mu\mu$ were evaluated using cut factorization:

- **W boson events:**
For the $W \rightarrow e/\mu/\tau + \nu$ events the cuts were already factorized at baseline level. The efficiency of the b-tagging requirement and the cut on the number of jets were factorized out. Furthermore, the cuts on each of the five observables (MET, $m_{\ell\ell}$, $\Delta\Phi_{\ell\ell}$, $p_{T,\text{b-jet}}$ and $p_{T,\text{Higgs}}$) were evaluated independently from each other and the efficiencies multiplied.
- **$Z \rightarrow ee/\mu\mu$ events:**
For the $Z \rightarrow ee/\mu\mu$ background, the MC statistics does not allow to evaluate the efficiencies after all optimized cuts. There are no MC events left for the last two cuts. Hence, the b-tagging requirement and the cut on the p_T of the leading b-jet was factorized out. The kinematics are not changed by that but effectively almost 100 times more MC events are gained.

The W+jets contribution is found to be negligible after all cuts. Its contribution was already very small at baseline level compared to the other backgrounds. In the published analysis, the W+jets contribution was found to be larger. This is understood as no lepton isolation was applied there. The QCD background is neglected as its contribution was very small after the baseline selection.

Process	Baseline	MET	$m_{\ell\ell}$	$\Delta\Phi$	$p_{T,\text{Higgs}}$	$p_{T,\text{bjet}}$	Coll. Approx.
$h/A/H$ (110 GeV)	6079	5848	5486	4810	4530	4036	2932
ttbar	157493	103969	41306	12644	10187	4946	1015
$Z \rightarrow \tau\tau$	8944	8283	8127	5569	5377	4681	3515
$Z \rightarrow ee$	14382	14382	3630	2513	2513	1447	373
$Z \rightarrow \mu\mu$	19859	18388	4903	3310	3187	1927	444
$W \rightarrow \tau\nu$	346	269	60	60	53	41	18
$W \rightarrow e\nu$	1384	1167	824	517	500	406	35
$W \rightarrow \mu\nu$	1354	1285	937	508	474	370	38

Table 8.7.: Cut flow for the full selection for a Higgs boson mass hypothesis of $m_A = 110$ GeV. Given are numbers of events normalized to an integrated luminosity of 30 fb^{-1} at $\sqrt{s} = 14$ TeV. The signal cross sections were evaluated for $\tan\beta = 30$.

Process	Baseline	MET	$m_{\ell\ell}$	$\Delta\Phi$	$p_{T,\text{Higgs}}$	$p_{T,\text{bjet}}$	Coll. Approx.
$h/A/H$ (130 GeV)	6330	5961	4916	4440	4102	3733	2919
ttbar	157493	103969	32396	11399	9106	5241	1376
$Z \rightarrow \tau\tau$	8944	8283	7309	4785	4681	4385	3167
$Z \rightarrow ee$	14382	14382	3630	2513	2513	1494	389
$Z \rightarrow \mu\mu$	19859	18388	4903	2697	2697	2003	472
$W \rightarrow \tau\nu$	346	269	60	60	53	42	19
$W \rightarrow e\nu$	1384	1167	549	323	312	268	23
$W \rightarrow \mu\nu$	1354	1285	479	244	227	188	19

Table 8.8.: Cut flow for the full selection for a Higgs boson mass hypothesis of $m_A = 130$ GeV. Given are numbers of events normalized to an integrated luminosity of 30 fb^{-1} at $\sqrt{s} = 14$ TeV. The signal cross sections were evaluated for $\tan\beta = 30$.

Process	Baseline	MET	$m_{\ell\ell}$	$\Delta\Phi$	$p_{T,\text{Higgs}}$	$p_{T,\text{bjet}}$	Coll. Approx.
$h/A/H$ (160 GeV)	4346	3732	3232	2988	2790	2556	1921
ttbar	157493	101577	39406	16935	13299	7501	2326
$Z \rightarrow \tau\tau$	8944	7222	5203	2958	2889	2697	1862
$Z \rightarrow ee$	14382	6004	3910	2374	2374	760	196
$Z \rightarrow \mu\mu$	19859	10542	5026	2452	2329	1306	304
$W \rightarrow \tau\nu$	346	231	102	102	91	73	32
$W \rightarrow e\nu$	1384	1049	528	293	284	243	21
$W \rightarrow \mu\nu$	1354	1285	545	277	258	214	22

Table 8.9.: Cut flow for the full selection for a Higgs boson mass hypothesis of $m_A = 160$ GeV. Given are numbers of events normalized to an integrated luminosity of 30 fb^{-1} at $\sqrt{s} = 14$ TeV. The signal cross sections were evaluated for $\tan\beta = 30$.

Process	Baseline	MET	$m_{\ell\ell}$	$\Delta\Phi$	$p_{T,\text{Higgs}}$	$p_{T,\text{bjet}}$	Coll. Approx.
$h/A/H$ (200 GeV)	2931	2494	2370	2193	1693	1579	1188
ttbar	157493	124278	77043	37965	20309	12611	3210
$Z \rightarrow \tau\tau$	8944	6682	4594	2314	2175	2053	1340
$Z \rightarrow ee$	14382	1815	1676	698	698	252	73
$Z \rightarrow \mu\mu$	19859	6375	5762	3065	2697	1903	297
$W \rightarrow \tau\nu$	346	269	120	120	106	85	38
$W \rightarrow e\nu$	1384	931	609	326	316	271	23
$W \rightarrow \mu\nu$	1354	1285	654	310	289	239	24

Table 8.10.: Cut flow for the full selection for a Higgs boson mass hypothesis of $m_A = 200$ GeV. Given are numbers of events normalized to an integrated luminosity of 30 fb^{-1} at $\sqrt{s} = 14$ TeV. The signal cross sections were evaluated for $\tan\beta = 30$.

Process	Baseline	MET	$m_{\ell\ell}$	$\Delta\Phi$	$p_{T,\text{Higgs}}$	$p_{T,\text{bjet}}$	Coll. Approx.
$h/A/H$ (300 GeV)	1163	984	912	722	459	418	296
ttbar	157493	146192	101315	37047	12185	6944	1802
$Z \rightarrow \tau\tau$	8944	5534	1618	365	313	261	122
$Z \rightarrow ee$	14382	1815	1815	419	419	156	48
$Z \rightarrow \mu\mu$	19859	6620	6375	1716	1348	1295	212
$W \rightarrow \tau\nu$	346	269	209	139	77	37	16
$W \rightarrow e\nu$	1384	913	519	190	180	144	12
$W \rightarrow \mu\nu$	1354	1056	447	167	150	113	11

Table 8.11.: Cut flow for the full selection for a Higgs boson mass hypothesis of $m_A = 300$ GeV. Given are numbers of events normalized to an integrated luminosity of 30 fb^{-1} at $\sqrt{s} = 14$ TeV. The signal cross sections were evaluated for $\tan\beta = 30$.

Process	Baseline	MET	$m_{\ell\ell}$	$\Delta\Phi$	$p_{T,\text{Higgs}}$	$p_{T,\text{bjet}}$	Coll. Approx.
$h/A/H$ (450 GeV)	306	263	221	171	101	91	63
ttbar	157493	138363	64923	22733	7763	4357	1146
$Z \rightarrow \tau\tau$	8944	4176	52	35	35	17	0
$Z \rightarrow ee$	14382	1257	279	0	0	0	0
$Z \rightarrow \mu\mu$	19859	4658	3187	981	613	599	87
$W \rightarrow \tau\nu$	346	192	85	47	26	13	6
$W \rightarrow e\nu$	1384	760	174	45	43	34	3
$W \rightarrow \mu\nu$	1354	872	133	29	26	20	2

Table 8.12.: Cut flow for the full selection for a Higgs boson mass hypothesis of $m_A = 450$ GeV. Given are numbers of events normalized to an integrated luminosity of 30 fb^{-1} at $\sqrt{s} = 14$ TeV. The signal cross sections were evaluated for $\tan\beta = 30$.

8.1.3. Results of the Event Selection

The collinear mass was reconstructed after all optimized cuts have been applied. For better visibility and comparability, all signal hypotheses were scaled to a cross section corresponding to $\tan\beta = 30$ in the m_h^{\max} scenario. The final mass spectra are illustrated in Figures 8.14-8.16. Although the background events mimic the signal kinematics and therefore peak mostly below the signal, a mass window cut was applied to further reduce the background contribution. These cuts are listed in Table 8.13. Taking into account that the $Z \rightarrow \tau\tau$ background shape is very different from the $t\bar{t}$ shape when reconstructing the collinear mass, a mass window cut is useful especially if the signal peaks well between the Z boson events and the $t\bar{t}$ events, which is the case for $m_A = 130$ GeV. The $m_{\tau\tau}$ window cut values are taken from [19], where they have been optimized including systematic uncertainties.

The corresponding results when the visible mass is reconstructed instead can be found in Appendix C: The reconstructed m_{vis} distributions are shown in Figure C.2, the number of events after all cuts are given in Table C.3, the statistical significances are given in Table C.4.

	110 GeV	130 GeV	160 GeV	200 GeV	300 GeV	450 GeV
$m_{\tau\tau}^{\text{low}}$ [GeV]	93	111	136	145	198	264
$m_{\tau\tau}^{\text{high}}$ [GeV]	171	198	240	270	384	568

Table 8.13.: The lower and upper edge of the collinear mass window cut for the different mass hypotheses.

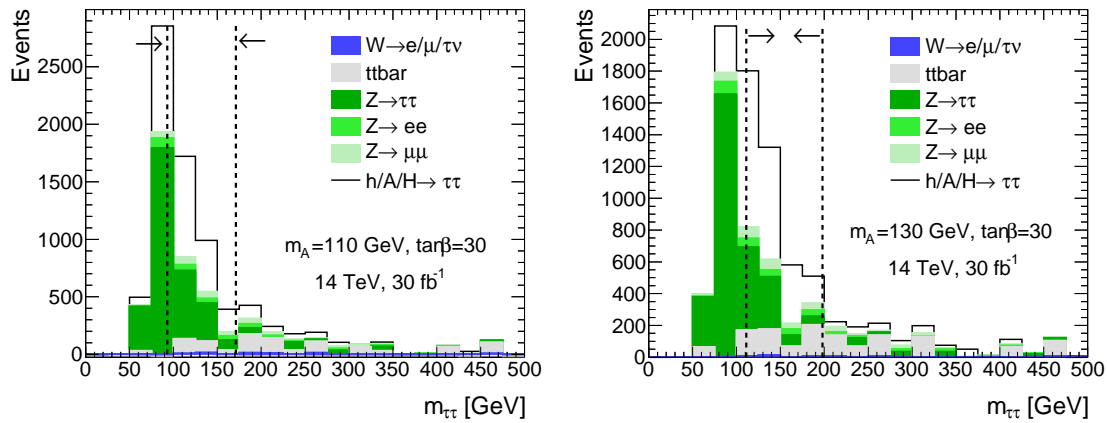


Figure 8.14.: Final $m_{\tau\tau}$ spectra with an integrated luminosity of 30 fb^{-1} , left for $m_A = 110$ GeV and right for $m_A = 130$ GeV. The mass window cut is indicated. The signal cross section corresponds to $\tan\beta = 30$ in the m_h^{\max} scenario.

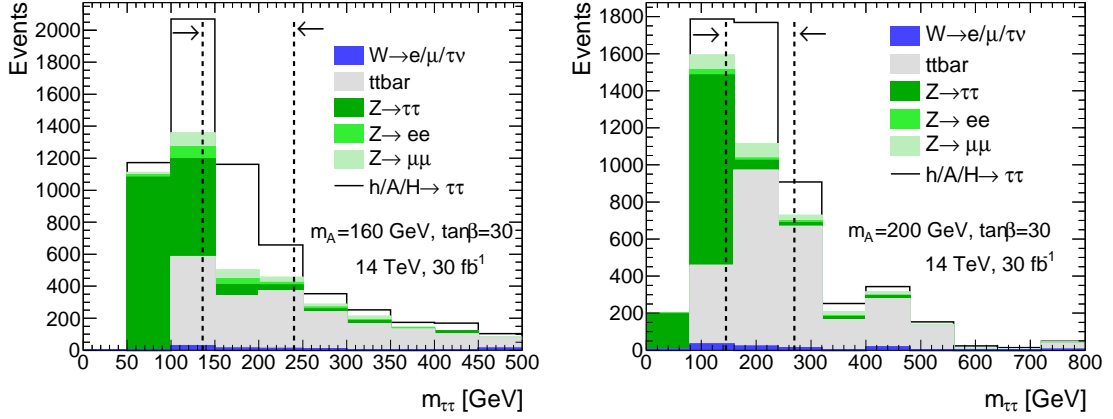


Figure 8.15.: Final $m_{\tau\tau}$ spectra, left for $m_A = 160$ GeV and right for $m_A = 200$ GeV. The mass window cut is indicated. The signal cross section corresponds to $\tan\beta = 30$ in the m_h^{\max} scenario.

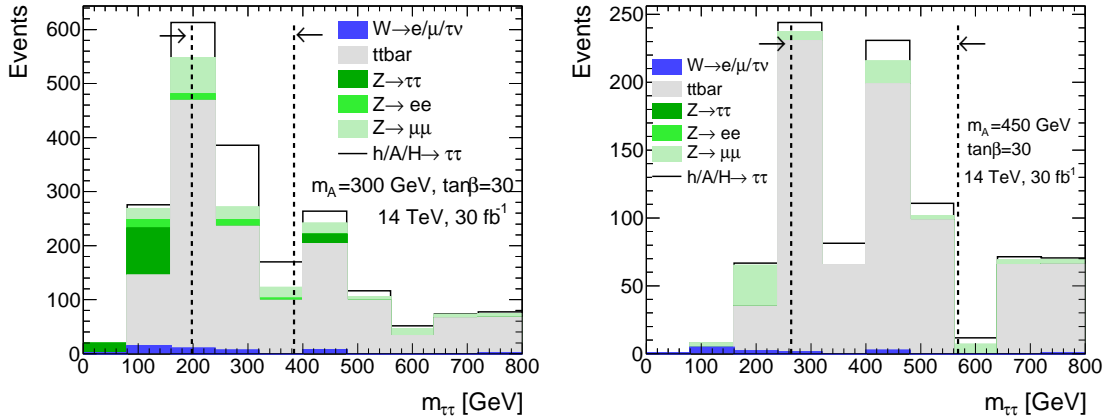


Figure 8.16.: Final $m_{\tau\tau}$ spectra, left for $m_A = 300$ GeV and right for $m_A = 450$ GeV. The mass window cut is indicated. The signal cross section corresponds to $\tan\beta = 30$ in the m_h^{\max} scenario.

The numbers of events for signal and the individual background processes passing the final mass window cut are listed in Table 8.14 for an integrated luminosity of 30 fb^{-1} and a signal cross section hypothesis corresponding to $\tan\beta = 30$.

It was tested how the statistical significance improves when the events passing the collinear mass window cut are combined with the events which fail the x_1 and x_2 cuts. For the latter case the visible mass was reconstructed instead. The visible mass for the case when the collinear mass reconstruction fails are illustrated for all six mass hypotheses in Figure 8.17. No mass window cut is applied in case the visible mass is reconstructed, since the background peaks well below the signal and the background shape resembles the signal shape.

The values of the statistical significance are listed in Table 8.15. In this table the statistical signifi-

Process	110 GeV	130 GeV	160 GeV	200 GeV	300 GeV	450 GeV
Signal	1746	1890	1083	864	203	47
$Z \rightarrow \tau\tau$	1479	644	191	122	0	0
ttbar	197	459	950	1245	524	459
$Z \rightarrow \ell\ell$	346	333	162	152	90	24
$W \rightarrow e/\mu/\tau\nu$	27	30	28	31	12	3

Table 8.14.: Numbers of events in 30 fb^{-1} after all selection cuts and the $m_{\tau\tau}$ window cuts have been applied. The signal prediction is given for $\tan\beta = 30$.

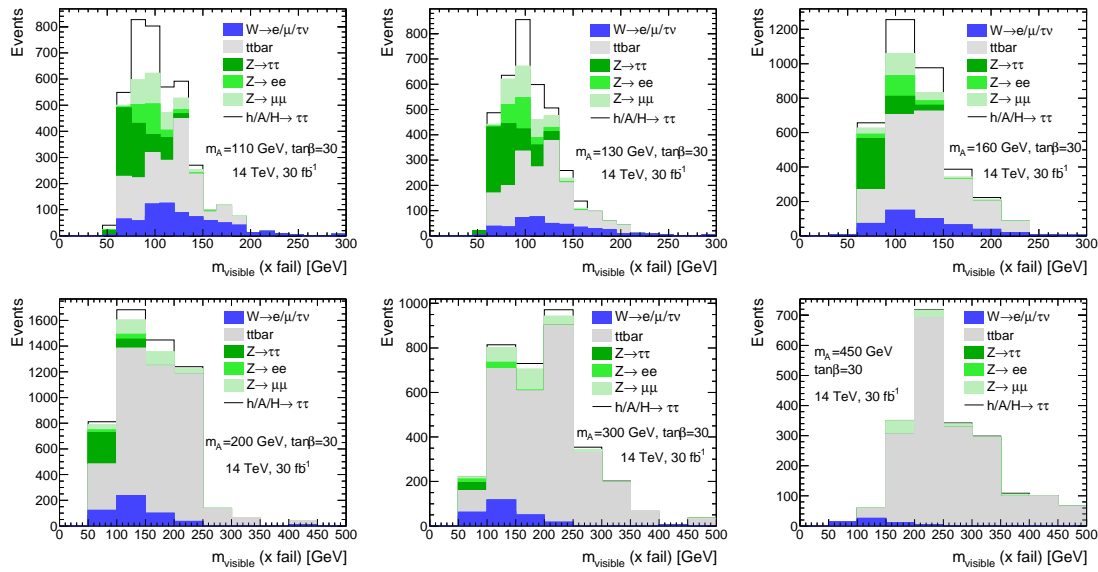


Figure 8.17.: The visible mass distributions for the events which fail the collinear approximation cuts on x_1 and x_2 .

cance of the collinear mass analysis is combined with the one from the events failing the collinear approximation. However, only a very small improvement of 3% or less is gained from this combination. Hence, for simplicity, the final discovery potential will be evaluated using only the events passing the collinear mass reconstruction.

The number of Higgs boson events in the final $m_{\tau\tau}$ mass window depends on the value of $\tan\beta$. In Figure 8.18 the signal yield is shown as a function of $\tan\beta$.

m_A [GeV]	$S_{m_{\tau\tau}}$	$B_{m_{\tau\tau}}$	$(S/\sqrt{B})_{m_{\tau\tau}}$	$(S/\sqrt{B})_{m_{\text{vis},x \text{ fail}}}$	$(S/\sqrt{B})_{\text{combined}}$
110	1746	2048	38.6	11.4	40.2
130	1890	1465	49.4	8.4	50.4
160	1083	1331	29.7	7.7	30.7
200	864	1550	22	3.0	22.2
300	203	626	8.1	1.5	8.2
450	47	485	2.11	0.37	2.14

Table 8.15.: Number of signal events S , background events B and statistical significance $(S/\sqrt{B})_{m_{\tau\tau}}$ if the collinear mass is reconstructed and the mass window cut is applied. The numbers are scaled to $\tan\beta = 30$ and 30 fb^{-1} at $\sqrt{s} = 14 \text{ TeV}$. The statistical significance for the events where the collinear mass reconstruction fails, $(S/\sqrt{B})_{m_{\text{vis},x \text{ fail}}}$, is also given and then combined with the significance from the events passing the collinear mass reconstruction, $(S/\sqrt{B})_{\text{combined}}$.

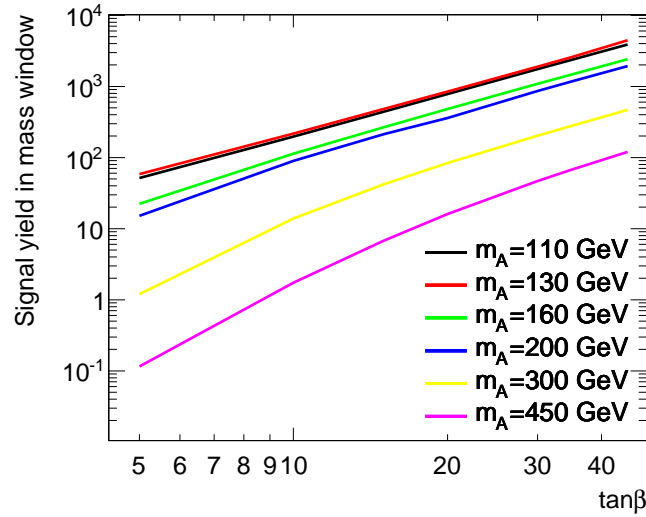


Figure 8.18.: Signal contribution to the event yield in the final mass window in 30 fb^{-1} as a function of $\tan\beta$.

With two remarks this subsection is closed. Firstly, the statistical significance was studied as a function of the $\Delta\Phi_{\ell\ell}$ cut. As discussed in Chapter 7, in similar studies the necessity of an upper cut was assumed, otherwise the collinear mass reconstruction would fail and the discovery potential would be underestimated. In Figure 8.19 the statistical significance is illustrated as a function of the upper cut on $\Delta\Phi_{\ell\ell}$ for two Higgs boson mass hypotheses when the mass window cut is applied or when a very loose window cut ($0 \text{ GeV} < m_{\tau\tau} < 500 \text{ GeV}$) is applied instead. The best significance is gained if no cut is applied. When a mass window cut is imposed for the Higgs boson signal with $m_A \leq 130 \text{ GeV}$, the significance stays almost constant for $\pi < \Delta\Phi_{\ell\ell} \leq 2.7$. For larger Higgs boson masses the significance decreases rapidly when applying a cut on $\Delta\Phi_{\ell\ell}$.

Secondly, the final $m_{\tau\tau}$ distribution for $m_A = 130$ GeV is illustrated once again but for two very different values of $\tan\beta$ in Figure 8.20. In the case when $\tan\beta = 10$, a discovery will be very difficult since no mass peak can be extracted but the signal events accumulate on the high mass tail of the Z peak. If systematic uncertainties are not controlled extremely well, a discovery cannot be claimed. In the case when $\tan\beta = 45$, a potential Higgs boson signal is hard to miss, again depending on the systematic uncertainties of the backgrounds. But even if there are large uncertainties on the signal cross section, the SM background-only hypothesis can be excluded easily in such a case.

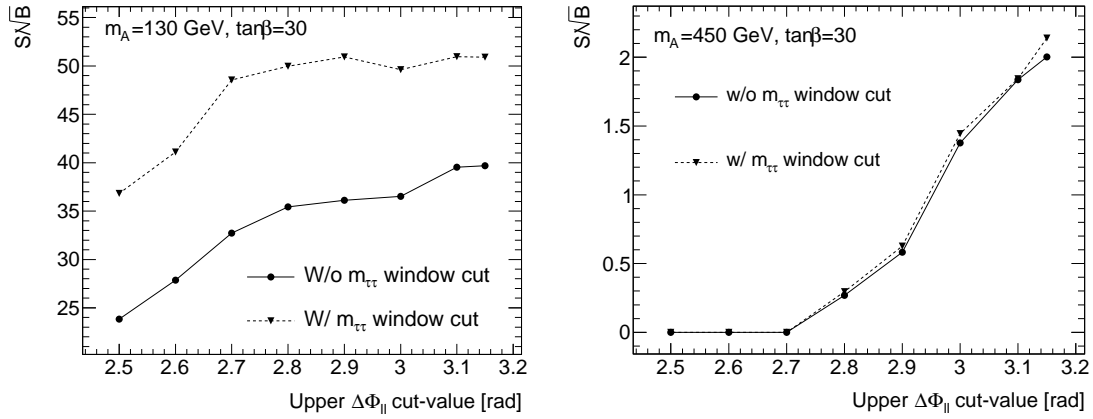


Figure 8.19.: The statistical significance as a function of an upper $\Delta\Phi$ cut between the two leptons for $m_A = 130$ GeV (left) and $m_A = 450$ GeV (right). The solid line shows the results if no mass window cut is applied, the dashed line illustrates the significance when counting events within the mass window. An upper cut on $\Delta\Phi_{\ell\ell}$ was not applied in this analysis, as it would not increase the discovery potential.

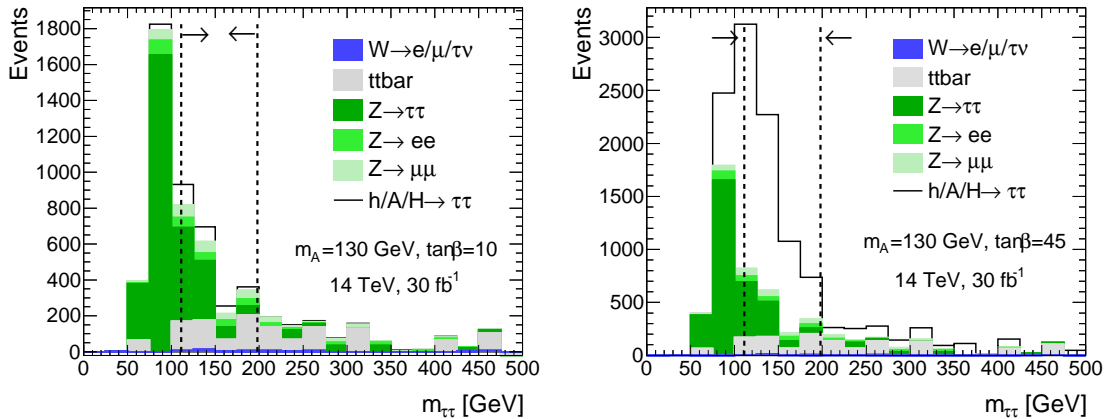


Figure 8.20.: The $m_{\tau\tau}$ distribution for $m_A = 130$ GeV, left for $\tan\beta = 10$ and right for $\tan\beta = 45$. The integrated luminosity assumed is 30 fb^{-1} . The plots visualize that a potential discovery is strongly dependent on the value of $\tan\beta$ realized in nature.

8.2. Systematic Uncertainties

The evaluation of the systematic uncertainties is the most important aspect of the analysis. Only if the background prediction is known with a large enough accuracy, a potential signal can be discovered or excluded with a large confidence level. If the background uncertainty is larger than a potential signal event yield, no discovery or exclusion is possible.

One source of uncertainties are simple statistical fluctuations. If the number of events N is large, the statistical uncertainty is \sqrt{N} . If more events are measured, the relative statistical uncertainty becomes smaller. Another source of uncertainty are systematic effects, which are due to limited detector resolutions or stem from differences between the MC simulation and the measurements. To reduce systematic uncertainties it is most useful to compare the observations in a potential signal region to the measurements in signal free control regions, hence to reduce the predictions made purely from the MC simulation.

In this section at first sources of systematic uncertainties are listed and their impact on the analysis is discussed. Then, a data-driven approach for the prediction of the $Z \rightarrow \tau\tau$ background in the Higgs boson signal region is presented.

8.2.1. Detector Related Uncertainties

In the following all detector related systematic uncertainties are listed. These expected uncertainties have been commonly used in [19] and were evaluated based on results from combined test-beam studies [77–79] and from [113]. They will also be called experimental uncertainties in the following to distinguish them from the theoretical uncertainties.

- Muons:
 - p_T scale: $\pm 1\%$,
 - p_T resolution: $\sigma\left(\frac{1}{p_T}\right) = \frac{0.011}{p_T} \oplus 0.00017$ (p_T in GeV),
 - Reconstruction efficiency: $\pm 1\%$.
- Electrons:
 - E_T scale: $\pm 0.5\%$,
 - E_T resolution: $\sigma(E_T) = 0.0073 \cdot E_T$,
 - Reconstruction efficiency: $\pm 0.2\%$.
- Jets:
 - E scale: $\pm 3\%$ ($|\eta| < 3.2$), $\pm 10\%$ ($|\eta| > 3.2$),
 - E_T resolution: $\sigma(E_T) = 0.45$ (0.63) $\cdot E_T$, for $|\eta| < 3.2$ ($|\eta| > 3.2$).
- Flavor tagging:
 - B-tagging efficiency: $\pm 5\%$,
 - Light jet rejection rate: $\pm 10\%$.
- Luminosity: $\pm 3\%$.

The variations are applied separately, one-by-one, on analysis level and the impact on the event selection is evaluated. For example, the jet energy scale (JES) uncertainty was applied by looping over all jets and scaling their energy with the corresponding larger or smaller factor. The resolution variations are applied by generating a Gaussian distribution around the mean of the initial p_T value and the width σ according to the smearing coefficients given above. The new p_T value is then probabilistically obtained from this Gaussian distribution. The reconstructed momentum values are effectively already smeared by the simulation, this resolution variation has to be understood as an additional smearing. The efficiency variations to lower values are applied by randomly removing the correct fraction of final state objects. The impact of an increased efficiency cannot be easily evaluated but is assumed to be of the same size as the down variation. The light-jet rejection variation is applied by shifting the IP3D+SV1 b-tagging weight such that the rejection rate is changed to 80% or 60% of its original value, keeping in mind that the rejection rate was decreased to 70% for the default analysis. The weight corrections are listed in Appendix B. For each scale and resolution variation, the uncertainty was propagated to the MET as follows:

$$\text{MET}^{\text{varied}} = \text{MET}^{\text{default}} - F \cdot (p_T^{\text{varied}} - p_T^{\text{default}}). \quad (8.3)$$

Usually, the factor F is 100%. In the case of the JES up and down variations, only 5% difference between the default and varied jet energy was propagated to the MET. This was used for both the SM and MSSM $H \rightarrow \tau\tau$ analysis in [19]. This is motivated by the fact that the MET calibration used with a well-understood detector will only be very weakly correlated to the JES.

Other sources for experimental uncertainties are the presence of pile-up and non-collision backgrounds (cavern background, cosmics, beam halo). Those effects have not been considered due to the unavailability of special MC samples.

8.2.2. Theory Related Uncertainties

Theoretical uncertainties are:

- PDF uncertainties,
- Scale uncertainties (especially renormalization and factorization scale),
- Phenomenological uncertainties (eg. parton shower description, soft QCD modeling).

These effects will result in cross section uncertainties, either integrated or differentially. The integrated cross section uncertainties have already been listed in Chapter 5.

The impact of the cross section uncertainties on the discovery potential will be evaluated separately, because in future these uncertainties might be strongly reduced by improved calculations or cross section measurements provided by the physics working groups.

8.2.3. Systematic Uncertainties of $t\bar{t}$

The variations were applied to the $t\bar{t}$ FULLSIM sample and the impacts on the event yield after the baseline selection is summarized in Table 8.16. Since the baseline selection by definition is the same for all Higgs boson mass hypotheses, the uncertainties obtained are also independent of m_A . The events passing the baseline selection are already very signal-like, further uncertainties arising from the optimized cuts should be small.

The baseline cuts are used, not the optimized cuts, in order to avoid the statistical contribution to the remaining uncertainties. It has been noticed in many other MC studies, eg. in [19], that the systematics are dominated by artificial statistical effects due to the limited size of the MC samples. Looser cuts assure that the remaining uncertainties are reasonable and therefore in agreement with [114], where it is stated that systematic uncertainties due to random variations or small shifts should not be large and if they are large they simply result from limited statistics of the MC samples.

The total experimental uncertainty is 4.8%. It was calculated from the sum of the squares of the single uncertainties assuming no correlations. In case of asymmetric up- and down- variations the larger uncertainty was used. The dominant experimental uncertainty on $t\bar{t}$ is the b-tagging efficiency with 3.7%. However, it is still small compared to the theoretical uncertainty of 12%. In the published analysis, the experimental $t\bar{t}$ uncertainties were evaluated after all cuts but using

Variation	Impact [%]
Electron Efficiency	0
Electron p_T Scale up	0.2
Electron p_T Scale down	0
Electron p_T Resol	-0.1
Muon Efficiency	-0.8
Muon p_T Scale up	0.2
Muon p_T Scale down	-0.1
Muon p_T Resol	0.1
JES up	0.2
JES down	-0.1
Jet Resolution	0.1
B-tagging Efficiency	-3.7
Light Jet Rej up	-0.1
Light Jet Rej down	0.2
Luminosity	3
Total exp. uncertainty	4.8
Theory uncertainty	12
Total uncertainty	12.9

Table 8.16.: Experimental and theoretical systematics for the $t\bar{t}$ background. The numbers are given in percent and denote the relative change of the number of events compared to the number of events when no variation is applied.

approximately 50 M ATLFast-I events. The results are comparable to the results in this thesis, total experimental uncertainties on $t\bar{t}$ vary around 5% depending on the m_A hypothesis, except for 7.4% at $m_A = 110$ GeV where the $t\bar{t}$ statistics is the smallest.

8.2.4. Data-Driven $Z \rightarrow \tau\tau$ Background Estimation

Motivation and Description of the Method

For A boson masses of less than 160 GeV, the $Z \rightarrow \tau\tau$ background is the dominant background. The $Z \rightarrow \tau\tau$ events pose an irreducible source of background accumulating at similar values of $m_{\tau\tau}$ as for the Higgs boson signal events. If the shape and yield of this background was known with a high accuracy, it could simply be subtracted from the final mass spectrum. However, this background cannot be selected without a signal contribution, especially in the case of a large $\tan\beta$. Instead, a method to estimate the shape of the $Z \rightarrow \tau\tau \rightarrow \mu\mu + 4\nu$ background from $Z \rightarrow \mu\mu$ (data) events was studied. This method was originally investigated for the SM $H \rightarrow \tau\tau$ analysis in [115] and applied to the MSSM $h/A/H \rightarrow \tau\tau$ channel in [19] for the first time.

The method is based on the idea, that a $Z \rightarrow \mu\mu$ (data) event is very similar to a $Z \rightarrow \tau\tau \rightarrow \mu\mu + 4\nu$ (data) event. For example, the kinematics and the number of accompanying jets are the same for both processes. The two muons will result in similar signals in the muon spectrometer. Since muons are minimal ionizing particles, the energy deposited in the calorimeter is small and only weakly dependent on the muon momentum, and no shower is developing for muons with $p_\mu \lesssim 200$ GeV. Figure 8.21 shows the MET_{calo} term (denotes as $\cancel{E}_T^{\text{calo}}$ in Section 6.5.2) for $Z \rightarrow \ell\ell$ and $Z \rightarrow \tau\tau \rightarrow \ell\ell + 4\nu$ events in the ee and $\mu\mu$ channel. Based on these considerations, the only remaining difference between $Z \rightarrow \mu\mu$ and $Z \rightarrow \tau\tau$ is the muon kinematics, which is well understood by former experiments at LEP and also very well modeled in the MC.

The first step of the data-driven $Z \rightarrow \tau\tau$ estimation is to select $Z \rightarrow \mu\mu$ (data) events. Then, the kinematics of the muons from the $Z \rightarrow \mu\mu$ (data) events is altered according to that expected in $Z \rightarrow \tau\tau \rightarrow \mu\mu + 4\nu$ reference histograms. The MET is recalculated to account for the different muon p_T values. Finally, the same cuts as for the Higgs boson analysis are applied and the shapes of the original and modeled $Z \rightarrow \tau\tau \rightarrow \mu\mu + 4\nu$ events are compared.

Furthermore, a method to estimate the number of $Z \rightarrow \tau\tau \rightarrow \ell\ell + 4\nu$ events in the signal region is investigated. Therefore $Z \rightarrow ee$ and $Z \rightarrow \mu\mu$ events are used from the control region, too. The method will be described in detail below.

$Z \rightarrow \ell\ell$ Control Region Selection

$Z \rightarrow \ell\ell$, $l = (e, \mu)$ events can be selected with high purity and large statistics by applying a few simple cuts. The following cuts apply to both the selection for $Z \rightarrow ee$ and $Z \rightarrow \mu\mu$. While for obtaining the $Z \rightarrow \tau\tau$ shape only the $\mu\mu$ channel is relevant, for the normalization also the ee channel is necessary. The control region cuts are the following:

- Trigger:
The following trigger items are used to select the control region: mu20, e25i, 2e15i. As was done in the main analysis, the trigger is realized by imposing p_T cuts.
- At least one b-tag:
This requirement strongly reduces the Z +light-jet contribution and therefore the event yield in the control region. However, the cut is applied to avoid a bias since in the signal regions this cut is needed.
- Less than three jets with $p_T > 15$ GeV:
As in the signal region, this cut reduces mainly the $t\bar{t}$ background contribution.

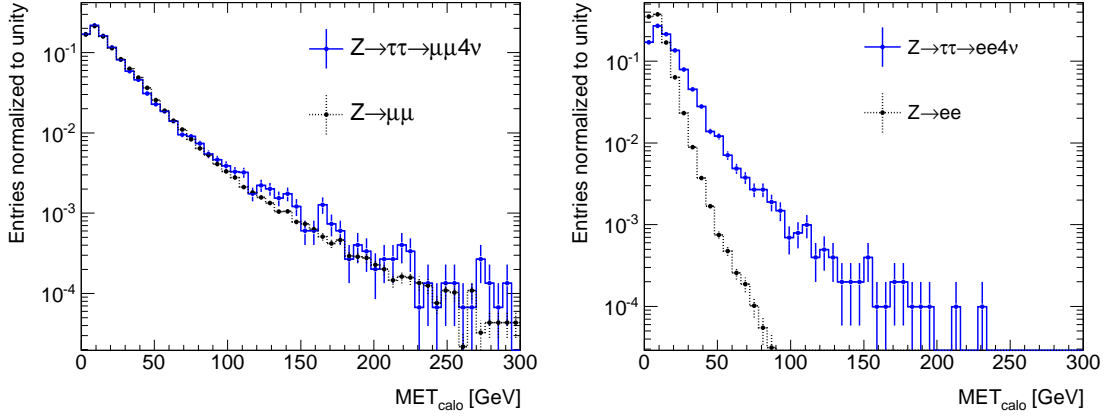


Figure 8.21.: The MET contribution from the calorimeter for the $\mu\mu$ channel (left) and ee channel (right), normalized to unity. The dotted black line shows the distribution for the prompt muons (electrons), the solid blue line illustrates the values for the muons (electrons) from the tau decay. In the muonic case the MET_{calo} distributions are very similar, while in the ee channel a clear difference is visible.

- Two isolated leptons with opposite charges and $p_T > 15$ GeV.
- $100 \text{ GeV} > m_{\ell\ell} > 80 \text{ GeV}$:
This is the key cut to select the $Z \rightarrow \ell\ell$ events. From previous experiments, the mass of the Z boson is well known and the resolution of the resonance in the detector is very good (the Gaussian width is less than 4 GeV) so that a clear peak is visible in the mass spectra of the data³.
- $E_{T,\text{miss}} < 25 \text{ GeV}$:
This cut is applied in order to suppress the $t\bar{t}$ background, $Z \rightarrow \tau\tau$ and Higgs boson events, since these processes contain true MET.

The distributions of the MET and $m_{\ell\ell}$ are illustrated in Figure 8.22, for the $\mu\mu$ channel only.

Purity and Event Yield of the Control Region

The purity of the $Z \rightarrow \ell\ell$ selection was determined for both the ee and $\mu\mu$ channel and is listed in Table 8.17. To obtain numbers for the W +jets and QCD backgrounds, the following cuts are factorized: The efficiency for the b-tagging and the jet multiplicity requirement is obtained independent from the other cuts. In addition, similar to the signal region, for the QCD events the lepton isolation is applied as a weight.

The event yields in the control regions as a function of the integrated luminosity and for different center-of-mass energies are illustrated in Figure 8.23. It should be noted, that approximately a factor 40 can be gained when dropping the b-tagging requirement. The $Z \rightarrow \ell\ell$ cross section for 10 TeV used here is $\sigma(10 \text{ TeV}) = 1422 \text{ pb}$, and for 7 TeV it is $\sigma(7 \text{ TeV}) = 954 \text{ pb}$. The Z boson

³First data results confirm this, the observation of Z bosons in the ATLAS detector at 3.5 TeV beam energy is for example described in [116].

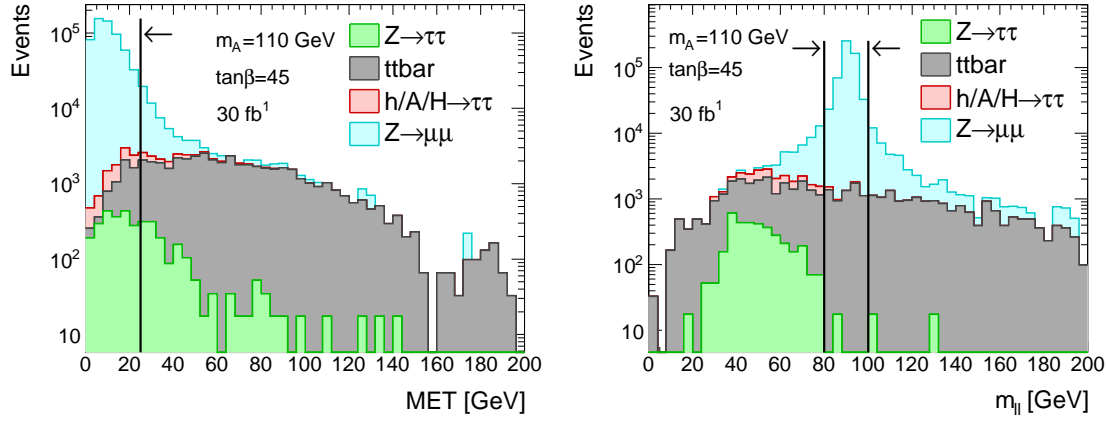


Figure 8.22.: The distributions of MET (left) and $m_{\ell\ell}$ (right) for the relevant processes for the $\mu\mu$ channel. The histograms are normalized to 30 fb^{-1} at $\sqrt{s} = 14 \text{ TeV}$, the cuts are indicated. A Higgs boson hypothesis of $m_A = 110 \text{ GeV}$ and $\tan\beta = 45$ is assumed. The plots were prepared after the control region cuts are applied except for the cuts on $m_{\ell\ell}$ and MET.

Process	ee channel	$\mu\mu$ channel
$Z \rightarrow ee$	419 030	0
$Z \rightarrow \mu\mu$	0	505 426
$h/A/H (110 \text{ GeV})$	146	219
$t\bar{t}$	459	426
$Z \rightarrow \tau\tau$	87	17
$W \rightarrow e\nu$	34.4	≈ 0
$W \rightarrow \mu\nu$	1.8	1.4
$W \rightarrow \tau\nu$	2.9	3.8
QCD J2	≈ 0	5.6
QCD J3	≈ 0	< 1
QCD J4	< 1	< 1
QCD J5	≈ 0	< 1
QCD J6	< 1	< 1
Purity [%]	99.8	99.9

Table 8.17.: Number of events in the $Z \rightarrow \ell\ell$ control regions normalized to 30 fb^{-1} . The signal contribution was evaluated for $m_A = 110 \text{ GeV}$ and $\tan\beta = 45$ at $\sqrt{s} = 14 \text{ TeV}$. The purity is stated in the last line. Where ' ≈ 0 ' is given, the available MC statistics were too small and the event number could not be evaluated.

production cross sections as a function of \sqrt{s} can be found for example in Ref. [117]. In the published analysis also a cut on the p_T of the leading b-jet was imposed to select the control

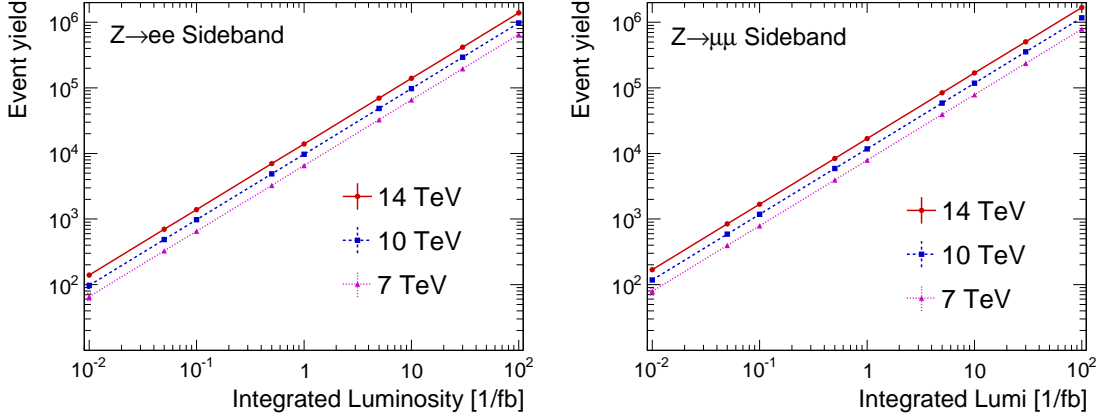


Figure 8.23.: The event yield in the $Z \rightarrow ee$ (left) and $Z \rightarrow \mu\mu$ control regions (right) as function of the integrated luminosity for three different center-of-mass energies. Statistical uncertainties are small and therefore not visible.

region. This cut was dropped in this thesis to avoid this unnecessary bias between the signal and control regions. The purity is not affected by dropping this cut and the efficiency is larger by 10%. The results here will be discussed after the baseline selection is applied, which does not include a cut on the p_T of the leading b-jet except for the p_T threshold for all jets of $p_T > 15$ GeV.

Estimation of the $Z \rightarrow \tau\tau \rightarrow \mu\mu + 4\nu$ Shape

To estimate the $m_{\tau\tau}$ shape of the $Z \rightarrow \tau\tau \rightarrow \mu\mu + 4\nu$ events, the first step is to fill 3-dimensional reference histograms. These histograms contain the energies of the two muons versus the angle between the negatively charged true τ in the Z rest frame and the direction of the Z boson. This angle is called the Gottfried-Jackson angle⁴, ζ [118]. The reference histogram is filled with MC events. To gain statistics a dedicated $Z \rightarrow \tau\tau$ sample with a two-muon filter was used (DS 9061). No further cuts except for the generator cuts are applied to the reference sample. The reference histogram is used to adapt the muon kinematics from the $Z \rightarrow \mu\mu$ events. To reduce computing time the 3-dimensional histogram is separated into five 2-dimensional slices of the cosine of the Gottfried-Jackson angle. Five bins have been proven to be adequate in previous studies. Figure 8.24 illustrates the 3D and one of the 2D reference histograms.

For each $Z \rightarrow \mu\mu$ event the two muons are boosted into the Z rest frame and the Gottfried-Jackson angle is calculated, this time from the negatively charged muon in the Z rest frame and the direction of the Z boson. The new muon energies of the $Z \rightarrow \mu\mu$ events are probabilistically obtained from the corresponding 2D reference histogram of $Z \rightarrow \tau\tau \rightarrow \mu\mu + 4\nu$ decays. The values obtained are distributed according to the energies in the reference process. The new momentum components of the muons from the $Z \rightarrow \mu\mu$ process, p_i^{new} , are calculated from the new energies as follows:

$$p_i^{\text{new}} = E^{\text{new}} \cdot \frac{p_i}{|\vec{p}|}. \quad (8.4)$$

⁴The Gottfried-Jackson angle (sometimes also called Jackson angle) was first introduced in the 1960s in the measurement of kaon and proton scattering processes.

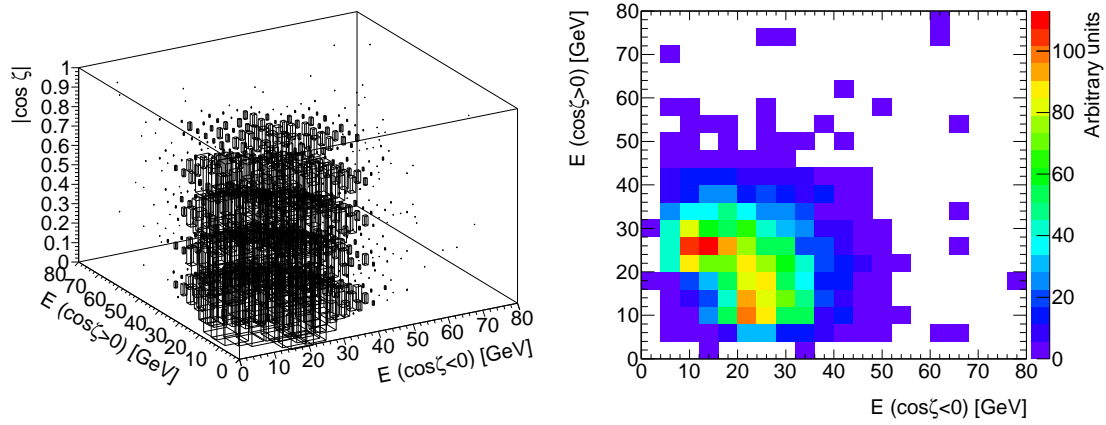


Figure 8.24.: The reference histogram filled with $Z \rightarrow \tau\tau \rightarrow \mu\mu + 4\nu$ MC events. Left: The complete 3-dimensional reference histogram. Right: One of the five 2-dimensional reference histograms, here for absolute values of the cosine of the Gottfried-Jackson angle ζ between 0.2 and 0.4.

Finally, the MET needs to be corrected. Since no shower develops from muons below $p_\mu \lesssim 200$ GeV, this is rather simple. The idea is to bring the MET back to balance by removing the former muon $p_{x,y}$ values and replacing them with the new $p_{x,y}$ values:

$$\begin{aligned} p_{x,\text{miss}}^{\text{new}} &= p_{x,\text{miss}} - p_x^{\text{new}} + p_x, \\ p_{y,\text{miss}}^{\text{new}} &= p_{y,\text{miss}} - p_y^{\text{new}} + p_y. \end{aligned} \quad (8.5)$$

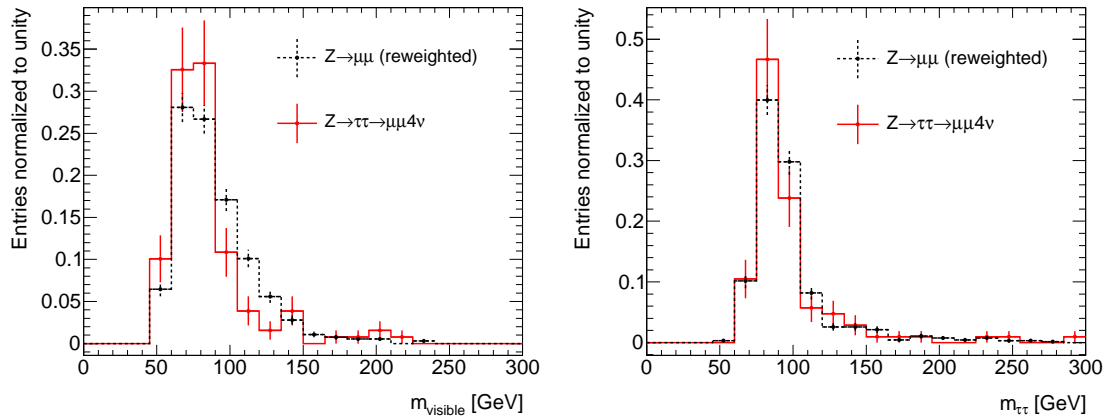


Figure 8.25.: Comparison of the visible mass (left) and collinear mass (right) between the $Z \rightarrow \tau\tau \rightarrow \mu\mu + 4\nu$ events (solid red line) and the reweighted $Z \rightarrow \mu\mu$ events (black dotted line). The error bars reflect the true MC statistics. The statistical uncertainties are large because for both processes the b-tagging requirement was applied. All distributions are normalized to unity.

With the recalculation of the MET the manipulation procedure is done. Now the same cuts, namely the baseline selection cuts, are applied to the altered $Z \rightarrow \mu\mu$ events and the events from the reference process and then the shapes are compared. Figure 8.25 presents the comparison of the shapes of the $m_{\tau\tau}$ and the m_{vis} distributions after the baseline selection. The result is not optimal, the m_{vis} distribution shows a few significant differences.

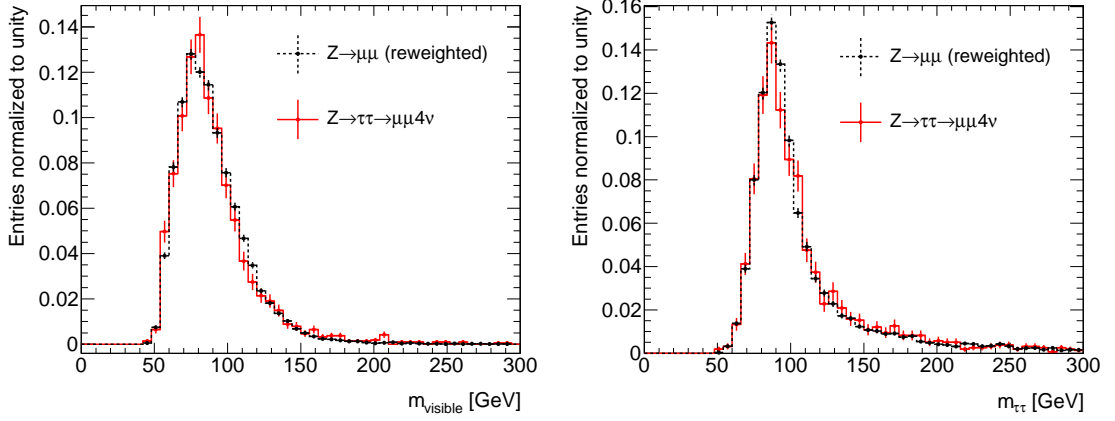


Figure 8.26.: The visible mass (left) and the collinear mass (right) without the b-tagging requirement.

To test the accuracy of the method using more statistics, for the following comparisons the b-tagging requirement was dropped for both the control region and the reference events. The collinear and visible mass distributions are compared in Figure 8.26. The resemblance is much better than the the comparison with the b-tagging requirement applied (Fig. 8.25). The disagreements in Figure 8.25 are therefore understood to be due to statistical limitations only.

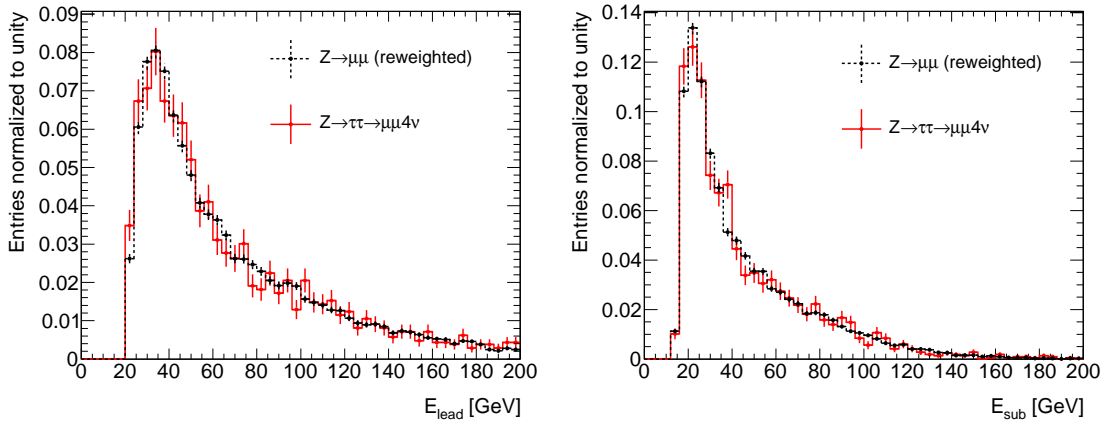


Figure 8.27.: The energies of the leading lepton (left) and sub-leading lepton (right). The b-tagging requirement was not applied to gain statistics. The error bars reflect the MC statistics, all distributions are normalized to unity.

Furthermore, any variable entering either the collinear mass reconstruction or the selection is compared. Figure 8.27 shows the energy of the muons, Figure 8.28 shows the x, y and z components of the two muon momenta. For all these distributions a very good agreement is visible.

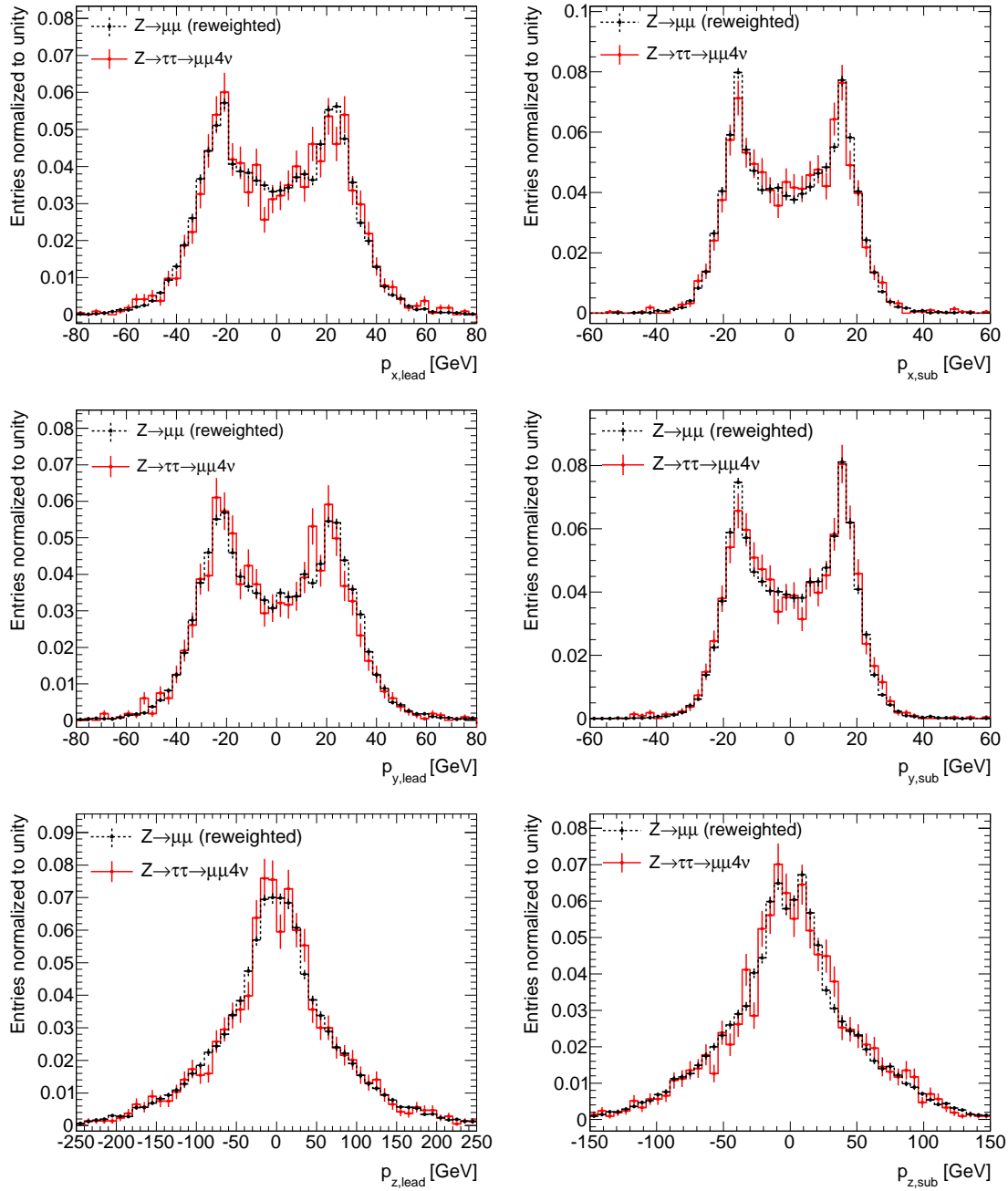


Figure 8.28.: The x, y and z components of the momentum for the leading lepton (left) and sub-leading lepton (right). The error bars reflect the MC statistics, all distributions are normalized to unity. No b-tag is required.

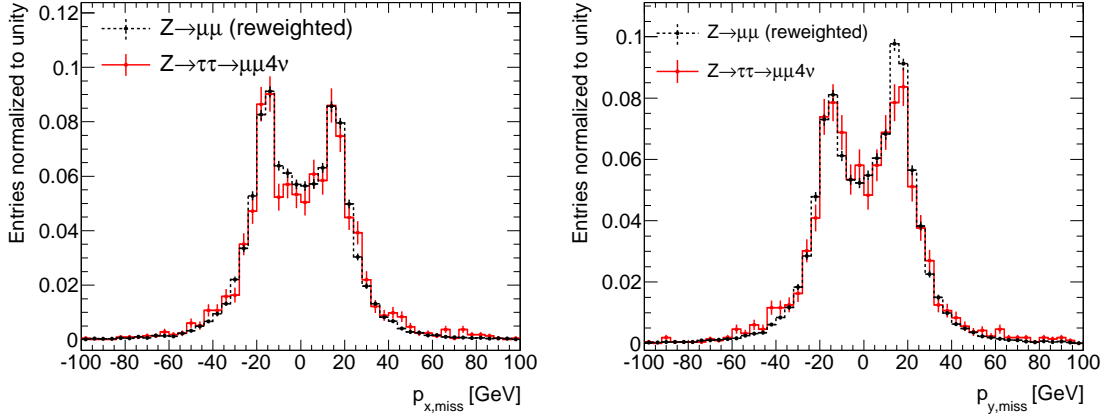


Figure 8.29.: The x component (left) and y component (right) of the MET. A good resemblance is observed. The error bars reflect the MC statistics, all distributions are normalized to unity. No b-tag is required.

Figure 8.29 compares the x and y components of the MET. Again, a very nice agreement between the shapes of the altered events from the control region and the events from the reference process is found. Figure 8.30 displays the comparison for the MET and the $\Delta\Phi_{\ell\ell}$. Here slight disagreements are visible. The components which enter into these observables do not show such deviations.

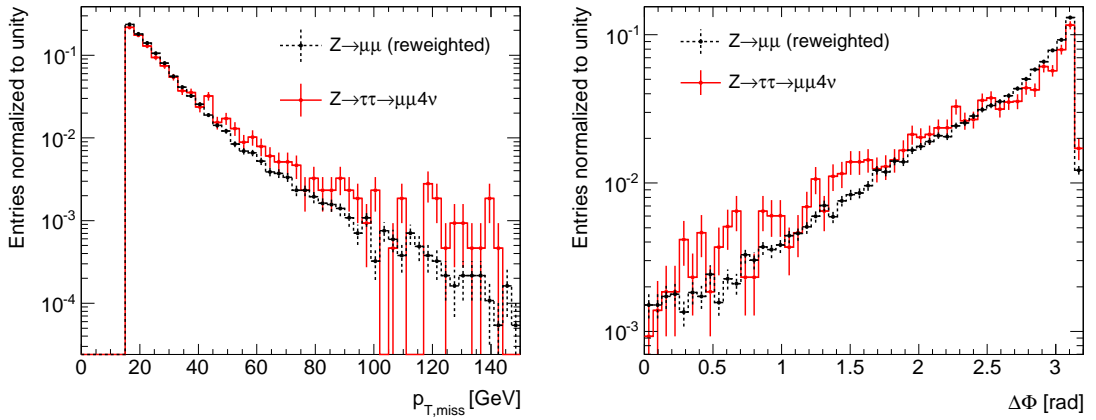


Figure 8.30.: The MET (left) and the $\Delta\Phi$ between the two leptons (right). These two distributions show some disagreements between the altered events from the control region and the reference events. The error bars reflect the MC statistics, all distributions are normalized to unity. No b-tag is required.

Discussion of the ee and $e\mu$ Channels

The shape estimation based on this rather simple momentum rescaling only gives reasonable results for the $Z \rightarrow \tau\tau \rightarrow \mu\mu + 4\nu$ channel. However, within the statistical uncertainties the $m_{\tau\tau}$ shape of the ee and $e\mu$ final states does not differ from the shape in the $\mu\mu$ channel, which is illustrated in Figure 8.31.

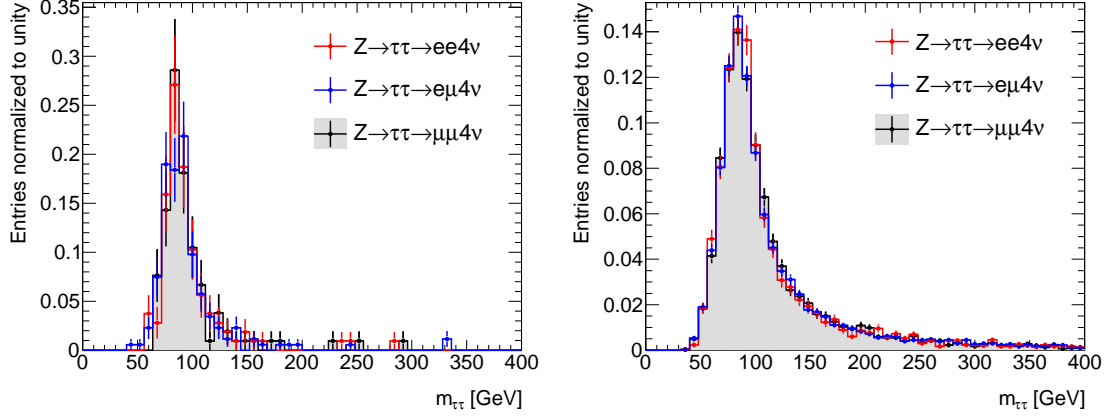


Figure 8.31.: The shape of the $m_{\tau\tau}$ distributions in the three sub-channels normalized to unity. In the left plot all baseline selection cuts except for the mass window cut are applied. In the right plot the b-tagging requirement was dropped to gain statistics. A good agreement between the different shapes is visible. The error bars show the statistical uncertainty of the MC samples used.

Data-driven methods are investigated to estimate the shape of the $Z \rightarrow \tau\tau \rightarrow ee + 4\nu$ background. In [119] the energy deposits from the electrons in $Z \rightarrow ee$ (real data) events are reweighted according to $Z \rightarrow \tau\tau \rightarrow \mu\mu + 4\nu$ reference histograms. In [120] this method was improved by parameterizing the shower shapes of the energy deposits from the electrons. In [121] a method is described based on the selection of a control sample containing muons and the re-scaling of the muon momenta, after which the muons are treated as τ -leptons by the MC event record and are then later recombined with the original event. This method was also applied to the hadronic final states and the estimation of $t\bar{t}$. Another technique called *embedding* has been successfully developed during the last years [122]. Here the deposits from muons in (real) $Z \rightarrow \mu\mu$ events in the spectrometer, calorimeters and inner detector are removed in a cone around the muons and replaced by the corresponding deposits from simulated $Z \rightarrow \tau\tau$ events. Then the reconstruction algorithms run on the altered events to recalculate the MET. This method, however, relies on the availability of the next higher data format (ESD). The simpler method of kinematic event manipulation - which was applied in this thesis - does not require special MC samples and already yields quite reasonable results.

Estimation of the $Z \rightarrow \tau\tau \rightarrow \ell\ell + 4\nu$ Normalization

The method outlined above and all the other methods mentioned in the last subsection only estimate the shape of the $Z \rightarrow \tau\tau$ background, not its normalization. In the SM $q\bar{q}H \rightarrow q\bar{q}\tau\tau$ channel the width of the reconstructed Higgs boson mass is much smaller, hence the data itself can be used for the normalization by fitting the $Z \rightarrow \tau\tau$ background. In [123] the mass resolution is stated as being 12 GeV to 14 GeV for a SM Higgs boson with a mass between 105 GeV and 135 GeV. In the MSSM, in the b-associated production, the low A mass signal almost completely spreads over the Z peak (as was illustrated in Figures 8.14 and 8.15), which makes a fit rather difficult.

It is not proposed to measure the Z cross section, the goal is to reduce systematic uncertainties. In the optimized signal regions influences from detector-related systematics might be large. It is therefore proposed to select $Z \rightarrow ee$ and $Z \rightarrow \mu\mu$ events in a signal-free control region, to exploit a double-ratio (data to MC events, control region to signal region events) and then become independent of the dominant systematic uncertainties. The $Z \rightarrow \ell\ell$ production cross section is no longer needed as an input, hence the theoretical uncertainty is irrelevant. This method was firstly discussed in [108] and applied in the published analysis in [19].

The selection of the $Z \rightarrow \ell\ell$ control region was already discussed above in Section 8.2.4. This selection in particular also included the b-tag and the cut on the number of high- p_T jets. These cuts are identical in the signal region. Hence, if for example the JES is shifted upwards, more events will pass the selection in both control and signal region. Or, if the b-tagging efficiency is lower, less events will pass the selection in both kinematic regions. If such a systematic difference exists between data and MC samples, the following ratios will deviate from unity (# denotes the number):

$$\begin{aligned} \frac{\#(Z \rightarrow ee)^{\text{MC}}}{\#(Z \rightarrow ee)^{\text{Data}}} &, \quad \frac{\#(Z \rightarrow \tau\tau \rightarrow ee + 4\nu)^{\text{MC}}}{\#(Z \rightarrow \tau\tau \rightarrow ee + 4\nu)^{\text{Data}}}, \\ \frac{\#(Z \rightarrow \mu\mu)^{\text{MC}}}{\#(Z \rightarrow \mu\mu)^{\text{Data}}} &, \quad \frac{\#(Z \rightarrow \tau\tau \rightarrow \mu\mu + 4\nu)^{\text{MC}}}{\#(Z \rightarrow \tau\tau \rightarrow \mu\mu + 4\nu)^{\text{Data}}}. \end{aligned} \quad (8.6)$$

It is now assumed that the following relations (and the same relations for the $\mu\mu$ channel) hold:

$$\begin{aligned} \frac{\#(Z \rightarrow ee)^{\text{MC}}}{\#(Z \rightarrow ee)^{\text{Data}}} &= \frac{\#(Z \rightarrow \tau\tau \rightarrow ee + 4\nu)^{\text{MC}}}{\#(Z \rightarrow \tau\tau \rightarrow ee + 4\nu)^{\text{Data}}}, \\ \frac{\#(Z \rightarrow ee)^{\text{MC}}}{\#(Z \rightarrow \tau\tau \rightarrow ee + 4\nu)^{\text{MC}}} &= \frac{\#(Z \rightarrow ee)^{\text{Data}}}{\#(Z \rightarrow \tau\tau \rightarrow ee + 4\nu)^{\text{Data}}}. \end{aligned} \quad (8.7)$$

In particular, the following double ratio should be unity if the relations from Equation 8.7 hold:

$$\frac{\frac{\#(Z \rightarrow ee)^{\text{MC}}}{\#(Z \rightarrow \tau\tau \rightarrow ee + 4\nu)^{\text{MC}}}}{\frac{\#(Z \rightarrow \tau\tau \rightarrow ee + 4\nu)^{\text{Data}}}{\#(Z \rightarrow ee)^{\text{Data}}}} = 1. \quad (8.8)$$

The assumptions were tested on FULLSIM MC samples. When no systematic variations are applied (the 'default' is used), it corresponds to the 'DATA', and if systematic biases are simulated it is labeled as 'MC' in the equations and as 'systematics' in the plots. Another possibility of testing the method would be to divide the samples into sub-samples ('data' and 'MC'), however, then

a small statistical bias will be introduced in that way, because the number of events passing the selection will be different between both sub-samples due to statistical fluctuations. The relations from Equation 8.7 are illustrated in Figure 8.32 for the default sample and the jet-related systematics. Statistical uncertainties of the ratios are indicated. The ratios are indeed equal, which is trivial for the default setting but non-trivial for the variations applied. However, it must be noted that in this analysis the impacts from variations of the JES are very small, because they are almost uncorrelated to the MET scale (the correlation factor is assumed to be only 5%). It is found that when assuming a 100% correlation of JES and MET scales, the ratios are no longer equal. A few more details are given in Appendix D. Cuts related to the MET are not equal for the signal and control regions.

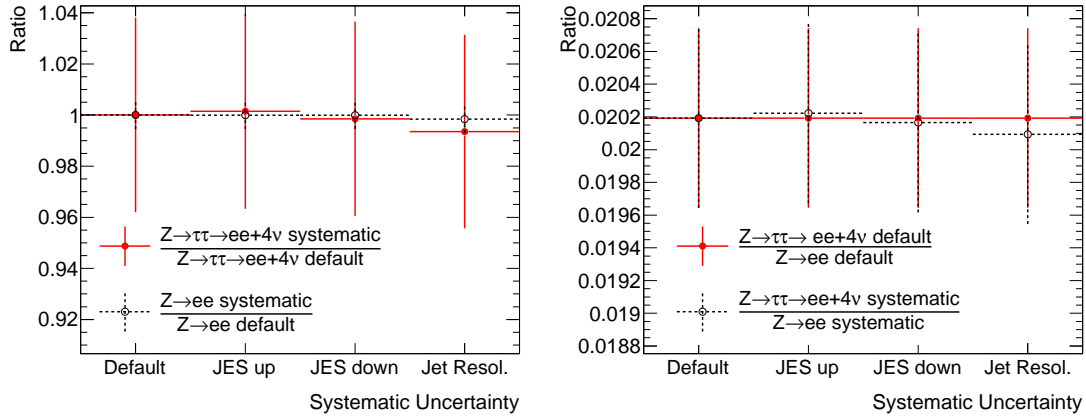


Figure 8.32.: The ratios for the default setting and the case when the jet variations are applied. On the $Z \rightarrow \ell\ell$ samples the control region cuts are applied, on the $Z \rightarrow \tau\tau$ sample the baseline selection is applied. The b-tagging requirement was dropped in all cases to gain statistics. The error bars reflect the statistical uncertainty from the available MC.

The double ratios (Equation 8.8) were calculated for all systematic variations and compared with each other. They are visualized in Figure 8.33. The statistical uncertainties are also marked. For the evaluation of the lepton and jet variations, the b-tagging requirement was dropped. It is obvious that the largest impact (relatively to the error bars) comes from the muon-related systematic variations (p_T scale and p_T resolution). The muon-related uncertainties were assumed to be more conservative than the corresponding uncertainties on electrons (see Section 8.2.1). The double-ratio for the JES and jet resolution variations are almost perfectly one. Considering the large statistical uncertainties, the same conclusion is made for the b-tagging related uncertainties. In Appendix D it is shown that the canceling of the impacts from variations of the b-tagging-related uncertainties hold even when increasing the variations.

The number of $Z \rightarrow \tau\tau$ events in MC, $\#(Z \rightarrow \tau\tau \rightarrow ee/\mu\mu + 4\nu)^{\text{MC}}$, is obtained by applying all signal region cuts and then scaling the number of MC events to 30 fb^{-1} . Using the relations from Equation 8.7, the corresponding number of $Z \rightarrow \tau\tau$ events in the signal region but now in real data, $\#(Z \rightarrow \tau\tau \rightarrow ee/\mu\mu + 4\nu)^{\text{Data}}$, can be calculated as follows:

$$\begin{aligned} \#(Z \rightarrow \tau\tau \rightarrow ee + 4\nu)^{\text{Data, signal}} &= \#(Z \rightarrow \tau\tau \rightarrow ee + 4\nu)^{\text{MC, signal}} \cdot \frac{\#(Z \rightarrow ee)^{\text{Data, control}}}{\#(Z \rightarrow ee)^{\text{MC, control}}}, \\ \#(Z \rightarrow \tau\tau \rightarrow \mu\mu + 4\nu)^{\text{Data, signal}} &= \#(Z \rightarrow \tau\tau \rightarrow \mu\mu + 4\nu)^{\text{MC, signal}} \cdot \frac{\#(Z \rightarrow \mu\mu)^{\text{Data, control}}}{\#(Z \rightarrow \mu\mu)^{\text{MC, control}}}. \end{aligned} \quad (8.9)$$

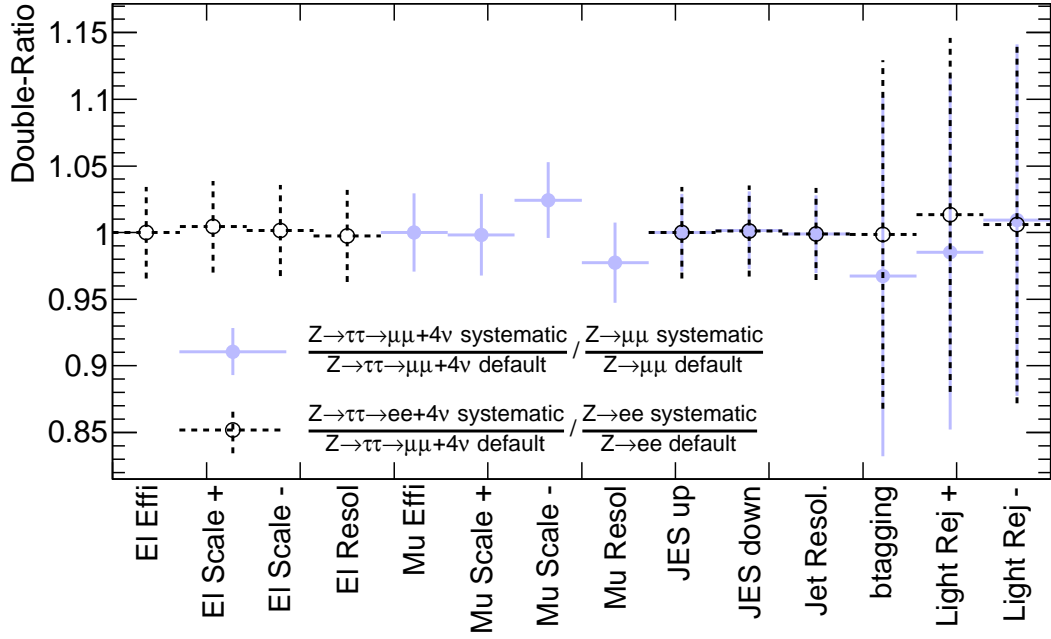


Figure 8.33.: Double-ratio for various systematic variations. The light blue (dotted black) lines mark the results from the $\mu\mu$ (ee) channel. The error bars reflect the real statistical uncertainties. They are larger for the flavor tagging related uncertainties because there the b-tagging requirement could not be dropped, as was done for the other systematic variations. Especially the double-ratios of the jet-related and b-tagging-related variations are consistent with unity which proves the uncertainty canceling.

The original idea of this method was to perform this calculation Equation 8.9 not by using all events passing the selection, but by calculating $\#(Z \rightarrow \tau\tau \rightarrow ee/\mu\mu + 4\nu)^{\text{Data, signal}}$ only for those events which have similar values of a variable which actually shows distinct differences between the $Z \rightarrow ee/\mu\mu$ and $Z \rightarrow \tau\tau \rightarrow ee/\mu\mu + 4\nu$ events, and then taking the sum of these bins. Particularly different are the p_T distributions of the two leptons. The prompt leptons from a $Z \rightarrow ee/\mu\mu$ decay show larger p_T values than the leptons from the tau decay in $Z \rightarrow \tau\tau \rightarrow ee/\mu\mu + 4\nu$. The idea is therefore to perform Equation 8.9 in 2-dimensional bins of the p_T of the leading lepton versus the p_T of the sub-leading lepton, which is given as follows for the ee channel:

$$\#(Z \rightarrow \tau\tau \rightarrow ee + 4\nu)^{\text{Data, signal}} = \sum_i \#(Z \rightarrow \tau\tau \rightarrow ee + 4\nu)_i^{\text{MC, signal}} \cdot \frac{\#(Z \rightarrow ee)_i^{\text{Data, control}}}{\#(Z \rightarrow ee)_i^{\text{MC, control}}}, \quad (8.10)$$

where i labels the index of the 2D bins. The calculation, however, will only yield correct results, if all the bins of the three involved samples are non-empty: In case $\#(Z \rightarrow \tau\tau \rightarrow ee/\mu\mu)_i^{\text{MC}}$ or $\#(Z \rightarrow ee/\mu\mu)_i^{\text{Data}}$ is zero, the number of events will be underestimated. In case $\#(Z \rightarrow ee/\mu\mu)_i^{\text{MC}}$ is zero Equation 8.10 cannot be evaluated and then zero is returned for that particular bin. The advantage of performing the calculation in each bin and summing the result is that variations of other relevant cut variables as a function of $p_{T,\ell}$ are correctly taken into account.

The 2-dimensional $p_{T,\ell}$ distributions used as input for Equation 8.10 are shown in Figure 8.34. The $Z \rightarrow ee/\mu\mu$ samples were each divided into 'Data' and 'MC' sub-samples of the same size,

the $Z \rightarrow \tau\tau$ sample was not divided, since this is not necessary. All baseline cuts are applied to the $Z \rightarrow \tau\tau$ sample, all control region cuts to the $Z \rightarrow \ell\ell$ samples.

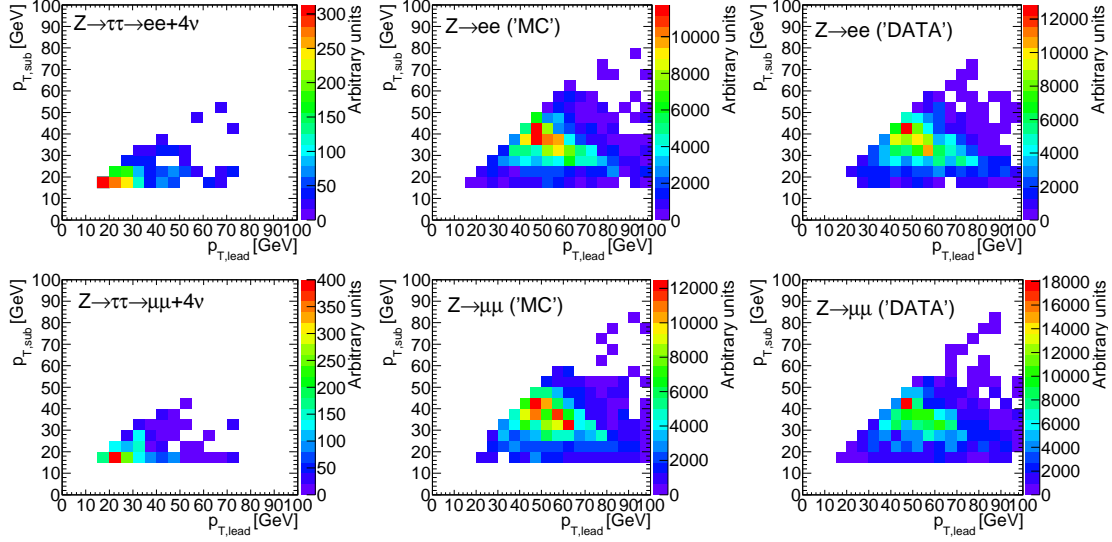


Figure 8.34.: The distribution of the p_T of the leading lepton vs. the p_T of the sub-leading lepton, upper (lower) row for the ee ($\mu\mu$) channel. The left plot shows the distribution for the $Z \rightarrow \tau\tau$ sample, the middle and right plots show the same for the $Z \rightarrow \ell\ell$ 'MC' and 'Data' samples, respectively. The distributions are normalized to 30 fb^{-1} .

The results of the estimation of the number of $Z \rightarrow \tau\tau \rightarrow \ell\ell + 4\nu$ events (Equation 8.10) are shown as a function of the binsize in Figure 8.35. A bias from empty bins is observed for small binsizes yielding in underestimation of the number of $Z \rightarrow \tau\tau \rightarrow \ell\ell + 4\nu$ events. This bias is the result of statistical limitations and does not reflect the limits of the normalization method. The number obtained by Equation 8.10 is therefore also compared to a *binned expectation*. The binned expectation is the sum of the number of $Z \rightarrow \tau\tau$ events in the $p_{T,\ell}$ bins, but only when all the terms from the right side of Equation 8.10 are non-zero. Only this value should be compared directly to the result from the binned normalization method. With a large enough binsize a plateau is visible (note the logarithmic scale of the abscissa), ie. the results from the binned calculation (and binned expectation) approach the number of $Z \rightarrow \tau\tau$ events as estimated from MC. The statistical uncertainty was evaluated by using Gaussian error propagation and taking into account the statistical uncertainties from the three MC samples involved. Although approximately $500\,000$ $Z \rightarrow \ell\ell$ events are selected in 30 fb^{-1} in the control region in each of the two channels, the events in the $Z \rightarrow \ell\ell$ MC sub-samples (the 'Data' and 'MC' sub-samples) are weighted with a factor larger than 200 in order to be scaled to 30 fb^{-1} . Hence, the real statistical uncertainties are large.

The bias from empty bins was not considered in the published analysis based on the same limited MC samples. Such a bias needs to be evaluated from the data samples when they are available. Then it can also be tested, if the introduced bias is smaller than the gain from the binned calculation. For the time being, the final calculation of the expected $Z \rightarrow \tau\tau$ events in the signal region is performed unbinned. The results are summarized in Table 8.18 and compared to the results from the binned calculation with a binsize of 10 GeV^2 . The non-binned calculation gives correct results

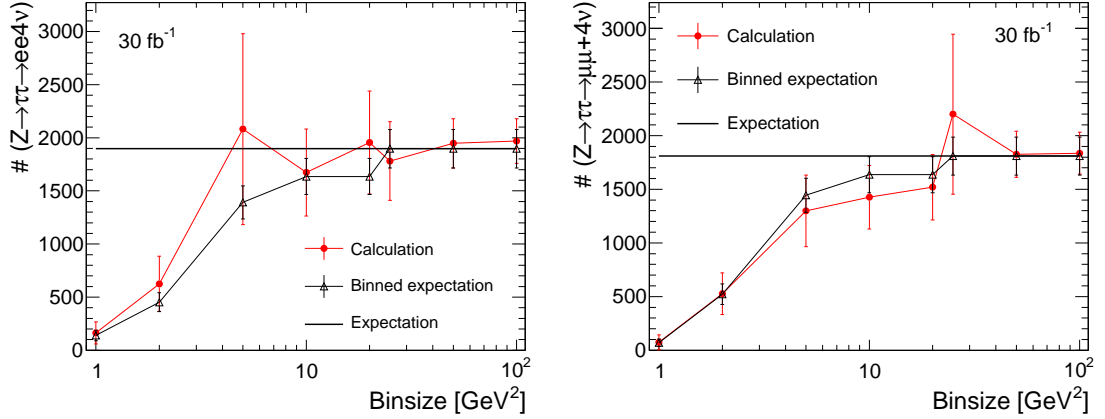


Figure 8.35.: The number of $Z \rightarrow \tau\tau$ events in the signal region, left for the ee channel and right for the $\mu\mu$ channel. The red (filled) circles show the results of Equation 8.10, the black (open) triangles show the number of the binned expectation as a function of the binsize. The black line ('Expectation') marks the number of $Z \rightarrow \tau\tau$ events in the signal region after the baseline selection, this is then independent of the binsize. The binned expectation is the sum of the number of $Z \rightarrow \tau\tau$ events in the $p_{T,\ell}$ bins, but only when the three terms from the right side of Equation 8.10 are non-zero. This number marks the best possible value of the estimated number of $Z \rightarrow \tau\tau$ events, because empty bins lead to a difference to the unbinned result.

A minimal binsize (depending on the available statistics) is necessary for the binned calculation to give correct results, ie. reaching the plateau value of the expectation. The results are normalized to 30 fb^{-1} , however, the error bars reflect the available MC statistics.

well within the statistical uncertainties.

Channel	Expectation	Result (unbinned)	Result (binned)
ee	1897 ± 182	1970 ± 210	1674 ± 410
$\mu\mu$	1810 ± 177	1836 ± 196	1426 ± 296

Table 8.18.: Results of the estimation of the number of $Z \rightarrow \tau\tau$ events in the signal region when using Equation 8.9 (unbinned) and when using Equation 8.10 (binned), compared to the expectation value. The expectation value is the number of $Z \rightarrow \tau\tau$ events passing the baseline selection, it is the same value as given by the horizontal line marked as 'Expectation' in Figure 8.35. The result of the binned calculation is only given for information, its difference to the expectation results from empty bins. The numbers are normalized to 30 fb^{-1} , however, the uncertainties reflect the MC statistics, the expected uncertainties are smaller. A binsize of 10 GeV^2 was chosen for the binned result.

To summarize this discussion, it could be shown that by using the double-ratios systematic uncertainties of the Z cross section, of the luminosity and of b-tagging-related quantities cancel. The jet-related uncertainties also cancel in case the JES and MET-scale are only slightly correlated. More work needs to be invested in order to understand if binning further reduces uncertainties.

Discussion of the $e\mu$ channel

The shape of the $e\mu$ final state is reasonably similar to the shape in the $\mu\mu$ channel. The normalization, however, cannot be calculated from Equation 8.9 since no $Z \rightarrow e\mu$ process exists. But it can be assumed that the systematic uncertainties on the jet energy scale and the b-tagging and light-jet rejection efficiencies behave similar as for the ee and $\mu\mu$ channels. Different detector and trigger acceptances for electrons and muons, however, lead to a non-negligible difference between the number of events in the ee and $\mu\mu$ channel. These acceptances, f , need to be evaluated from real data by studying trigger turn-on curves for instance. If they are known, the number of $Z \rightarrow \tau\tau \rightarrow e\mu + 4\nu$ events could be calculated as follows:

$$\#(Z \rightarrow \tau\tau \rightarrow e\mu + 4\nu) = \sqrt{\#(Z \rightarrow \tau\tau \rightarrow ee + 4\nu) \cdot \#(Z \rightarrow \tau\tau \rightarrow \mu\mu + 4\nu)} \cdot f, \quad (8.11)$$

where the numbers of $Z \rightarrow \tau\tau \rightarrow ee + 4\nu$ and $Z \rightarrow \tau\tau \rightarrow \mu\mu + 4\nu$ are obtained from the data-driven normalization method.

Remaining Experimental Uncertainties

The remaining uncertainties on the $Z \rightarrow \tau\tau$ background were evaluated after the baseline selection is applied and are summarized in Table 8.19. The results are compared with the normalization method applied and for comparison without the method, except for the $e\mu$ channel, where the normalization method was not applicable. It should be noted that the luminosity uncertainty cancels in case the method is applied. The total experimental uncertainty is the sum of the squares of the individual uncertainties for each channel, assuming that they are uncorrelated. In case of asymmetric up- and down- variations the larger uncertainty was used. The total uncertainty is then the weighted sum of the channel-dependent uncertainties. After the baseline selection 1 897 $Z \rightarrow \tau\tau$ events are expected in the ee channel, 1 810 events in the $\mu\mu$ channel and 3 115 events in the $e\mu$ channel. The uncertainties of each channel are weighted with the relative fraction of $Z \rightarrow \tau\tau$ events in each channel to the overall number.

The total detector-related uncertainty, taking into account the normalization method for the ee and $\mu\mu$ channels, is given as $\Delta_{Z \rightarrow \tau\tau}^{\text{w/normal.method}} = 3.4\%$. For information, if the normalization method was not applied in the ee and $\mu\mu$ channel, the total experimental uncertainty would be $\Delta_{Z \rightarrow \tau\tau}^{\text{w/o normal.method}} = 6.8\%$. Furthermore, the uncertainty on the Z boson cross section cancels in the ee and $\mu\mu$ channel (see also Section 8.2.5).

In the published analysis the normalization method was also applied and remaining uncertainties were evaluated for the $m_A = 110$ GeV hypothesis (having the largest MC statistics available). The results found here are consistent. In the published analysis, however, the uncertainties for the $e\mu$ channel have not been evaluated but were neglected instead (assuming future data-driven methods to evaluate the number of events also in the $e\mu$ channel). Hence, the final uncertainty on the total $Z \rightarrow \tau\tau$ background here is larger than in [19]. The most important aspect of this work is that the canceling of the uncertainties by the double-ratio could be shown, which was already assumed but not proven in the published analysis.

Variation	ee channel		$\mu\mu$ channel		$e\mu$ channel
	w/ method	w/o method	w/ method	w/o method	w/o method
El Efficiency	0.41	0.15	0	0	0.1
El p_T Scale up	-0.11	0.07	0	0	0
El p_T Scale down	-0.32	-0.51	0	0	-0.42
El p_T Resol	-0.33	-0.29	0	0	-0.03
Mu Efficiency	0	0	-0.49	-2.44	-1.01
Mu p_T Scale up	0	0	1.54	1.59	0.21
Mu p_T Scale down	0	0	-1.55	-1.8	-0.87
Mu p_T Resol	0	0	0.05	0.05	-0.1
JES up	0	0.15	0	0.21	0.28
JES down	0	-0.15	0	-0.21	-0.52
Jet Resolution	0	-0.66	0	0.58	1.08
B-tagging Efficiency	0	-0.92	0	-3.85	-2.31
Light Jet Rej up	0	-0.92	0	-1.92	-2.31
Light Jet Rej down	0	4.59	0	6.73	4.62
Luminosity	0	3	0	3	3
Sum of uncertainties	0.61	5.63	1.62	8.87	6.25
Total exp. uncertainty in the $ee/\mu\mu$ channel (with normalization): 1.11 %					
Total exp. uncertainty in the $e\mu$ channel (without normalization): 6.25 %					
Total exp. uncertainty: 3.41 %					

Table 8.19.: Systematic detector-related uncertainties for the $Z \rightarrow \tau\tau$ background. Given are relative uncertainties in percent. The total uncertainty was calculated as the sum of the squares of the individual uncertainties, weighted with the fraction of expected number of events in the $ee/\mu\mu$ or $e\mu$ channel to the total number of events. In case of up and down variations, the one with the larger impact was taken into account.

8.2.5. Summary of Background Uncertainties

The experimental uncertainties on background from $W \rightarrow e/\mu/\tau + \nu$, $Z \rightarrow ee$ and $Z \rightarrow \mu\mu$ have not been evaluated. A 10% uncertainty is assumed instead, which is most conservative in a scenario assuming an integrated luminosity of 30 fb^{-1} . However, the impact on the discovery potential is negligible because of the small remaining amounts of those background processes. In the published analysis the W +jets background was larger since lepton isolation was not applied. There the uncertainty was evaluated using cut factorization and found to be in the order of 5%. A summary of the experimental, theoretical and total uncertainties on the background processes is given in Table 8.20.

Process	Exp.	Theory	Total Uncertainty
$W \rightarrow e/\mu/\tau \nu$	10 %	3 %	10.4 %
$Z \rightarrow ee/\mu\mu$	10 %	3 %	10.4 %
$Z \rightarrow \tau\tau \rightarrow ee/\mu\mu + 4\nu$	1.11 %	0 %	1.1 %
$Z \rightarrow \tau\tau \rightarrow e\mu + 4\nu$	6.25 %	3 %	6.9 %
ttbar	4.8 %	12 %	12.9 %

Table 8.20.: Summary of the experimental and theoretical systematics of the backgrounds. The theory uncertainty cancels for the $Z \rightarrow \tau\tau \rightarrow ee/\mu\mu$ background due to the data-driven approach.

8.2.6. Systematic Uncertainties of the Signal Process

For the exclusion of a background-only hypothesis (thus a model-independent 'discovery'), systematic uncertainties on the signal are irrelevant. The relevant question is how large the background fluctuation is. If, however, an excess is measured which clearly goes beyond the expected background fluctuation, the background-only hypothesis must be rejected (this will be discussed in detail in Chapter 9 where the profile likelihood method is described). If an excess of real data events is found, the discovery needs to be specified. Assuming a special MSSM scenario, the signal cross section and event yield is predicted at each point in the $m_A - \tan\beta$ plane given a certain analysis. The question now is, to which cross section times BR does the measured excess of events correspond. This depends not only on the background accuracy, it also requires the knowledge of the signal uncertainty. Experimental and theoretical uncertainties are discussed in the following. The m_A -dependent cross section uncertainties are presented in Chapter 5, Figure 5.1. They range from 30% at $m_A = 110 \text{ GeV}$ to 8% for $m_A = 450 \text{ GeV}$. In the published analysis smaller cross section uncertainties were considered (18%-5%), based on former calculations. The experimental uncertainties are evaluated by applying the systematic variations after the baseline selection. The results are listed in Table 8.21. The total experimental uncertainties are calculated as the sum of the squares of the individual uncertainties and were found to be of the order of 6%-7%. In case of asymmetric up- and down- variations the larger uncertainty was used. The dominant impact is due to the b-tagging efficiency variation with $\approx 5\%$. The experimental uncertainties, however, are negligible compared to the cross section uncertainty, in particular for small A masses.

Variation	110 GeV	130 GeV	160 GeV	200 GeV	300 GeV	450 GeV
El Efficiency	0	0	-0.1	0	-0.1	0.1
El p_T Scale up	0	0	-0.1	0	0.2	0.1
El p_T Scale down	0.3	-0.3	-0.3	-0.5	0	-0.1
El p_T Resol	-0.3	-0.8	-0.3	0.1	-0.1	0.1
Mu Efficiency	-1.5	-1.4	-0.7	-1.5	-1.4	-1
Mu p_T Scale up	1.2	0	-0.1	1	0.1	0.1
Mu p_T Scale down	-0.6	-0.8	-0.1	-0.2	-0.3	-0.1
Mu p_T Resol	0	0	0	0	0.2	0
JES up	0.6	0.5	0.8	0.7	0.4	0.8
JES down	-1.5	-0.8	-1.3	-0.7	-0.7	-0.3
Jet Resolution	0.3	-0.5	-1.4	0.1	-1.2	0.2
B-tagging Efficiency	-5.2	-5.7	-5	-4.6	-4.9	-4.8
Light Jet Rej up	-0.9	-0.5	-0.4	0	-0.2	-0.6
Light Jet Rej down	0	1.1	0.7	1.1	0.5	0.8
Luminosity	3	3	3	3	3	3
Total exp. uncertainty	6.5	6.9	6.2	6	6.1	5.8
Theory uncertainty	30	24	19	15	10	8
Total uncertainty	30.7	25	20	16.2	11.7	9.9

Table 8.21.: Experimental and theoretical systematics for the signal process. Given are relative uncertainties in percent. The total uncertainty was obtained by adding the individual contributions in quadrature. In case of different impacts from up- and down variations only the larger uncertainty was used.

8.3. Discovery and Exclusion Potential in the Dilepton Channel

8.3.1. Discovery

In the following the discovery potential for $h/A/H \rightarrow \tau_\ell \tau_\ell$ in b -associated production is evaluated in the m_h^{\max} scenario assuming an integrated luminosity of 30 fb^{-1} at $\sqrt{s} = 14 \text{ TeV}$ and three different uncertainty scenarios of the background prediction. The significance is calculated from the approximation $Z = S/\sqrt{B}$. This approximation follows from the exact treatment using Poisson statistics when $B \gg 0$ and $S \ll B$. A comparison of this approximation and the significance calculated by using the profile likelihood method is presented in Appendix E.

1. Statistical uncertainties only (will be labeled as 'no systematics'):

In this case the background fluctuation is \sqrt{B} and the statistical significance is given as

$$Z = \frac{S}{\sqrt{B}}, \quad (8.12)$$

where B labels the sum of all background yields and S denotes the signal expectation. This significance is unrealistic and only given for information. Uncertainties on the signal are not evaluated in this case.

2. Statistical and experimental uncertainties:

Given a relative experimental uncertainty on a background process i , ϵ_i^{exp} , the total background uncertainty is now given by $\Delta B = \sqrt{B + \sum_i (\epsilon_i^{\text{exp}} \cdot B_i)^2}$ and the significance therefore becomes:

$$Z = \frac{S}{\sqrt{B + \sum_i (\epsilon_i^{\text{exp}} \cdot B_i)^2}}. \quad (8.13)$$

This scenario is realistic, assuming that in future the theoretical uncertainties will be strongly reduced by new calculations or measurements of cross section. For the discovery and exclusion limits the signal uncertainties are irrelevant, but they are considered to state optimistic and a pessimistic significance which will be drawn as a band around the limits:

$$Z = \frac{S \pm \Delta S}{\sqrt{B + \sum_i (\epsilon_i^{\text{exp}} \cdot B_i)^2}}. \quad (8.14)$$

ΔS is the signal uncertainty which is again separated into two scenarios: First considering experimental uncertainties only, $\Delta S = \epsilon_S^{\text{exp}}$, and second also including the theoretical uncertainties, $\Delta S = \sqrt{(\epsilon_S^{\text{exp}})^2 + (\epsilon_S^{\text{theory}})^2}$.

3. Statistical, experimental and theoretical uncertainties:

In the third background scenario the relative theoretical uncertainties, ϵ^{theory} , are included,

and the significance is given as:

$$Z = \frac{S}{\sqrt{B + \sum_i \left((\epsilon_i^{\text{exp}} \cdot B_i)^2 + (\epsilon_i^{\text{theory}} \cdot B_i)^2 \right)}}. \quad (8.15)$$

The signal uncertainties are handled in the same way as was done for the second background systematics scenario.

The statistical uncertainties of the MC samples are not considered in order to not artificially worsen the limits. Instead in a data-driven approach the statistical uncertainties are assumed to be these expected in 30 fb^{-1} . This was already adopted in the published analysis.

The significances were evaluated for 7 values of $\tan\beta$ ($\tan\beta = 5/10/15/20/30/35/45$) and 6 values of m_A (110/130/160/200/300/450 GeV), giving 42 points in the $m_A - \tan\beta$ plane. Figure 8.36 presents the significance for each scenario as a function of m_A for two representative values of $\tan\beta$. A discovery is claimed in case the significance reaches a value of 5 or more. An improvement of the discovery potential for $m_A = 130 \text{ GeV}$ is visible. Furthermore, the significance steeply falls with increasing values of m_A . The reason for the peak at 130 GeV is that at this A boson mass all three Higgs bosons are mass degenerate and the cross section is the sum of the h, H and A. Furthermore, the position of the signal peak at 130 GeV between the peak of the $Z \rightarrow \tau\tau$ and $t\bar{t}$ background allows a strong background suppression when the mass window cut is applied (compare to Figure 8.14).

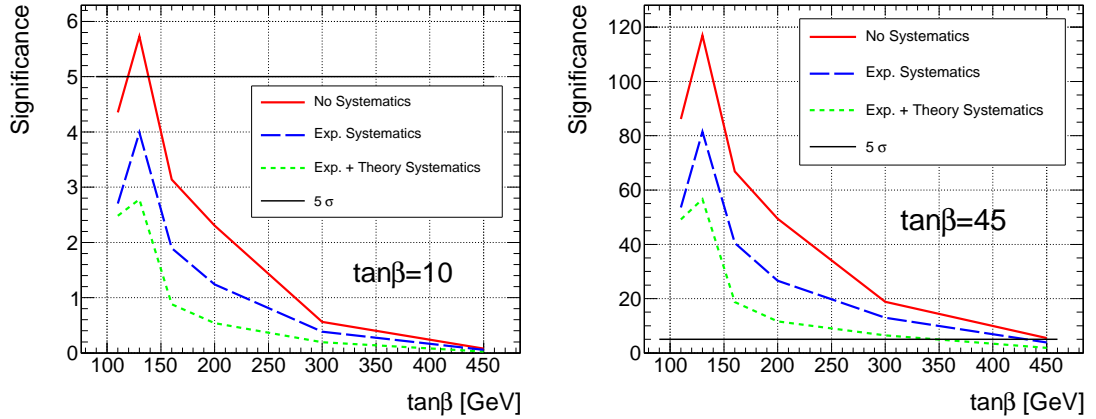


Figure 8.36.: Significances for the three background uncertainty scenarios as a function of m_A , left for $\tan\beta = 10$ and right for $\tan\beta = 45$. In the case of a low $\tan\beta$ only a 3σ evidence is possible when all uncertainties are taken into account. For $\tan\beta = 45$ the significance exceeds the 5σ level in almost the complete mass range.

The significances as a function of $\tan\beta$ for each mass hypothesis are presented in Figure 8.37. A quadratic dependence of the discovery potential on $\tan\beta$ is visible, which is due to the dependence of the signal cross section on $\tan^2\beta$.

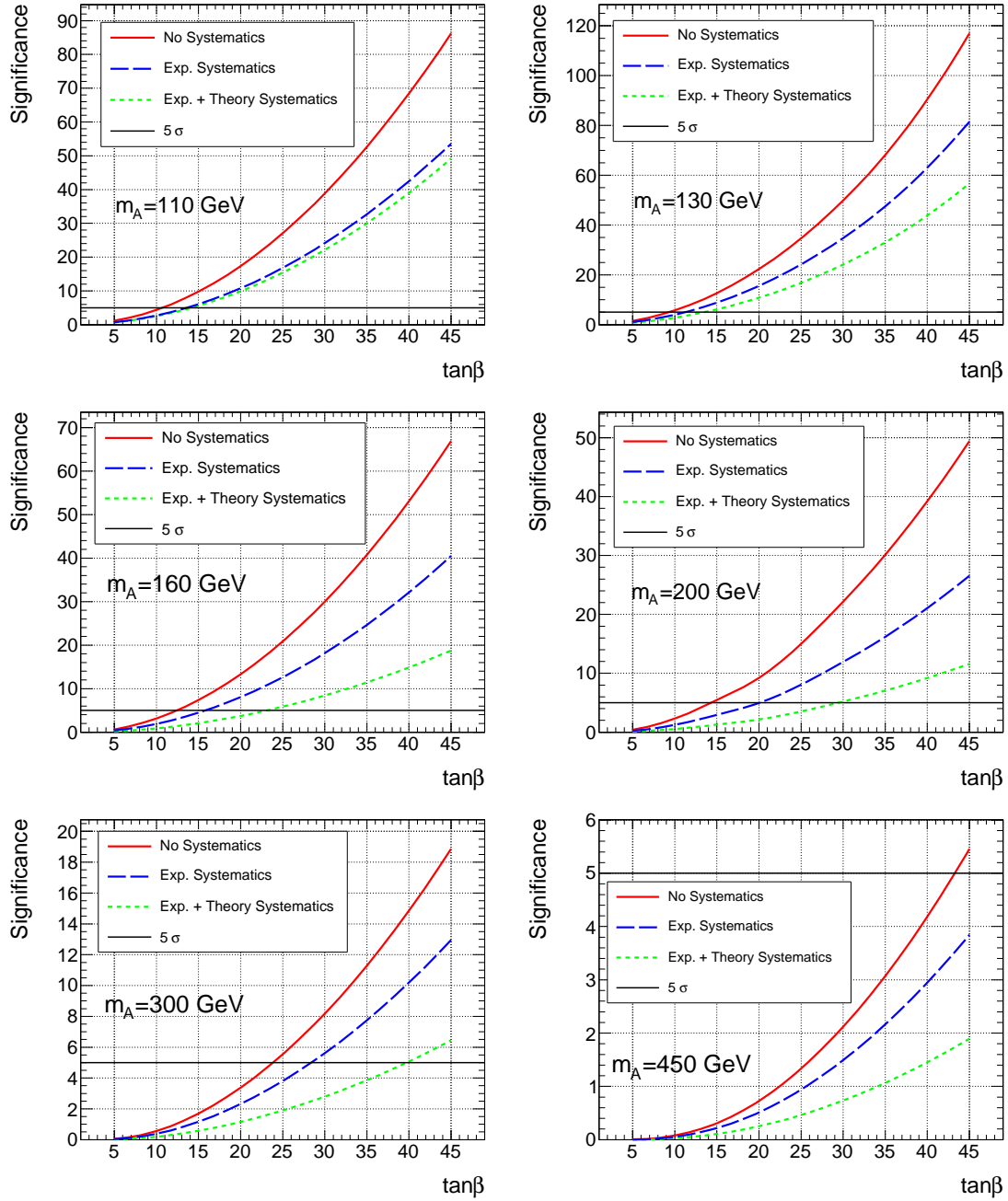


Figure 8.37.: Significance with different background uncertainties as a function of $\tan\beta$ for different Higgs boson mass hypotheses, as indicated in the plots. The integrated luminosity is 30 fb^{-1} . The significance scales with $\tan\beta^2$.

Finally, the 5σ contours were extracted in the $m_A - \tan\beta$ plane in Figure 8.38. For this illustration also the optimistic and pessimistic signal prediction bands are included. A clear degradation of the discovery potential is visible when the theoretical uncertainties are included, because they are the dominant source of systematics (compare to Table 8.20). The largest cross section uncertainty is assumed for the $t\bar{t}$ background, which is the dominant background for the larger A masses. As a consequence, the discovery potential becomes particularly low for the large A boson mass region. A data-driven approach for the estimation of the $t\bar{t}$ background or a precise cross section measurement will be most useful (see Appendix I). A data-driven method for the $t\bar{t}$ estimation was developed and applied to the lepton-hadron channel and will be discussed in the next Chapter.

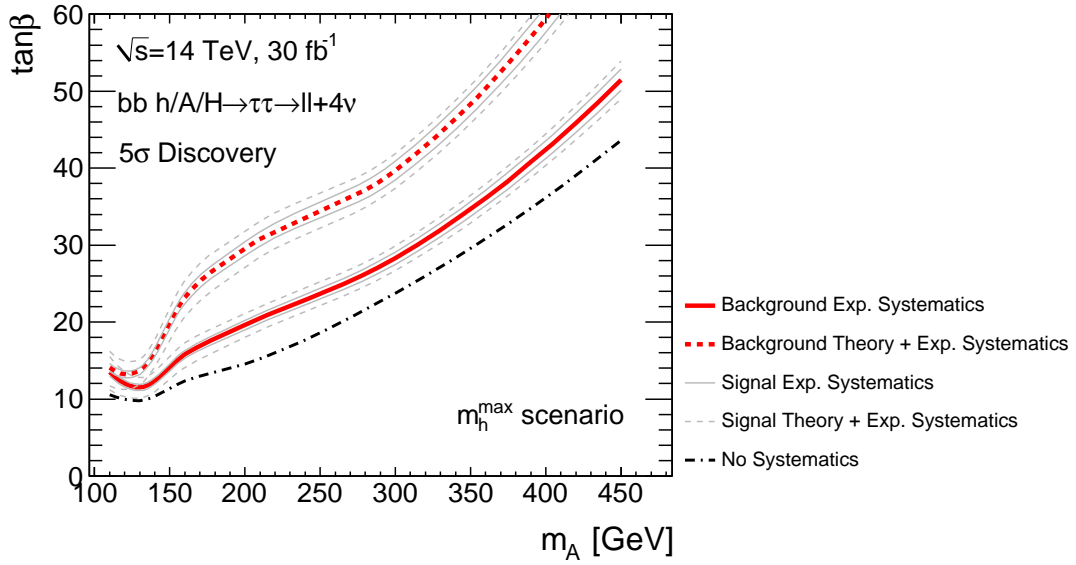


Figure 8.38.: 5σ discovery contours for three background uncertainty scenarios indicated in the legend. The grey bands illustrate the signal uncertainty. The solid grey line corresponds to the experimental uncertainty, the dashed grey line includes also the theoretical uncertainties. The signal uncertainties in the low A mass region are completely dominated by the cross section uncertainties.

8.3.2. Exclusion

Claiming an exclusion is equivalent to rejecting the signal+background ($S+B$) hypothesis when observing B events. This can be rephrased in the question which size of a background fluctuation $\Delta B \equiv S$ is still compatible with a background-only hypothesis. A confidence limit (CL) of 95% was chosen to establish the limit. This corresponds to a probability of 5% that more events than $S+B$ are observed. This is also equivalent to a significance of 1.64σ . The statement of exclusion is therefore weaker than the statement of discovery. For a discovery five standard deviations are required, corresponding to a probability that this measurement is the result of a fluctuation of the background of $2.87 \cdot 10^{-7}$.

The number of signal events corresponding to a significance of 1.64σ are converted into an upper limit of $\tan\beta$. Poisson statistics and the ROOSTATS program are used for performing

the calculation. A more detailed discussion of the statistical methods is given in Section 9.3.1. The exclusion limits for the three background uncertainty scenarios are presented in Figure 8.39 for 30 fb^{-1} . Similar as for the discovery, in the case when the theoretical uncertainties on the backgrounds are included, the limit deteriorates strongly especially for large A masses. In the region of low m_A and large $\tan\beta$ the sensitivity to the MSSM Higgs boson is the largest, for higher A masses and/or lower values of $\tan\beta$ the sensitivity decreases.

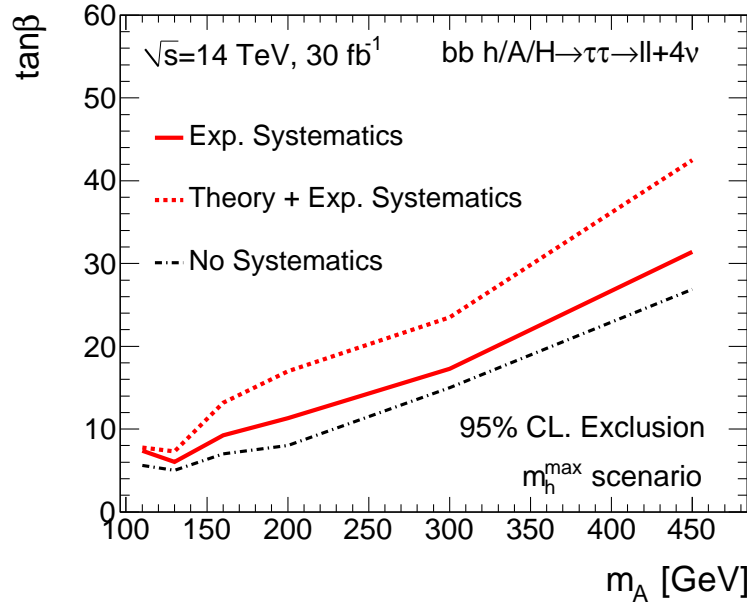


Figure 8.39.: 95% CL. exclusion limits in the $m_A - \tan\beta$ plane for the m_h^{\max} -scenario for different uncertainty scenarios as indicated in the legend. The integrated luminosity assumed is 30 fb^{-1} . The best sensitivity for a MSSM Higgs boson decaying to tau-pairs in the dilepton channel is found at low A or large $\tan\beta$ values.

8.3.3. Comparison to Published Analysis

The results published two years ago in [19] are compared to the updated analysis of the dilepton channel described in this thesis. There are numerous differences between both analyses which were mentioned at the relevant sections throughout this chapter. In Figure 8.40 the 5σ discovery contours and the 95% CL. limits are shown.

It should be noted, that the contour labeled with '+10% $\sigma(\bar{t}\bar{t})$ ' includes all experimental uncertainties plus 10% uncertainty on the $\bar{t}\bar{t}$ cross section. Cross section uncertainties from W and Z boson backgrounds were neglected in the published analysis. In this work, cross section uncertainties of 12% for $\bar{t}\bar{t}$ and 3% for W and Z production were considered. The experimental uncertainties obtained in the updated and the published analysis are comparable.

The discovery contours in the published analysis are similar compared to the updated results for $m_A \leq 130 \text{ GeV}$. The updated sensitivity is worse than the published analysis in the m_A range from 160 GeV up to 300 GeV. For $m_A \geq 300 \text{ GeV}$ the updated sensitivity is better. Similar observations

are made when comparing the exclusion limits.

The cuts for $m_A \geq 300$ GeV of the updated analysis are better since they result in more signal and less background events. The results from the published analysis were too conservative for the high mass range. For $m_A < 300$ GeV the expected number of signal and background events is comparable between both analyses. The remaining differences result mostly from the fact that the contours in the published analysis were fitted with a function proportional to $\tan^2 \beta$ to smooth unphysical artifacts from computing routines extrapolating between the studied mass points.

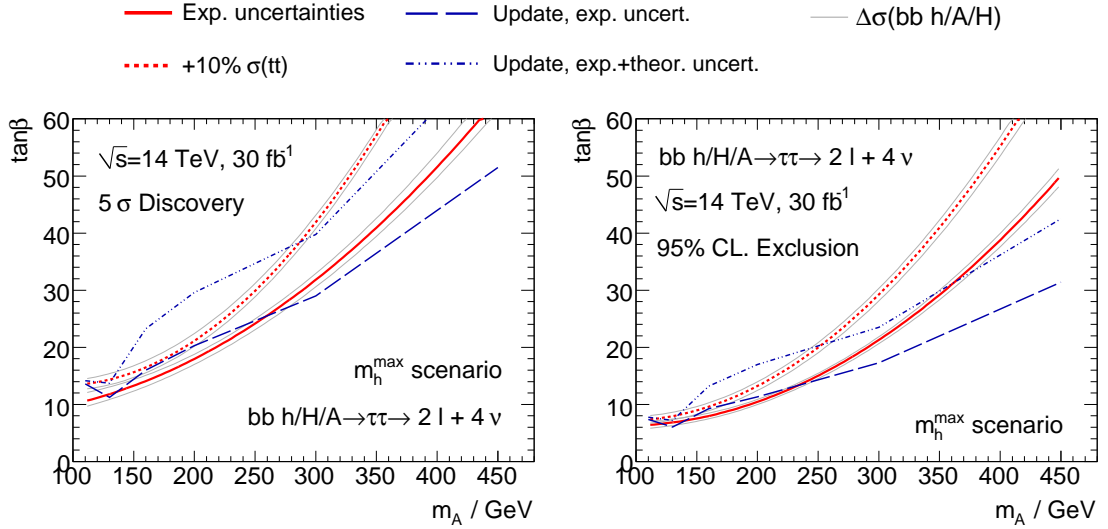


Figure 8.40.: The 5σ discovery contours (left) and 95% CL. exclusion limits (right) from the published analysis in [19] (red lines). The updated results of this work are also given (blue lines). The dashed red line presents the limit when considering experimental uncertainties and 10% cross section uncertainty on $\bar{t}\bar{t}$. The contours of the former study were fitted by quadratic functions for technical reasons, which explains most of the differences for $m_A < 300$ GeV. For $m_A \geq 300$ GeV more efficient selection cuts lead to better results of the updated analysis.

8.3.4. Discussion

The discovery potential for the MSSM Higgs bosons in the $\tau_\ell \tau_\ell$ channel is strongly dependent on the $m_{\tau\tau}$ resolution and the systematic uncertainties. The reconstructed width of the signal in b-associated production is very large, ranging from 25 GeV for A masses as low as 110 GeV up to 90 GeV for $m_A = 450$ GeV. As a consequence, the number of background events in the signal region is large: There are several thousand events expected in 30 fb^{-1} at $\sqrt{s} = 14$ TeV for low A masses, still 500 events for $m_A = 450$ GeV, compare to Table 8.14⁵. The cuts applied in the analysis are optimized for the best statistical significance. If background uncertainties are included,

⁵It might be interesting to compare the number of signal and background events in the low Higgs boson mass region to the SM VBF $H \rightarrow \tau\tau \rightarrow \ell\ell + 4\nu$ analysis from [19]. For 30 fb^{-1} at $\sqrt{s} = 14$ TeV and within a mass window of $m_{\tau\tau} < 180$ GeV, approximately 10 signal events are left for $m_H = 120$ GeV. The $Z \rightarrow \tau\tau$ contributions contains ≈ 50 events and there are 3 $\bar{t}\bar{t}$ events. This, however, is not only related to the better mass resolution, but also to the rather hard cuts selecting events with the VBF topology.

the impact on the discovery potential is severe. Better sensitivity could be achieved by optimizing the cuts including systematic uncertainties. Further improvements could also be obtained by performing multi-variate techniques instead of a simple cut-based analysis. However, the remaining limiting factor will always be the mass resolution.

The sensitivity of this analysis was also evaluated for lower integrated luminosities down to 1 fb^{-1} , assuming the same center-of-mass energy, the same cross sections and especially the same systematic uncertainties. The results are presented in Figure 8.41. It is remarkable that even with 1 fb^{-1} a large part of the $m_A - \tan\beta$ plane is still covered by this analysis alone. Another observation is that the degradation of the discovery potential - when also including the theoretical uncertainties - decreases, when lower luminosities are assumed. This is understood as the number of background events is much smaller with lower luminosities so that the impact of the systematic uncertainties becomes smaller, although the relative statistical uncertainty of the background is larger.

Even though the results of this channel look very promising, they will be re-discussed in the following chapter when the discovery potential of the lepton-hadron channel is assessed. It will be shown that lepton-hadron channel offers an even better discovery potential than the dilepton channel.

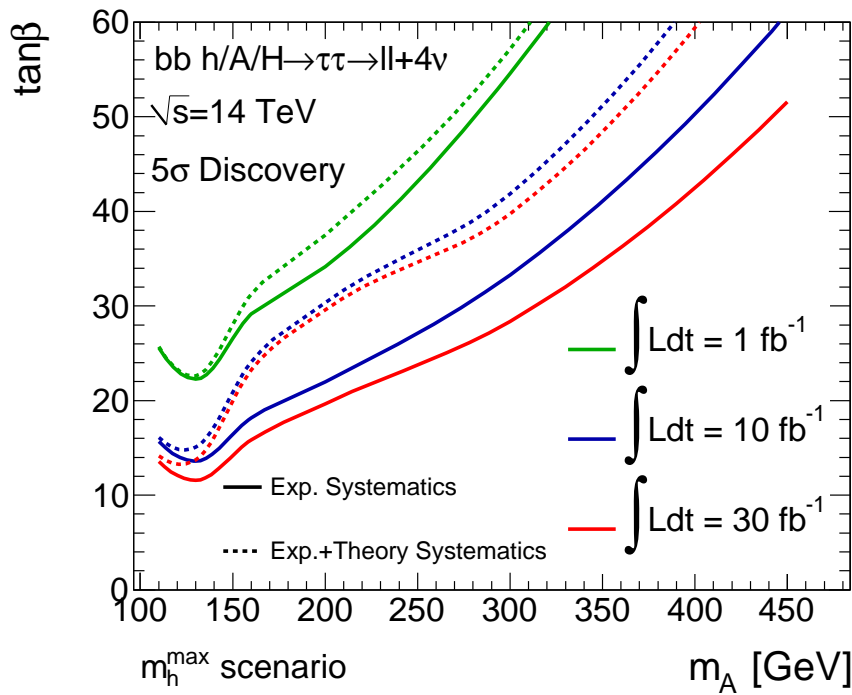


Figure 8.41.: The 5σ contours with experimental background uncertainties (solid lines) or experimental and theoretical uncertainties (dashed lines), for different integrated luminosities. Even with 1 fb^{-1} a very large part of the $m_A - \tan\beta$ plane is still covered by this analysis alone.

Analysis of the Lepton-Hadron Channel

In approximately 45% of the $\tau\tau$ decays one tau decays leptonically (to electron/muon) and the other one decays hadronically. The fully leptonic final state only appears in $\approx 12\%$ of the cases. The semi-leptonic final state therefore offers in principle better discovery possibilities than the dileptonic channel. However, the correct identification of hadronic τ -leptons is a crucial point. Furthermore, background processes with only one true lepton become more important now.

The analysis presented in this chapter is published in [124], further details are collaboration internally available in [85]. Higgs boson masses between 150 GeV and 800 GeV have been considered. The lepton-hadron channel was studied in detail before, previous results are published in [113] and [109] and will be compared to the results obtained in this thesis later.

In this analysis also the Higgs boson signal produced in gluon fusion is included for Higgs boson masses up to 450 GeV. The lowest Higgs boson mass hypothesis considered here is $m_A = 150$ GeV. Therefore, no contribution from the SM-like h boson is included. The cross section of the signal is the sum of the cross sections of the H and A bosons.

The study is based on ATLFast-II samples, details were summarized already in Chapter 5. The basic object selection was described in Chapter 6 but important aspects will be repeated in the relevant sections. In this chapter first the event selection is described, which is separated into a baseline analysis and then split into individual analyses. A b -tagged and a non b -tagged analysis are optimized separately given different background contributions, and finally both analyses are combined. Then, the systematic uncertainties are summarized. A special emphasis is given to the description of a data-driven $t\bar{t}$ estimation procedure. Finally, the discovery potential is presented.

9.1. Event Selection

In this analysis the Higgs boson is either produced in gluon fusion or in association with b -quarks. The signal signature includes the presence of a high- p_T lepton, a hadronic high- p_T τ candidate, missing E_T and in the case of b -associated production one or more b -jets.

The requirement of the presence of a b -tag jet will enhance the b -associated production. After a basic pre-selection (the baseline analysis), the analysis is therefore split into a *non b -tagged analysis* with a veto on b -tags and a *b -tagged analysis*, where at least one b -tagged jet is required. Finally, as was done for the dileptonic channel, Higgs boson mass-dependent cuts are applied to exploit the full discovery potential.

9.1.1. Baseline Selection

Trigger

The following trigger items based on the identification of high p_T electrons or muons were chosen:

- e20 (Chain: L1_EM18, L2_e20_medium1, EF_e20_medium1) :
The event is triggered when at least one electron with a p_T larger than 20 GeV is found.
- mu20 (Chain: L1_MU20, L2_mu20, EF_mu20):
The event is triggered when at least one muon with a p_T larger than 20 GeV is found.

The event is triggered if any of the two trigger items fired. Since this analysis is based on ATLAS-II samples, no trigger information was available. Instead in [124] dedicated FULLSIM samples were used, one with $m_A = 150$ GeV and one with $m_A = 600$ GeV. The results are used in this thesis.

The efficiency of the single lepton triggers with respect to the reconstructed, isolated leptons was obtained from the turn-on curve as illustrated in Figure 9.1. The trigger turn-on curves were found to be universal, independent of the Higgs boson mass and independent of the physics process. The turn-on curves were extracted from the combination of the two signal FULLSIM samples (for $m_A = 150$ GeV and $m_A = 600$ GeV). The curves were fitted with an error function of the form:

$$f(p_T) = 0.5 \cdot \left[1 + \operatorname{erf} \left(\frac{p_T - p_0}{\sqrt{2} \cdot p_1} \right) \right] \cdot p_2, \quad (9.1)$$

where p_0 is the lepton momentum where the trigger efficiency reaches half of its maximum value, p_1 is the slope of the curve and p_2 is the maximum efficiency in the plateau region. The plateau is reached at approximately 24 GeV. In the further selection the electrons and muons are therefore required to have at least $p_T > 24$ GeV. The trigger efficiencies obtained are:

- e20: $p_2 = (97.7 \pm 0.3) \%$,
- mu20: $p_2 = (81.1 \pm 0.4) \%$.

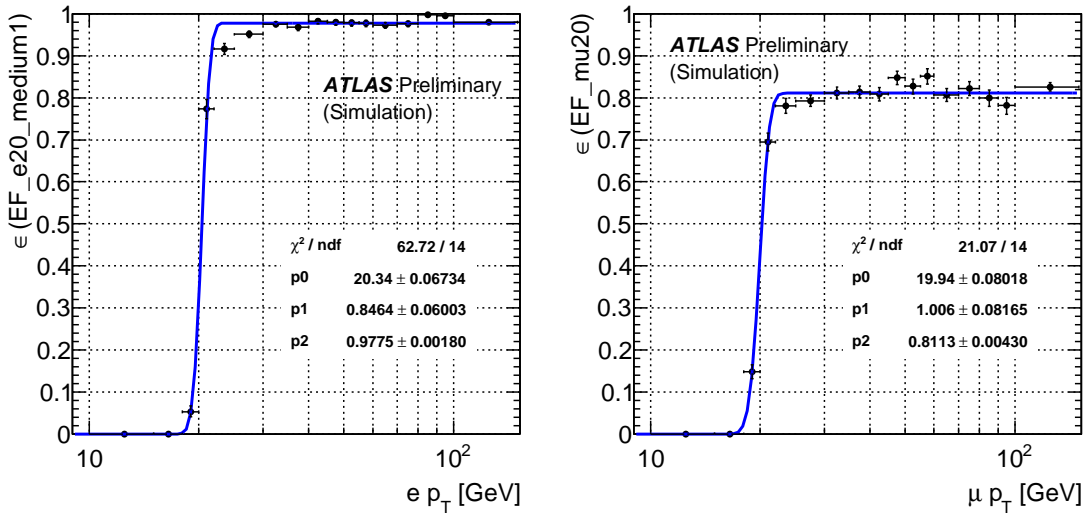


Figure 9.1.: The turn-on curves for e20 (left) and mu20 (right) (taken from [124]). Shown is the efficiency as a function of the lepton p_T . The efficiency is a constant above ≈ 24 GeV.

Z Mass Veto

To suppress $Z \rightarrow ee$ and $Z \rightarrow \mu\mu$ events a Z mass veto is applied. All combinations of e^+e^- and $\mu^+\mu^-$ candidates are tested whether the invariant mass of the combination falls within ± 10 GeV of the nominal Z mass. If that is the case the event is rejected. The loss of Higgs boson events is below 1%.

Lepton Selection and Isolation

At least one electron passing the loose object selection with $p_T > 24$ GeV is required. The lepton with the highest p_T is chosen for the further analysis. The trigger efficiency is applied as an event weight, depending on whether the chosen lepton is an electron or muon.

The electron or muon has to pass track and calorimeter isolation cuts:

- $\frac{E_T^{\text{cone0.2}}}{p_T} < 0.1$,
- $\# \text{tracks} (\Delta R < 0.3) < 2$.

In addition, the electron candidate has to pass the isEM: ElectronTight flag. As was done in the dilepton analysis, for the QCD events the isolation and tight electron ID cuts are realized by applying the cut efficiency as an event weight to gain MC statistics. The weights are listed in Appendix F.

Electrons and muons passing these selection criteria will also be denoted as tight leptons.

The number of tracks in a cone of size $\Delta R = 0.3$ around the leading electron or muon are illustrated in Figure 9.2.

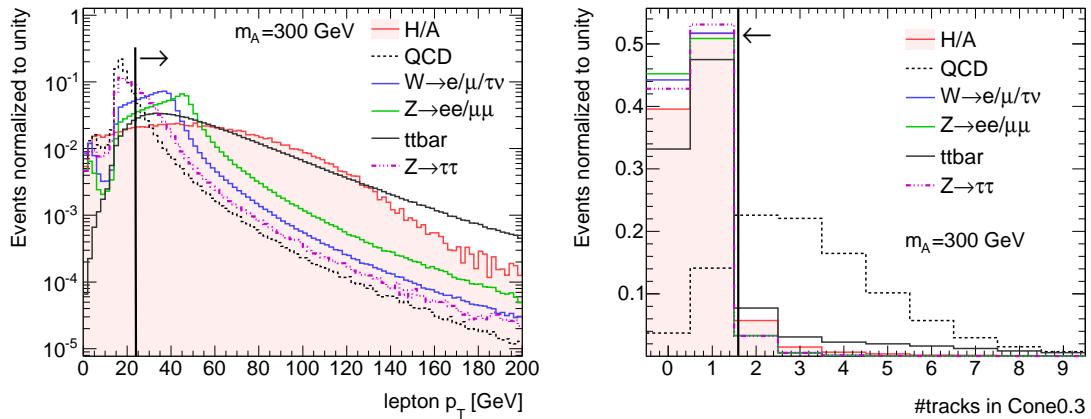


Figure 9.2.: Left: The p_T of electrons and muons. Right: The number of tracks in a cone with $\Delta R = 0.3$ around the leading electron or muon. The cuts are indicated. The distributions are normalized to unity. The Higgs boson signal contains events produced in gluon fusion and in association with b-quarks. Both plots were prepared for all events containing at least one electron or muon, no object ID criteria were required.

Tau Selection

The τ ID is separated into a loose and a tight selection. For the following background processes the loose τ ID is applied via cuts and the tight efficiency is applied as an event weight: $W \rightarrow e\nu$, $W \rightarrow \mu\nu$, $W \rightarrow \tau\nu$, QCD, $Z \rightarrow ee$ and $Z \rightarrow \mu\mu$. The τ candidates are categorized according to the truth particle, matched to the reconstructed τ candidate in a cone of $\Delta R < 0.2$. More details and the obtained weights are listed in Appendix F.

The loose τ candidate is seeded by both the track and the calorimeter based algorithms. It is further required to have the opposite charge of the selected electron or muon and a p_T of at least 24 GeV. The number of associated tracks of the τ candidate is required to be 1 or 3 (corresponding to 1- or 3-prong τ candidates). A loose τ likelihood (LLH) cut of at least 3 is required. The distributions of p_T , the LLH and the number of associated tracks for the leading τ candidate are given in Figure 9.3.

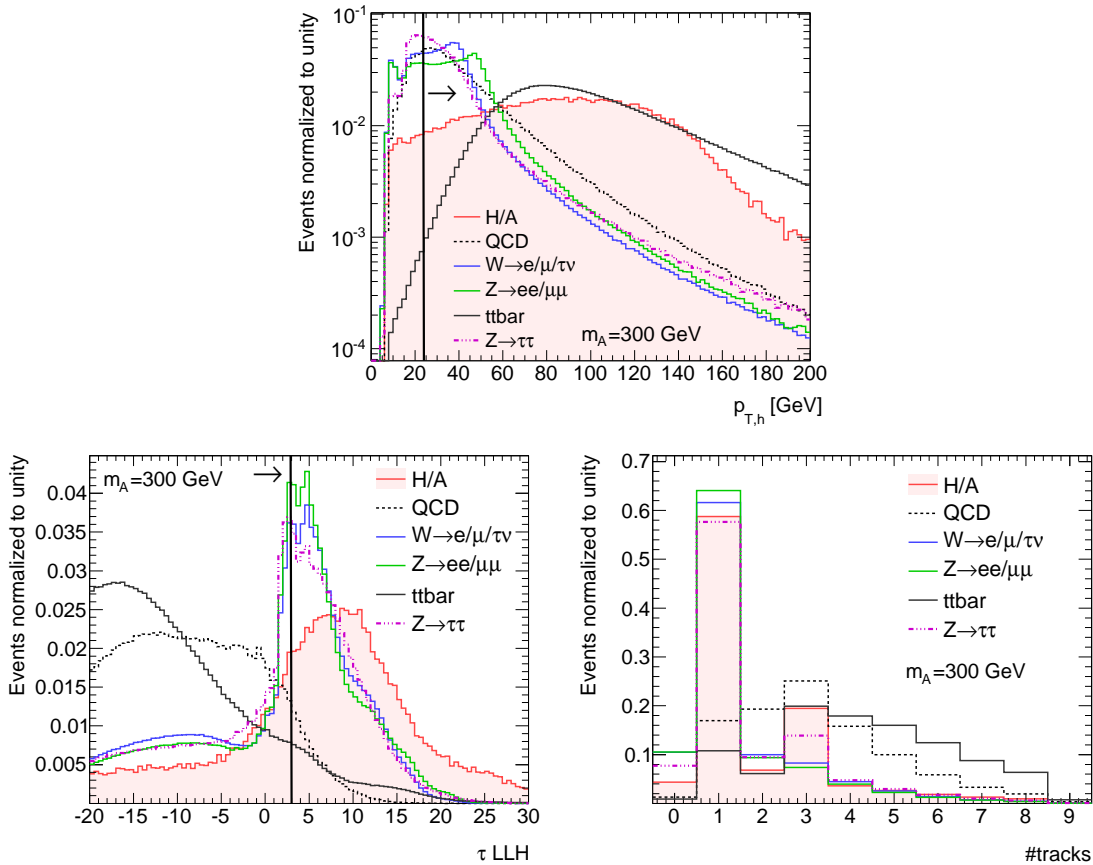


Figure 9.3.: Upper plot: The p_T of the leading τ candidate, the cut is indicated. Lower left: The LLH of the τ -lepton. The loose cut is indicated. Lower right: The number of tracks associated to the τ . Only τ candidates with 1 or 3 tracks will be selected. All distributions are normalized to unity. The Higgs boson signal contains events produced in gluon fusion and in association with b-quarks. All plots are prepared if at least one τ candidate is found, no object ID criteria are required.

For the tight selection a LLH cut is applied to the τ candidates. The cut values are binned in $p_{T,h}$ and were taken from [85]. The idea of the binned LLH cut is to assure a flat event selection efficiency of 75% with respect to the loose selection over the full p_T range. The cut values are listed in Table 9.1.

$p_{T,h}$ [GeV]	LLH cut
24 - 45	> 5.5
45 - 80	> 6.7
80 - 100	> 6.0
100+	> 7.5

Table 9.1.: Tight τ LLH ratio cut.

Kinematic Cuts

The following cuts on the event kinematics are applied:

- **MET > 20 GeV:**
This cut efficiently reduces QCD dijet events. The cut is chosen to be larger than in the dilepton analysis, since more QCD events are expected in this channel than in the dilepton channel. Furthermore, a larger MET is expected for the Higgs boson events in the lepton-hadron channel than for the dilepton channel due to the odd number of neutrinos stemming from the Higgs boson decay.
- **$m_T > 25$ GeV:**
The transverse mass is defined as the invariant mass of the MET and the p_T of the electron or muon. It can be calculated as follows:

$$m_T = \sqrt{2 \cdot p_{T,\ell} \cdot E_{T,\text{miss}} \cdot (1 - \cos \Phi_{\ell,\text{MET}})}. \quad (9.2)$$

This cut reduces especially W +jets, and also $t\bar{t}$ background. In theory the relation $m_T < m_W$ holds, but detector effects smear the edge. The distribution of m_T is presented in Figure 9.4.

- **Collinear approximation:** $0 < x_1 < 1$ and $0 < x_2 < 1$.

9.1.2. Split into non b-tagged and b-tagged Analysis

After object ID, trigger, lepton and tau selection are passed, the analysis is split into two independent sub-analyses. The idea is to exploit the different signatures when the signal is produced by two mechanisms. In the non b-tagged analysis a veto on b-tags is imposed, in the b-tagged analysis at least one b-tagged jet is required. The IP3D+SV1 weight cut is required to be larger than 4 for a jet to be b-tagged.

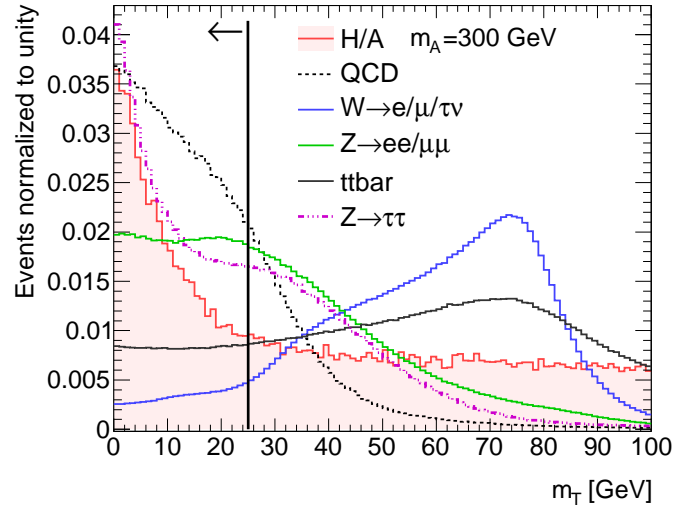


Figure 9.4.: The transverse mass for various processes. The W +jets and $t\bar{t}$ events have a sharp edge at the W mass and a Jacobi-Peak below m_W . All distributions are normalized to unity, the cut is indicated. The Higgs boson signal contains events produced in gluon fusion and in association with b -quarks. The plot was prepared for all events containing at least one τ candidate and one electron or muon, no further object ID or selection criteria are required to be fulfilled.

m_A -dependent Cuts in the non b -tagged Analysis

A veto on b -tags decreases the $t\bar{t}$ contribution. In the dilepton analysis an upper cut on the number of jets was used to suppress the $t\bar{t}$ background. Here this cut is not applied because $t\bar{t}$ is already suppressed. Instead, kinematic cuts on $p_{T,h}$, MET and $\Delta\Phi_{\ell h}$ are chosen and they depend on m_A . The cut values are summarized in Table 9.2. The distributions of the observables for all six mass hypotheses are illustrated in Figures 9.5 and 9.6, for events passing the baseline cuts.

m_A	150 GeV	200 GeV	300 GeV	450 GeV	600 GeV	800 GeV
# Tracks	1 or 3	1 or 3	1 or 3	1 or 3	1	1
MET	> 20 GeV	> 20 GeV	> 20 GeV	> 20 GeV	> 60 GeV	> 60 GeV
$p_{T,h}$	> 40 GeV	> 50 GeV	> 70 GeV	> 90 GeV	> 100 GeV	> 100 GeV
$\Delta\Phi_{\ell h}$	< 3.0	< 3.0	< 3.0	< 3.0	< 3.05	< 3.05

Table 9.2.: The m_A -dependent cuts in the non b -tagged analysis.

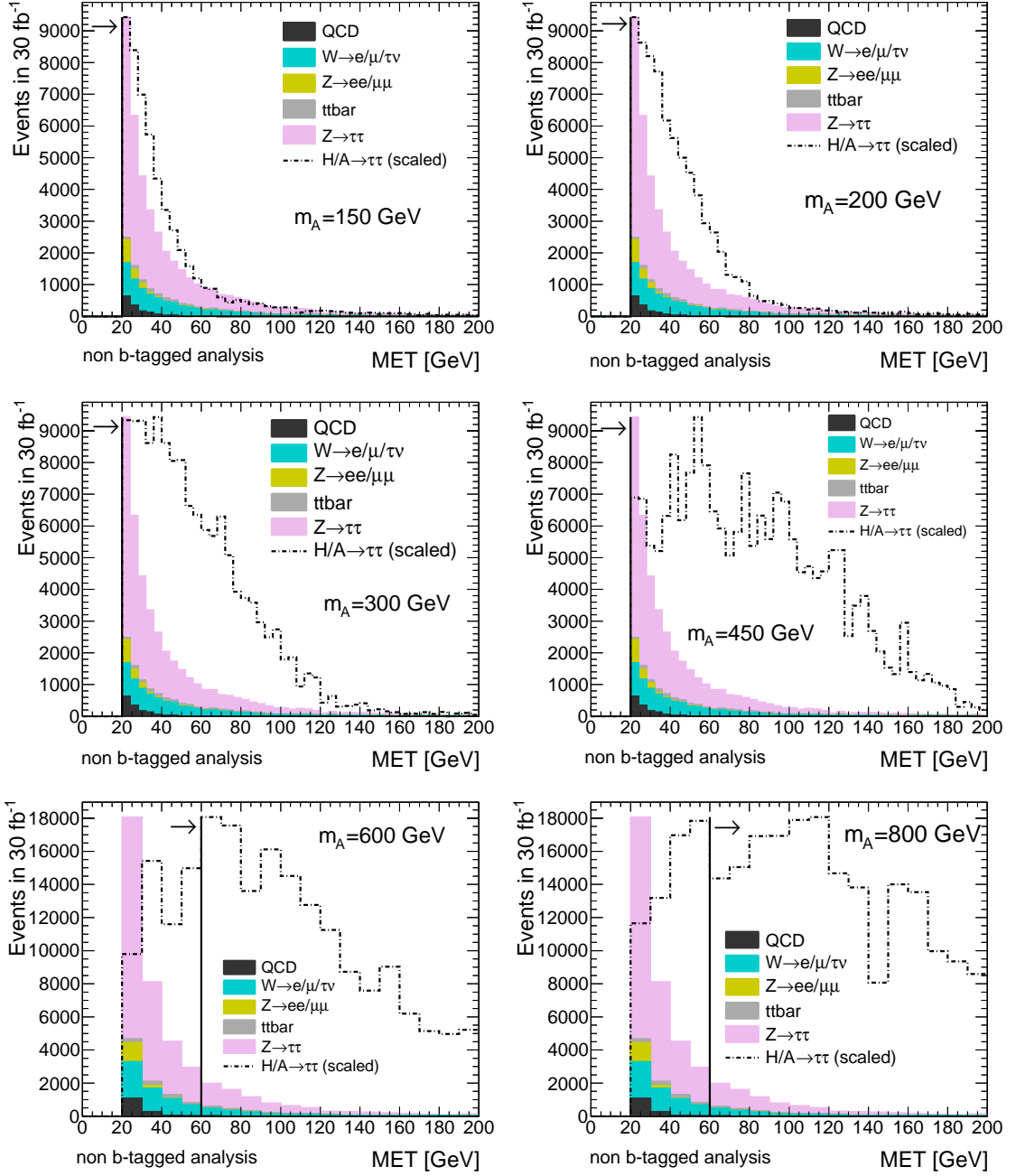


Figure 9.5.: Distributions of MET for signal (dotted black line) and various background processes in the non b-tagged analysis for different values of m_A as indicated in the plots. The signal is scaled to the background for better visibility. The cut values are indicated; the arrows point to the events which are kept in the analysis. The plots were prepared with the baseline cuts and the b-veto applied.

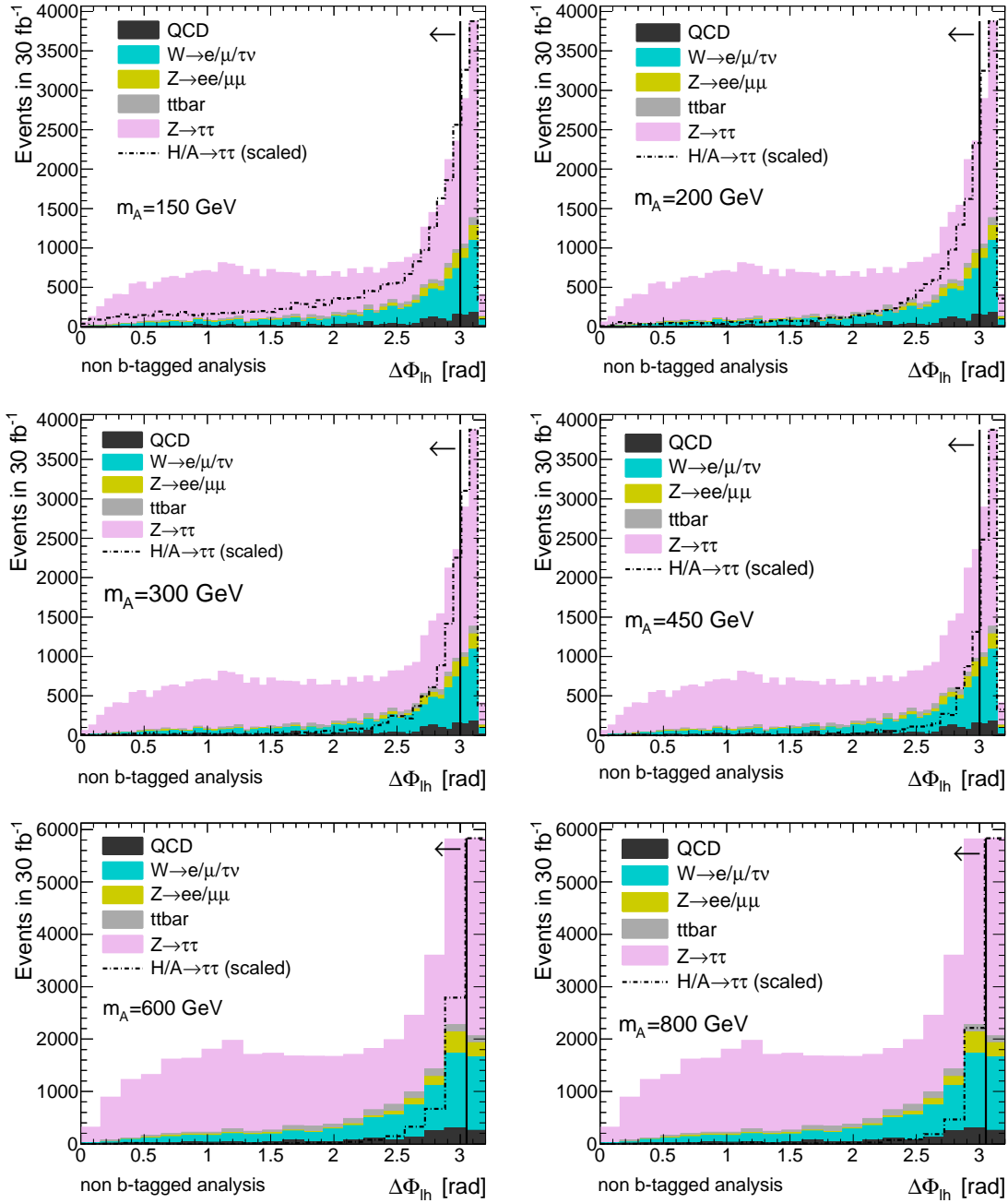


Figure 9.6.: Distributions of $\Delta\Phi_{\ell h}$ for signal (dotted black line) and various background processes in the non b-tagged analysis for different values of m_A as indicated in the plots. The signal is scaled to the background for better visibility. The cut values are indicated; the arrows point to the events which are kept in the analysis. The plots were prepared with the baseline cuts and the b-veto applied.

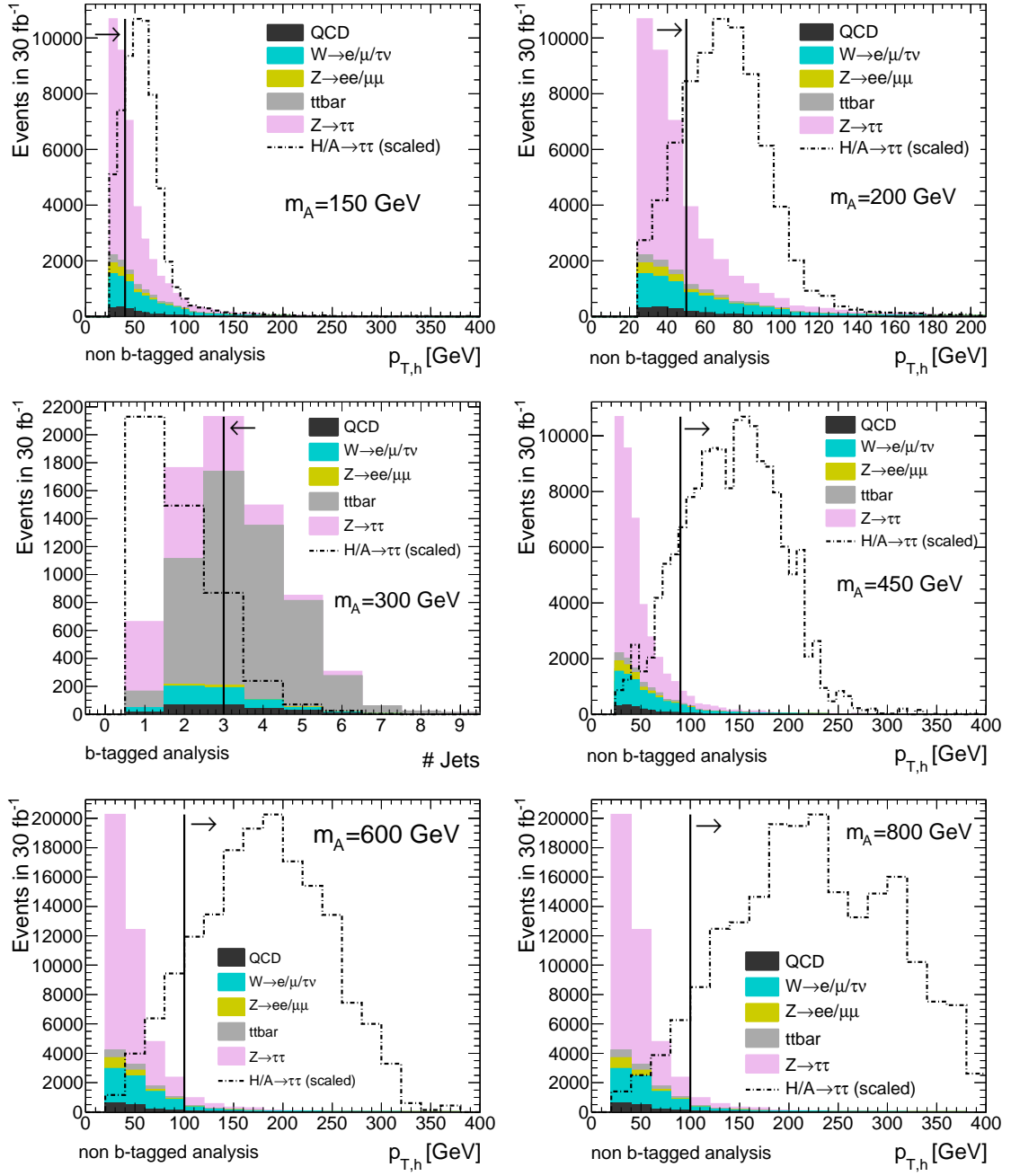


Figure 9.7.: Distributions of $p_{T,h}$ for signal (dotted black line) and various background processes in the non b-tagged analysis for different values of m_A as indicated in the plots. The signal is scaled to the background for better visibility. The cut values are indicated; the arrows point to the events which are kept in the analysis. The plots were prepared with the baseline cuts and the b-veto applied.

m_A -dependent Cuts in the b-tagged Analysis

The requirement of at least one b-tag increases the relative $t\bar{t}$ contribution. Since $t\bar{t}$ events contain on average more jets than all other processes, a cut on less than 3 jets with $p_T > 20$ GeV is applied. In Figure 9.8 the multiplicity of high- p_T jets is illustrated, on the left for the case when the b-veto is applied, and on the right in the b-tagged case. The different amounts of $t\bar{t}$ are visible.

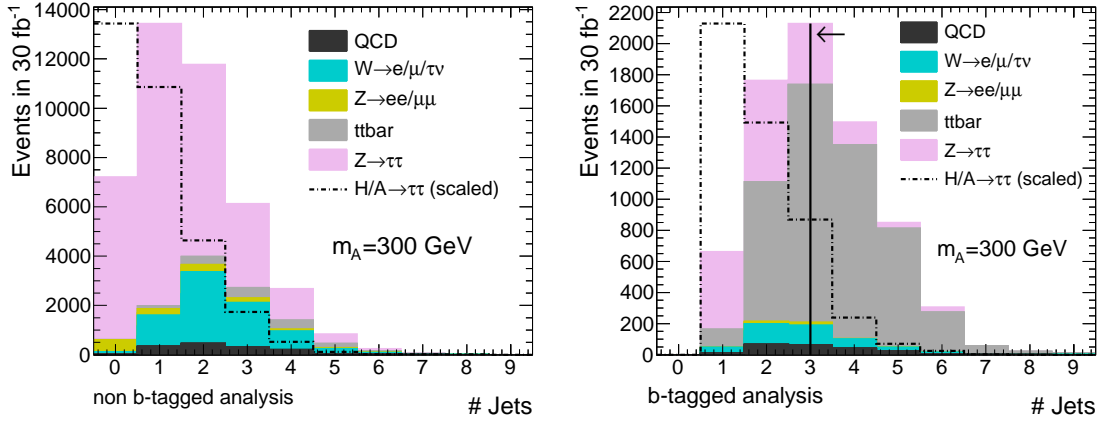


Figure 9.8.: The number of jets with $p_T > 20$ GeV, left for the non b-tagged analysis and right for the b-tagged analysis. All baseline cuts are applied. A signal mass of $m_A = 300$ GeV is assumed, the signal is scaled to the backgrounds for better visibility. In the left plot the b-veto and in the right plot at least one b-tag are required to be fulfilled. The different amounts of $t\bar{t}$ relative to the other background contributions are visible. The cut on the number of jets applied in the b-tagged analysis is marked.

m_A	150 GeV	200 GeV	300 GeV	450 GeV	600 GeV	800 GeV
# Tracks	1 or 3	1 or 3	1 or 3	1 or 3	1 or 3	1 or 3
# Jets	< 3	< 3	< 3	< 3	< 3	< 3
MET	> 20 GeV	> 20 GeV	> 25 GeV	> 60 GeV	> 60 GeV	> 60 GeV
$p_{T,h}$	< 90 GeV	> 30 GeV	> 50 GeV	> 90 GeV	> 130 GeV	> 130 GeV
$\Delta\Phi_{\ell h}$	< 3.0	< 3.0	< 3.0	< 3.0	< 3.05	< 3.05
$\Delta\Phi_{\ell h}$	> 1.7	> 2.2	> 2.4	> 2.6	> 2.6	> 2.8

Table 9.3.: The m_A -dependent cuts in the b-tagged analysis. A cut on the number of jets is applied in order to suppress the $t\bar{t}$ contribution which is enhanced in this analysis relative to the non b-tagged analysis.

Similar to the non b-tagged analysis, cuts on p_T , MET and $\Delta\Phi_{\ell h}$ are chosen depending on m_A . In this analysis the cuts were optimized to maximize the statistical significance. In the region of $m_A \geq 600$ GeV the background yield is very low and also the signal cross section is small. Therefore, looser cuts have been used for the highest two mass points to avoid considerable influences

on the cut optimization by statistical fluctuations. The cut values are summarized in Table 9.3. The distributions relevant for the cut analysis are given in Figures 9.9-9.11.

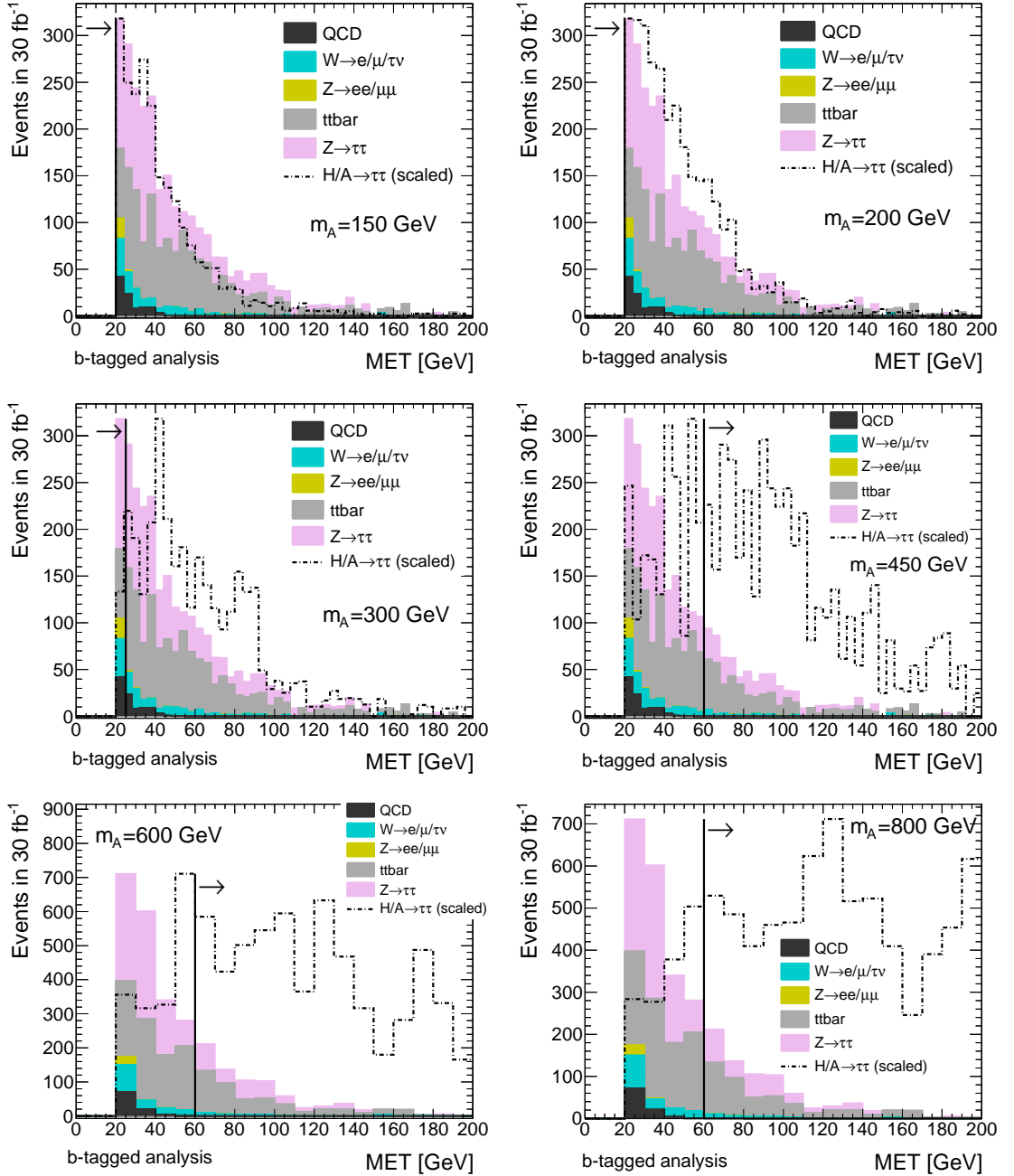


Figure 9.9.: Distributions of MET for signal (dotted black line) and various background processes in the b-tagged analysis for different values of m_A as indicated in the plots. The signal is scaled to the background for better visibility. The cut values are indicated; the arrows point to the events which are kept in the analysis. The plots were prepared with the baseline cuts and the b-veto applied.

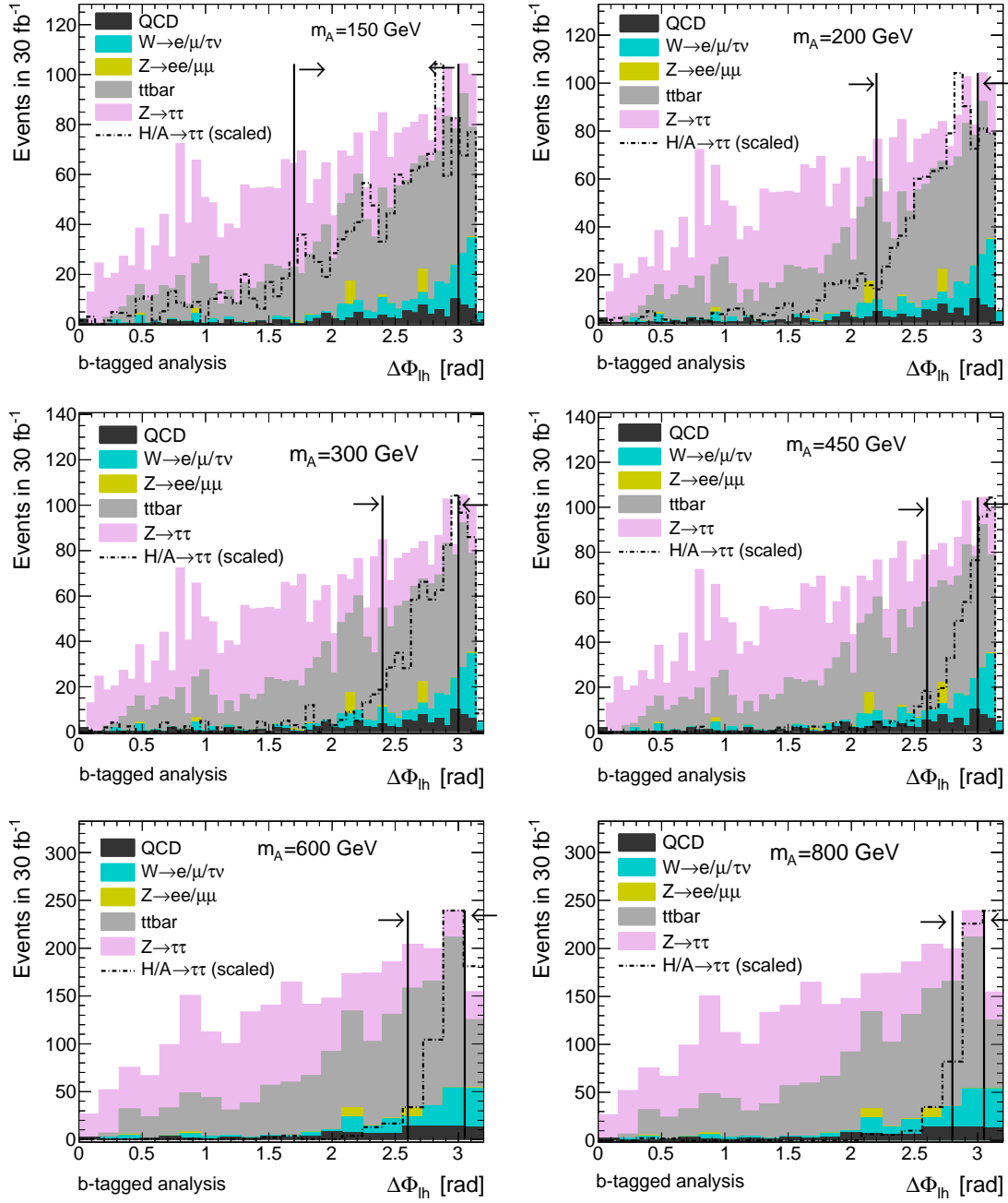


Figure 9.10.: Distributions of $\Delta\Phi_{\ell h}$ for signal (dotted black line) and various background processes in the b-tagged analysis for different values of m_A as indicated in the plots. The signal is scaled to the background for better visibility. The cut values are indicated; the arrows point to the events which are kept in the analysis. The plots were prepared with the baseline cuts and the b-veto applied.

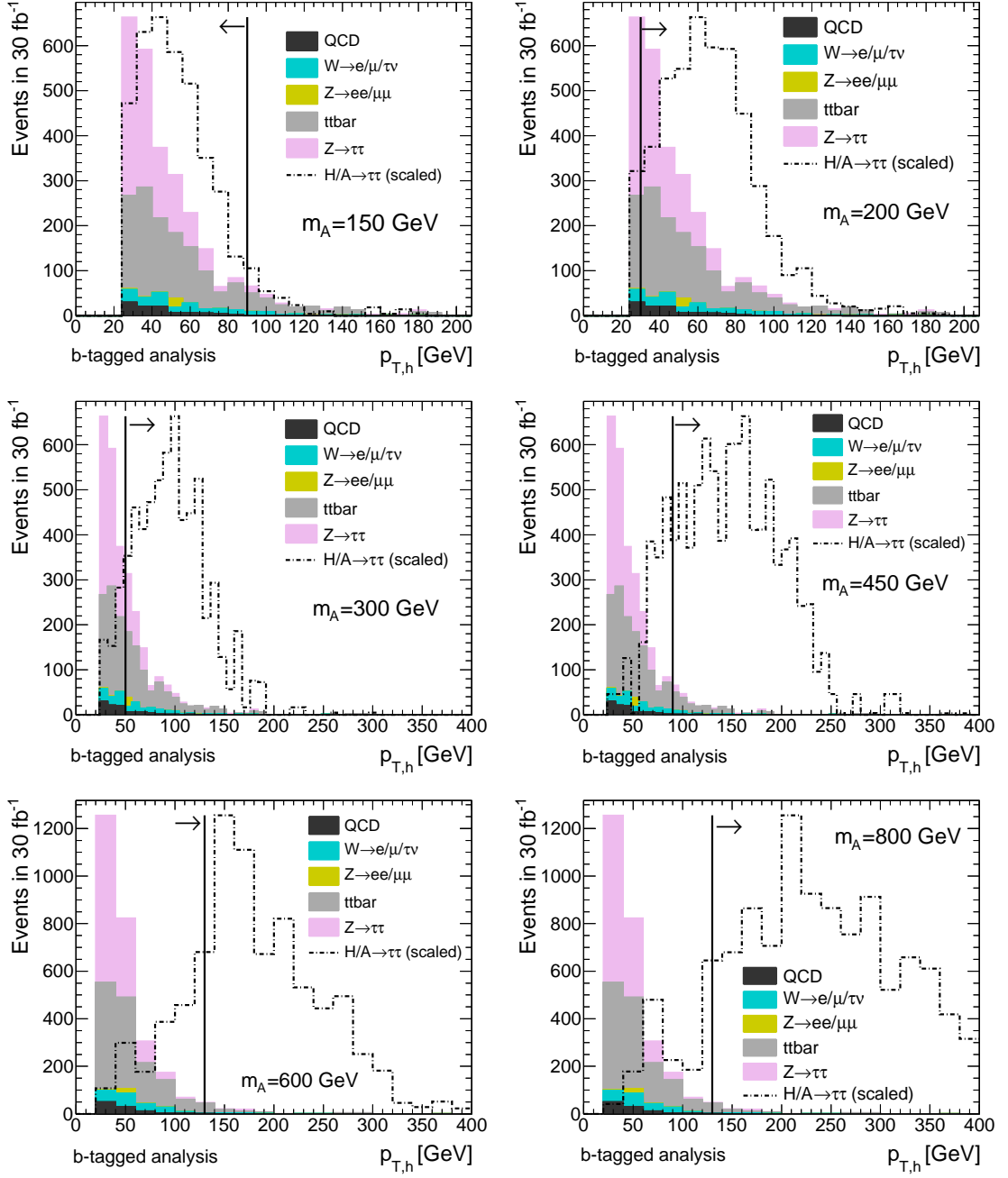


Figure 9.11.: Distributions of $p_{T,h}$ for signal (dotted black line) and various background processes. The value of m_A is indicated in the plots. The signal is scaled to the background for better visibility. The cut values are indicated; the arrows point to the events which are kept in the analysis. The plots were prepared with the baseline cuts, the b-tag and the cut on the number of jets applied.

Mass Window Cut and Correlation to the $\Delta\Phi_{\ell h}$ Cut

The collinear mass is used for the signal extraction. The $m_{\tau\tau}$ windows are chosen to be equal for the non b-tagged and the b-tagged analyses, although the mass resolutions are different for the two signal processes (compare to Figure 7.6). Different mass windows would complicate the analysis unnecessarily, because also in the non b-tagged analysis a contribution from b-associated Higgs boson signal appears, and vice versa. The mass window cut values are listed in Table 9.4.

m_A [GeV]	150	200	300	450	600	800
$m_{\tau\tau}$ low edge [GeV]	121	145	210	340	420	545
$m_{\tau\tau}$ high edge [GeV]	187	255	370	540	740	915

Table 9.4.: The cut values for the mass window. The same mass window was chosen for the non b-tagged analysis and the b-tagged analysis.

In the distributions visualizing the cut variables (Figures 9.5-9.11), an upper cut on $\Delta\Phi_{\ell h}$ seems poorly chosen since the signal peaks at $\Delta\Phi_{\ell h} \approx \pi$. This cut was intended to improve the mass resolution. As was seen in the dilepton channel (Figure 8.19), the dependence of the significance from a slight $\Delta\Phi_{\ell h}$ cut becomes small if a mass window cut is applied, but only for low values of m_A . In Figure 9.12, the dependence of the $\Delta\Phi_{\ell h}$ distribution on the mass window cut is shown for $m_A = 150$ GeV. The mass window cut removes in particular events with a poorly reconstructed $m_{\tau\tau}$, which are correlated to the fact that $\Delta\Phi_{\ell h} \approx \pi$ (compare also to Figure 7.10). However, despite to applying the mass window, signal events will be lost by cutting on $\Delta\Phi_{\ell h}$. In future studies no such cut should be applied, here it was applied to be more consistent with [124].

9.1.3. Results of the Event Selection

Single Top Contribution

In previous $H/A \rightarrow \tau\tau$ studies the single top contribution was neglected, since its cross section is small compared to $t\bar{t}$. However, since single top also contains true b-jets, this background was included in the b-tagged analysis. In the non b-tagged analysis the b-veto leads to a much smaller $t\bar{t}$ contribution and therefore single top events are neglected.

The procedure of the single top estimation from MC based on cut factorization and comparison with the $t\bar{t}$ background is outlined in Appendix G. The results are considered to be very conservative and they are summarized in Table 9.5. The single top contributions for the three lowest mass points were included indirectly by scaling the $t\bar{t}$ contribution with the corresponding ratio in the last column of Table 9.5. For higher A masses single top background is negligible.

Cut Flows

The cut flows for the signal processes and all background contributions are given in Tables 9.6-9.11. The first table includes the complete cut flow (ie. the baseline selection), the following tables contain only the numbers of the non b-tagged and b-tagged analysis cuts. The numbers are given

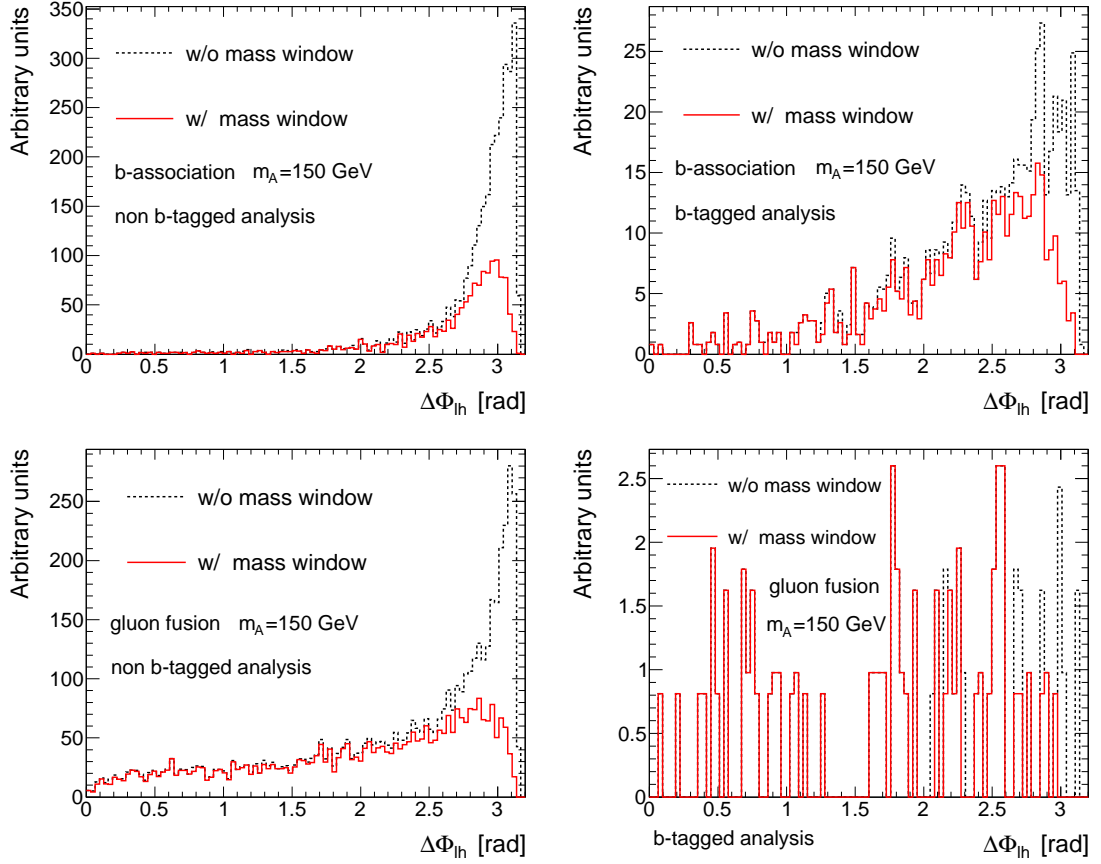


Figure 9.12.: The distributions of $\Delta\Phi_{lh}$ for $m_A = 150$ GeV, not normalized but to the number of MC events. The red solid lines show the distributions when the mass window cut is applied; the dotted black lines show $\Delta\Phi_{lh}$ without this cut. The upper row shows signal events produced in associated with b-quarks, the lower plots contain the signal produced by gluon fusion. The left (right) plots show the $\Delta\Phi_{lh}$ distributions with the b-veto (b-tag). Mostly events with $\Delta\Phi_{lh} \approx \pi$ are removed by the mass window cut.

m_A [GeV]	Single top	$t\bar{t}$	$\frac{\text{Single top}}{t\bar{t}}$
150	0.723	7.481	10.3 %
200	0.517	7.911	6.53 %
300	0.175	5.532	3.16 %

Table 9.5.: Results for the single top estimation in comparison to $t\bar{t}$ in the b-tagged analysis for the three lowest mass points. The numbers in the 2nd and 3rd column are accepted cross sections in fb.

as cross section in fb. The number of events expected in 30 fb^{-1} at $\sqrt{s} = 14 \text{ TeV}$, for example, is then given by the cross section in fb times 30.

	Associated	Fusion	W + jets	Z($\rightarrow \ell\ell$) + jets	Z($\rightarrow \tau\tau$) + jets	$t\bar{t}$	QCD
Total	4.3e+03	9.7e+02	2.6e+07	3.2e+06	3.1e+05	4.5e+05	2.2e+08
Lepton Preselection	6.2e+02	2.1e+02	1.3e+07	8.5e+05	8.6e+04	1.7e+05	4.2e+05
$E_T^{\text{miss}} > 20\text{GeV}$	3.4e+02	1.2e+02	1.2e+07	2.7e+05	3.2e+04	1.5e+05	7.3e+04
$m_{\tau\tau} < 25\text{GeV}$	1.5e+02	80	1.1e+05	1.2e+04	1.4e+04	1.7e+04	4.6e+04
$n_\tau = 1$	70	37	4.9e+04	2.1e+03	2.5e+03	9.9e+02	1.4e+04
τ ID	57	29	1.3e+03	1.6e+02	1.9e+03	6e+02	1.6e+02
Coll. Approx.	28	17	4.8e+02	65	1.1e+03	2.8e+02	72
Opposite sign leptons	28	17	2.8e+02	49	1.1e+03	2.4e+02	39
non b-tagged	22	16	2.7e+02	48	1e+03	56	35
$p_{T,h} > 40\text{GeV}$	19	12	1.7e+02	22	4.9e+02	36	15
$\Delta\Phi_{lh} < 3.00\text{rad}$	10	9.3	1.2e+02	18	3.9e+02	32	11
$121\text{ GeV} < m_{\tau\tau} < 187\text{ GeV}$	6.7	7.6	29	8.3	52	5.8	4.1
b-tagged	5.7	0.39	9.5	1.3	58	1.8e+02	4.5
$\eta_{\text{jets}} < 3$	4.7	0.2	6.5	0.92	39	46	3
$p_{T,h} < 90\text{GeV}$	4.4	0.17	5.8	0.91	38	40	2.9
$\Delta\Phi_{lh} < 3.00\text{rad}$	3.9	0.16	5.3	0.9	37	37	2.5
$\Delta\Phi_{lh} > 1.70\text{rad}$	3.3	0.12	3.5	0.85	14	26	1.8
$121\text{ GeV} < m_{\tau\tau} < 187\text{ GeV}$	2.6	0.093	1.4	0.33	2.1	8.1	0.57

Table 9.6.: Full cut flow of the signal and background processes in fb for the Higgs boson mass hypothesis of $m_A = 150\text{GeV}$ at $\tan\beta = 10$. Numbers for the two signal production modes where the Higgs boson is produced either in association with b-quarks (associated) or by gluon fusion (fusion) are given separately.

	Associated	Fusion	W + jets	$Z(\rightarrow \ell\ell) + \text{jets}$	$Z(\rightarrow \tau\tau) + \text{jets}$	$\bar{t}\bar{t}$	QCD
Total	1.8e+03	2.2e+02	2.6e+07	3.2e+06	3.1e+05	4.4e+05	2.2e+08
Baseline	24	6.8	2.8e+02	49	1.1e+03	2.3e+02	39
non b-tagged	19	6.7	2.7e+02	48	1e+03	54	35
$p_{T,h} > 50\text{GeV}$	15	5.1	1.3e+02	12	2.8e+02	27	9.6
$\Delta\Phi_{\ell h} < 3.00\text{ rad}$	7.3	3.5	87	8.5	2.3e+02	23	6.9
$145\text{ GeV} < m_{\tau\tau} < 255\text{ GeV}$	5.6	3.1	34	4.5	28	8.5	3.8
b-tagged	5.4	0.14	9.5	1.3	58	1.8e+02	4.5
$n_{\text{jets}} < 3$	4.5	0.083	6.5	0.92	39	45	3
$p_{T,h} > 30\text{GeV}$	4.2	0.082	5.1	0.86	28	39	2.3
$\Delta\Phi_{\ell h} < 3.00\text{ rad}$	3.5	0.077	4.5	0.85	28	35	2
$\Delta\Phi_{\ell h} > 2.20\text{ rad}$	2.9	0.04	2.2	0.78	5.3	20	1.3
$145\text{ GeV} < m_{\tau\tau} < 255\text{ GeV}$	2.4	0.036	0.91	0.33	1.5	8.2	0.46

Table 9.7.: Cut flow of the signal and background processes in fb, for the Higgs boson mass hypothesis of $m_A = 200\text{GeV}$, at $\tan\beta = 10$. Numbers for the two signal production modes where the Higgs boson is produced either in association with b-quarks (associated) or by gluon fusion (fusion) are given separately.

	Associated	Fusion	W + jets	$Z(\rightarrow \ell\ell) + \text{jets}$	$Z(\rightarrow \tau\tau) + \text{jets}$	$\bar{t}t$	QCD
Total	8.1e+02	47	2.6e+07	3.2e+06	3.1e+05	4.3e+05	2.2e+08
Baseline	21	2.5	2.8e+02	49	1.1e+03	2.4e+02	39
non b-tagged	16	2.5	2.7e+02	48	1e+03	53	35
1-prong τ	11	1.7	64	37	6.5e+02	26	10
$p_{T,h} > 70\text{GeV}$	8.5	1.2	18	2.6	78	6.6	1.3
$\Delta\Phi_{\ell h} < 3.00\text{ rad}$	3.4	0.74	12	2	64	5.4	0.79
$210\text{ GeV} < m_{\tau\tau} < 370\text{GeV}$	2.9	0.66	4.9	0.6	5.2	2.2	0.4
b-tagged	5.2	0.064	9.5	1.3	58	1.8e+02	4.5
$n_{\text{jets}} < 3$	4.3	0.037	6.5	0.92	39	44	3
$E_{\text{T}}^{\text{miss}} > 25\text{GeV}$	4.1	0.037	5.3	0.092	33	41	1.7
$p_{T,h} > 50\text{GeV}$	3.6	0.033	2.3	0.048	8.6	20	0.42
$\Delta\Phi_{\ell h} < 3.00\text{ rad}$	2.7	0.028	2	0.048	8.4	17	0.34
$\Delta\Phi_{\ell h} > 2.40\text{ rad}$	2.2	0.017	1.1	0.028	0.29	9.3	0.24
$210\text{ GeV} < m_{\tau\tau} < 370\text{GeV}$	1.8	0.015	0.53	0.0064	0.17	5.6	0.16

Table 9.8.: Cut flow of the signal and background processes in $t\bar{t}$, for the Higgs boson mass hypothesis $m_A = 300\text{ GeV}$, at $\tan\beta = 15$. Numbers for the two signal production modes where the Higgs boson is produced either in association with b-quarks (associated) or by gluon fusion (fusion) are given separately.

	Associated	Fusion	W + jets	Z($\rightarrow \ell\ell$) + jets	Z($\rightarrow \tau\tau$) + jets	$t\bar{t}$	QCD
Total	2.2e+02	8.5	2.6e+07	3.2e+06	3.1e+05	4.1e+05	2.2e+08
Baseline	8.4	0.65	2.8e+02	49	1.1e+03	2.4e+02	39
non b-tagged	6.5	0.64	2.7e+02	48	1e+03	51	35
1-prong τ	4.6	0.45	64	37	6.5e+02	25	10
$p_{T,h} > 90\text{GeV}$	3.8	0.37	11	1	40	4.3	0.61
$\Delta\Phi_{\ell h} < 3.00\text{ rad}$	1.1	0.19	7.1	0.92	32	3.4	0.35
$340\text{ GeV} < m_{\tau\tau} < 540\text{ GeV}$	0.82	0.18	2.4	0.14	1.3	0.94	0.071
b-tagged	1.9	0.016	9.5	1.3	58	1.7e+02	4.5
$n_{\text{jets}} < 3$	1.6	0.0086	6.5	0.92	39	42	3
$E_{\text{T}}^{\text{miss}} > 60\text{GeV}$	1.1	0.0079	2.1	0.022	10	15	0.01
$p_{T,h} > 90\text{GeV}$	0.96	0.0072	0.35	0.0064	0.89	2.8	0.0033
$\Delta\Phi_{\ell h} < 3.00\text{ rad}$	0.59	0.0061	0.24	0.0064	0.85	2.3	0.0031
$\Delta\Phi_{\ell h} > 2.60\text{ rad}$	0.51	0.0024	0.15	0.0064	0.063	1.2	0.0027
$340\text{ GeV} < m_{\tau\tau} < 540\text{ GeV}$	0.44	0.0021	0.045	0	0.031	0.46	0.00015

Table 9.9.: Cut flow of the signal and background processes in fb, for the Higgs boson mass hypothesis $m_A = 450\text{GeV}$, at $\tan\beta = 20$. Numbers for the two signal production modes where the Higgs boson is produced either in association with b-quarks (associated) or by gluon fusion (fusion) are given separately.

	Associated	W + jets	Z($\rightarrow \ell\ell$) + jets	Z($\rightarrow \tau\tau$) + jets	$t\bar{t}$	QCD
Total	1.6e+02	2.6e+07	3.2e+06	3.1e+05	4.1e+05	2.2e+08
Baseline	6.9	2.8e+02	49	1.1e+03	2.4e+02	39
non b-tagged	5.1	2.7e+02	48	1e+03	51	35
$E_{\tau}^{\text{miss}} > 60\text{GeV}$	3.9	69	0.7	2e+02	23	0.15
1-prong τ	2.8	18	0.17	1.4e+02	12	0.049
$p_{T,h} > 100\text{GeV}$	2.6	4.4	0.034	18	2.2	0.017
$\Delta\Phi_{\ell h} < 3.05\text{ rad}$	1.1	3.1	0.026	15	1.9	0.006
$420\text{ GeV} < m_{\tau\tau} < 740\text{ GeV}$	0.95	1.1	0.0045	0.9	0.45	0.0028
b-tagged	1.8	9.5	1.3	58	1.7e+02	4.5
$\eta_{\text{jets}} < 3$	1.4	6.5	0.92	39	42	3
$E_{\tau}^{\text{miss}} > 60\text{GeV}$	1.1	2.1	0.022	10	15	0.01
$p_{T,h} > 130\text{GeV}$	0.93	0.13	0.0064	0.53	0.88	0.00067
$\Delta\Phi_{\ell h} < 3.05\text{ rad}$	0.66	0.11	0.0064	0.52	0.81	0.00044
$\Delta\Phi_{\ell h} > 2.60\text{ rad}$	0.62	0.058	0.0064	0.038	0.45	0.0002
$420\text{ GeV} < m_{\tau\tau} < 740\text{ GeV}$	0.54	0.026	0	0.02	0.21	3.9e-05

Table 9.10.: Cut flow of the signal and background processes in fb, for the Higgs boson mass hypothesis $m_A = 600\text{ GeV}$, at $\tan\beta = 30$. Numbers for the signal where the Higgs boson is produced in association with b-quarks (associated) are given.

	Associated	W + jets	$Z(\rightarrow \ell\ell) + \text{jets}$	$Z(\rightarrow \tau\tau) + \text{jets}$	$\bar{t}\bar{t}$	QCD
Total	1.1e+02	2.6e+07	3.2e+06	3.1e+05	4.1e+05	2.2e+08
Baseline	5	2.8e+02	49	1.1e+03	2.4e+02	39
non b-tagged	3.6	2.7e+02	48	1e+03	51	35
$E_T^{\text{miss}} > 60\text{GeV}$	2.9	69	0.7	2e+02	23	0.15
1-prong τ	2.3	18	0.17	1.4e+02	12	0.049
$p_{T,h} > 100\text{ GeV}$	2.2	4.4	0.034	18	2.2	0.017
$\Delta\Phi_{\ell h} < 3.05\text{ rad}$	0.83	3.1	0.026	15	1.9	0.006
$545\text{ GeV} < m_{\tau\tau} < 915\text{ GeV}$	0.7	0.69	0.004	0.42	0.21	0.0019
b-tagged	1.4	9.5	1.3	58	1.7e+02	4.5
$n_{\text{jets}} < 3$	1	6.5	0.92	39	42	3
$E_T^{\text{miss}} > 60\text{GeV}$	0.87	2.1	0.022	10	15	0.01
$p_{T,h} > 130\text{GeV}$	0.78	0.13	0.0064	0.53	0.88	0.00067
$\Delta\Phi_{\ell h} < 3.05\text{ rad}$	0.52	0.11	0.0064	0.52	0.81	0.00044
$\Delta\Phi_{\ell h} > 2.80\text{ rad}$	0.41	0.04	0.0064	0.033	0.45	0.00014
$545\text{ GeV} < m_{\tau\tau} < 915\text{ GeV}$	0.35	0.014	0	0.014	0.065	1.6e-05

Table 9.11.: Cut flow of the signal and background processes in fb, for the Higgs boson mass hypothesis $m_A = 800\text{GeV}$, at $\tan\beta = 45$. Numbers for the signal where the Higgs boson is produced in association with b-quarks (associated) are given.

Final Mass Spectra

The final $m_{\tau\tau}$ distributions resulting from each of the m_A -dependent analyses are presented in Figures 9.13-9.14. The left hand side plots show the results for the non b-tagged analyses. Here, the contributions from $Z(\rightarrow \tau\tau) + \text{jets}$ and $W + \text{jets}$ are considerably large. In the right hand side plots the results for the b-tagged analyses are visualized. Here, the contribution of $t\bar{t}$ is much larger in comparison to the non b-tagged analyses.

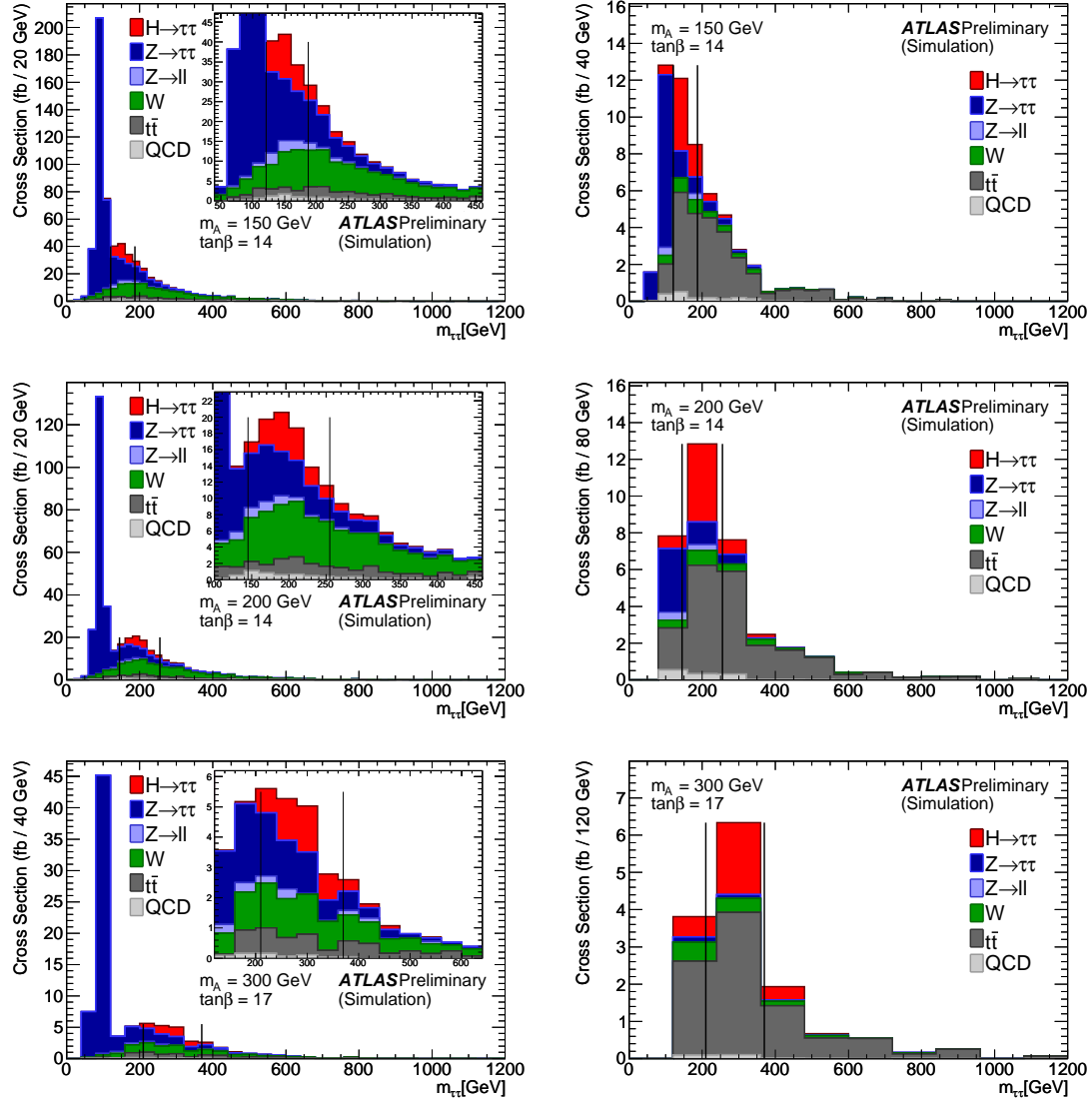


Figure 9.13.: The collinear mass spectra for $m_A = 150$ GeV (1st row), $m_A = 200$ GeV (2nd row) and $m_A = 300$ GeV (3rd row), left for the non b-tagged analysis and right for the b-tagged analysis. The results are scaled to 30 fb^{-1} , the signal cross sections are evaluated for different values of $\tan\beta$ as indicated in the plots. The histograms give cross sections in fb.

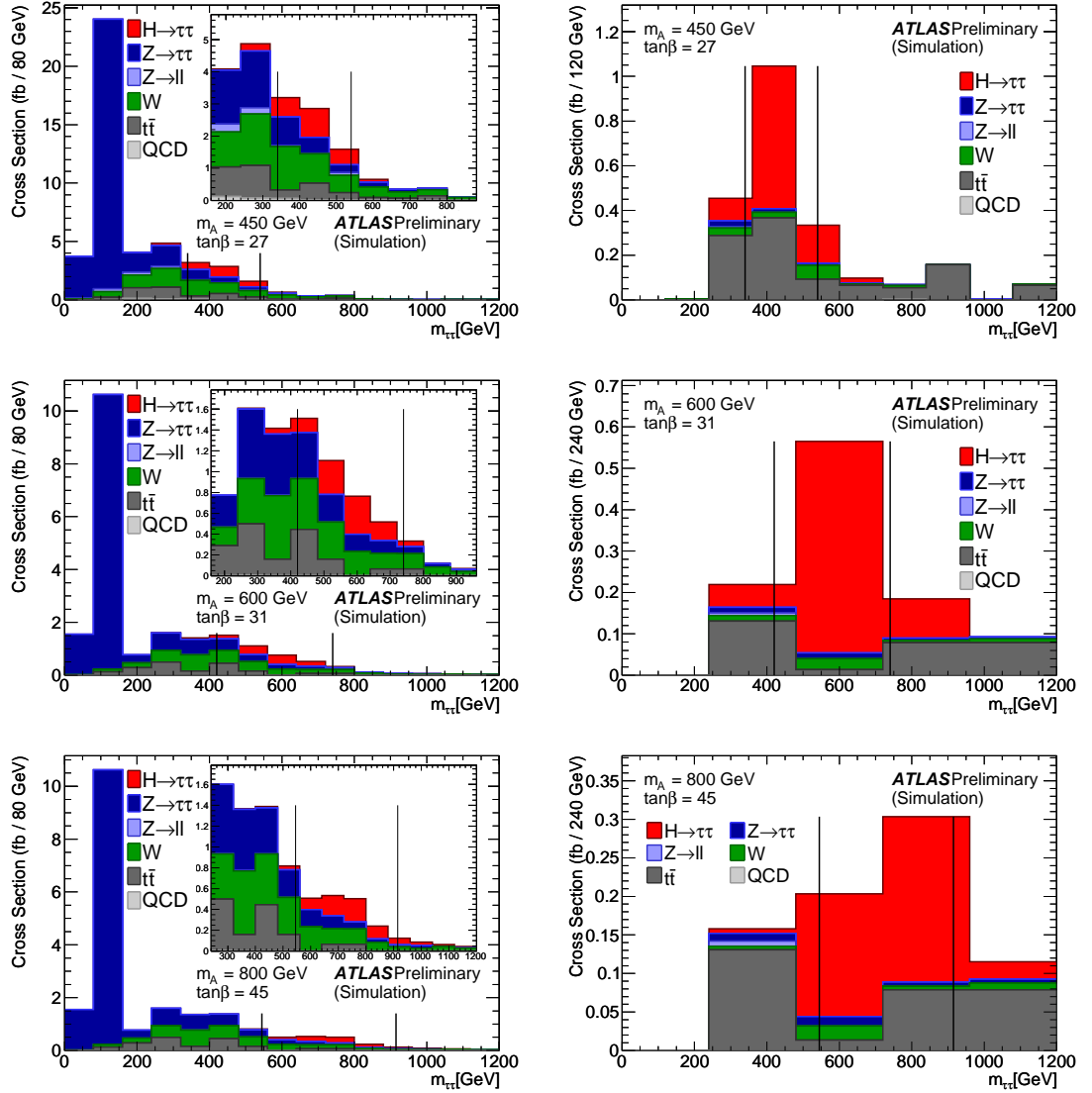


Figure 9.14.: The collinear mass spectra for $m_A = 450$ GeV (1st row), $m_A = 600$ GeV (2nd row) and $m_A = 800$ GeV (3rd row), left for the non b-tagged analysis and right for the b-tagged analysis. The results are scaled to 30 fb^{-1} , the signal cross sections are evaluated for different values of $\tan\beta$ as indicated in the plots. The histograms give cross sections in fb.

9.2. Systematic Uncertainties

9.2.1. Sources of Systematic Uncertainties

Detector-related uncertainties have already been discussed for the dilepton analysis in Chapter 8. The same uncertainties are relevant in this analysis. However, in the lepton-hadron analysis additional uncertainties arise from the identification of hadronically decaying τ -leptons. They are listed below:

- τ energy scale: $\pm 5\%$,
- τE_T resolution $\sigma(E_T) = 0.45 \cdot \sqrt{E_T}$,
- τ reconstruction efficiency: $\pm 5\%$.

The MET is corrected accordingly after each scale and resolution variation is applied, see Equation 8.3. As it is the case for the QCD jets, also for the hadronic τ system the impact on the MET scale is assumed to be only 5%. Similar as was done in the lepton-lepton analysis, the variations have been applied one-by-one and the impact on the number of events passing the selection was evaluated. Assuming no correlations, the total uncertainty is then the sum of the squares of the individual uncertainties.

9.2.2. Data-driven $t\bar{t}$ Background Estimation in the b-tagged Analysis

The $t\bar{t}$ background is the dominant background process in the b-tagged analysis since it contains true b-jets. A large cross section uncertainty of 12% demands for the use of a data-driven background estimation procedure. In the following two approaches will be discussed: The first method is based on the jet multiplicity distribution which is estimated from control regions. The second method used the same control regions and is not based on the multiplicity distribution but uses an extrapolation ratio. Both methods aim at the estimation of the number of $t\bar{t}$ events in the signal region and not at the estimation of the $m_{\tau\tau}$ shape.

$t\bar{t}$ Estimation Using Jet Multiplicities

$t\bar{t}$ events show higher jet multiplicities than any other SM background process and the Higgs boson events. For jet multiplicities higher than three $t\bar{t}$ is the dominant process. This is used to estimate its contribution to the Higgs boson signal regions at low jet multiplicities. Exploiting the jet multiplicity is a general method used for example in measurements of the $t\bar{t}$ cross section [125]. However, using the jet multiplicity to estimate the $t\bar{t}$ contribution in a Higgs boson analysis is investigated here for the first time. In the following the method will be outlined and applied to the b-tagged analyses for Higgs boson masses below 450 GeV. The results of this work were published in [124].

Figure 9.15 shows the jet multiplicity distribution for various processes after the basic object selection and the requirement of at least one b-tagged jet. No cut on the number of jets was applied.

A $t\bar{t}$ control region is defined for each Higgs boson mass hypothesis in order to get a handle on the $t\bar{t}$ jet multiplicity distribution from data. This control region is constructed such that it contains $t\bar{t}$ events with a very high purity. A precondition of the method is that the multiplicity spectra are

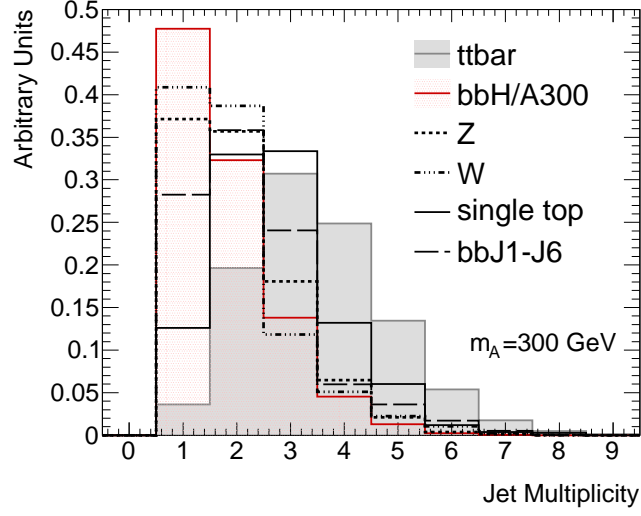


Figure 9.15.: Jet multiplicity distribution after basic object selection and at least one b-jet has been found. $t\bar{t}$ events show a higher jet multiplicity than all other processes. The distributions are normalized to unity.

similar for the $t\bar{t}$ events in the signal and control regions. This, however, requires the tuning of cuts which are correlated to the jet multiplicity distribution.

The correct normalization of the multiplicity distribution is achieved by dropping the cut on the number of jets to be less than three in the signal region. This cut was established to suppress $t\bar{t}$ events, but for the $t\bar{t}$ estimation this cut is not applied. Dropping this cut opens another $t\bar{t}$ control region, but this region will still be labeled as signal region to avoid confusion. The low jet multiplicity bins are populated by Higgs boson events and various background processes, but the bins containing events with many jets are dominated by $t\bar{t}$ events.

The bins with a high jet multiplicity from the control region are scaled to the integral of the bins with a high jet multiplicity of the signal region. The bins used for the normalization contain events with more than three jets. The bin with the number of jets equal to three is not used for the normalization because it is usually highly contaminated by other processes. Also, the migration of events from neighboring bins is therefore suppressed.

The normalization method can conveniently be written as a single formula. The number of $t\bar{t}$ events in the signal region at low multiplicities $N_{t\bar{t}, \text{signal region}}^{n_{\text{jets}} < 3}$ is calculated as follows:

$$N_{t\bar{t}, \text{signal region}}^{n_{\text{jets}} < 3} = N_{\text{control region}}^{n_{\text{jets}} < 3} \cdot \frac{N_{\text{signal region}}^{n_{\text{jets}} > 3}}{N_{\text{control region}}^{n_{\text{jets}} > 3}}. \quad (9.3)$$

Here, $N_{\text{control region}}^{n_{\text{jets}} < 3}$ is the number of events in the $t\bar{t}$ control region containing less than three jets. The shape of these jet multiplicity needs to be equal to the shape of the multiplicity in the signal region in order for the method to give correct results. $N_{\text{signal region}}^{n_{\text{jets}} > 3}$ is the number of events in the signal region if the events contain more than three jets, and $N_{\text{control region}}^{n_{\text{jets}} > 3}$ is the number of events in the $t\bar{t}$ control region containing more than three jets.

The advantage of using this method is that the amount of input from MC simulation is reduced. The simulated data was only needed to tune the cuts to obtain similar jet multiplicities in both signal and control regions. In particular, the $t\bar{t}$ cross section is not needed as an input. Therefore, the large uncertainty of 12% of $\sigma_{t\bar{t}}$ now becomes irrelevant. The luminosity uncertainty also cancel in the ratio. The $t\bar{t}$ jet multiplicity shape is extracted from data and then normalized to that in the signal region also by using data. Therefore it becomes completely irrelevant whether, for example, the b-tagging efficiency is larger in data than expected in MC. Remaining systematic uncertainties, however, arise from the tuning of the cuts and remaining impurities in the control regions and the signal regions at large multiplicities. They are discussed below.

Using this method only the number of $t\bar{t}$ events can be extracted from data, not its $m_{\tau\tau}$ shape. In a counting experiment, the background shape is in principle not needed, except when a mass window cut is applied. This method is able to give an estimate of the number of $t\bar{t}$ events inside the mass window. This is achieved by using the jet multiplicity distribution in the signal region only for events passing all cuts including the mass window cut.

For using the method a reasonable amount of events is needed. The expected numbers of $t\bar{t}$ events in 30 fb^{-1} for the analyses of $m_A = 600 \text{ GeV}$ and $m_A = 800 \text{ GeV}$ are too low for this estimation procedure. This is a consequence of the analysis strategy that at each Higgs boson mass hypothesis the cuts have been chosen separately for obtaining the best significance. Since the H/A bosons will be the heaviest objects in the event, they can be selected with only very little background. Irreducible background processes are expected to be very small in the search for Higgs bosons with masses above 500 GeV (this will be discussed again at the end of this chapter).

$t\bar{t}$ Control Regions

The $t\bar{t}$ control regions are constructed such that they contain large amounts of $t\bar{t}$ events and only very little contamination from other backgrounds and Higgs boson events. At the same time it is checked that the multiplicity distributions of the $t\bar{t}$ events are similar between control and signal region.

Cut / m_A	150 GeV	200 GeV	300 GeV	450 GeV
$\Delta\Phi_{\ell h}$	> 1.7	> 2.2	> 2.4	-
	< 3.0	< 3.0	< 3.0	-
$p_{T,h}$	$> 24 \text{ GeV}$	$> 30 \text{ GeV}$	$> 50 \text{ GeV}$	$> 90 \text{ GeV}$
$p_{T,\ell}$	$> 24 \text{ GeV}$	$> 24 \text{ GeV}$	$> 24 \text{ GeV}$	$> 24 \text{ GeV}$
$p_{T,b\text{-jet}}$	$> 50 \text{ GeV}$	$> 60 \text{ GeV}$	$> 20 \text{ GeV}$	$> 20 \text{ GeV}$
m_{vis}	$> 100 \text{ GeV}$	$> 100 \text{ GeV}$	$> 100 \text{ GeV}$	$> 100 \text{ GeV}$
		$< 140 \text{ GeV}$	$< 140 \text{ GeV}$	$< 140 \text{ GeV}$
$p_{T,\text{miss}}$	$> 100 \text{ GeV}$	$> 100 \text{ GeV}$	$> 100 \text{ GeV}$	$> 100 \text{ GeV}$
m_T	$> 0 \text{ GeV}$	$> 10 \text{ GeV}$	$> 80 \text{ GeV}$	$> 80 \text{ GeV}$

Table 9.12.: Cut values for the $t\bar{t}$ control regions. m_A -dependent control regions were constructed to get a good resemblance of the jet multiplicity distributions for $t\bar{t}$ events from signal and control regions.

The cuts for the control regions are found by starting from the same cuts as for the signal region and basically inverting the cut on the transverse mass, m_T , since this cut strongly suppresses W+jets events and $t\bar{t}$ events. The requirement of tight lepton isolation is dropped in order to reduce the relative contribution of backgrounds containing real leptons such as $W \rightarrow e\nu$ and $W \rightarrow \mu\nu$ and to gain more $t\bar{t}$ statistics. The cut on the number of jets to be less than three is dropped as well as the requirements on x_1 and x_2 and the cut on the $m_{\tau\tau}$ mass window. Trigger efficiencies have been folded in exactly as it was done for the signal regions. Other cuts such as the p_T of the leading b-jet, MET and the visible mass, m_{vis} , are used to further increase the $t\bar{t}$ purity. Finally, the cut on m_T has then been tuned in steps of 10 GeV for best agreement of the jet multiplicity distributions between signal and control region in the low multiplicity bins. Table 9.12 lists the control region cuts for the various Higgs boson mass hypotheses.

The object definitions have been described in Chapter 6. The jets are reconstructed by a Cone algorithm with a cone size of 0.4. Jets are required to have a minimum p_T of 20 GeV. Tight tau identification is required in all of the regions used. For the W boson, QCD, $Z \rightarrow ee$ and $Z \rightarrow \mu\mu$ backgrounds the tight τ ID efficiency was applied as an event weight.

The single top contribution was neglected due to the limited MC statistics. Former studies and the results from the single top estimation in the signal region suggest that its contributions is small (less than 10% compared to $t\bar{t}$). The uncertainties from the cut factorization are large. In the signal region these uncertainties were compensated by multiplying the number of remaining single top events with a factor 1.5. However, for the $t\bar{t}$ estimation method an overestimation of the single top contribution would spoil the results unnecessarily.

Process / m_A	150 GeV	200 GeV	300 GeV	450 GeV
$t\bar{t}$	5210.8	1726.3	836.7	339.9
$Z \rightarrow \tau\tau$	20.4	3.8	3.8	0
$Z \rightarrow ee$	0	0	0	0
$Z \rightarrow \mu\mu$	0.4	0.1	0	0
$W \rightarrow e\nu$	32	7.3	1.4	0.8
$W \rightarrow \mu\nu$	44.2	12.5	3.9	2.6
$W \rightarrow \tau\nu$	13	4.8	0.5	0.6
$A/H \rightarrow \tau\tau$	0	9.9	3.7	1.4
QCD	44.5	2.6	0.9	2.1
Purity [%]	97.1	97.7	98.3	97.8

Table 9.13.: Composition of the $t\bar{t}$ control regions and $t\bar{t}$ purity for various Higgs boson mass hypotheses. The table shows the expected number of events normalized to an integrated luminosity of 30fb^{-1} at $\sqrt{s} = 14$ TeV. The contributions from the Higgs boson processes have been evaluated at $\tan\beta = 45$.

Table 9.13 gives the composition of the processes in the control regions and the purity of the $t\bar{t}$ contribution. The $t\bar{t}$ purity is at least 97%. When the cut on the number of jets is dropped in the signal region, the high jet multiplicity bins represent another $t\bar{t}$ control region (used for the normalization). The composition of these regions for jet multiplicities larger than three was also

checked and the $t\bar{t}$ purity was evaluated. The results are summarized in Table 9.14. It was found that the $t\bar{t}$ purity in the high multiplicity bins in the signal region depends on the value of $\tan\beta$. If $\tan\beta$ is large, more signal will accumulate in particular in the four jet bin. Thus, it must be concluded, that the cuts chosen are sub-optimal in case a large value of $\tan\beta$ is realized in nature. It should be noted, however, that if $\tan\beta > 30$ a Higgs boson signal will be hard to miss, even when there are large uncertainties of the $t\bar{t}$ background. The method becomes more important for low values of $\tan\beta$. If $\tan\beta$ is small, it is much more important to control the systematic uncertainties of the backgrounds.

Process / m_A	150 GeV	200 GeV	300 GeV	450 GeV
$t\bar{t}$	254.5	258.8	161.3	36.5
$Z \rightarrow \tau\tau$	0	24.2	46.9	0
$Z \rightarrow ee$	0	0	0	0
$Z \rightarrow \mu\mu$	0.9	0.3	0	0
$W \rightarrow e\nu$	4.9	6.2	1.3	0
$W \rightarrow \mu\nu$	7.7	7	2.3	0
$W \rightarrow \tau\nu$	3.1	2.1	2.2	0.3
QCD	11.9	4	0.9	0
$A/H \rightarrow \tau\tau, \tan\beta = 5$	0.5	0.8	0.2	0.1
$A/H \rightarrow \tau\tau, \tan\beta = 20$	7.6	12.1	3.4	0.9
$A/H \rightarrow \tau\tau, \tan\beta = 45$	42	64.7	21.3	7.1
Purity [%], $\tan\beta = 5$	88.6	92.7	75	99.1
Purity [%], $\tan\beta = 20$	87.5	82.2	73.9	96.8
Purity [%], $\tan\beta = 45$	78.3	70.4	68.3	83.3

Table 9.14.: Composition of the signal regions for events containing at least three jets. The table shows the expected numbers of events normalized to an integrated luminosity of 30fb^{-1} . The signal contributions have been evaluated for three different values of $\tan\beta$ and the purity is stated for each $\tan\beta$ hypothesis.

Figures 9.16-9.17 display the jet multiplicity distributions for each Higgs boson mass hypothesis including contributions from all background processes considered and the Higgs boson events at high $\tan\beta$. The agreement of the distributions of the $t\bar{t}$ events between control and signal regions after normalizing them to jet multiplicities higher than three is also illustrated. Important hereby is the match between the shapes in the first two jet bins, since there the Higgs boson signal is expected to accumulate.

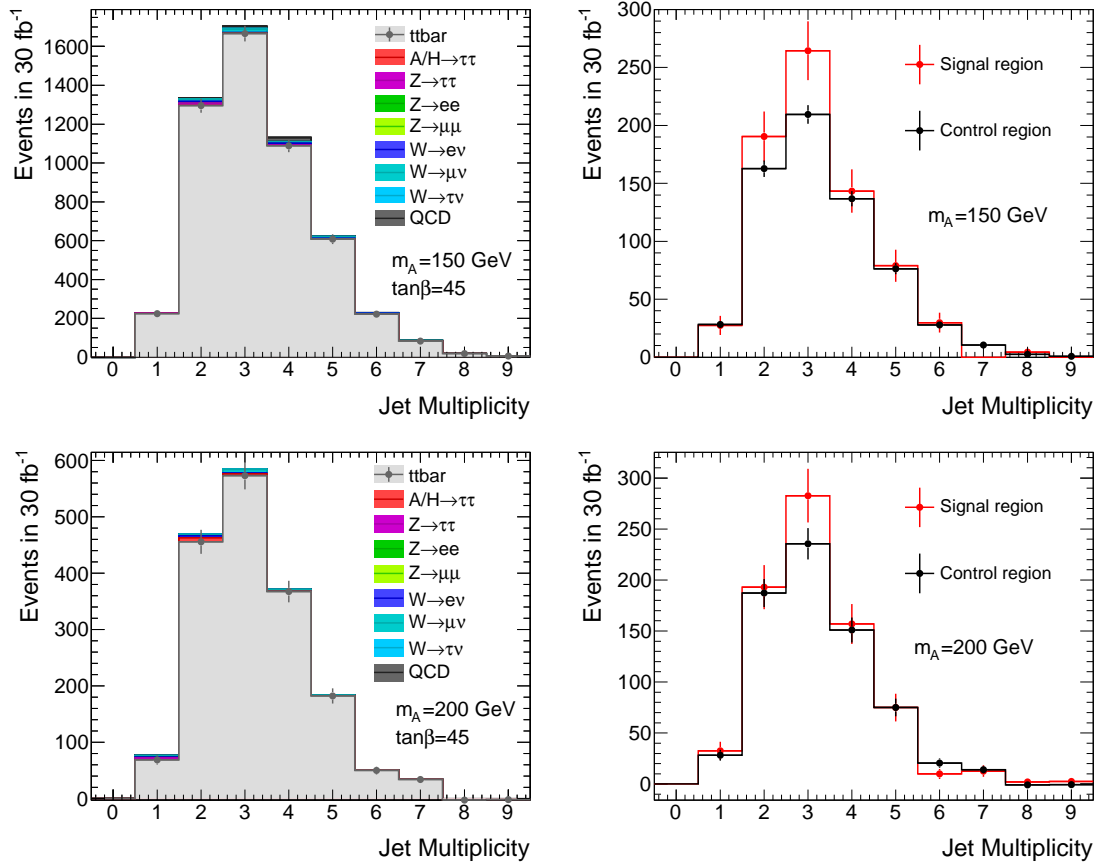


Figure 9.16.: Left: Jet multiplicity distribution in the control regions for $m_A = 150$ GeV (upper plots) and $m_A = 200$ GeV (lower plots) normalized to an integrated luminosity of 30 fb^{-1} . The expected statistical uncertainties for 30 fb^{-1} of the number of $t\bar{t}$ events are indicated. Right: Comparison of the multiplicity distributions for the $t\bar{t}$ events from signal and control region after normalization to the integral of the bins with a number of jets larger than three. Here, uncertainties arising from the available Monte Carlo statistics are marked.

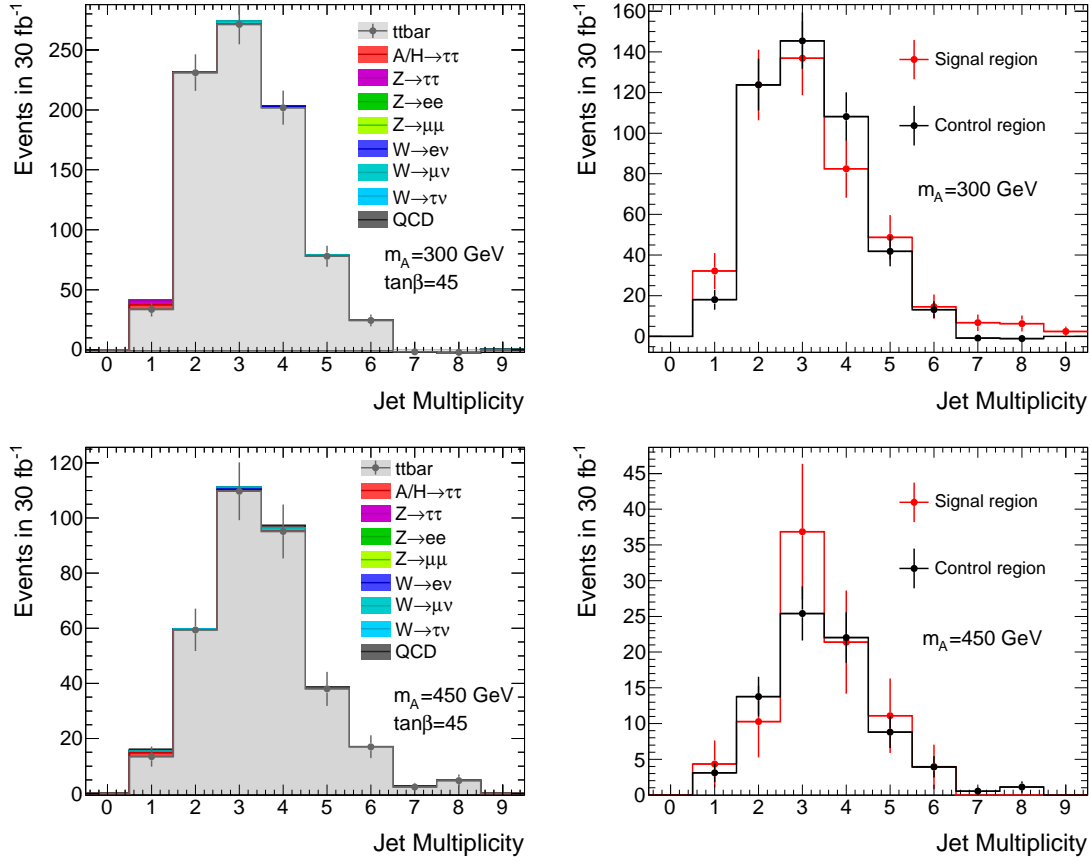


Figure 9.17.: Left: Jet multiplicity distribution in the control regions for $m_A = 300$ GeV (upper plots) and $m_A = 450$ GeV (lower plots) normalized to an integrated luminosity of 30 fb^{-1} . The expected statistical uncertainties for 30 fb^{-1} of the number of $t\bar{t}$ events are indicated. Right: Comparison of the multiplicity distributions for the $t\bar{t}$ events from signal and control region after normalization to the integral of the bins with a number of jets larger than three. Here, uncertainties arising from the available Monte Carlo statistics are marked.

Results of the $t\bar{t}$ Estimation Using Jet Multiplicities

Figure 9.18 illustrates the jet multiplicity distributions in the signal regions with the dropped cut on the number of jets. The multiplicity distribution obtained from the control region is normalized to the high multiplicity bins of the signal regions and is displayed as well. The lowest high multiplicity bin ($\# \text{jets} = 4$) from the signal region show some contaminations from background processes such as Z boson and W boson decays, especially for low Higgs boson masses. A very good agreement between the estimated $t\bar{t}$ jet multiplicity distribution from the control region and the $t\bar{t}$ jet multiplicity distribution from the signal region is observed for the low mass analyses. For $m_A = 300$ GeV and $m_A = 450$ GeV the resemblance is not good but still reasonable, taking into account the larger statistical uncertainties.

Tables 9.15-9.17 list the expected and estimated number of $t\bar{t}$ events and statistical uncertainties

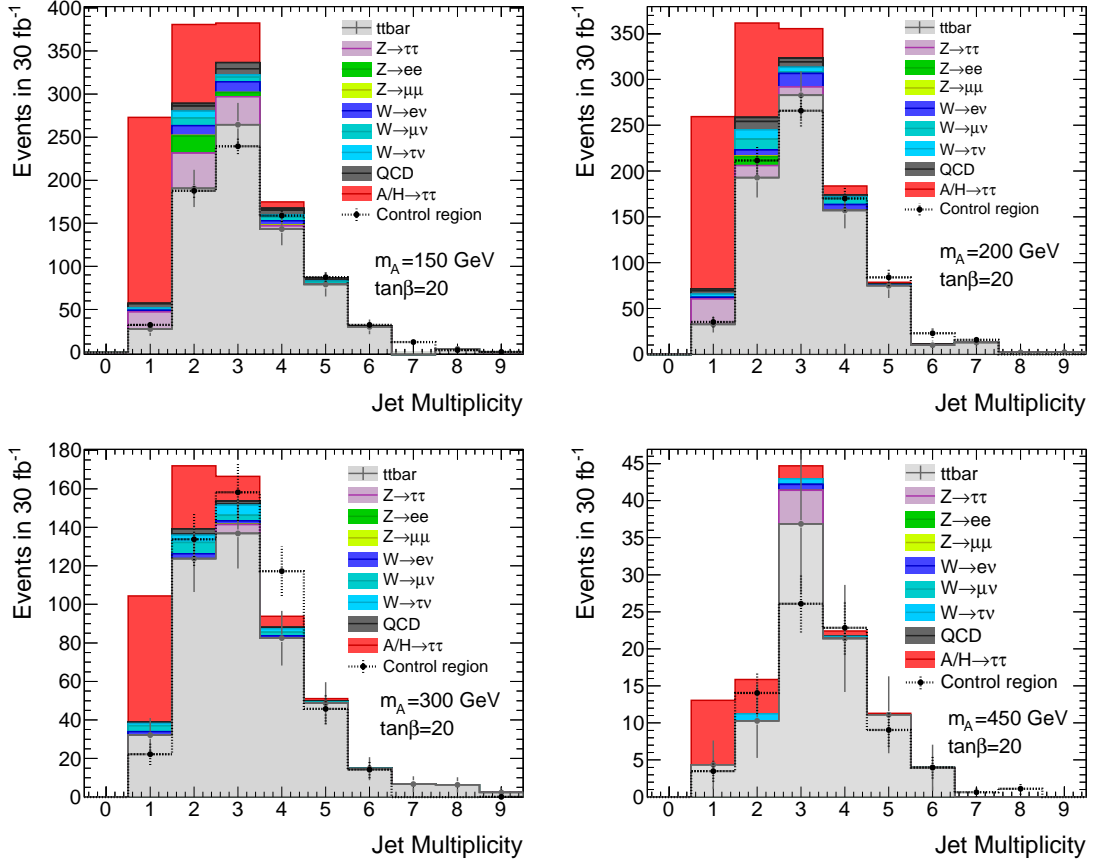


Figure 9.18.: Jet multiplicity distribution in the signal region with dropped cut on the number of jets, upper row left for $m_A = 150$ GeV and right for $m_A = 200$ GeV; bottom row left for $m_A = 300$ GeV and right for $m_A = 450$ GeV. The signal cross sections were scaled to $\tan\beta = 20$. The black dotted line shows the $t\bar{t}$ multiplicity distribution from the control region which is normalized to the bins with the number of jets larger than three from the signal region. The results and expected statistical uncertainties are shown for integrated luminosities of 30 fb^{-1} at $\sqrt{s} = 14$ TeV.

for each of the Higgs boson mass hypotheses for three different values of $\tan\beta$. The results are reasonable within statistical uncertainties, however, a dependence of the outcome from the $t\bar{t}$ estimation method on the value of $\tan\beta$ is obvious. This dependence was not considered in [124]. The dependence on the value of $\tan\beta$ stems from the contamination of the high multiplicity bins in the signal region with Higgs boson events. Bins with events having more than 3 jets are used for the normalization of the multiplicity distribution from the control region. Especially the bin with four jets still contains some signal, which becomes larger with increasing values of $\tan\beta$. The statistical uncertainties have been evaluated by using Gaussian error propagation. There are three terms contributing to the total statistical uncertainty $\Delta N_{t\bar{t}}$:

$$\left(\Delta N_{t\bar{t}, \text{signal region}}^{n_{\text{jets}} < 3}\right)^2 = \left(\Delta N_{t\bar{t}, \text{control region}}^{n_{\text{jets}} > 3}\right)^2 + \left(\Delta N_{t\bar{t}, \text{control region}}^{n_{\text{jets}} < 3}\right)^2 + \left(\Delta N_{t\bar{t}, \text{signal region}}^{n_{\text{jets}} > 3}\right)^2. \quad (9.4)$$

The expected statistical uncertainty for an integrated luminosity of 30fb^{-1} has been evaluated as well as the real uncertainty due to limited Monte Carlo statistics. The contribution to the statistical uncertainty from the control regions is smaller than that from the signal regions due to higher event statistics in the control regions.

m_A	150 GeV	200 GeV	300 GeV	450 GeV
$N_{\text{control}}^{n_{\text{jets}}>3}$	2096	636	304	160
$N_{\text{control}}^{n_{\text{jets}}<3}$	1564	539	270	74
$N_{\text{signal}}^{n_{\text{jets}}>3}$	287	279	168	37
$N_{\text{tt,signal}}^{n_{\text{jets}}<3}$	218 ± 23	225 ± 23	156 ± 19	15 ± 6
$N_{\text{tt,signal}}^{n_{\text{jets}}<3, \text{estimated}}$	214 ± 23	237 ± 31	150 ± 27	17 ± 6

Table 9.15.: Number of events in the various regions scaled to an integrated luminosity 30fb^{-1} . The Higgs boson signal was scaled to a cross section corresponding to $\tan\beta = 5$. The result of the method, the number of $t\bar{t}$ events in the signal region in the low multiplicity bins estimated from the control region, is given by $N_{\text{tt,signal}}^{n_{\text{jets}}<3, \text{estimated}}$. This needs to be compared to the expected number of $t\bar{t}$ events as predicted by the MC, $N_{\text{tt,signal}}^{n_{\text{jets}}<3}$. The statistical uncertainties on the expected and estimated number of $t\bar{t}$ events are also given. The uncertainties reflect the available MC statistics, the uncertainties expected in 30fb^{-1} are smaller.

m_A	150 GeV	200 GeV	300 GeV	450 GeV
$N_{\text{control}}^{n_{\text{jets}}>3}$	2096	636	304	160
$N_{\text{control}}^{n_{\text{jets}}<3}$	1564	540	270	75
$N_{\text{signal}}^{n_{\text{jets}}>3}$	294	291	175	38
$N_{\text{tt,signal}}^{n_{\text{jets}}<3}$	218 ± 23	225 ± 23	156 ± 19	15 ± 6
$N_{\text{tt,signal}}^{n_{\text{jets}}<3, \text{estimated}}$	220 ± 23	247 ± 32	156 ± 27	18 ± 6

Table 9.16.: Number of events in the various regions, scaled to an integrated luminosity 30fb^{-1} . The Higgs boson signal is scaled to a cross section corresponding to $\tan\beta = 20$. More explanations can be found in the caption of Table 9.15.

The variation of the number of $t\bar{t}$ events for values of $\tan\beta$ between 5 and 45 is summarized in Table 9.18. This needs to be taken into account as a systematic uncertainty, which is larger than the cross section uncertainty of the $t\bar{t}$ production.

m_A	150 GeV	200 GeV	300 GeV	450 GeV
$N_{\text{control}}^{\text{njets}>3}$	2096	636	304	160
$N_{\text{control}}^{\text{njets}<3}$	1564	546	273	76
$N_{\text{signal}}^{\text{njets}>3}$	329	343	213	44
$N_{\text{ff,signal}}^{\text{njets}<3}$	218 ± 23	225 ± 23	156 ± 19	15 ± 6
$N_{\text{ff,signal}}^{\text{njets}<3, \text{estimated}}$	245 ± 25	294 ± 37	192 ± 32	21 ± 7

Table 9.17.: Number of events in the various regions, scaled to an integrated luminosity 30 fb^{-1} . The Higgs boson signal was scaled to a cross section corresponding to $\tan\beta = 45$. More explanations can be found in the caption of Table 9.15.

m_A	150 GeV	200 GeV	300 GeV	450 GeV
ΔN_{ff}	31	57	42	4
$\Delta N_{\text{ff}}/N_{\text{ff}}^{\tan\beta=20}$	14%	23%	26%	22%

Table 9.18.: The difference in the number of estimated $\text{t}\bar{\text{t}}$ events when the value of $\tan\beta$ varies between 5 and 45. $\Delta N_{\text{ff}}/N_{\text{ff}}^{\tan\beta=20}$ denotes the relative difference with respect to the results of the $\text{t}\bar{\text{t}}$ estimation for $\tan\beta = 20$.

Systematic Uncertainties for the $\text{t}\bar{\text{t}}$ Estimation Based on Jet Multiplicities

The $\text{t}\bar{\text{t}}$ cross section and luminosity uncertainties are canceling completely in this method. Remaining uncertainties might arise from the contamination of the control region by other processes, the contamination of the high jet multiplicity bins in the signal region, deviations between the multiplicity distributions between signal and control region and statistical fluctuations in the multiplicity distributions.

Further uncertainties arise from pile-up and variations of the factorization scale. The impact of these sources could not be evaluated because this required special MC samples which were not available.

Table 9.19 lists the purity of the $\text{t}\bar{\text{t}}$ control samples and the impact of systematic variations on the purity. It is found that the control sample purity is very stable with respect to systematic variations. The $\text{t}\bar{\text{t}}$ purity in the high multiplicity bins of the signal regions and its stability with respect to systematic variations were also checked. The results are listed in Table 9.20. The signal regions are slightly more affected by impurities than the control regions but they also contain less events and the numbers might contain statistical components.

m_A	150 GeV	200 GeV	300 GeV	450 GeV
Default Purity	97.1	97.7	98.3	97.8
Electron Efficiency down	0	0	0	0
Electron E scale up	0	0	0.1	0.1
Electron E scale down	0.31	0	0	0.1
Electron E resolution	-0.1	-0.1	0	0.41
Muon Efficiency down	0	0	0	0
Muon E scale up	0.31	0	0.1	0
Muon E scale down	0	0	0.1	0.1
Muon E resolution	0	0	0.1	0.1
Tau Efficiency down	-0.1	-0.1	0	0.2
Tau E scale up	0	0	0.1	0.2
Tau E scale down	-0.1	-0.31	-0.2	0.31
Tau E resolution	0	0	0.1	0
Jet E scale up	0.1	0	0.1	0.1
Jet E scale down	0.1	-0.1	0	0
Jet E resolution	0	0	0.1	0.1
B-tagging Effi. down	0	0	0.1	0
Light jet rejection up	-0.1	-0.1	0	-0.1
Light jet rejection down	-0.21	0.1	0.1	0.2
Total variation	0.42	0.37	0.35	0.63

Table 9.19.: The purity of the $t\bar{t}$ control regions for each Higgs boson mass hypothesis and the impact of systematic variations on the purity. Given are relative variations in percent. The total variation is the sum of the squares of the individual variations. In the case of up- and down variations, the larger variation has been taken into account. A value of $\tan\beta = 45$ was assumed.

m_A	150 GeV	200 GeV	300 GeV	450 GeV
Default Purity	77.4	75.4	75.6	83.3
Electron Efficiency down	0	0	0	0
Electron E scale up	0.13	-0.27	0	-2.28
Electron E scale down	-0.65	-0.27	0.26	0
Electron E resolution	-1.55	-0.13	0.4	-1.2
Muon Efficiency down	-0.26	-0.53	0	0
Muon E scale up	-0.26	0.13	-0.26	-0.96
Muon E scale down	0.65	0.93	-0.13	0
Muon E resolution	-0.39	-0.13	0	0
Tau Efficiency down	-1.42	-0.53	-0.93	-1.2
Tau E scale up	0.9	-0.53	1.19	-1.2
Tau E scale down	2.07	-1.46	2.38	-0.24
Tau E resolution	-0.13	-0.4	0.26	-1.2
Jet E scale up	-3.23	-2.12	-0.4	-3.12
Jet E scale down	2.33	1.06	3.04	-2.52
Jet E resolution	-1.16	-0.4	0.26	0
B-tagging Effi. down	0	-0.13	0	0
Light jet rejection up	-0.52	0.13	1.19	0.24
Light jet rejection down	-0.52	0.27	1.59	0.6
Total variation	4.67	2.93	4.33	4.69

Table 9.20.: The purity of the $t\bar{t}$ contribution in the high multiplicity bins in the signal regions. Events with more than three jets were considered. The impact of systematic variations on the purity was evaluated for each Higgs boson mass hypothesis. Given are relative variations in percent. The total variation is the sum of the squares of the individual variations. In the case of up- and down variations, the larger variation has been taken into account. A value of $\tan\beta = 45$ was assumed.

The impact of systematic variations on the number of estimated $t\bar{t}$ events has been studied. This was evaluated for each of the four Higgs boson mass hypotheses. The impact of the systematic variations on each of the four kinematic regions was also checked. The four kinematic regions are: The signal regions at low and high multiplicities and the $t\bar{t}$ control regions at low and high multiplicities. In the $t\bar{t}$ control regions the events from all processes were summed up. In the signal region at high multiplicities also events from all processes were taken into account. The number $N_{\text{signal}}^{\text{njets}<3}$, however, denotes only the number of $t\bar{t}$ events in the low multiplicity bins in the signal region.

For the four kinematic regions, the total uncertainty of the variations is the sum of the squares of the individual uncertainties. Each individual uncertainty is calculated by comparing the number of events after the variation is applied to the default number. In case of asymmetric results for up- and down-variations, only the larger uncertainty was taken into account. The results for a Higgs boson mass hypothesis of $m_A = 150$ GeV are listed in Table 9.21. The corresponding tables for the other mass hypotheses are listed in Appendix H¹.

The uncertainty of the estimated number of $t\bar{t}$ events, $N_{\text{signal}}^{\text{njets}<3, \text{estimated}}$, needs to be calculated differently. It is not the sum of the squares of the individual uncertainties. Of course, this number also changes with each variation which is applied. But this is expected and by the data-driven approach it does not matter at all whether, for example, the b-tagging efficiency is higher or lower as expected in the simulation because only data enters the calculation. Such a variation, however, might change the matching of the multiplicity spectra between the signal and the control regions. Hence, the important quantity is the difference between the estimated number to the expected number, $N_{\text{signal}}^{\text{njets}<3}$, when the same variation is applied. This number is denoted as ΔN in Table 9.21. The total uncertainty is then the sum of the squares of the individual values of ΔN . If ΔN is non-zero in case no variation is applied (the *default* case, ΔN_0), this initial bias is not summed up in the total uncertainty but is taken into account only once. The other values of ΔN are then given as $\Delta N - \Delta N_0$.

To conclude, in case the number of $t\bar{t}$ events is estimated from data by using jet multiplicities ($N_{\text{signal}}^{\text{njets}<3, \text{estimated}}$), the luminosity uncertainty and the cross section uncertainty are irrelevant, because no MC input is needed at all. If the number of $t\bar{t}$ events is estimated from MC ($N_{\text{signal}}^{\text{njets}<3}$), the cross section uncertainty is the dominant uncertainty. The systematic uncertainty is 16% in case the $t\bar{t}$ contributions is estimated from MC. With the data-driven method this uncertainty is reduced to 11%. However, taking into account also the dependence of the estimated number of $t\bar{t}$ events on the value of $\tan \beta$ (Tables 9.15-9.17) leads to a total uncertainty of $\approx 25\%$.

¹The tables with the systematic uncertainties in Appendix H do not contain the relative variations but list the number of events in each region, which might be useful to the interested reader.

Variation	$N_{\text{control}}^{\text{njets}>3}$	$N_{\text{control}}^{\text{njets}<3}$	$N_{\text{signal}}^{\text{njets}>3}$	$N_{\text{signal}}^{\text{njets}<3}$	$N_{\text{signal}}^{\text{njets}<3 \text{ estimated}}$	ΔN
Default	2096	1564	294	218	220	-2
El. efficiency	0	0	0	0	0	0
El. E_T scale up	0.4	0.7	0.7	-2.2	0.8	-2.9
El. E_T scale down	-1.2	-2.3	-2.3	0	-1.6	1.7
El. E_T resolution	0.1	0.3	0.3	-5.5	0.4	-5.8
Muon efficiency	-0.6	-0.7	-0.7	-0.9	-0.5	-0.4
Muon p_T scale up	-0.3	-1.4	-1.4	-1.6	-0	-1.6
Muon p_T scale down	-0.3	2.6	2.6	-0.2	2.8	-2.9
Muon p_T resolution	0.1	-1.3	-1.3	0	-1.4	1.5
Tau efficiency	-5.7	-5.4	-5.4	-1.8	-5.2	3.5
Tau E_T scale up	0.3	4.6	4.6	0.2	5.3	-4.9
Tau E_T scale down	-0.4	0.2	0.2	-2.4	-2.6	0.3
Tau E_T resolution	-0.2	-0.1	-0.1	-3.3	0.4	-3.6
Jet E scale up	6	7.9	7.9	-4.9	-2.2	-2.7
Jet E scale down	-5.1	-5.1	-5.1	2.9	0.4	2.4
Jet E_T resolution	0	-3.9	-3.9	-0.9	-4	3.2
B-tagging efficiency	-0.9	-0	-0	1.1	0.7	0.4
Light jet rej. up	-5.4	-3.5	-3.5	-3.1	-4.5	1.5
Light jet rej. down	6.6	3.4	3.4	4	4	-0
Luminosity	3	3	3	3	3	0
Total exp.	11.2	10.9	12.8	10.4	10.9	11.1
Cross Section	12	12	12	12	12	0
Total exp.+theor.	16.4	16.2	17.5	15.9	16.2	11.1

Table 9.21.: The impact of systematic variations on the number of events in each of the kinematic regions and the uncertainty for the data-driven method. The Higgs boson mass assumed is $m_A = 150$ GeV and $\tan\beta = 20$. Given are relative variations in percent. The line 'Default' states the number of events scaled to 30 fb^{-1} . The uncertainties of $N_{\text{control}}^{\text{njets}>3}$, $N_{\text{control}}^{\text{njets}<3}$, $N_{\text{signal}}^{\text{njets}>3}$ and $N_{\text{signal}}^{\text{njets}<3}$ are given for information. The variation of $N_{\text{signal}}^{\text{njets}<3, \text{ estimated}}$ when systematics are applied is also given for information and this is not the uncertainty of the data-driven method. The uncertainty of the data-driven method is given by comparing the number $N_{\text{signal}}^{\text{njets}<3}$ to $N_{\text{signal}}^{\text{njets}<3, \text{ estimated}}$ after each variation, ΔN . The default difference is taken into account only once in the calculation of the total uncertainty of the data-driven method. More information is given in the text.

Estimation of $t\bar{t}$ Events Using an Extrapolation Ratio

In the method described advantage has been taken of the characteristic jet multiplicity distribution of the $t\bar{t}$ events. The results of the $t\bar{t}$ estimation, however, depend on the correct tuning of the cut on m_T . The tuning was necessary to obtain a good resemblance of the jet multiplicity shapes for events with less than three jets in both the signal and the control regions. The resemblance of the jet multiplicity distributions is the precondition that the estimated number of $t\bar{t}$ events is correct. For the $m_A = 300$ GeV analysis the tuning was not very successful as one can see for example

in Figure 9.18, where the bin with four jets from the control region shows a significant deviation from the corresponding bin of the signal region.

Furthermore, a dependence of the results for the $t\bar{t}$ estimation on $\tan\beta$ is obvious. The contribution of Higgs boson events to the high multiplicity bins from the signal regions is non-negligible. For large values of $\tan\beta$ the normalization factor $\frac{N_{t\bar{t}, \text{signal region}}^{\text{njets}>3}}{N_{t\bar{t}, \text{control region}}^{\text{njets}>3}}$ changes and therefore also the number of estimated $t\bar{t}$ events.

These problems can be avoided when introducing an extrapolation ratio, R , which describes the differences between the data (control region) and MC (signal region). This approach, for example, was used in the $H \rightarrow WW$ analysis in ATLAS [126], where all important background contributions are obtained from control regions and scaled with extrapolation ratios. It is also used in [124] for the estimation of the W +jets background. Such an factor, however, depends on the MC simulation and systematic uncertainties need to be evaluated carefully. Using an extrapolation ratio, the number of $t\bar{t}$ events is given as follows:

$$N_{t\bar{t}, \text{signal region}}^{\text{njets}<3} = R \cdot N_{\text{control region}} \cdot \frac{N_{t\bar{t}, \text{signal region}}^{\text{njets}>3}}{N_{t\bar{t}, \text{control region}}^{\text{njets}>3}} \quad (9.5)$$

In the first method the factor R was substituted by the fraction $\frac{N_{t\bar{t}, \text{signal region}}^{\text{njets}>3}}{N_{t\bar{t}, \text{control region}}^{\text{njets}>3}}$ which was obtained purely from data.

In the second approach R is obtained from MC and depends on the Higgs boson mass hypothesis:

$$R = \frac{N_{t\bar{t}, \text{signal region}}^{\text{MC}}}{N_{t\bar{t}, \text{control region}}^{\text{MC}}} \quad (9.6)$$

All jet multiplicity bins are used in the control region, the one and two jet bins are used in the signal region. The same m_A -dependent control regions as used were used here for convenience. Using a m_A -independent control region is also possible, as long as it contains $t\bar{t}$ events with a very large purity.

By applying this approach the uncertainties of the $t\bar{t}$ cross section and luminosity cancel. Furthermore, uncertainties which are similar between the control and signal region might also cancel, such as the b-tagging efficiency uncertainty. Remaining systematic uncertainties of the ratio R are listed in Table 9.22. The largest contributions come from the variations of the τ and jet energy scales. The uncertainties for the $m_A = 450$ GeV analysis contain a large statistical component and are given for information. The method is supposed to be also applicable to the mass hypotheses of 600 GeV and 800 GeV.

To conclude, the systematic uncertainty is the smallest when using a MC based extrapolation ratio. A total $t\bar{t}$ uncertainty of 11% is used in the evaluation of the discovery potential for each of the Higgs boson mass hypotheses in the b-tagged analysis.

In the non b-tagged analysis the MC statistics is not sufficient to evaluate the uncertainties from the MC based estimation, instead a total experimental uncertainty of 10% is assumed.

Variation	150 GeV	200 GeV	300 GeV	450 GeV
Default	0.042	0.131	0.186	0.043
Electron efficiency	0	0	0.3	0.7
Electron E_T scale up	-2.6	-2.7	-1.8	-1.4
Electron E_T scale down	0.5	0.8	-0	-0.7
Electron E_T resolution	-5.4	0.5	-1.2	-0.4
Muon efficiency	-0.6	-0.8	0.5	13.5
Muon p_T scale up	-2.1	-1.5	-2.4	1.9
Muon p_T scale down	0.2	1.6	2.5	12.7
Muon p_T resolution	-0	0.1	0.2	0
Tau efficiency	3.8	-0.2	3.6	-12.3
Tau E_T scale up	-0	-0.4	-0.4	1.2
Tau E_T scale down	-0.9	8.4	-4.8	26.1
Tau E_T resolution	-3.1	-1	-0.6	0
Jet E scale up	-6.7	-5.2	-4.8	-1.3
Jet E scale down	4.6	3.8	3	0.6
Jet E_T resolution	-0.9	-1.4	-2.1	-1.9
B-tagging efficiency	1.7	-1.2	-1.5	0.6
Light jet rej. up	2.8	2.8	-3.9	-27.1
Light jet rej. down	-1.4	-2.8	5	10.8
Luminosity	0	0	0	0
Cross Section	0	0	0	0
Total uncertainty	11	11	10.1	43.8

Table 9.22.: The impact of systematic variations on the extrapolation ratio R . Given are relative uncertainties in percent. The line 'default' states the value of the ratio. The total systematic uncertainty is the sum of the squares of the individual uncertainties. In case of asymmetric up- and down-variations, only the larger uncertainty was taken into account. The large uncertainties for $m_A = 450$ GeV are due to statistical fluctuations.

9.2.3. $Z \rightarrow \tau\tau$ Background Uncertainties

No data-driven estimation of the $Z \rightarrow \tau\tau$ background is used in this thesis. A pure $Z \rightarrow \tau\tau$ control region cannot be constructed. Hence, the uncertainties for the estimation from MC had to be fully evaluated for the $Z \rightarrow \tau\tau$ events. In [124] a data-driven method is discussed for $Z \rightarrow \tau\tau$ which is based completely on the method used in the dilepton analysis described in Chapter 8 and which was adopted to the lepton-hadron analysis. There, a $Z \rightarrow ee/\mu\mu$ control region is used to estimate the shape and the normalization of the $Z \rightarrow \tau\tau$ background. However, systematic uncertainties of the normalization could not be evaluated due to limited MC statistics and remaining uncertainties

of the $Z \rightarrow \tau\tau$ shape need to be studied further before this method can be applied.

Analysis	Non b-tagged	B-tagged
Electron efficiency	-0.1	-0.4
Electron E_T scale up	0.3	0
Electron E_T scale down	-0.1	0.4
Electron E_T resolution	-0	-0.3
Muon efficiency	-0.5	-0.6
Muon p_T scale up	0.4	1.3
Muon p_T scale down	0	-0.4
Muon p_T resolution	0	0
Tau efficiency	-4.9	-6
Tau E_T scale up	2.1	3.6
Tau E_T scale down	-2.2	-3.3
Tau E_T resolution	0	0.3
Jet E scale up	0.4	-0.9
Jet E scale down	-0.3	1.3
Jet E_T resolution	-0.1	1.1
B-tagging efficiency	0	-0.6
Light jet rej. up	0.3	-5.6
Light jet rej. down	-0.3	7.9
Luminosity	3	3
Total	6.2	11.2

Table 9.23.: The impact of systematic variations on the number of $Z \rightarrow \tau\tau$ events for the b-tagged analysis and the non b-tagged analysis. The total systematic uncertainty is the sum of the squares of the individual uncertainties. In case of asymmetric up- and down-variations, only the larger uncertainty was taken into account.

The impact of systematic variations for the b-tagged and the non b-tagged analysis were evaluated and are listed in Table 9.23. The uncertainties were obtained at the reference point in the cut flow where the split into the two analyses is performed: In the case of the non b-tagged analysis after the b-veto is applied and for the b-tagged analysis after the requirement of at least one b-tag and the cut on less than three jets. At this point the most relevant cuts are applied and enough statistics is left for the calculation of the systematic uncertainties. In the non b-tagged analysis, the largest impact comes from variations of τ -related quantities. In the b-tagged analysis the dominant uncertainty comes from variations of the light jet rejection and the second largest impact from the variations on the description of the hadronic τ decay products.

The systematic uncertainties obtained in this thesis are different to the numbers published in [124]. In the publication several methods were investigated how to reduce the statistical component in the

systematic uncertainties. The systematics were then obtained at a stage in the cut flow where the numbers still seemed to be reasonably small; most of the uncertainties were evaluated before the split into b-tagged and non b-tagged analysis. This procedure clearly led to smaller but probably unrealistic uncertainties.

9.2.4. W+jets Background Uncertainties

In [124] a data-driven estimation of the W+jets background is discussed and applied in the non b-tagged analysis. The idea is to select a W+jets sideband by inverting the cut on m_T and by dropping the cuts on x_1 and x_2 . The number of estimated W+jets events is given as follows:

$$N_W^{\text{signal region}} = N_W^{\text{control region}} \cdot R, \quad (9.7)$$

where R is an extrapolation factor which is obtained from MC. Systematic uncertainties of R were evaluated in [124] and the results will be used in this thesis. The uncertainties of R are listed in Table 9.24. They are 5% – 9% depending on the Higgs boson mass hypothesis. An average uncertainty of 7% is used to evaluate the discovery potential in order not to complicate the analysis unnecessarily.

In the b-tagged analysis the W+jets background is very small and a total experimental uncertainty of 10% was assumed.

m_A	150 GeV	200 GeV	300 GeV	450 GeV	600 GeV	800 GeV
Uncertainty [%]	5.5	5.2	5.4	6.7	8.6	7.8

Table 9.24.: Relative uncertainties of the extrapolation factor R for the estimation of the W+jets background for all Higgs boson mass hypotheses in the non b-tagged analysis.

9.2.5. Summary of Background Uncertainties

A mixture of data-driven and MC-based background estimation procedures is used for the calculation of the discovery potential. The cross section uncertainties are only relevant where no data-driven approach is used. In case the MC statistics was too small to evaluate the systematic uncertainties by applying variations, a total experimental uncertainty of 10% was assumed. This was the case for W+jets in the b-tagged analysis, for $t\bar{t}$ in the non b-tagged analysis and for QCD and $Z \rightarrow e\bar{e}/\mu\bar{\mu}$ in both analyses. The summary of experimental and theoretical uncertainties for all background processes is given in Table 9.25 for the b-tagged and the non b-tagged analysis.

9.2.6. Systematic Uncertainties of the Signal Process

Theoretical Uncertainties

The theoretical uncertainties for the b-associated and the direct production were already discussed in Chapter 5 and illustrated as a function of m_A in Figure 5.1. In Table 9.26 the uncertainties are listed for each Higgs boson mass hypothesis.

Process	Non b-tagged Analysis		B-tagged Analysis	
	Exp.	Theory	Exp.	Theory
$t\bar{t}$	10%	12%	11%	0%
$Z \rightarrow \tau\tau$	6.2%	3%	11.2%	3%
$W \rightarrow e/\mu/\tau\nu$	7%	3%	10%	3%
$Z \rightarrow ee/\mu\mu$	10%	3%	10%	3%
QCD	10%	50%	10%	50%

Table 9.25.: Summary of systematic uncertainties for all process in the b-tagged and non b-tagged analysis.

m_A	150 GeV	200 GeV	300 GeV	450 GeV	600 GeV	800 GeV
$\Delta\sigma(gg \rightarrow b\bar{b} A/H)$	20%	15%	10%	7.5%	6.5%	5.5%
$\Delta\sigma(gg \rightarrow A/H)$	12%	11%	10%	10.5%	-	-

Table 9.26.: Cross section uncertainties of the signal processes. The contribution of the gluon fusion signal becomes negligible for $m_A \geq 600$ GeV.

Experimental Uncertainties

The impact of systematic uncertainties on the Higgs boson events is discussed in the following. Although the uncertainties were in principle evaluated in [124], they are probably not realistic since they have been obtained before the split of the main analysis into b-tagged and non b-tagged analysis. In Table 9.27 the results are listed for each Higgs boson mass hypothesis in the non b-tagged analysis. The total experimental uncertainties of the signal process are found to be $\approx 6\%$ in the non b-tagged analysis and $\approx 8\% - 9\%$ in the b-tagged analysis. The results are compatible with the uncertainties found in the dilepton channel (compare to Table 8.21), where the uncertainties were $5\% - 6\%$. In the lepton-hadron channel the systematic uncertainties are larger due the uncertainties from the identification of hadronic τ candidates.

Variation	150 GeV	200 GeV	300 GeV	450 GeV	600 GeV	800 GeV
Electron efficiency	-0.2	-0.1	-0.2	-0.1	0	-0.1
Electron E_T scale up	0	-0.1	0.1	-0.1	0.2	0.1
Electron E_T scale down	0	-0.1	0.1	-0	0.1	-0.2
Electron E_T resolution	-0.3	-0.2	0.2	0.3	0.1	0.2
Muon efficiency	-0.6	-0.4	-0.6	-0.4	-0.7	-0.6
Muon p_T scale up	-0	-0.3	-0.1	0	0.2	-0.3
Muon p_T scale down	0.6	0.1	0.2	0.5	0.3	0.3
Muon p_T resolution	-0.2	0	-0	-0.1	0	0
Tau efficiency	-5	-5.3	-4.9	-4.9	-4.4	-5
Tau E_T scale up	0.6	-0.1	-0.5	0.1	-0.3	0.1
Tau E_T scale down	-0.2	-0	0.5	0	0.2	-0.1
Tau E_T resolution	0.3	-0.2	0.2	-0.2	0	0
Jet E scale up	0.2	-0.1	-0	-0.1	-0.2	-0.2
Jet E scale down	0	0.2	0.2	-0.2	0.1	0.5
Jet E_T resolution	0.1	-0.1	0	-0	-0.1	-0.3
B-tagging efficiency	0.2	0.1	0.2	0	0	0
Light jet rej. up	1.3	1	1.5	1.5	1.4	2.1
Light jet rej. down	-1.5	-1	-1.1	-1.3	-1.7	-2.6
Luminosity	3	3	3	3	3	3
Total	6.1	6.2	6	6	5.6	6.4

Table 9.27.: The impact of systematic variations on the number of events for the Higgs boson signal events in the **non b-tagged analysis**. Given are relative uncertainties in percent. The total systematic uncertainty is the sum of the squares of the individual uncertainties. In case of asymmetric up- and down-variations, only the larger uncertainty was taken into account.

Variation	150 GeV	200 GeV	300 GeV	450 GeV	600 GeV	800 GeV
Electron efficiency	-0.2	-0.3	0	-0.5	0	0
Electron E_T scale up	0.4	-0.1	0.3	0.5	0	0
Electron E_T scale down	0.3	0.1	0.3	-0.5	0	0.4
Electron E_T resolution	0.8	-0.6	0.5	0	-1.3	-1.1
Muon efficiency	-0.1	-0.2	-0.5	0	0	0
Muon p_T scale up	-0.1	0	-0.3	-0.8	-0.3	-0.9
Muon p_T scale down	0.7	-0.3	0	-0.1	0.3	0
Muon p_T resolution	0.1	-0.2	0	-0.1	0	0
Tau efficiency	-5.3	-5.3	-4.1	-3.8	-5.6	-3.2
Tau E_T scale up	1.4	-0.5	-0.6	0	-0.7	0.4
Tau E_T scale down	-0.1	-0.8	-0.3	0	-0.3	0.4
Tau E_T resolution	-0.5	-0.3	1.1	0	-0.7	0.1
Jet E scale up	1.5	0.2	-0.3	0.3	-1.3	-1.2
Jet E scale down	-0.2	-1.3	0.1	0.1	1.6	2.8
Jet E_T resolution	0.5	-0.7	0.3	0	-1	0
B-tagging efficiency	-0.6	-0.4	-0.9	0.5	0	0.4
Light jet rej. up	-4.8	-4.8	-6.5	-5.7	-3.8	-3.4
Light jet rej. down	6	4	4.4	5.2	4.2	6.9
Luminosity	3	3	3	3	3	3
Total	8.9	8	8.4	7.6	8	8.8

Table 9.28.: The impact of systematic variations on the number of events for the Higgs boson signal events in the **b-tagged analysis**. Given are relative uncertainties in percent. The total systematic uncertainty is the sum of the squares of the individual uncertainties. In case of asymmetric up- and down-variations, only the larger uncertainty was taken into account.

9.3. Discovery Potential

In this section the statistical methods used to assess the discovery potential are described. The results in the lepton-hadron channel are presented and then combined with the results from the lepton-lepton analysis. A discussion of the different potentials of both search channels and a comparison of the results with other publications conclude the chapter.

9.3.1. Profile Likelihood Method

The profile likelihood method (PLH) is described in detail elsewhere [127]. A few important aspects of the PLH will be summarized in this subsection. In this procedure systematic uncertainties enter as nuisance parameters. Nuisance parameters are not parameters of interest, they influence the model but it is not pivotal to predict or measure them.

Considering a counting experiment, a single channel and a histogram (eg. a mass distribution) with n bins, then the number of events in bin i , N_i , is modeled as a Poisson variable with mean value

$$\langle N_i \rangle = \mu \cdot S_i + B_i. \quad (9.8)$$

μ is a signal strength parameter, if it is zero the signal is absent. For claiming a discovery, μ is the only parameter of interest. If, however, for example also the Higgs boson mass is to be measured, other parameters of interest enter as well.

B is the number of background events which is predicted by MC simulations. B can also be obtained by a subsidiary measurement from a sideband, where Y events are measured and then B is given as $B = Y/\tau$. τ is a scaling parameter which is assumed to be known. In reality, however, τ is afflicted with systematic uncertainties complicating the model. In the real measurement, when the background is estimated from MC only, τ is the ratio of the integrated luminosity of the MC sample to the luminosity of the data sample. In this work τ was assumed to equal unity in order to be consistent with the dilepton channel and to not decrease the discovery potential artificially due to the limited MC samples. It is assumed that at a time when 30 fb^{-1} of data have been recorded, considerable more MC events will be available as well. This work claims to predict the expected significance.

The likelihood function for a single channel j is constructed as follows:

$$L_j(\mu, \theta) = \prod_{i=1}^n \frac{(\mu \cdot S_i + B_i(\theta))^{N_i}}{N_i!} \cdot e^{-(\mu \cdot S_i + B_i(\theta))}. \quad (9.9)$$

θ denotes a vector of nuisance parameters, each nuisance parameter is distributed according to a Gaussian. Using the logarithm simplifies Equation 9.9 to

$$\ln L_j(\mu, \theta) = \sum_{i=1}^n (N_i \ln(\mu \cdot S_i + B_i(\theta)) - (\mu \cdot S_i + B_i(\theta))), \quad (9.10)$$

where the term $\sum \ln N_i!$ was neglected because it is constant and irrelevant for the minimization. The likelihood for more than one channel is then the product of the individual likelihoods times the probability density function for each of the nuisance parameters, $f_j(B, \sigma)$, in case they are

uncorrelated between the channels j :

$$L(\mu, \theta) = \prod_j L_j(\mu, \theta) \cdot f_j(B, \sigma), \quad (9.11)$$

where B denotes the number of background events and σ is the background uncertainty in the channel j . The profile likelihood ratio, $\lambda(\mu)$, is constructed as follows:

$$\lambda(\mu) = \frac{L(\mu, \hat{\hat{\theta}})}{L(\hat{\mu}, \hat{\hat{\theta}})}. \quad (9.12)$$

$\hat{\hat{\theta}}$ denotes the value of θ that maximizes L for the specified μ , i.e. $\hat{\hat{\theta}}$ is the conditional maximum-likelihood estimator of θ . The denominator is the maximized full likelihood function, i.e. $\hat{\theta}$ and $\hat{\mu}$ are the maximum-likelihood estimators. It is convenient to define the test quantity q_μ :

$$q_\mu = -2 \ln \lambda(\mu). \quad (9.13)$$

For large datasets the sampling distribution of q_μ for a specific μ , $f(q_\mu|\mu)$, will follow the distribution of a χ^2 (*Wilks' theorem*, proof given in [128]). The compatibility between an observed value $q_{\mu, \text{obs}}$ and a hypothesized value of q_μ is given by the p-value, defined as follows:

$$p_\mu = \int_{q_{\mu, \text{obs}}}^{\infty} f(q_\mu|\mu) dq_\mu. \quad (9.14)$$

The p-value states the probability of the observed data given an assumption about the value of μ . The background-only hypothesis for example corresponds to $\mu = 0$. Establishing a discovery is equal to rejecting the background-only hypothesis. A p-value of equal or less than $2.8 \cdot 10^{-7}$ is considered to be a discovery. A perfect agreement of the observed data to the hypothesis corresponds to a p-value of 0.5.

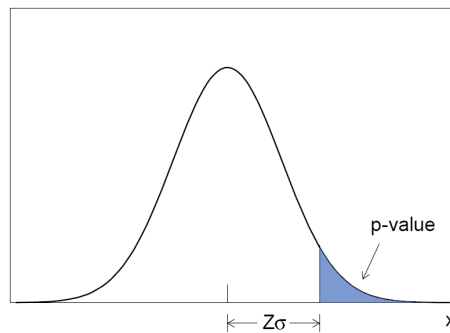


Figure 9.19.: Illustration of the p-value and the definition of the Gaussian significance (taken from [19]).

The significance corresponding to a p-value is given as the number of standard deviations Z at which a Gaussian random variable around zero mean would give a one-sided tail equal to the

p-value:

$$p = \int_Z^{\infty} \frac{1}{\sqrt{2\pi}} e^{-x^2/2} dx = 1 - \Phi(Z). \quad (9.15)$$

This is illustrated in Figure 9.19. $\Phi(Z)$ is the cumulative distribution for the standard Gaussian. Z can be calculated by

$$Z = \Phi^{-1}(1 - p). \quad (9.16)$$

Furthermore, it can be shown [129] that Z relates to Equation 9.13 as follows:

$$Z = \sqrt{q_0} = \sqrt{-2 \ln \lambda(0)}. \quad (9.17)$$

For the case of a single channel and a single bin, Equation 9.13 approaches the following form for $\mu = 0$ in the limit that B is perfectly known and $N \geq B$ ($N = S + B$):

$$\ln \lambda(0) = -N \ln \frac{N}{B} + N - B = -(S + B) \ln \frac{S + B}{B} + S. \quad (9.18)$$

Combining this with Equation 9.17 yields

$$Z = \sqrt{2 \left((S + B) \ln \left(1 + \frac{S}{B} \right) - S \right)}. \quad (9.19)$$

Taking the limit $S \ll B$ and $B \gg 0$ and neglecting $\mathcal{O}(S^3)$ in Equation 9.17 leads to

$$\ln \lambda(0) \approx \frac{S^2}{B}, \quad (9.20)$$

which leads to the following form for Z :

$$Z \approx \frac{S}{\sqrt{B}}. \quad (9.21)$$

Establishing an exclusion means rejecting the signal+background hypothesis ($\mu > 0$). In the SM theory the cross section of the Higgs boson is only a function of its mass, it is therefore common to calculate limits on μ given a certain confidence level (CL.). Choosing a CL. of 95% corresponds to a p-value of $p = 1 - 0.95 = 0.05$. The p-value is obtained for a variety of values for μ , the upper limit on μ is then given when the p-value becomes equal or less than 0.05. The 95% refers to the fact that in the approximation of repeating the same experiment infinite times, in 5% of the cases the presence of a true signal would result in a larger number of events. In the MSSM, however, the Higgs boson cross section is not only a function of m_A but of $\tan \beta$ as well. Therefore, in this thesis no upper limit on μ is calculated but an upper limit on the value of $\tan \beta$. This is achieved by testing when the observation of S+B events reaches a p-value of equal or less than 0.05, the number of signal events is then converted into the corresponding value of $\tan \beta$. The corresponding value of $\tan \beta$ given a number of signal events can be obtained from plotting the significance (or the

p-value) versus $\tan\beta$ and interpolating between the analyzed points (see Figures 9.21 and 8.37). This procedure is equivalent to checking when the significance Z reaches a value of $Z = 1.64$, since $p(Z = 1.64) = 0.05$.

9.3.2. Results for the Lepton-Hadron Channel

In the following the results for the b-tagged and the non b-tagged analysis will be discussed separately. The discovery potential was evaluated for six values of $\tan\beta$ (5/10/15/20/30/50) and six Higgs boson mass points (150/200/300/450/600/800 GeV). The significances were evaluated using the PLH; in case the PLH calculation resulted in instabilities the significance was approximated with $Z = S/\sqrt{B}$. More details can be found in Appendix E. In this work, the PLH was applied using the ROOSTATS program [130].

In Figure 9.20 the discovery significances of the b-tagged and the non b-tagged analysis are illustrated as a function of m_A for two values of $\tan\beta$. The results when assuming statistical background uncertainties only are also shown. For $m_A > 400$ GeV the b-tagged analysis yields slightly better results than the non b-tagged analysis. The impact of the systematic uncertainties decreases for larger m_A because a smaller number of events is expected. The impact of systematic uncertainties in the non b-tagged analysis is larger than for the b-tagged analysis for $m_A < 400$ GeV because more events are expected there. With $\tan\beta = 50$ Higgs bosons with masses up to 700 GeV (800 GeV) could be discovered by the non b-tagged (b-tagged) analysis.

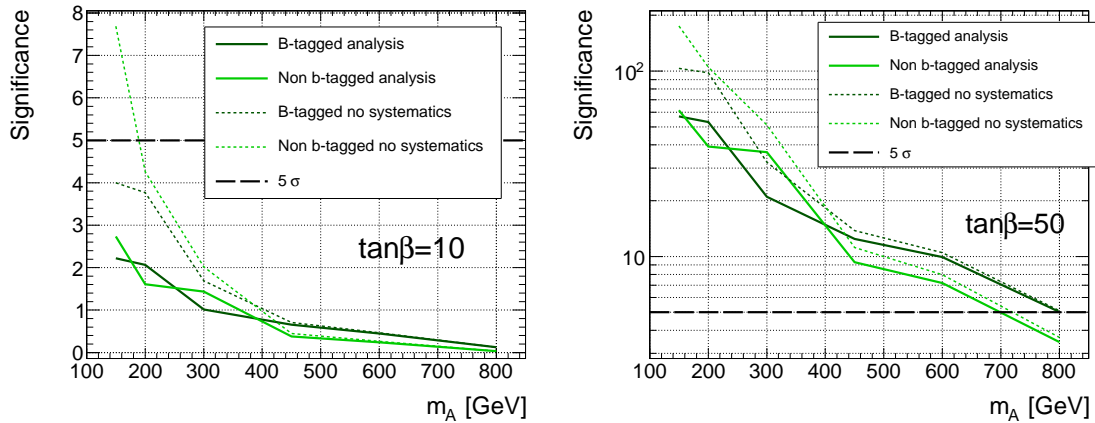


Figure 9.20.: Discovery significance as a function of m_A for $\tan\beta = 10$ (left) and for $\tan\beta = 50$ (right). The solid lines show the significances including the full systematics. The dashed lines show the significances without any background uncertainty. The results for the b-tagged analysis are given in dark green (dark grey) and the results for the non b-tagged analysis in light green (grey).

In Figure 9.21 the significance for the b-tagged and the non b-tagged analysis are shown as functions of $\tan\beta$ for each Higgs boson mass hypothesis. The results assuming only statistical background uncertainties are also given. As was observed before, the impact of systematic uncertainties on the significance decreases for larger Higgs boson masses, and the b-tagged analysis is the slightly stronger analysis for $m_A > 400$ GeV.

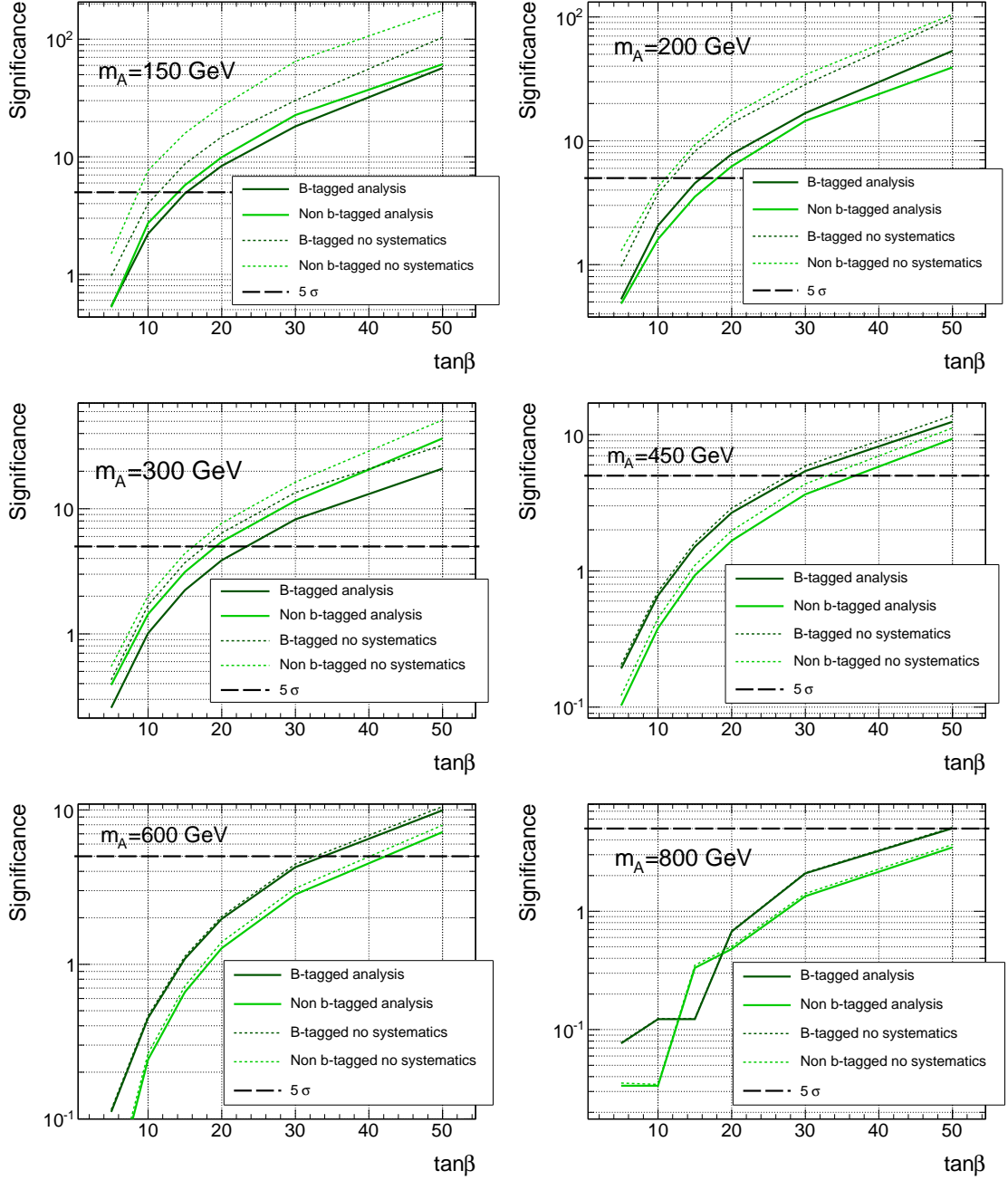


Figure 9.21.: Significance as a function of $\tan\beta$ for different Higgs boson mass hypotheses as indicated in the plots. The solid lines show the significances including the full systematics. The dashed lines show the significances when assuming statistical background uncertainties only. The results for the b-tagged analysis are given in dark green (dark grey) and the results for the non b-tagged analysis in light green (grey).

9.3.3. Combination with the Lepton-Lepton Channel

The results of the b-tagged and the non b-tagged analysis are combined with the discovery potential of the dilepton channel. The analysis of the fully leptonic state was extensively discussed in Chapter 8; the results used for the combination include experimental and theoretical uncertainties on the backgrounds. To increase the overlap between the two analysis, the results in the dilepton channel for $m_A = 160$ GeV and the results in the lepton-hadron channel for $m_A = 150$ GeV are combined to a mass point of $m_A = 155$ GeV. The error resulting from this is small since the reconstructed mass resolution at $m_A = (150 - 160)$ GeV is 20 GeV for gluon fusion and 30 GeV for b-associated production. The combined discovery potential was evaluated for 8 mass points (110/130/155/200/300/450/600/800 GeV) and 6 values of $\tan\beta$ (5/10/15/20/30/50). For $m_A \leq 130$ GeV ($m_A \geq 600$ GeV) only the results from the lepton-lepton (lepton-hadron) channel were available.

In Figure 9.22 the significances of the dilepton channel, the combination of the b-tagged and non b-tagged analysis (denoted as lepton-hadron) and the combination off all three analysis are shown as a function of m_A and $\tan\beta$. The lepton-hadron channel yields a higher significance and is completely dominating for large values of m_A . The dilepton channel improves the combined significance only for low Higgs boson masses. Unfortunately, no lepton-hadron analysis at $m_A < 150$ GeV was performed. It might be very interesting to evaluate the potential of the lepton-hadron channel for lower Higgs boson masses in future studies.

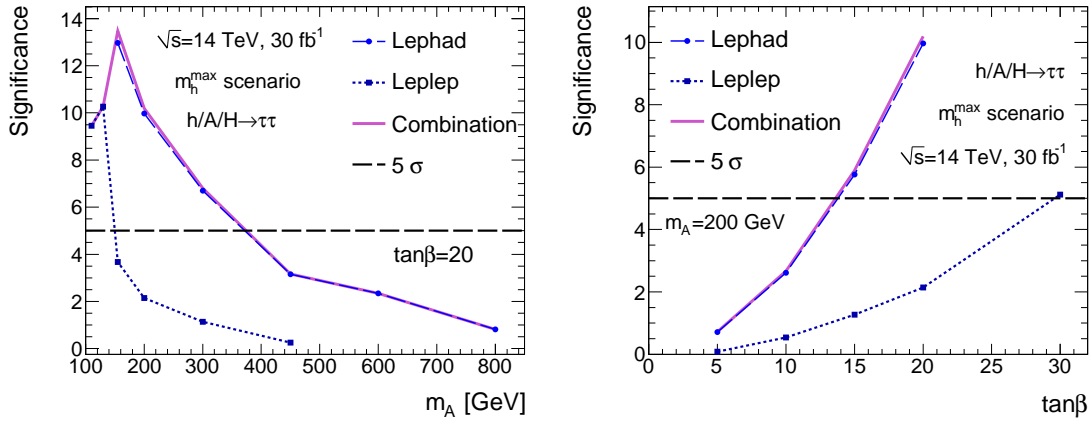


Figure 9.22.: Significance as a function of m_A for $\tan\beta = 20$ (left) and as a function of $\tan\beta$ for $m_A = 200$ GeV (right). The line labeled as *Lephad* is the combined significance from the b-tagged and non b-tagged analyses. The line labeled as *Combination* is the combined significance from the dilepton analysis and the two lepton-hadron analyses.

In Figure 9.23, the 5σ discovery limits are presented for the dilepton channel, the lepton-hadron channel and the combination. The discovery contour assuming no background systematics is also given. It is observed that the impact of systematic uncertainties becomes smaller for larger Higgs boson masses. This can be explained by the decreasing number of background events for the larger Higgs boson mass hypotheses, keeping in mind that different cuts were applied for each mass point studied. The combined 5σ contour for the lepton-hadron channel obtained in this thesis is completely comparable to the contour stated in [124], although the systematics were treated

a bit differently as was discussed before. In Figure 9.24 the 95% CL. exclusion contour is presented for the combination. The case assuming statistical background uncertainties only was also evaluated. The 95% CL. is equivalent to 1.64σ significance.

In Appendix I, Figures I.2 and I.3, the discovery and exclusion contours are displayed assuming a data-driven $t\bar{t}$ estimation applied also in the dilepton channel. This improves the sensitivity for the low m_A -region.

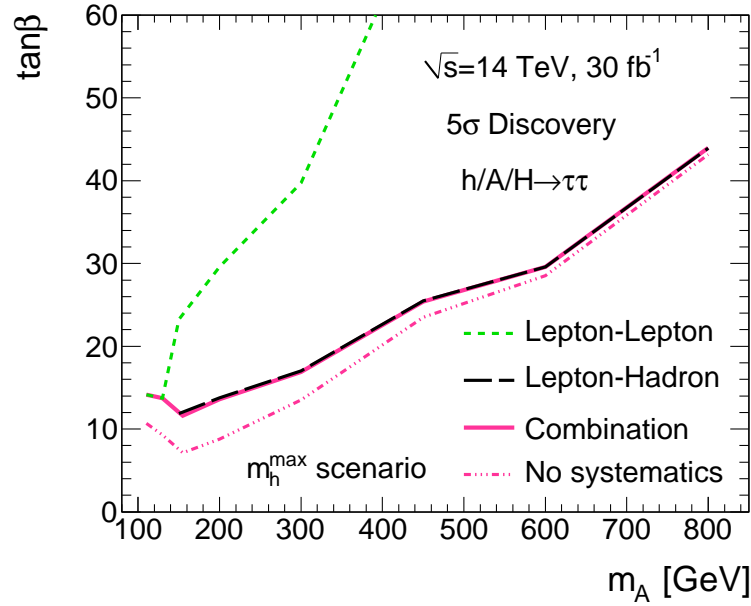


Figure 9.23.: The 5σ discovery contour, for the dilepton channel (green dashed line), the combination of b-tagged and non b-tagged analyses in the lepton-hadron channel (black dashed line) and the combination of the two final states (pink solid line). The combined result is also given for the case the systematic background uncertainties is zero (pink dash-dotted line). The dilepton channel only contributes to the significance for the very low Higgs boson mass region. For $m_A \geq 160$ GeV the discovery potential is completely dominated by the lepton-hadron channel.

The combined significance is ultimately evaluated also for other values of the integrated luminosities. The results are presented in Figure 9.25. It is found that the discovery potential deteriorates especially for the large Higgs boson mass hypotheses when the integrated luminosity decreases. This can be explained by the low number of expected signal events since the background uncertainty is assumed to remain the same. On the other hand, for $m_A \leq 200$ GeV the sensitivity can hardly be improved by larger luminosities. In that case one way to gain an improvement is by reducing systematic uncertainties. The results for different luminosities, however, have to be understood as rough indications of the true discovery potential. Depending on the available amount of real data, special Higgs boson searches might need to be performed which include for example looser cuts if the signal yield expected is too small.

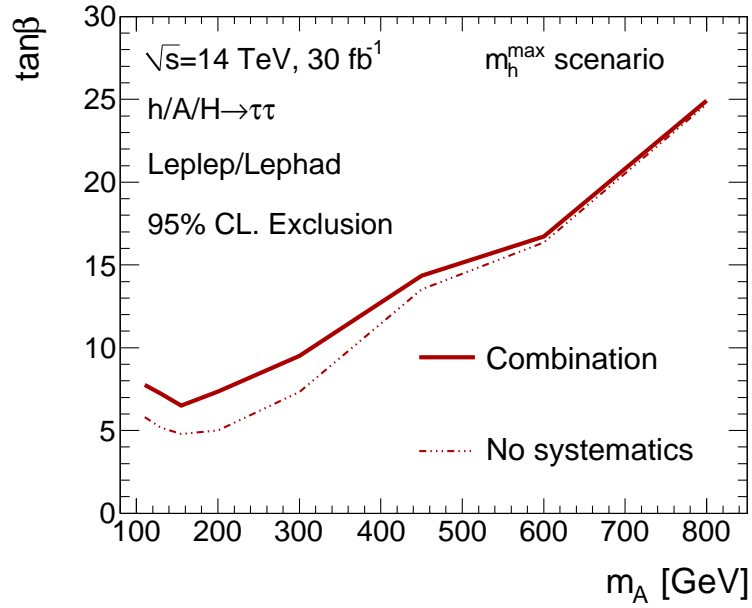


Figure 9.24.: The 95% CL. exclusion contours in the $m_A - \tan\beta$ plane of the combination of the dilepton and lepton-hadron channels. This is equivalent to a significance of 1.64σ . The dashed-dotted line gives the exclusion in case only statistical background uncertainties are assumed.

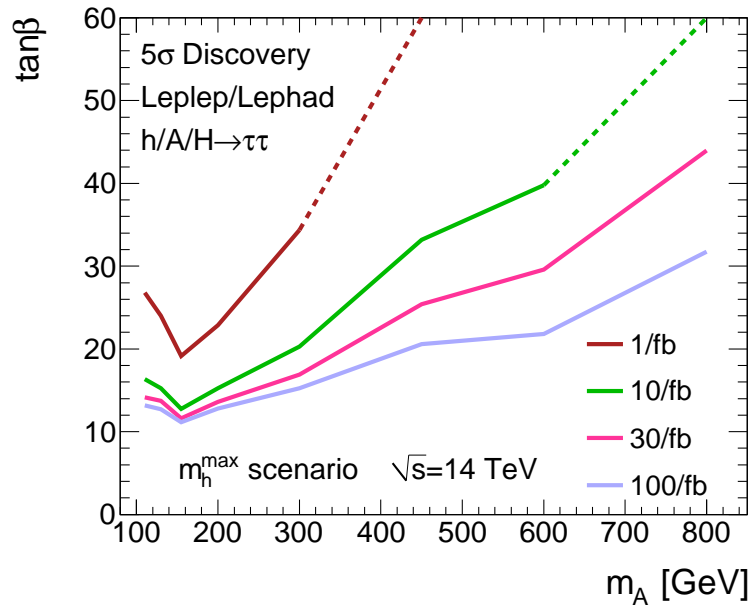


Figure 9.25.: The discovery contour of the combination of the dilepton and lepton-hadron channels for different values of the integrated luminosity. The dashed lines indicate that the predictions are not completely reliable for these regions. A larger integrated luminosity will in particular improve the discovery potential in the large Higgs boson mass region.

9.3.4. Discussion

The lepton-hadron analysis yields a better discovery potential than the dileptonic channel at larger m_A , despite the fact that the lepton-lepton final state offers a particularly clean signature resulting in negligible QCD and W+jets contributions. The discovery contour in the $m_A - \tan\beta$ plane is steeper for the dilepton analysis. Although the analyses cannot be compared directly, they are similarly designed: Both analyses attempt to maximize the discovery potential by selecting signal events m_A -dependently after a mass-independent baseline selection is applied.

The lepton-hadron channel comprises approximately 45% of all $\tau\tau$ decays. The fully leptonic channel only covers a fraction of 12%. This results in almost a factor 4 in terms of cross section times branching ratio. The electron or muon in the lepton-hadron final state is most useful for triggering and the suppression of QCD events and other fully hadronic backgrounds. But there is another reason why the lepton-hadron channel is the most powerful channel in the large A-mass region. The argument is outlined below.

In Figure 9.26 the p_T distributions of the hadronic system of the leading τ candidate are compared to the p_T of the leading lepton, for a light and a heavy Higgs boson mass. All baseline cuts are applied. It is obvious that the two p_T distributions differ; the lepton p_T peaks at much lower values. This can be explained by the fact that a leptonic tau decay always involves two neutrinos and therefore results in more MET. The hadronic tau decay involves only one neutrino. The hadronic system of the τ decay therefore has a larger p_T on average.

This is further demonstrated in Figure 9.27. In the left plot the MET distributions for the different final states are illustrated. Due to the back-to-back topology, in particular for the heavy Higgs bosons, the p_T of the neutrinos balance each other, thus do not appear as MET. This balancing in the lepton-hadron final state is not so distinct since one neutrino is emitted on one side and two neutrinos on the other side. The neutrinos are indirectly visible in the SumET distribution in the right plot. The SumET observable is defined as the scalar sum of the energy deposits weighted with the $\sin\theta$ w.r.t. the beam (E_T) in the calorimeters. Since the neutrinos remove a large fraction of the E_T , the SumET is considerably smaller when more neutrinos are present in the final state.

Selecting hadronic high- p_T τ candidates becomes the key cut for the large A boson mass analysis (compare to Figures 9.7 and 9.11). Applying this cut results in almost no background, since the H/A bosons are then the heaviest objects in the detector. Almost no irreducible SM background processes remain.

The fully leptonic channel is most useful for low A masses, since it offers a better QCD background reduction. The lepton-hadron channel, however, is an outstanding discovery channel for large A boson masses. Since in the MSSM the coupling to vector bosons is suppressed, the decay to $\tau\tau$ becomes the most relevant channel, taking into account that the Higgs boson decay to $b\bar{b}$ cannot be distinguished from pure QCD events by the trigger.

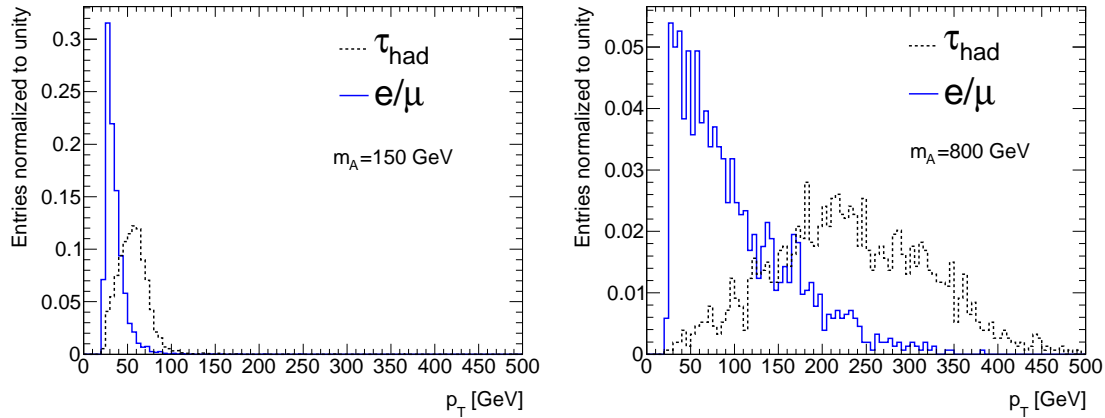


Figure 9.26.: The visible p_T of the leading hadronic τ candidate compared to that of the leading electron or muon, left for $m_A = 150$ GeV and right for $m_A = 600$ GeV. The hadronically decaying τ has a larger p_T on average. In the lepton-hadron analysis, for large A boson masses, a separation of signal and background is therefore easier and results in a better discovery potential.

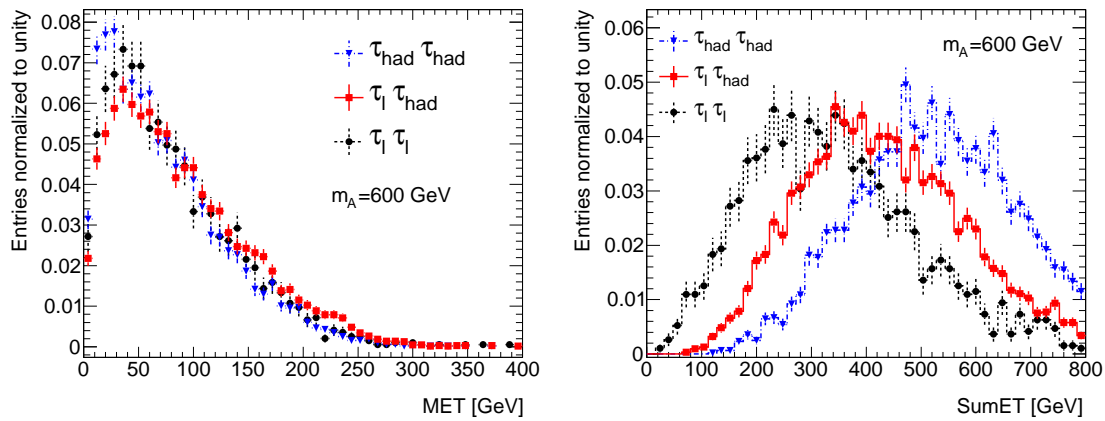


Figure 9.27.: Left: The MET distribution after baseline cuts for a Higgs boson signal with $m_A = 600$ GeV, broken down into the three different $\tau\tau$ decay final states. Although there are four neutrinos in the dilepton final state, the MET in the lepton-hadron channel is the largest, because of the odd number of neutrinos emitted. Right: The SumET distribution for the same Higgs boson events. The neutrinos are visible as missing SumET.

9.3.5. Comparison to Other Publications

The results obtained in this thesis are finally compared to other publications. In Figure 9.28 (left) the 5σ contours are shown based on the former analysis of the lepton-hadron channel in ATLAS [109]. The results from an analysis of the fully hadronic final states are also given [131]. In this analysis from 2003 aiming at an integrated luminosity of 30 fb^{-1} no systematic uncertainties were included. It therefore must be compared with the corresponding (dashed pink) contour

in Figure 9.23. The lepton-hadron analysis here is based on this publication, where also a splitting into a b-tagged and a non b-tagged analysis was performed. The former analysis and the results here are very similar. In [109] systematic uncertainties were shortly discussed and assumed to be in the order of 25%, however, they have not been incorporated into the discovery potential. In this thesis it has been shown that the systematic uncertainties are much smaller and can be reduced further by the use of data-driven background estimation procedures.

In Figure 9.28 (right) the results obtained by the CMS experiment are presented. These results are a combination of the $\tau_e \tau_h$, $\tau_\mu \tau_h$ and $\tau_e \tau_\mu$ channels. The cross sections were scaled to values corresponding to a LHC center-of-mass-energy of $\sqrt{s} = 7$ TeV and a luminosity of 1 fb^{-1} was assumed. This CMS combination and first data extrapolation is published in [132] and based on [133–135]. It needs to be understood as a rough indication of the physics potential, because these results are based on analyses not designed for first data.

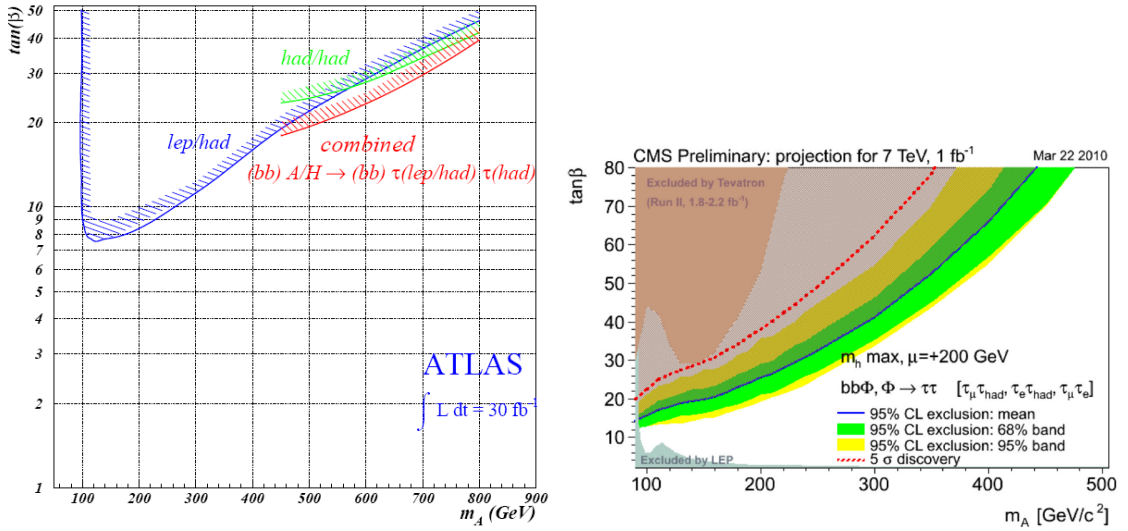


Figure 9.28.: Left: 5σ discovery contour obtained in the former ATLAS analyses of the lepton-hadron channel [109] (blue) and hadron-hadron channel [131] (green) analyses and combination (red). The contours do not contain systematic uncertainties. Both signal production modes (association with b-quarks and direct production) are included. Right: CMS first data extrapolation of the potential of MSSM $h/H/A \rightarrow \tau\tau$ produced in association with b-quarks [132]. Shown are the 5σ discovery contour (red dashed line) and exclusion limit (blue solid line), the 1σ and 2σ uncertainty bands on the exclusion limit and the excluded regions from LEP and Tevatron. All results are obtained for the m_h^{max} scenario.

For comparing to the CMS first data expectations, the results of this work were also scaled to an integrated luminosity of 1 fb^{-1} and the cross sections were scaled to their corresponding values of 7 TeV. The scaling factors of the cross sections used when extrapolating from 14 TeV to 7 TeV are listed in Table 9.29 and were taken from [136] and [117]. The signal cross sections were scaled with a factor of 0.25 in accordance with [137]. The same systematic uncertainties as for 30 fb^{-1} were assumed here, which is most probably too optimistic. The discovery and exclusion contours are presented in Figure 9.29. The results obtained are in general comparable to the CMS results. They are, however, better for $m_A \geq 150 \text{ GeV}$ and worse for $m_A < 150 \text{ GeV}$. Only the dilepton channel was evaluated for $m_A < 150 \text{ GeV}$, which explains the difference in the low mass region. The

CMS analyses only include the contribution from b-associated Higgs boson production, leading to slightly worse results for $m_A \geq 150$ GeV.

Process	$\sigma \cdot BR \cdot (14 \text{ TeV})$	$\sigma \cdot BR (7 \text{ TeV})$	Scaling factor
$t\bar{t}$	461 pb	160 pb	0.347
$Z \rightarrow \ell\ell$	2036 pb	954 pb	0.469
$W \rightarrow \ell\nu$	20460 pb	9813 pb	0.480
QCD	-	-	0.5
ggH, bbH	-	-	0.25

Table 9.29.: Cross sections at 14 TeV and 7 TeV for various processes. The ratio of both values (the scaling factor) is also given. For the signal and the QCD processes scaling factors of 0.25 and 0.5 were used.

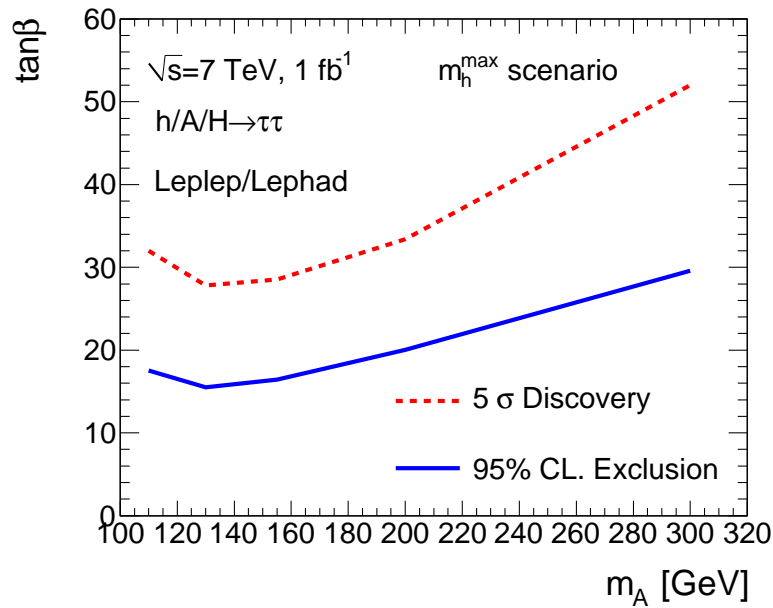


Figure 9.29.: The 5σ discovery contour (blue dashed line) and 95% CL. exclusion limits (red solid line) when rescaling the results to 1 fb^{-1} and 7 TeV cross sections. The results of this thesis are slightly better than the CMS results for $m_A \geq 150$ GeV, taking into account that only b-associated Higgs boson production was considered by CMS. For $m_A < 150$ GeV only the dilepton channel was evaluated and therefore the results obtained in this thesis are worse than CMS for $m_A < 150$ GeV. Above Higgs boson masses of 300 GeV there is no more sensitivity.

10

Conclusions

10.1. Status of LHC and ATLAS

The LHC restarted in fall 2009 with a center-of-mass energy of 900 GeV but soon advanced to $\sqrt{s} = 7$ TeV. ATLAS is taking data since then. Up to now more than 3.7 pb^{-1} were delivered by the machine and 3.5 pb^{-1} have been recorded (09/2010). Major successes of the early data taking phase were for example the observation of high energetic jets and the commissioning of the jet trigger, the identification of hadrons such as pions, kaons, J/Ψ resonances [138], and the measurement of charged track multiplicities as a probe of the underlying event [139]. Later on in 2010, the W and Z bosons were re-discovered and cross section measurements have started [116], [140]. Lately, even $t\bar{t}$ candidates have been identified [141]. Performance studies have been conducted since then. In-situ techniques, like for example the jet energy or missing E_T calibration, are under development [142, 143]. The identification of b-jets and the reconstruction of hadronic τ candidates is already well established [144, 145]. Studies of SM processes as backgrounds to Higgs boson searches have started and will be intensified.

To give an example of the recent progress, an event display of a $Z \rightarrow \tau\tau \rightarrow \mu + \text{had} + 3\nu$ decay candidate is presented in Figure 10.1, recorded on August the 3rd by the ATLAS detector in 7 TeV collisions [146]. The hadronic τ candidate has three well identified tracks and is therefore classified as a 3-prong candidate.

The performance of the ATLAS detector so far is truly outstanding and exceeds the most optimistic expectations of the scientists involved all around the world. If the successful running continues like that, the discovery of Higgs bosons and/or processes beyond the Standard Model seems to be only a matter of time and luminosity. An upgrade of the energy to 7 TeV per beam is intended but will mainly depend on the performance of the training of the super-conducting magnets at high currents. The shutdown and upgrade of the LHC is planned to begin after Christmas 2011. In 2012 the data recorded up to then will be re-analyzed intensively. In 2013, hopefully, the quest will continue with focus on possible discoveries which might be *just around the corner*.

The search for Higgs bosons will commence with integrated luminosities of 1 fb^{-1} but will be intensified with increasing amounts of data and in particular after the LHC upgrade. The earliest sensitivity to a SM Higgs boson of $m_A \approx 160 \text{ GeV}$ is given by the $H \rightarrow WW$ decay, for larger masses it is the decay to Z pairs with subsequent decay to four leptons. The low Higgs mass region is harder to cover. There the decay to photon pairs offers the best possibilities.

10.2. Search for Supersymmetric Higgs Bosons

In the MSSM the $\tau\tau$ channel offers an excellent discovery potential for the Higgs bosons and the channel is applicable over the full allowed Higgs boson mass range up to 1 TeV. In this work

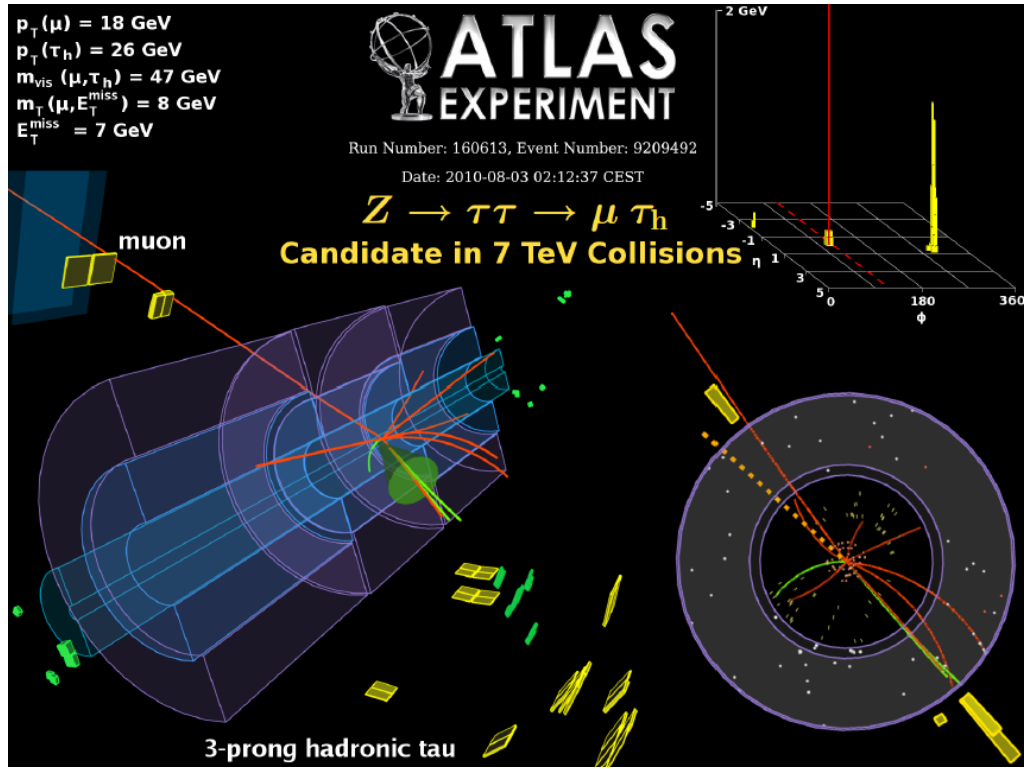


Figure 10.1.: Event display of a $Z \rightarrow \tau\tau \rightarrow \mu + \text{had} + 3\nu$ event candidate (taken from [146]), recorded in August 2010. The hadronic τ candidate has three well identified tracks and it has the opposite charge of the muon. In the event display the τ candidate is marked with a green cone and its associated tracks with green lines. Other tracks and the muon track are indicated by orange lines. The missing E_T is visualized by the dotted yellow line. Energy deposits in calorimeters are marked by yellow or green fields.

the design of a search aiming at an integrated luminosity of 30 fb^{-1} has been studied. Selection strategies were developed and experimental difficulties were identified. Important aspects and conclusions of this work are summarized in the following.

- Phenomenology:

The properties of the neutral MSSM Higgs bosons are given as function of m_A and $\tan\beta$. At $m_A = 130 \text{ GeV}$ all three bosons are almost degenerate in mass. For $m_A < 130 \text{ GeV}$ ($m_A > 130 \text{ GeV}$) the h and the A (the H and the A) are degenerate, resulting in one signal with a mass of m_A . For $m_A > 130 \text{ GeV}$, the mass of the h boson is a constant at 130 GeV and its discovery could be mistaken for the SM Higgs boson. It is therefore crucial also to look for heavy Higgs bosons. The discovery of two Higgs boson signals would be a strong evidence for realization of a two doublet Higgs field model in nature.

Since the coupling of the H and A bosons to vector bosons is suppressed or even absent, the decay to $\tau\tau$ has the second largest branching fraction after the decay to $b\bar{b}$. The coupling to down-type fermions is enhanced with the value of $\tan\beta$. The MSSM Higgs is produced either in association with b -quarks or by gluon fusion. Depending on the value of $\tan\beta$, the cross section of b -associated Higgs boson production is several orders of magnitude larger

than in the SM. For low values of m_A and large value of $\tan\beta$ the gluon fusion process is dominant, for $m_A > 500$ GeV the gluon fusion signal becomes negligible.

- Event generation:

The results of this work were obtained from official and validated MC samples exclusively. The signal process was either generated with the SHERPA event generator or with PYTHIA. The dilepton analysis is based completely on fully simulated events, for the analysis of the lepton-hadron final state ATLFastII was used. It has been found that it is inevitable to apply generator filters in order to evaluate also non-dominant backgrounds.

For the case when the MC statistics was still not sufficient to evaluate the contribution of a certain process, the efficiency of few selection cuts were applied as event weights and/or cuts have been factorized.

The analyses aim at 30 fb^{-1} , statistical uncertainties from limited MC samples were not considered.

- Signal signature and object identification:

The Higgs boson decay to τ pairs is classified by the subsequent decay of the taus. The case of a fully leptonic decay and the case of one leptonic and one hadronic τ decay have been considered. Though the branching ratio of the lepton-hadron final state is large, it involves the difficulties of the correct identification of hadronic τ -leptons and the separation from QCD jets. In the lepton-hadron final state background processes involving only one or even no true electron or muon become more important than in the dilepton channel.

The reconstruction of the signal process requires further the correct identification of electrons, muons, jets and the tagging of b-jets. Furthermore, the neutrinos from the τ decays result in large MET. Medium (tight) lepton selection criteria were applied in the dilepton (lepton-hadron) analysis.

- Higgs boson mass reconstruction:

Due to the presence of neutrinos the Higgs boson mass cannot be fully reconstructed. The collinear approximation is used to compensate the loss of information. Since the neutrinos and the visible τ decay products are emitted into the same direction, p_T conservation is used to scale the momentum of the visible particles to the momentum of the τ leptons. This approximation results in a small left-shift of the reconstructed particles with respect to the true value of m_A .

The reconstructed Higgs boson mass is very broad. The width depends strongly on the production process but depends only very little on the decay final state. The Gaussian width of the central part of the peak of a signal produced in association with b-quarks ranges from 30 GeV at low m_A up to 100 GeV for $m_A = 800$ GeV. The peak width of a signal produced in gluon fusion ranges from 20 GeV at low m_A up to 40 GeV for $m_A = 450$ GeV.

The width of the mass peak and therefore the discovery potential crucially depend on the MET resolution.

- Event selection:

In both analyses a m_A -independent baseline selection was applied which already removes the majority of the background processes. In the dilepton analysis only the b-associated signal was considered and at least one b-tag was required. A b-tag removes contributions from

W and Z boson decays significantly but enhances the relative contribution of the $t\bar{t}$ background, which is why a cut on the number of jets was applied. In the lepton-hadron channel also the gluon fusion signal was considered and the analysis was split into one where a b-veto was applied and another one where at least one b-tag was required. Then m_A -dependent cuts were optimized to maximize the statistical significance.

Higgs boson masses between 110 GeV and 800 GeV were considered. Applying m_A dependent cuts and choosing a mass window results in a change of the final background compositions in the signal regions. In the dilepton analysis at low m_A the $Z \rightarrow \tau\tau$ background is dominating, for $m_A > 160$ GeV the $t\bar{t}$ background is the most prominent process. In the lepton-hadron channel in the non b-tagged analysis, at low m_A the $Z \rightarrow \tau\tau$ background is dominating and at high m_A the W background is larger. In the b-tagged analysis the $t\bar{t}$ background is dominating.

- Data-driven $Z \rightarrow \tau\tau \rightarrow \ell\ell + 4\nu$ estimation in the dilepton analysis:
A $Z \rightarrow e\bar{e}/\mu\bar{\mu}$ control region was selected. To estimate the $Z \rightarrow \tau\tau$ shape, the muon kinematics from $Z \rightarrow \mu\bar{\mu}$ events was changed according to $Z \rightarrow \tau\tau$ reference histograms and the MET re-calculated. The number of $Z \rightarrow \tau\tau$ events was estimated by weighting the number of MC events with the ratio of the number of $Z \rightarrow \ell\bar{\ell}$ events in data to that number in MC. By that systematic uncertainties affecting equally the signal and the sideband regions cancel. The Z cross section and luminosity cancel, too.
- Data-driven $t\bar{t}$ estimation in the lepton-hadron analysis:
For the first time a method was investigated how to estimate the number of $t\bar{t}$ events in the signal region by exploiting the jet multiplicity distribution measured in a control region. The shape of the multiplicity distribution is normalized to the high multiplicity bins in the signal region. Preliminary results look promising but the method depends on the careful tuning of cuts and the impact of the value of $\tan\beta$ on the result increases the systematic uncertainty. A second method was also explored. The number of $t\bar{t}$ events was measured in a control region and an extrapolation ratio obtained from MC was used to estimate the corresponding number of $t\bar{t}$ events in the signal region. The systematics on that ratio were evaluated. The $t\bar{t}$ cross section and luminosity uncertainties cancel.
- Systematic uncertainties:
Experimental systematic uncertainties of the dominant processes were assessed by applying variations to the various objects and evaluating the impact on the number of events passing the selection. The results from the data-driven methods were used.
In the dilepton analysis the experimental uncertainty on $Z \rightarrow \tau\tau$ was found to be 3.4%, the uncertainty on $t\bar{t}$ was evaluated to be 5 %, the signal uncertainty is 6%-7 %.
In the lepton-hadron channel in the non b-tagged analysis the experimental uncertainties on $W \rightarrow e\mu/\tau\nu$, $Z \rightarrow \tau\tau$ and the signal processes were found to be 6%-7%. In the b-tagged analysis the experimental uncertainties on $Z \rightarrow \tau\tau$ and $t\bar{t}$ were found to be 11%, the signal uncertainty is 8%-9%.
Cross section uncertainties - if not canceled by the data-driven methods - are added in quadrature to the experimental uncertainties.
- Discovery potential:
The discovery potential was evaluated for each of the individual analyses and then the anal-

yses were combined using the profile likelihood method. Assuming 30 fb^{-1} the discovery (exclusion) of the MSSM Higgs boson with m_A can be expected when a $\tan\beta$ value of at least 11 (7) is realized in nature. A very heavy Higgs boson with $m_A = 800 \text{ GeV}$ could be discovered (excluded) for $\tan\beta \geq 44$ ($\tan\beta \geq 25$).

The combined result was also evaluated scaling the cross sections to $\sqrt{s} = 7 \text{ TeV}$ and assuming 1 fb^{-1} . It was found that the discovery (exclusion) of a signal with low m_A can be claimed with $\tan\beta \geq 30$ ($\tan\beta \geq 15$). For the discovery (exclusion) of a signal with $m_A \approx 300 \text{ GeV}$ a $\tan\beta$ of at least 52 (28) needs to be realized in nature.

The lepton-hadron channel is the more powerful search channel especially for large m_A because the signal events can easily be discriminated from background processes. The dilepton channel can contribute significantly to the low Higgs boson mass region when the systematic uncertainties are well under control.

- Possible improvements:
 - The gluon fusion contribution in the lepton-lepton channel was not considered. A splitting into a b-tagged and a non b-tagged analysis like it was done in the lepton-hadron analysis would improve the significance.
 - It was found that the relative impact of systematic uncertainties is larger when there is a large number of background events. Choosing tighter cuts should be explored and systematic uncertainties should always be incorporated when optimizing cuts.
 - Multi-variate techniques have not been exploited; their usage might lead to a significant improvement of the discovery potential but need a very good understanding of correlations between variables.
 - The influence of pile-up and non-collision backgrounds have not been considered. It will be very important to study the loss in efficiency concerning for example the τ identification and how this could be recovered.
 - The trigger was either imposed as cuts or as event weights. This certainly needs to be improved by using the simulated trigger menus available in the full ATLAS simulation.
 - No data-driven background estimation methods were used for the $t\bar{t}$ background in the dilepton analysis and the $Z \rightarrow \tau\tau$ background in the lepton-hadron analysis. Applying data-driven methods will decrease the systematic uncertainties.
 - A combination with the fully hadronic final state would be interesting and increase the sensitivity.

Comparison of the Collinear Mass between FULLSIM and ATLFast-II

It was studied how the performance of the collinear mass varies with different simulation software and release versions. The dilepton channel was chosen for this direct comparison, because hadronic taus are treated very unequally by the different simulation packages. The collinear mass using the FullSim Samples of Rel. 12 was compared to the collinear mass using the Rel. 14 samples which were processed with ATLFast-II. The same kinematic cuts on p_T and η have been applied to the datasets used for the comparison. No MET cut was applied. Since the Rel. 12 dataset was produced with up to 2 jets and the Rel. 14 sample contains up to 3 jets from the hard process, a cut of less than three jets was applied.

Important input quantities for the collinear mass are compared for a Higgs boson mass hypothesis of $m_A = 200$ GeV. In Figure A.1 the $\Delta\Phi_{\ell\ell}$ distributions and the p_T of the leptons are compared. Both distributions show a good agreement. The energy of the leptons and the $p_{T,\text{miss}}$ distributions are displayed in Figure A.2. Here a good agreement is observed, too.

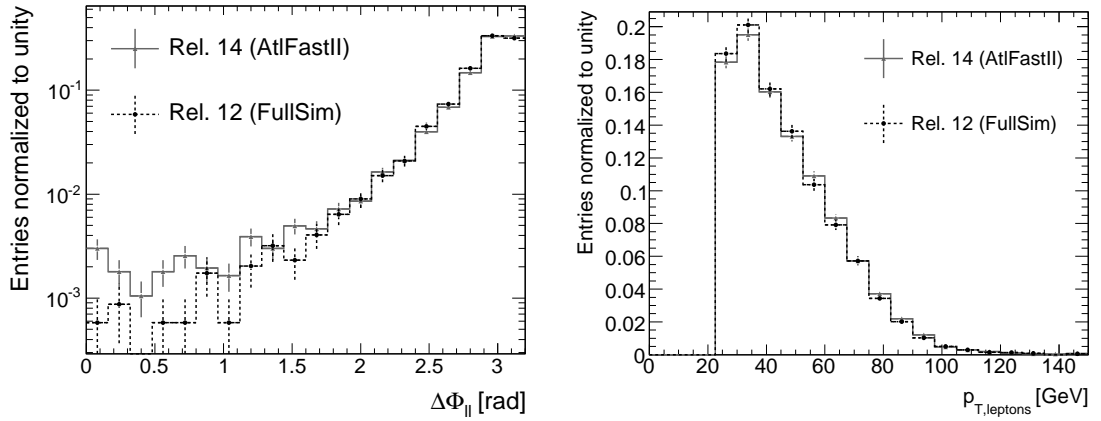


Figure A.1: Left: The $\Delta\Phi$ distribution of the two leptons for a Higgs boson mass hypothesis of 200 GeV. The histograms are normalized to unity. The events simulated in Rel. 14 (dashed black line) seem to have a slightly larger $\Delta\Phi_{\ell\ell}$ than the events which were fully simulated in Rel. 12 (solid grey line). Right: The distribution of the p_T of the two leptons. A good agreement between the two histograms is observed.

The invariant dilepton mass is presented in the left plot of Figure A.3, and the invariant ditau mass is given in the right plot of the same figure. In both plots, the mass resolutions show some differences. The collinear mass was fitted with a simple Gaussian to quantify the difference. The peak

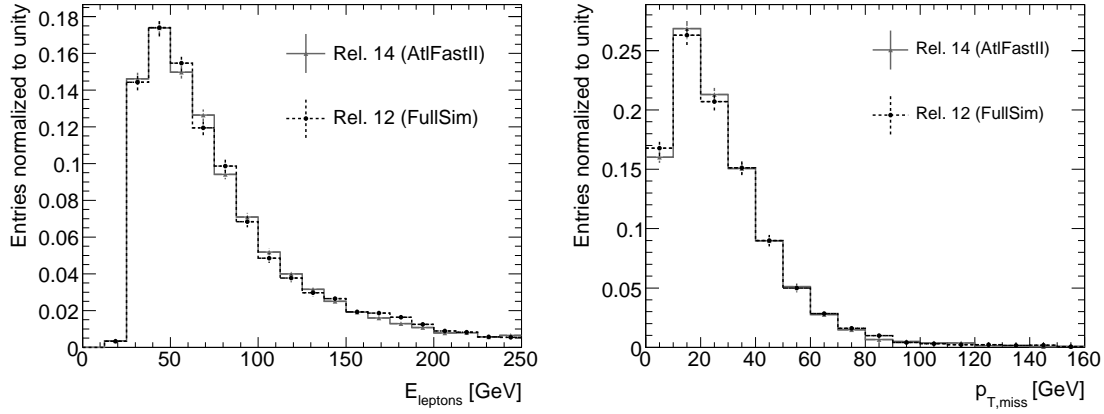


Figure A.2.: Comparison of the energy of the two leptons (left) and the $p_{T,\text{miss}}$ (right) for $m_A = 200$ GeV. There is a good agreement between the histograms in both plots.

positions do agree, but the width in Rel. 12 is 3 GeV smaller than in Rel. 14. This effect however is smaller than the sum of the fit uncertainties and therefore not significant.

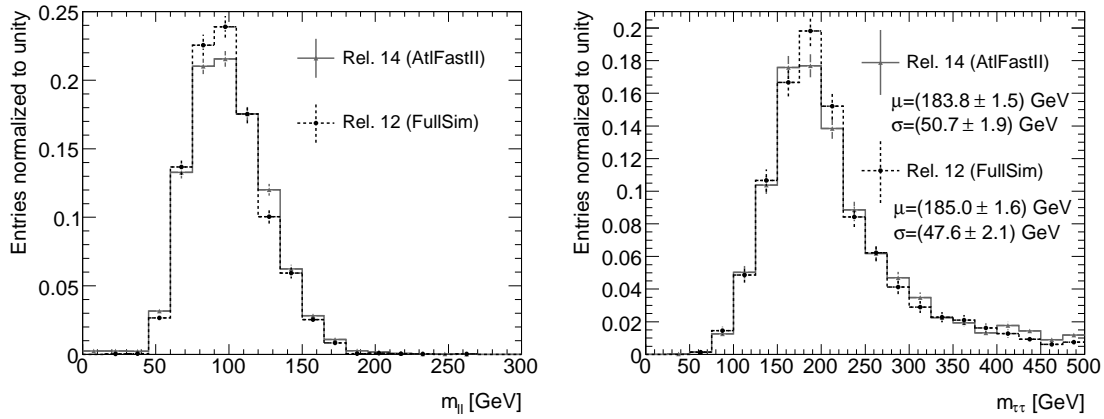


Figure A.3.: The invariant dilepton mass (left) and the collinear mass (right) for a Higgs boson mass hypothesis of 200 GeV. Both plots show differences between the two software releases. The $m_{\tau\tau}$ peak was fitted with a Gaussian. The difference in the width is small compared to the uncertainties from the fit.

B

B-Tagging Weight Corrections for Rel. 12 Samples

Table B.1 lists the datasets and the weight corrections applied to the IP3D+SV1 b-tagging weight for all samples used in Release 12. The procedure how they have been obtained is described in Section 6.4.3.

Dataset ID	Correction for 70 %	Correction for 60 %	Correction for 80 %
5200	0.82	1.17	0.58
5210	0.83	1.17	0.55
5358	0.96	1.25	0.65
9061	0.8	1.1	0.5
5144	0.67	0.95	0.5
5145	0.67	0.95	0.5
5146	0.64	0.95	0.5
9060	0.8	1.1	0.5
9084	0.7	1.1	0.5
9085	0.75	1.1	0.5
9086	0.82	1.1	0.65
9087	0.7	1.1	0.5
5011	0.67	0.92	0.24
5012	0.72	1.02	0.45
5013	0.82	1.19	0.52
5014	0.92	1.35	0.59
5015	1.12	1.64	0.69

Table B.1.: Weight correction values for the truth light-jets in Rel. 12.

Visible Mass in the Dileptonic Channel

C.1. Visible Mass at Baseline Selection Level

When applying the baseline cuts in the lepton-lepton analysis, as was described in Section 8.1.1, a first estimate for the expected discovery potential can be made. The results for the collinear mass analysis at baseline level are also given in Section 8.1.1. In case the visible mass is reconstructed no cuts on x_1 and x_2 are applied, the event yield is therefore larger and the background composition is also different to when reconstructing the collinear mass. The m_{visible} distributions for a signal hypothesis of $\tan\beta = 45$ are displayed in Figure C.1.

For the calculation of the statistical significance, S/\sqrt{B} , a mass window cut is applied:

$$m_0 - 1.5 \cdot \sigma < m_{\text{visible}} < m_0 + 2.0 \cdot \sigma.$$

The numbers for m_0 , σ and the upper and lower edge of the m_{visible} window are given in Table C.1.

m_A [GeV]	m_0 [GeV]	σ [GeV]	$m_{\text{visible}}^{\text{low}}$	$m_{\text{visible}}^{\text{high}}$
110	73	20	43	113
130	81	26	42	134
160	94	35	41	165
200	110	46	41	203
300	156	72	47	300
450	215	110	50	434

Table C.1.: The m_{visible} mass window cut chosen for the baseline level. $m_{\tau\tau}^{\text{low}}$ and $m_{\tau\tau}^{\text{high}}$ denote the lower (upper) edge of the window, m_0 is the position where the signal peaks, σ is the mass resolution.

Table C.2 lists the statistical significance for each mass hypothesis and a value of $\tan\beta = 45$. The visible mass leads to a lower significance than if the signal is extracted from the collinear mass.

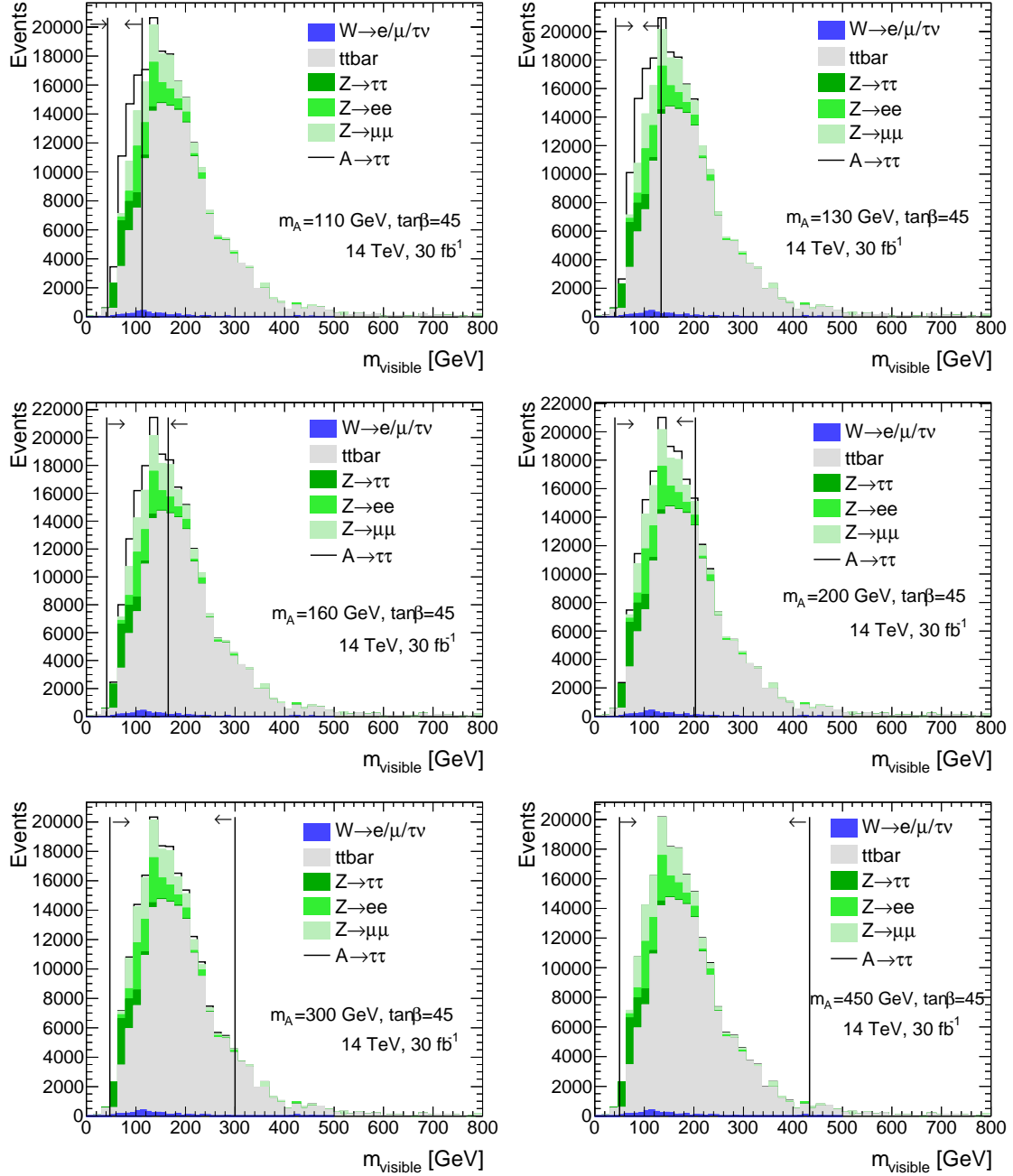


Figure C.1.: Reconstructed visible mass after the baseline selection for various Higgs boson mass hypotheses as indicated in the plots, all for $\tan\beta = 45$. The mass window cuts are indicated by lines, the arrows point to the events kept in the analysis.

m_A	S	B	S/\sqrt{B}
110 GeV	2391	44775	11.3
130 GeV	2619	63472	10.4
160 GeV	1922	101676	6.0
200 GeV	1163	143697	3.1
300 GeV	466	187763	1.1
450 GeV	101	202229	0.2

Table C.2.: Number of signal events S , background events B and statistical significance S/\sqrt{B} in the mass window for $\tan\beta = 45$ and 30 fb^{-1} , when reconstructing the visible mass after the baseline selection. This needs to be compared to Table 8.4.

C.2. Visible Mass after Optimized Cuts

The visible mass is reconstructed after all baseline and optimized cuts are applied, except for the cuts on x_1 and x_2 . The results for an integrated luminosity of 30 fb^{-1} are shown in Figure C.2. Compared to the collinear mass shape, here the background and signal shapes seem to be even more similar. The events from the different processes are shifted together and peak at approximately the same mass value. A visible separation of signal and background is not possible. Furthermore, even a mass window cut is not useful.

The number of signal events and the background composition is summarized in Table C.3. Since no cuts on x_1 and x_2 are applied, more events are reconstructed when using the visible mass instead of the collinear mass. Especially the $Z \rightarrow ee/\mu\mu$ and W +jet contributions are considerably larger than for the case of the collinear mass reconstruction. The statistical significance was evaluated for each mass hypotheses and is listed in Table C.4.

Process	110 GeV	130 GeV	160 GeV	200 GeV	300 GeV	450 GeV
Signal	3591	3395	2353	1405	383	79
$Z \rightarrow \tau\tau$	4176	3898	2297	1653	157	0
ttbar	2358	2817	4193	7239	4553	3046
$Z \rightarrow \ell\ell$	1418	1497	908	734	530	172
$W \rightarrow e/\mu/\tau\nu$	817	498	530	595	293	67

Table C.3.: Numbers of events in 30 fb^{-1} after all selection cuts. The visible mass has been reconstructed and no mass window cut is applied. The signal cross section was scaled to a hypothesis of $\tan\beta = 30$.

m_A [GeV]	$S_{m_{\text{vis}}}$	$B_{m_{\text{vis}}}$	$(S/\sqrt{B})_{m_{\text{vis}}}$
110	3591	8770	38.4
130	3395	8710	36.4
160	2353	7928	26.4
200	1405	10221	13.9
300	383	5533	5.2
450	79	3285	1.38

Table C.4.: Number of signal events S , background events B and statistical significance S/\sqrt{B} if the visible mass is reconstructed. The numbers are scaled to $\tan\beta = 30$ and 30 fb^{-1} . This needs to be compared to Table 8.15.

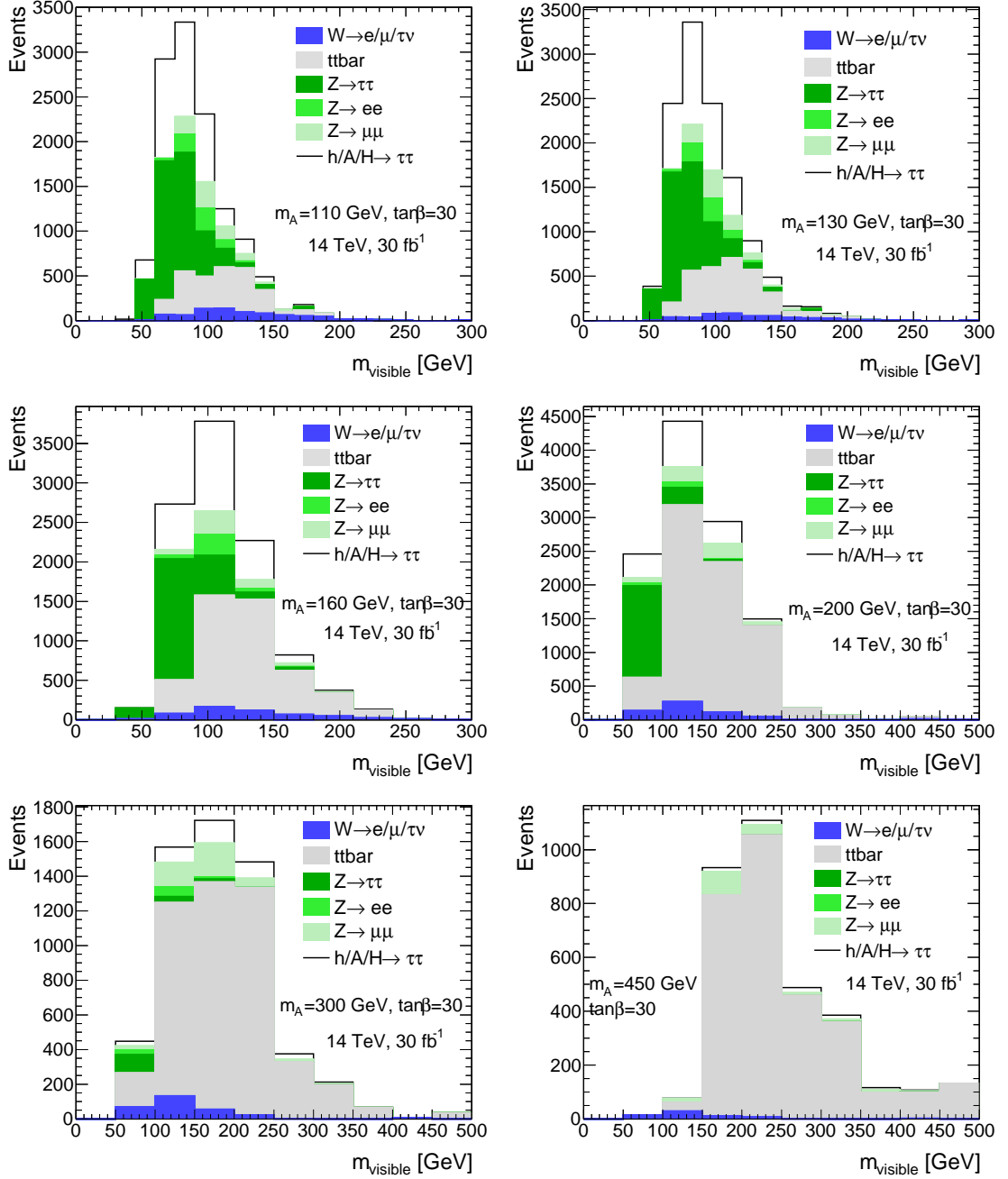


Figure C.2.: Reconstructed visible mass after all cuts for various Higgs boson mass hypotheses as indicated in the plots, all for $\tan\beta = 30$ and 30 fb^{-1} .

Canceling of Systematic Uncertainties by $Z \rightarrow \tau\tau$ to $Z \rightarrow \ell\ell$ Ratios

As follow-up on the data-driven estimation of the $Z \rightarrow \tau\tau \rightarrow \ell\ell$ normalization from Section 8.2.4, a closer look on the canceling of systematic uncertainties is given in this appendix.

It is assumed that jet-related and b-tagging-related uncertainties cancel when constructing a control region for $Z \rightarrow \ell\ell$ events which is 'similar' to the signal regions. This is achieved in principle by applying a cut on the number of jets, requiring a b-tag and by using the same minimal p_T cut for the jets in both regions. Then the Equations 8.7 are supposed to hold and if this is the case the double-ratios from Equation 8.8 will be unity.

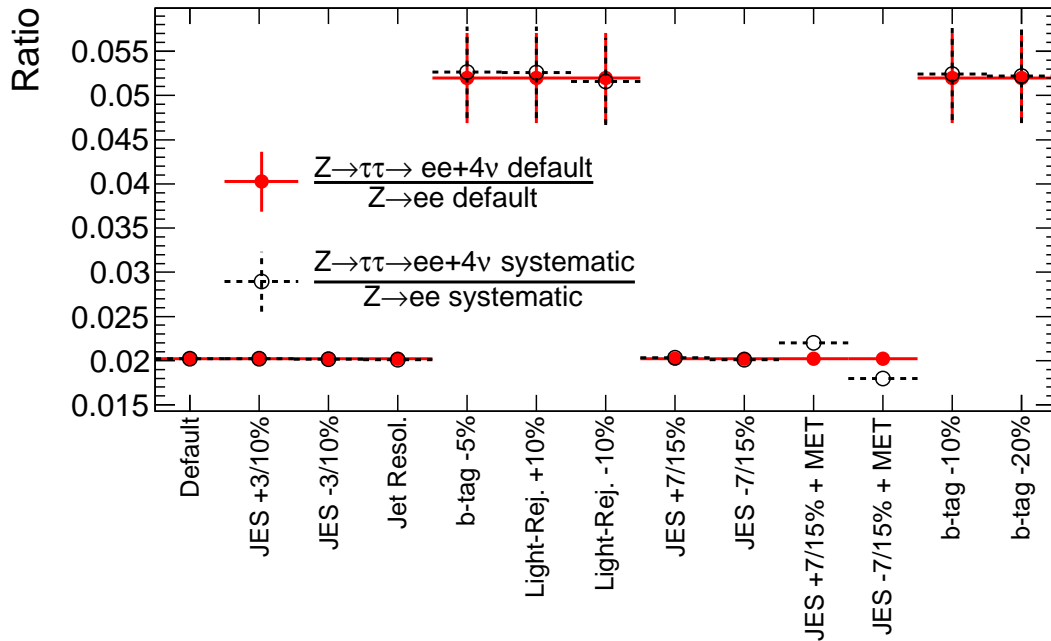


Figure D.1.: The ratio $\frac{\#(Z \rightarrow \tau\tau \rightarrow ee+4\nu)}{\#(Z \rightarrow ee)}$ for the default setting and when systematic variations are applied. The strength of the variations is given in the abscissa. The different values of the ratios (≈ 0.02 and ≈ 0.05) are resulting from the fact that for the evaluation of the jet-related uncertainties no b-tag was required in order to gain statistics. This, however, could of course not be done for the b-tagging-related uncertainties. For the variations 'JES $\pm 7/15\%$ + MET' the JES and the MET scale were correlated with 100%.

In Figure D.1 the ratio $\frac{\#(Z \rightarrow \tau\tau \rightarrow ee+4\nu)}{\#(Z \rightarrow ee)}$ is shown for the default setting and when several systematic variations are applied. This is an extended version of Figure 8.32 (right). The ratios of the default settings and when systematics are applied are supposed to be equal. This is the case for all b-tagging-related uncertainties and also for the jet-related uncertainties when the correlation to the MET is only 5% (see also Equation 8.3). For the case when the correlation between JES and MET is assumed as 100% the ratios are not equal.

In Figure D.2 the ratios $\frac{\#(Z \rightarrow \tau\tau \rightarrow ee+4\nu)^{sys}}{\#(Z \rightarrow \tau\tau \rightarrow ee+4\nu)^{def}}$ and $\frac{\#(Z \rightarrow ee)^{sys}}{\#(Z \rightarrow ee)^{def}}$ are displayed for different systematic variations. This plot is an extended version of Figure 8.32 (left). These ratios are supposed to be equal to each other if the assumptions hold. The same observations as for Figure D.1 are made here. If the JES and the MET are correlated with 100%, then the impacts from JES variation on the $Z \rightarrow \tau\tau$ events are much larger than the impacts on the $Z \rightarrow \ell\ell$ events. This is understood to result from the fact that only in the signal region cuts on x_1 and x_2 are applied, and these cuts are related to the MET. The same observations are made when calculating the same ratios for the $\mu\mu$ channel.

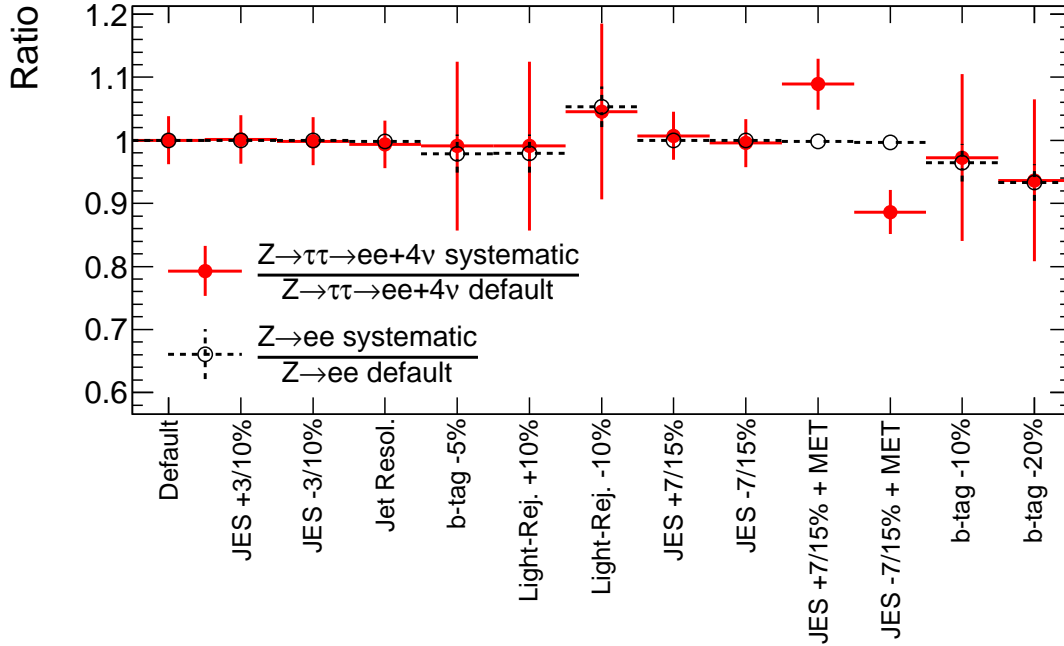


Figure D.2.: The ratios $\frac{\#(Z \rightarrow \tau\tau \rightarrow ee+4\nu)^{sys}}{\#(Z \rightarrow \tau\tau \rightarrow ee+4\nu)^{def}}$ and $\frac{\#(Z \rightarrow ee)^{sys}}{\#(Z \rightarrow ee)^{def}}$ when systematic variations are applied. The strength of the variations is given in the abscissa. The jet-related uncertainties were evaluated without requiring a b-tag in both regions to gain statistics. For the variations 'JES \pm 7/15% + MET' the JES and the MET scale were correlated with 100%.

In Figure D.3 the double ratios from Equation 8.8 are displayed for different variations for both ee and $\mu\mu$ channel (compare also to Figure 8.33). The ratios are supposed to be unity when the systematics cancel. Again, the the double-ratios differ from unity when the JES and the MET are correlated with 100%. In all other cases the uncertainties indeed cancel.

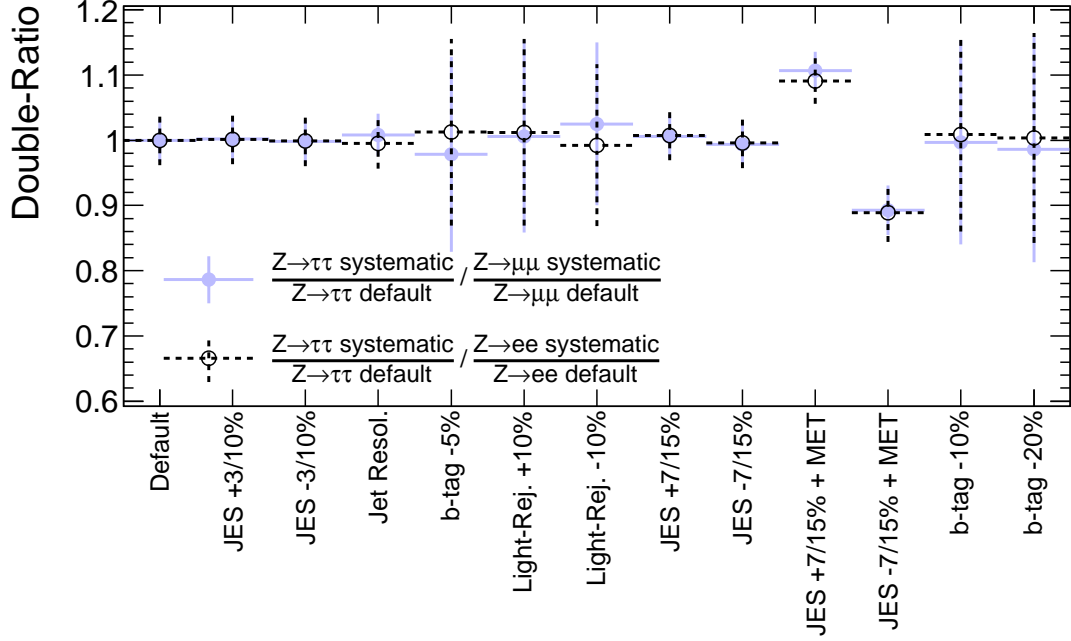


Figure D.3.: Double-ratio for various systematic variations and when increasing variations. The variations are indicated in the plot. The light blue (dotted black) lines mark the results from the $\mu\mu$ (ee) channel. The error bars reflect the real statistical uncertainties. They are larger for the b-tagging-related uncertainties because there the b-tagging requirement could not be dropped, as was done for the other systematic variations. For the variations 'JES \pm 7/15% + MET' the JES and the MET scale were correlated with 100%.

To conclude, in this appendix larger variations on the jet- and b-tagging-related uncertainties were assumed to test the canceling of the uncertainties by the normalization method outlined in Chapter 8. Such large uncertainties, however, are not reasonable and are not expected in 30 fb^{-1} . The uncertainties cancel indeed, but the JES uncertainty does not cancel when the MET is correlated to the JES with 100% due to different MET-related cuts in the signal and control regions.

Comparison of Significance Calculations

For the calculation of the significance in the dilepton channel (Chapter 8) the approximation $Z = S/\sqrt{B}$ was used. This approximation follows from the exact treatment using Poisson statistics when assuming $B \gg 0$ and $S \ll B$. The corresponding equations can be found in Section 9.3.1. The condition that B needs to be large is always fulfilled in the analysis of the dilepton channel. The lowest background contributions are expected at $m_A = 450$ GeV where 485 events are found in the mass window (compare to Table 8.15). $S \ll B$ is in general valid for large Higgs boson mass hypotheses. However, for large $\tan\beta$ or/and low Higgs boson masses the number of signal events will become very large and sometimes even larger than B , because $S \sim \tan^2\beta$.

The approximation is compared to the significance using the profile likelihood method (PLH) based on Poisson errors, using the ROOSTATS program [130]. The p-value obtained is converted into the number of Gaussian standard deviations. In Table E.1 a few representative p-values and the corresponding values of Z are listed. It was observed that for extremely small p-values the calculation could not be performed on a standard computer since the numbers could not be represented by the usual formats¹. This resulted in a break-down of the profile likelihood method for the cases where the significances are very large. For the combination of the dilepton and the lepton-hadron channels this is of no relevance, because only the discovery and exclusion limits are given, not the significance over the whole $m_A - \tan\beta$ plane. In case no significance could be obtained by ROOSTATS for the individual channels the approximation S/\sqrt{B} was used.

Z	5	10	30	37
p-value	$2.9 \cdot 10^{-7}$	$7.6 \cdot 10^{-24}$	$4.9 \cdot 10^{-198}$	$5.7 \cdot 10^{-300}$

Table E.1.: P-values and corresponding Gaussian standard deviations.

In Figure E.1 the significance calculations are shown as a function of m_A and $\tan\beta$ for two representative points. As expected, when the number of signal events is large (low m_A and/or large $\tan\beta$) a slight difference is observed. The general agreement, however, is very good. For the comparison, only points in the $m_A - \tan\beta$ plane are chosen where the PLH calculation did not break-down. The full background systematics (experimental and theoretical uncertainties) are assumed. The ratios of the approximate significance to the PLH calculation at the 5σ limit for each

¹In C++, a number in the commonly used *double* format yields numbers up to 10^{308} and has a precision of 16 decimal digits. *double* refers to the fact that this format has twice the precision as the *float* or *floating point* format. A *floating point* number is the numerical representation of a real number which is based on some approximations, as for example rounding, when the representation needs more bits than which are allocated. This leads to non-mathematical effects especially at the edge of the range intended for use [147].

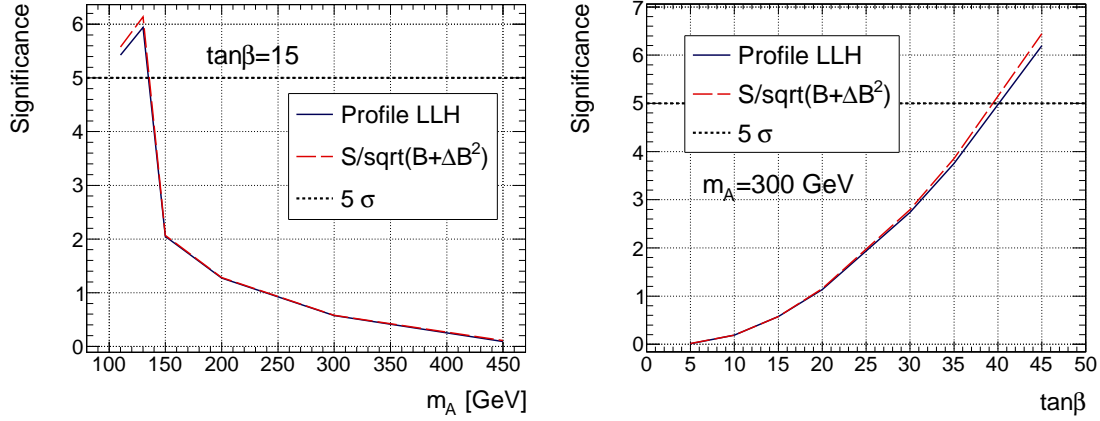


Figure E.1.: Comparison of the significance calculated by $Z = S/\sqrt{B}$ and the profile likelihood method (PLH), left as a function of m_A for $\tan\beta = 15$ and right as a function of $\tan\beta$ for $m_A = 300$ GeV. The calculation of the PLH did not result in instabilities for the parameter points shown. The difference of the two significance calculations are in general very small but increase for large S .

mass hypothesis are listed in Table E.2. The ratios are very close to unity.

m_A [GeV]	110	130	160	200	300
$Z_{S/\sqrt{B}}/Z_{\text{PLH}}$	1.022	1.026	1.011	1.015	1.031

Table E.2.: Ratio of approximate significance $Z = S/\sqrt{B}$ to the PLH calculation at the value of $\tan\beta$ where the 5σ limit is reached, assuming experimental and theoretical background systematics. A very good agreement between both calculations is observed, but in general the approximate significance yields larger values than the PLH.

Lepton and τ Identification Weights for the Lepton-Hadron Analysis

In the lepton-hadron analysis (Chapter 9), the tight lepton and/or τ ID were factorized for several background processes to gain MC statistics. The efficiencies were obtained from [85] and the same numbers are used in this thesis. The probability that a loose lepton passes the tight ID is factorized for the QCD dijet events. The weights are given in Table F.1.

Dataset ID	Electron efficiency	Muon efficiency
209642	0.0366497	0.00885103
209643	0.011053	0.00122046
209644	0.00623608	0.000195496
209645	0.00594227	0.000237151
209646	0.00594227	0.000237151
209542	0.0449031	0.0102355
209543	0.0122404	0.0013221
209544	0.00683304	0.000289165
209545	0.00636605	4.1159e-05
209546	0.00973574	2.35388e-05

Table F.1.: Tight lepton ID weights for the QCD dijet samples.

QCD jets might be misidentified as τ -leptons. Due to a low fake rate when applying a tight ID, the fraction of events passing the τ selection cut will be extremely low. However, this number becomes relevant for the QCD events with a large cross section. The probability of a loose τ candidate to pass the tight ID is factorized and applied as event weights. The weights for the dijet backgrounds are listed in Table F.3, the weights for the $W \rightarrow e/\mu/\tau + \nu$, $Z \rightarrow ee$ and $Z \rightarrow \mu\mu$ backgrounds are given in Table F.4. The weights are obtained in five $p_{T,h}$ bins:

- $p_{T,1} :$ $10 \text{ GeV} < p_{T,h} < 24 \text{ GeV}$
- $p_{T,2} :$ $24 \text{ GeV} < p_{T,h} < 45 \text{ GeV}$
- $p_{T,3} :$ $45 \text{ GeV} < p_{T,h} < 70 \text{ GeV}$
- $p_{T,4} :$ $80 \text{ GeV} < p_{T,h} < 100 \text{ GeV}$
- $p_{T,5} :$ $100 \text{ GeV} < p_{T,h}$

The weights depend on the truth type matched to the reconstructed τ candidate. The truth types were classified as b-jets, electrons, muons and if it is neither a b-jet, nor an electron, nor a muon, it is labeled as *other*. If the truth type is a b-jet, the candidates are further classified. If an electron or muon is matched to the b-jet then its labeled as b-jet (ℓ), otherwise as b-jet (h).

Dataset ID	Type	$p_{T,1}$	$p_{T,2}$	$p_{T,3}$	$p_{T,4}$	$p_{T,5}$
209642	b-jet (ℓ)	0.06428	0.0094	0.00152	0.00602	0
	b-jet (h)	0.02861	0.00721	0.00293	0.00095	0
	muon	0.19779	0.07133	0.04075	0	0
	electron	0.01365	0.01412	0.0045	0	0
	other	0.03362	0.01364	0.00946	0.00519	0
209643	b-jet (ℓ)	0.07685	0.02993	0.00686	0.00529	0.00146
	b-jet (h)	0.03972	0.00777	0.00306	0.00229	0.00143
	muon	0.22197	0.04704	0.03571	0.03448	0
	electron	0.03176	0.01474	0.00044	0.00149	0
	other	0.03064	0.01341	0.00616	0.00759	0.00589
209644	b-jet (ℓ)	0.06393	0.01662	0.00393	0.01229	0.00385
	b-jet (h)	0.0362	0.01123	0.00373	0.00213	0.00231
	muon	0.10413	0.01541	0	0	0
	electron	0.0544	0.00062	0.01371	0.0087	0.00355
	other	0.02413	0.01057	0.00756	0.00838	0.00685
209645	b-jet (ℓ)	0.03533	0.0181	0.00278	0.00477	0.00467
	b-jet (h)	0.0193	0.00498	0.0022	0.00286	0.00167
	muon	0.18633	0.0496	0	0.06666	0
	electron	0.02408	4e-05	0.00214	0.01064	0.00361
	other	0.02227	0.00998	0.00462	0.00659	0.00546
209646	b-jet (ℓ)	0.03533	0.0181	0.00278	0.00477	0.00467
	b-jet (h)	0.0193	0.00498	0.0022	0.00286	0.00167
	muon	0.18633	0.0496	0	0.06666	0
	electron	0.02408	4e-05	0.00214	0.01064	0.00361
	other	0.02227	0.00998	0.00462	0.00659	0.00546

Table F.2.: Tight τ ID weights for the QCD dijet samples with a pair of b-quarks and one electron or muon on generator level. The weights are obtained in 5 $p_{T,h}$ bins, depending on the truth type of the τ candidate. More information is given in the text.

Dataset ID	Type	$p_{T,1}$	$p_{T,2}$	$p_{T,3}$	$p_{T,4}$	$p_{T,5}$
209542	b-jet (ℓ)	0.04575	0.01742	0.00516	0	0
	b-jet (h)	0.03602	0.00688	0.00221	0.01064	0
	muon	0.13018	0.07087	0	0	0
	electron	0.07509	0.00757	0.0145	0.07143	0
	other	0.04199	0.01711	0.00895	0.00941	0
209543	b-jet (ℓ)	0.0501	0.02508	0.00116	0.01242	0.02057
	b-jet (h)	0.03394	0.00723	0.0032	0.00179	7e-05
	muon	0.25816	0.09199	0.02708	0	0
	electron	0.02963	0.01061	0.00313	0.0073	0.0001
	other	0.03363	0.01345	0.00641	0.00956	0.00581
209544	b-jet (ℓ)	0.07673	0.0113	0.01148	0.00569	0.00844
	b-jet (h)	0.04415	0.01116	0.00367	0.00185	0.00333
	muon	0.16274	0.04823	0.01887	0.00046	0.03515
	electron	0.0118	0.00838	0.00638	0.01176	0.00476
	other	0.02895	0.01135	0.00681	0.00549	0.00834
209545	b-jet (ℓ)	0.03534	0.01708	0.00846	0.00649	0.00777
	b-jet (h)	0.04791	0.00549	0.00279	0.00282	0.004
	muon	0.06785	0.05415	0.02104	0	0.00407
	electron	0.05212	0.01485	0.00563	0.00841	0.00344
	other	0.0281	0.0139	0.00558	0.00532	0.0059
209546	b-jet (ℓ)	0.06648	0.0021	0.00534	0.00746	0.00113
	b-jet (h)	0.01997	0.01411	0.00613	0	0.00171
	muon	0.07099	0.02324	0	0.03408	0.00187
	electron	0.02499	0.01176	0.00571	0.00526	0.00024
	other	0.02928	0.01029	0.0036	0.00495	0.00355

Table F.3.: Tight τ ID weights for the QCD dijet samples with one electron or muon on generator level. The weights are obtained in 5 $p_{T,h}$ bins, depending on the truth type of the τ candidate. More information is given in the text.

Dataset ID	Type	$p_{T,1}$	$p_{T,2}$	$p_{T,3}$	$p_{T,4}$	$p_{T,5}$
209530	b-jet (ℓ)	0.05302	0.00839	0.00173	0.0075	0
	b-jet (h)	0.04743	0.0093	0.00201	0.00418	0.00034
	muon	0.13124	0.07262	0.03898	0.01413	0.00448
	electron	0.05797	0.02767	0.01635	0.01579	0.0071
	other	0.0772	0.04381	0.02134	0.01558	0.0095
209531	b-jet (ℓ)	0.08129	0.00651	0.00172	0.00693	0.00337
	b-jet (h)	0.03878	0.00476	0.00295	8e-05	0.00596
	muon	0.15422	0.0743	0.02274	0.00988	0.01041
	electron	0.05334	0.02734	0.01405	0.00792	0.00491
	other	0.07561	0.04473	0.0223	0.01709	0.00981
209533	b-jet (ℓ)	0.03439	0.00408	0.01284	0.00204	0.00442
	b-jet (h)	0.03451	0.00703	0.00278	0.00195	0.00663
	muon	0.15015	0.06015	0.03504	0.01334	0.01155
	electron	0.05146	0.03125	0.01306	0.00817	0.00583
	other	0.07711	0.04576	0.02733	0.02222	0.01432
209520	b-jet (ℓ)	0.05154	0.02281	0.00207	0.00603	0.00318
	b-jet (h)	0.04007	0.01003	0.00386	0.0043	0.00017
	muon	0.22146	0.08753	0.0311	0.0103	0.01203
	electron	0.46511	0.47863	0.39535	0.17544	0.10067
	other	0.07768	0.04449	0.0246	0.01597	0.01034
209521	b-jet (ℓ)	0.08465	0.01258	0.00372	0.00638	0.00585
	b-jet (h)	0.04181	0.00826	0.00605	0.00239	0.00151
	muon	0.82327	0.64194	0.37194	0.20373	0.09678
	electron	0.04882	0.02606	0.0136	0.00331	0.00384
	other	0.07819	0.04327	0.02345	0.01622	0.0098

Table F.4.: Tight τ ID weights for the $W \rightarrow e/\mu/\tau + \nu$ and $Z \rightarrow ee/\mu\mu$ samples. The weights are obtained in 5 $p_{T,h}$ bins, depending on the truth type of the τ candidate. More information is given in the text.



Single Top Estimation from Monte Carlo in the Lepton-Hadron Analysis

Single top has not been considered in earlier MSSM $H/A \rightarrow \tau\tau$ analyses and was always assumed to be very small and therefore unimportant. But due to at least one true b-tag in its final state, the single top contribution might still be considerable large in the b-tagged analysis and had to be estimated from statistically limited Monte Carlo samples.

G.1. Contributing Processes

Single top can be produced in three different ways: In association with W bosons, in s-channel and in t-channel production. Since the cross section for s-channel production with 10.65 pb is rather low compared to the t-channel with 246 pb and the Wt channel with 66 pb, the s-channel has not been considered in the analysis [95, 96].

G.2. Cut Factorisation and Correction Factors

The only available Wt sample does not contain a lepton-hadron final state, since in that sample one W boson always decayed to $e/\mu/\tau$ and the other one only to $q\bar{q}$ pairs. Therefore a correction factor C_τ has been applied at the level of the loose τ selection cut. This correction factor was estimated to be $C_\tau = 3.43$ and was found by scaling the single top selection efficiency after the loose τ selection cut to the same selection efficiency as the $t\bar{t}$ sample. Table G.1 lists the accepted cross sections for $t\bar{t}$ and single top from the start of the analysis to the loose τ selection cut.

Cut factorization had to be used since the available Monte Carlo samples did not yield enough statistic to pass every cut in the b-tagged analysis. The cut on the transverse mass m_T from the baseline analysis had an especially low efficiency and was chosen to be taken out from the chain of cuts and instead applied as a weight. Further cuts used for the factorization were the tight tau efficiency and the b-tagging efficiency. The final mass window cut has been applied as a weight for the Wt sample in the $m_A = 200$ GeV analysis and to both the single top processes in the $m_A = 300$ GeV analysis. The mass window efficiency has been determined after the collinear approximation step, because this cut has a strong effect on the mass shapes. Figure G.1 shows the $m_{\tau\tau}$ distribution for both single top processes. Table G.2 lists the cutflow for single top for the remaining selection cuts starting from the tight τ cut.

Cut/Process	ttbar	Wt	t-channel
Z veto	401 700	28 607	80 656
Loose lepton	240 600	13 836	33 461
Tight lepton	175 100	10 768	26 175
$E_{T,miss} > 20$ GeV	139 300	8 366	20 662
$m_T > 25$ GeV	15 570	968	1 530
Loose τ	916	16.58	20.63
Loose $\tau \cdot C_\tau$	916	56.95	20.63

Table G.1.: Accepted cross sections in fb from start of the analysis to the loose tau selection cut. The low efficiency for the loose tau selection cut in the Wt sample is understood to result from the missing lepton-hadron final state. This is corrected for by the factor $C_\tau=3.43$ which was obtained by scaling the number of Wt events passing the loose τ selection cut to number of $t\bar{t}$ events passing the same cut.

Cut/Process	Wt			t-channel		
Tight τ	44.25			18.09		
Coll. approximation	9.70			3.31		
Opposite signs	8.20			2.13		
≥ 1 b-tag	4.79			1.27		
number of jets < 3	1.98			0.83		
m_A [GeV]	150	200	300	150	200	300
$E_{T,miss}$	1.989	1.989	1.724	0.830	0.830	0.737
$p_{T,\tau}$	1.989	1.360	0.498	0.830	0.612	0.124
$\Delta\Phi_{\ell,\tau}$	1.443	0.779	0.298	0.528	0.179	0.085
$m_{\tau\tau}$ window	0.265	0.281	0.093	0.217	0.064	0.024

Table G.2.: Accepted cross sections in fb for further event selection steps including the A-mass dependent cuts. The efficiency of the m_T cut, the b-tag and tight tau efficiency have been applied as weights to gain statistics. The Wt sample has been corrected by the factor C_τ to account for the missing final state. The final mass window cut has been applied as a weight for the Wt sample in the $m_A = 200$ GeV analysis and to both the single top processes in the $m_A = 300$ GeV analysis.

G.3. Results

In Ref. [85] a cross check with a 10 TeV Wt sample confirmed that the chosen method gave correct results for Wt despite to the missing final state. However, to be very conservative, the final single top results were scaled with a factor of 1.5 to take into account vague uncertainties from the cut factorization and the correction factors for the missing final state.

Table G.3 lists the final estimated single top contributions at the three lowest A boson hypotheses and their contribution relative to the $t\bar{t}$ contribution. Following the trend visible from Table G.3,

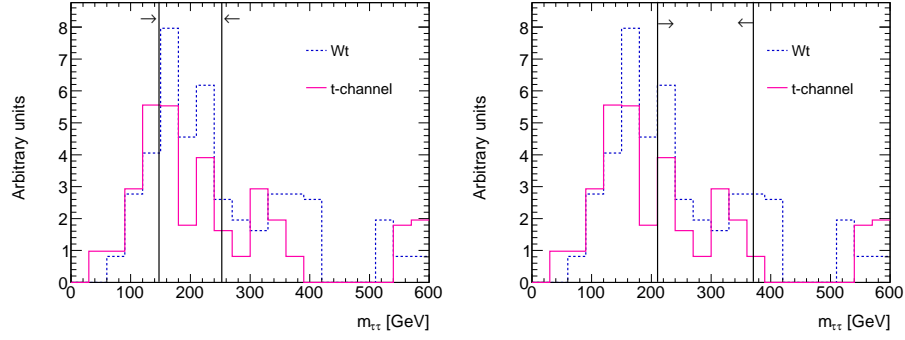


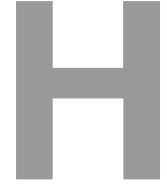
Figure G.1: $m_{\tau\tau}$ distribution after collinear approximation step for Wt and t-channel events. The black lines indicate the mass window cuts applied as weights at the end of the analysis, left for $m_A = 200$ GeV and right for $m_A = 300$ GeV. The arrows indicate the events kept in the selection.

single top is expected to be negligible for the $m_A \geq 450$ GeV mass hypotheses.

m_A [GeV]	Single top [fb]	$t\bar{t}$ [fb]	$\frac{\text{Single top}}{t\bar{t}}$
150	0.723	7.481	10.3 %
200	0.517	7.911	6.53 %
300	0.175	5.532	3.16 %

Table G.3: Final results for the single top estimation in comparison to $t\bar{t}$ in the b-tagged analysis. A very conservative factor of 1.5 has been multiplied to the final single top results to take into account uncertainties from the cut factorization.

The single top contribution was included in the b-tagged analysis of the lepton-hadron channel by scaling the $t\bar{t}$ accepted cross sections.



Systematic Uncertainties of $t\bar{t}$ Estimation Based on Jet Multiplicities

As follow-up on the description of the data-driven $t\bar{t}$ estimation from Section 9.2.2, Tables H.1-H.4 list for each systematic variation the expected number of events in each of the four kinematic regions and the difference between the expected and estimated number of $t\bar{t}$ events for the data-driven $t\bar{t}$ estimation method explained in Section 9.2.2.

The uncertainties become larger with increasing m_A . The numbers for the analyses at $m_A = 300$ GeV and $m_A = 450$ GeV contain statistical components which artificially increase the systematic uncertainties.

Variation	$N_{\text{control}}^{\text{njets}>3}$	$N_{\text{control}}^{\text{njets}<3}$	$N_{\text{signal}}^{\text{njets}>3}$	$N_{\text{signal}}^{\text{njets}<3}$	$N_{\text{signal}}^{\text{njets}<3 \text{ estimated}}$	ΔN
Default	2096	1564	294	218	220	-2
El. efficiency	2096	1564	294	218	220	0
El. E_T scale up	2105	1573	296	213	221	-6
El. E_T scale down	2070	1555	288	218	216	4
El. E_T resolution	2098	1568	295	206	221	-13
Muon efficiency	2084	1558	292	216	219	-1
Muon p_T scale up	2090	1583	290	214	220	-4
Muon p_T scale down	2091	1565	302	218	226	-7
Muon p_T resolution	2098	1564	291	218	217	3
Tau efficiency	1977	1479	279	214	208	7
Tau E_T scale up	2102	1580	308	218	231	-11
Tau E_T scale down	2087	1514	295	213	214	1
Tau E_T resolution	2092	1569	294	211	221	-8
Jet E scale up	2222	1503	318	207	215	-6
Jet E scale down	1989	1571	279	224	221	5
Jet E_T resolution	2096	1563	283	216	211	7
B-tagging efficiency	2077	1562	294	220	221	1
Light jet rej. up	1983	1465	284	211	210	3
Light jet rej. down	2235	1677	304	227	228	-0
Luminosity	2159	1611	303	224	226	0
Total exp. [%]	11.2	10.9	12.8	10.4	10.9	11.1
Cross Section	2348	1752	330	244	246	0
Total exp.+theor. [%]	16.4	16.2	17.5	15.9	16.2	11.1

Table H.1.: The impact of systematic variations of the number of events in each of the kinematic regions and the uncertainty for the data-driven method. The Higgs boson mass assumed is $m_A = 150$ GeV and $\tan\beta = 20$. Given are absolute numbers scaled to 30 fb^{-1} . The variations of $N_{\text{control}}^{\text{njets}>3}$, $N_{\text{control}}^{\text{njets}<3}$, $N_{\text{signal}}^{\text{njets}>3}$ and $N_{\text{signal}}^{\text{njets}<3}$ are given for information. The variation of $N_{\text{signal}}^{\text{njets}<3 \text{ estimated}}$ when systematics are applied is also given for information and this is not the uncertainty of the data-driven method. The uncertainty of the data-driven method is given by comparing the number $N_{\text{signal}}^{\text{njets}<3}$ to $N_{\text{signal}}^{\text{njets}<3 \text{ estimated}}$ after each variation, ΔN . The default difference is taken into account only once in the calculation of the total uncertainty of the data-driven method.

Variation	$N_{\text{control}}^{\text{njets}>3}$	$N_{\text{control}}^{\text{njets}<3}$	$N_{\text{signal}}^{\text{njets}>3}$	$N_{\text{signal}}^{\text{njets}<3}$	$N_{\text{signal}}^{\text{njets}<3 \text{ estimated}}$	ΔN
Default	636	540	291	225	247	-21
El. efficiency	636	540	291	225	247	0
El. E_T scale up	641	544	288	221	245	-3
El. E_T scale down	630	538	288	225	246	1
El. E_T resolution	639	535	290	225	243	3
Muon efficiency	632	540	285	224	243	2
Muon p_T scale up	632	546	293	222	253	-10
Muon p_T scale down	642	551	300	230	258	-6
Muon p_T resolution	634	540	289	225	246	1
Tau efficiency	613	517	284	215	239	-3
Tau E_T scale up	634	536	306	223	259	-15
Tau E_T scale down	624	516	290	238	239	20
Tau E_T resolution	634	540	289	223	246	-2
Jet E scale up	670	518	301	218	233	6
Jet E scale down	584	547	282	227	264	-15
Jet E_T resolution	637	543	286	223	244	0
B-tagging efficiency	628	536	288	221	246	-3
Light jet rej. up	597	515	278	220	240	1
Light jet rej. down	669	582	301	232	262	-9
Luminosity	655	557	299	232	254	0
Total exp. [%]	11.7	11.5	9.8	10	12.5	14.6
Cross Section	713	605	325	253	276	0
Total exp.+theor. [%]	16.8	16.6	15.5	15.6	17.3	14.6

Table H.2.: The impact of systematic variations on the number of events in each of the kinematic regions and the data-driven method for $m_A = 200$ GeV and $\tan\beta = 20$. More information is given in the caption to Table H.1.

Variation	$N_{\text{control}}^{\text{njets}>3}$	$N_{\text{control}}^{\text{njets}<3}$	$N_{\text{signal}}^{\text{njets}>3}$	$N_{\text{signal}}^{\text{njets}<3}$	$N_{\text{signal}}^{\text{njets}<3 \text{ estimated}}$	ΔN
Default	304	270	175	156	156	-0
El. efficiency	304	270	175	156	156	0
El. E_T scale up	304	272	175	153	157	-4
El. E_T scale down	304	272	178	156	159	-4
El. E_T resolution	299	268	177	152	159	-7
Muon efficiency	300	270	175	156	158	-2
Muon p_T scale up	302	264	174	150	152	-2
Muon p_T scale down	304	276	175	160	160	0
Muon p_T resolution	302	270	175	156	157	-1
Tau efficiency	295	259	170	154	149	5
Tau E_T scale up	294	284	185	157	179	-21
Tau E_T scale down	290	252	173	141	150	-9
Tau E_T resolution	306	272	178	156	158	-2
Jet E scale up	319	258	187	149	151	-2
Jet E scale down	290	275	167	160	158	2
Jet E_T resolution	306	270	178	153	157	-4
B-tagging efficiency	304	262	175	152	151	1
Light jet rej. up	286	257	170	144	153	-10
Light jet rej. down	324	281	188	171	163	8
Luminosity	313	278	180	161	161	0
Total exp. [%]	10.6	11.3	12.7	15.8	17.4	15.2
Cross Section	340	303	196	175	175	0
Total exp.+theor. [%]	16	16.5	17.5	19.8	21.1	15.2

Table H.3.: The impact of systematic variations on the number of events in each of the kinematic regions and the data-driven method for $m_A = 300$ GeV and $\tan\beta = 20$. More information is given in the caption to Table H.1.

Variation	$N_{\text{control}}^{\text{njets}>3}$	$N_{\text{control}}^{\text{njets}<3}$	$N_{\text{signal}}^{\text{njets}>3}$	$N_{\text{signal}}^{\text{njets}<3}$	$N_{\text{signal}}^{\text{njets}<3 \text{ estimated}}$	ΔN
Default	160	75	38	15	18	-3
El. efficiency	160	72	38	15	17	1
El. E_T scale up	165	75	33	15	15	2
El. E_T scale down	163	75	38	15	17	0
El. E_T resolution	164	77	35	15	17	1
Muon efficiency	160	75	38	17	18	2
Muon p_T scale up	158	73	36	15	16	1
Muon p_T scale down	163	76	38	17	18	2
Muon p_T resolution	160	74	38	15	17	0
Tau efficiency	158	77	35	13	17	-2
Tau E_T scale up	157	73	35	15	16	1
Tau E_T scale down	155	66	37	17	16	4
Tau E_T resolution	160	75	35	15	16	1
Jet E scale up	174	71	38	15	15	2
Jet E scale down	149	77	33	15	17	1
Jet E_T resolution	167	77	38	15	17	0
B-tagging efficiency	160	77	38	15	18	-1
Light jet rej. up	146	70	38	10	18	-5
Light jet rej. down	172	77	40	17	18	2
Luminosity	165	77	39	15	18	0
Total exp. [%]	14.3	16	22.8	43.4	24.2	51.4
Cross Section	180	84	42	16	20	0
Total exp.+theor. [%]	18.7	20	25.8	45	27	51.4

Table H.4.: The impact of systematic variations on the number of events in each of the kinematic regions and the data-driven method for $m_A = 450$ GeV and $\tan\beta = 20$. More information is given in the caption to Table H.1.

Combined Discovery Potential Assuming No $\Delta\sigma_{t\bar{t}}$ in the Dilepton Channel

In the following the combined discovery potential of the lepton-lepton analysis and the lepton-hadron analysis will be evaluated assuming no uncertainty of the $t\bar{t}$ cross section in the dilepton channel. In the dilepton analysis (Chapter 8) the $t\bar{t}$ contribution was estimated from MC only. However, it is straight forward to find a $t\bar{t}$ control region and to estimate the number of $t\bar{t}$ events in the signal region from the number found in data in the control region times an extrapolation ratio:

$$N_{t\bar{t}, \text{signal region}}^{\text{njets} < 3} = R \cdot N_{\text{control region}}, \quad (\text{I.1})$$

where R is calculated from MC as follows:

$$R = \frac{N_{t\bar{t}, \text{signal region}}^{\text{MC}}}{N_{\text{control region}}^{\text{MC}}}. \quad (\text{I.2})$$

By this method, the large cross section uncertainty, $\Delta\sigma = 12\%$, cancels. Preliminary work has shown that it is feasible also in the dilepton channel to find a very pure $t\bar{t}$ control region containing several thousand $t\bar{t}$ events [148]. Indeed, due to the requirement to find two leptons, such a $t\bar{t}$ control region will be less contaminated with W decay events and the selection cuts can even be loosened. Possible cuts to define this control regions are: Large MET, leptons with large p_T and at least one b-tag. The cuts on the p_T of the jets and in particular the cut on the p_T on the b-jets should be chosen similar to the corresponding cut values for the signal region.

The remaining task is to evaluate the impact of systematic variations on the ratio R . Due to the very limited MC statistics in the dilepton channel, this could not be done. Instead, for the following study only experimental uncertainties on $t\bar{t}$ were assumed: 4.8% (details were given in Table 8.16). In Figure I.1 the significance of the dilepton channel and the combination with the lepton-hadron channel are shown as a function of m_A for $\tan\beta = 20$ and as a function of $\tan\beta$ for $m_A = 200$ GeV. The needs to be compared to Figure 9.22 where the fully $t\bar{t}$ systematics was included. A general improvement of the significance for $m_A < 400$ GeV is visible, a clear improvement is found for $m_A = 130$ GeV and also for the combined analysis at $m_A = 155$ GeV¹. The value of $\tan\beta$ needed for a 5σ discovery decreases slightly.

In Figure I.2 the 5σ discovery contours are shown for the dilepton and lepton-hadron analyses and the combination. This needs to be compared to Figure 9.23. A slight improvement is found for low m_A . Unfortunately, no lepton-hadron mass point was available for $m_A < 150$ GeV. The kink of the contour at $m_A = 150$ GeV could be removed by a combination of both analyses down

¹The mass point $m_A = 155$ GeV combines the dilepton analysis for $m_A = 160$ GeV and the lepton-hadron analysis for $m_A = 150$ GeV.

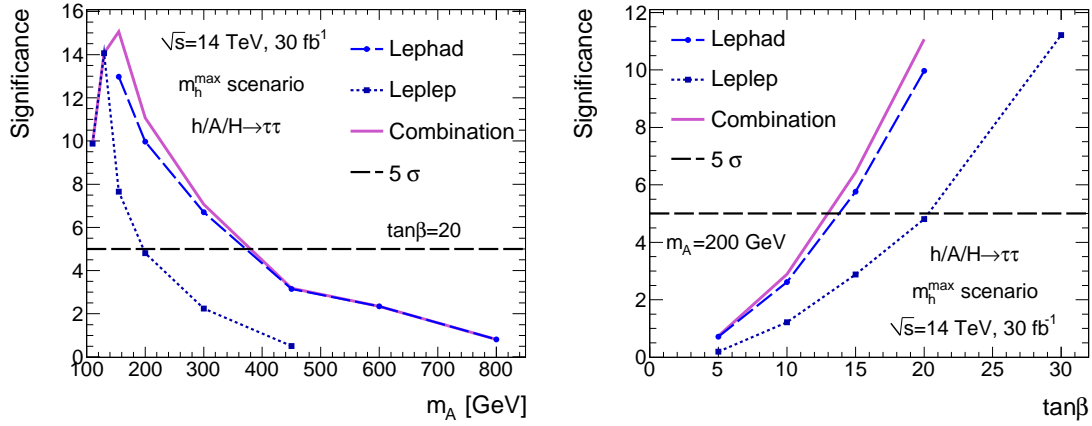


Figure I.1: Significance as a function of m_A for $\tan\beta = 20$ (left) and as a function of $\tan\beta$ for $m_A = 200$ GeV (right). The line labeled as *lepton-hadron* is the combined significance from the b-tagged and non b-tagged analyses. The line labeled as *combination* is the combined significance from the dilepton analysis and the two lepton-hadron analyses. In the dilepton analysis no uncertainty on the $t\bar{t}$ cross section was assumed.

to $m_A = 110$ GeV.

In Figure I.3 the 95% CL. exclusion contour is shown, which needs to be compared to Figure 9.24. Only a very slight improvement is visible at $m_A \approx 130$ GeV. Also here, the kink of the contour at $m_A = 150$ GeV stems from the fact that no lepton-hadron mass point was available at m_A lower than 150 GeV.

To conclude, if the systematic uncertainties are well under control, the dilepton channel indeed is a valuable addition to the lepton-hadron channel. At very low m_A the dilepton channel is probably even stronger. It might be useful to evaluate this in detail in future studies. The stronger potential at low m_A results from the fact that in the lepton-hadron analysis a hard cut of $p_T > 24$ GeV was required for the electron or muon. This cut reduces the signal contribution strongly for low m_A . However, the cut is necessary to suppress QCD events. In the dilepton analysis this cut was chosen to be $p_T > 15$ GeV, because by the requiring the presence of two isolated leptons the QCD contribution is already well suppressed.

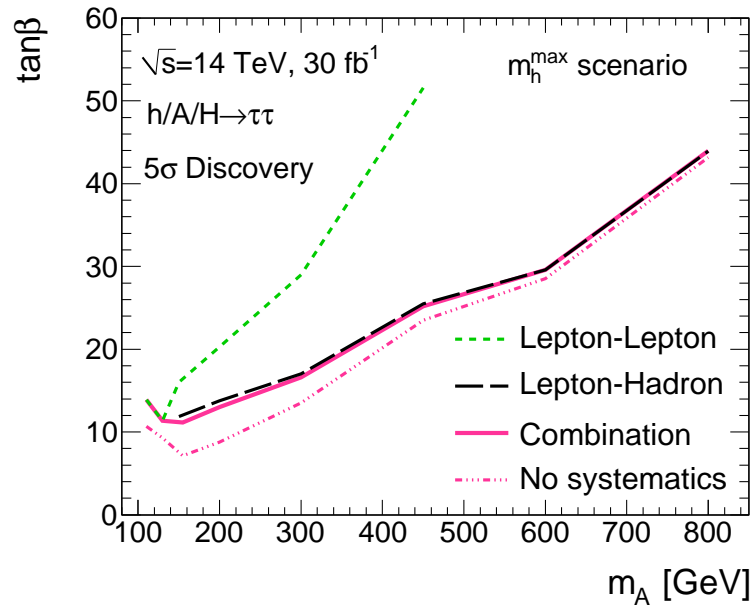


Figure 1.2.: The 5σ discovery contour for the dilepton channel (green dashed line), the combination of b-tagged and non b-tagged analyses in the lepton-hadron channel (blue dashed line) and the combination of the two final states (pink solid line). The combined result is also given for the case the background is known with an accuracy of 100 % (pink dash-dotted line). The dilepton channel only contributes to the significance for the very low Higgs boson mass region. For $m_A \geq 160$ GeV the discovery potential is completely dominated by the lepton-hadron channel. In the dilepton analysis no uncertainty on the $t\bar{t}$ cross section was assumed.

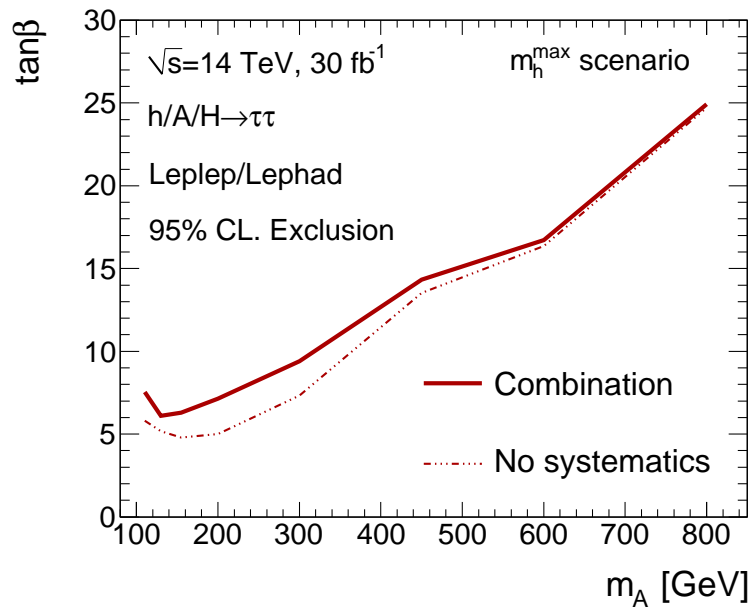


Figure I.3.: The 95% CL. exclusion contours in the $m_A - \tan\beta$ plane of the combination of the dilepton and lepton-hadron channels. This is equivalent to a significance of 1.64σ . In the dilepton analysis no uncertainty on the $t\bar{t}$ cross section was assumed. The dashed-dotted line gives the exclusion in case only statistical background uncertainties are assumed.

Bibliography

- [1] ATLAS Collaboration, *Technical Proposal for a General Purpose pp Experiment at the Large Hadron Collider at CERN*, CERN/LHC (1994).
- [2] ALEPH, DELPHI, L3 & OPAL Collaborations, *Search for the Standard Model Higgs boson at LEP*, Phys. Lett. **B 565** (2003).
- [3] CDF Collaboration, D0 Collaboration, *Combined CDF and D0 Upper Limits on Standard Model Higgs-Boson Production with up to 6.7 fb^{-1} of Data*, **arXiv:1007.4587v1**, **FERMILAB-CONF-10-267-E** (2010).
- [4] V. Rubin, *Rotation of the Andromeda Nebula from a Spectroscopic Survey of Emission Regions*, Astrophys. **159** (1970).
- [5] S.L. Glashow, Nucl. Phys. **22** (1961),
S. Weinberg, Phys. Rev. Lett. **19** (1967),
A. Salam, in Elementary Particle Theory, Stockholm, *Almqvist and Wiksell* (1968).
- [6] Y. Nambu and G. Jona-Lasinio, Phys. Rev. **122**, 345-358 (1961); Phys. Rev. **124**, 246-254 (1961),
M. Gell-Mann, Phys. Lett. **8**, 214 (1964),
D.J. Gross and F. Wilczek, *Ultraviolet Behaviour of non-abelian Gauge Theories*, Phys. Rev. Lett. **30**, 1343-1346 (1973),
D.J. Gross and F. Wilczek, *Asymptotically Free Gauge Theories. I*, Phys. Rev. **D 8**, 3633-3652 (1973),
H.D Politzer, *Reliable Perturbative Results for Strong Interaction?*, Phys. Rev. Lett **30**, 1346-1349 (1973),
H.D Politzer, *Asymptotic Freedom: An Approach to Strong Interactions*, Phys. Rept. **14**, 129-180 (1974),
M. Gell-Mann, Physics **1**, 63 (1973),
H. Fritzsch, M. Gell-Mann and P. Minkowski, Phys. Lett. **B 59**, 256 (1975),
S. Weinberg, Physica **A 96**, 327 (1979),
J. Gasser and H. Leutwyler, Ann. Phys. **158**, 142 (1984); Nucl. Phys. **B 250**, 465 (1985).
- [7] C. Amsler et al. (Particle Data Group), Physics Letters **B 667**, 1 (2008).
- [8] C.S. Wu, E. Ambler, R.W. Hayward, D.D. Hoppes and R.P. Hudson, *Experimental Test of Parity Conservation in Beta Decay*, Phys. Rev. **105**, 1413–1415 (1957).
- [9] L. G. M. Goldhaber and A. Sunyar, *Helicity of the Neutrino*, Phys. Rev. **109**, 1015–1017 (1958).

- [10] E. Noether and M. Travel, *Invariant Variation Problems*, **arXiv:physics/0503066v1** (1918, 2005).
- [11] M. Veltman and G. 't Hooft, *Regularization and renormalization of gauge fields*, Nucl. Phys. **B 44** (1972).
- [12] B. Pontecorvo, *Neutrino Experiments and the Problem of Conservation of Leptonic Charge*, Sov. Phys. JETP **26**, 984 (1968).
- [13] Superkamiokande Collaboration, *Evidence for an oscillatory signature in atmospheric neutrino oscillation*, Phys. Rev. Lett. **93**, 101801 (2004).
- [14] Peter W. Higgs, *Broken Symmetries and the Masses of Gauge Bosons*, Phys. Rev. Lett. **13** (1964),
Peter W. Higgs, *Spontaneous symmetry breakdown without massless bosons*, Phys. Rev. **145** (1966),
Peter W. Higgs, *Broken symmetries, massless particles and gauge fields*, Phys. Lett. **12** (1964),
F. Englert and R. Brout, *Broken symmetry and the mass of gauge vector mesons*, Phys. Rev. Lett. **13** (1964),
G.S. Guralnik, C.R. Hagen and T.W.B. Kibble, *Global conservation laws and massless particles*, Phys. Rev. Lett. **13** (1964),
T.W.B. Kibble, *Symmetry breaking in non-Abelian gauge theories*, Phys. Rev. **155** (1967).
- [15] J. Goldstone, A. Salam and S. Weinberg, *Broken Symmetries*, Phys. Rev. **127**, 965–970 (1962).
- [16] K. Riesselmann, *Limitations of a Standard Model Higgs Boson*, **arXiv:hep-ph/9711456v1** (1997).
- [17] A. Djouadi, *The Anatomy of Electro-Weak Symmetry Breaking. I: The Higgs Boson in the Standard Model*, **arXiv:hep-ph/0503172v2** (2005).
- [18] H. Flücher, M. Goebel, J. Haller, A. Höcker, K. Mönig, J. Stelzer, *Revisiting the Global Electroweak Fit of the Standard Model and Beyond with Gfitter*, Eur. Phys. J. **C 60**, 543 (2009).
- [19] Atlas Collaboration, *Expected performance of the ATLAS experiment: Detector, Trigger and Physics*, Technical Report CERN-OPEN-2008-020, Geneva (2008).
- [20] CMS Collaboration, *CMS physics: Technical Design Report. Volume I.*, CERN-LHCC-2006-021; CMS-TDR-008-2, 2006.
- [21] H. Kalka, G.Soff, *Supersymmetrie*, Teubner Studienbuecher, 1997.
- [22] F. Zwicky, *Die Rotverschiebung von extragalaktischen Nebeln*, Helvetica Physics Acta **6**, 110–127 (1933).
- [23] R. Massey, J. Rhodes, R. Ellis, N. Scoville, A. Leauthaud, A. Finoguenov, P. Capak, D. Bacon et al., *Dark matter maps reveal cosmic scaffolding*, Nature **445**, 286–290 (2007).

-
- [24] G. Hinshaw, J. L. Weiland, R. S. Hill, N. Odegard, D. Larson, C. L. Bennett, J. Dunkley, B. Gold, M. R. Greason, N. Jarosik, E. Komatsu, M. R. Nolta, L. Page, D. N. Spergel, E. Wollack, M. Halpern, A. Kogut, M. Limon, S. S. Meyer, G. S. Tucker, E. L. Wright, *Five-Year Wilkinson Microwave Anisotropy Probe (WMAP) Observations: Data Processing, Sky Maps, and Basic Results*, **arXiv:physics/0803.0732v2** (2008).
- [25] Th. M. Nieuwenhuizen, *Do non-relativistic neutrinos constitute the dark matter?*, Europhysics Letters **86**, 57001 (2009).
- [26] D. Hooper, T. Plehn, *Supersymmetric Dark Matter: How light can the LSP be?*, Physics Letters **B 562**, 18–27 (2003).
- [27] G.R. Farrar, P. Fayet, *Phenomenology of the Production, Decay and Detection of New Hadronic States Associated with Supersymmetry*, Phys. Lett. **B 76**, 575 (1978).
- [28] H. Baer, X. Tata, *Weak Scale Supersymmetry*, Cambridge, 2006.
- [29] C.T. Hill, E.H. Simmons, *Strong dynamics and electroweak symmetry breaking*, Physics Reports **381**, 235–402 (2003).
- [30] S.P. Martin, *A Supersymmetry Primer*, **arXiv:hep-ph/9709356v5** (2008).
- [31] L. Alvarez-Gaume, E. Witten, *Gravitational Anomalies*, Nucl. Phys. **B 234** (1984).
- [32] I. Simonsen, *A Review of Minimal Supersymmetric Electro Weak Theory*, **arxiv:hep-ph/9506369** (1995).
- [33] R.V. Harlander, W.B. Kilgore, *Higgs boson production in bottom quark fusion at next-to-next-to-leading order*, Phys. Rev. Lett. **D 68**, 013001 (2003).
- [34] S. Heinemeyer, W. Hollik, G. Weiglein, *Constraints on $\tan\beta$ in the MSSM from the Upper Bound on the Mass of the Lightest Higgs boson*, **arxiv:hep-ph/9909540v2** (2000).
- [35] C. Csaki, *The Minimal Supersymmetric Standard Model (MSSM)*, **arxiv:hep-ph/9606414** (1996).
- [36] P. Bechtle, K. Desch, M. Uhlenbrock, P. Wienemann, *Constraining SUSY models with Fittino using measurements before, with and beyond the LHC*, **arxiv:hep-ph/0907.2589** (2009).
- [37] M. Carena, S. Heinemeyer, C.E.M. Wagner, G. Weiglein, *Suggestions for Improved Benchmark Scenarios for Higgs Boson Searches at LEP2*, **arxiv:hep-ph/9912223** (1999).
- [38] M. Carena, S. Heinemeyer, C.E.M. Wagner, G. Weiglein, *Suggestions for Benchmark Scenarios for MSSM Higgs Boson Searches at Hadron Colliders*, Eur. Phys. J. **C 26**, 601–607 (2003).
- [39] A.D. Sakharov, JETP Lett. **5**, 24 (1967),
A. Pilaftis, Phys. Rev. **D 58**, 096010 (1998),
Phys. Lett. **B 435**, 88 (1998).
-

- [40] M. Frank, T. Hahn, S. Heinemeyer, W. Hollik, H. Rzehak, G. Weiglein, *The Higgs Boson Masses and Mixings of the Complex MSSM in the Feynman-Diagrammatic Approach*, **arXiv:hep-ph/0611326v2** (2007).
- [41] G. Degrandi, S. Heinemeyer, W. Hollik, P. Slavich, G. Weiglein, *Towards High-Precision Predictions for the MSSM Higgs Sector*, **arXiv:hep-ph/0212020v2** (2002).
- [42] S. Heinemeyer, W. Hollik, G. Weiglein, *The Masses of the Neutral CP-even Higgs Bosons in the MSSM: Accurate Analysis at the Two-Loop Level*, **arXiv:hep-ph/9812472v1** (1998).
- [43] S. Heinemeyer, W. Hollik, G. Weiglein, *FeynHiggs: A program for the calculation of the masses of the neutral CP-even Higgs bosons in the MSSM*, **arXiv:hep-ph/9812320v1** (1998).
- [44] M. Warsinsky, *Studies of b-associated production and muonic decays of neutral Higgs bosons at the ATLAS experiment within the Minimal Supersymmetric Standard Model*, Ph.D. thesis, TU Dresden (2009).
- [45] ALEPH Collaboration, Phys. Lett. **B 495**, 1 (2000).
- [46] DELPHI Collaboration, Phys. Lett. **B 499**, 23 (2001).
- [47] L3 Collaboration, Phys. Lett. **B 495**, 18 (2000).
- [48] OPAL Collaboration, Phys. Lett. **B 499**, 38 (2001).
- [49] Aleph, Delphi, L3 and Opal Collaborations, The LEP working group for Higgs boson searches, *Searches for Higgs bosons: Preliminary combined results using LEP data collected at energies up to 202 GeV*, CERN-EP **2000-055** (2000).
- [50] ALEPH, DELPHI, L3 & OPAL Collaboration. The LEP Working Group for Higgs Boson Searches., *Search for Neutral MSSM Higgs boson at LEP*, Eur. Phys. J. **C 47**, 547 (2006).
- [51] CDF Collaboration, D0 Collaboration, *Combined CDF and D0 Upper Limits on Standard Model Higgs-Boson Production with 2.1 - 5.4 fb⁻¹ of Data*, **arXiv:0911.3930v1**, **FERMILAB-CONF-09-557-E** (2009).
- [52] CDF Collaboration, D0 Collaboration, *Combined CDF and D0 Upper Limits on Standard Model Higgs-Boson Production with up to 4.2 fb⁻¹ of Data*, **FERMILAB-PUB-09-060-E** (2009).
- [53] CDF Collaboration and D0 Collaboration, FERMILAB-PUB-09-394-E, CDF Note 9888, D0 Note 5980-CONF.
- [54] CDF Collaboration, D0 Collaboration, *Combined CDF and D0 Upper Limits on MSSM Higgs boson production in tau-tau final states with up to 2.2 fb⁻¹*, **arxiv:hep-ph/1003.3363v2** (2010).
- [55] L. Evans, P. Bryant (editors), *LHC Machine*, JINST **3**, S08001 (2008).

- [56] *Interim summary report on the analysis of the 19 September 2008 incident at the LHC*, CERN/ATL/PhL, Document EDMS 973073.
- [57] S. Myers, *LHC Status*, talk given at 22nd July 2009, <http://indico.cern.ch/getFile.py/access?resId=0&materialId=slides&confId=62277>.
- [58] ATLAS Collaboration, *Detector and Physics Performance. Technical Design Report. Volume I.*, CERN/LHC, 1999.
- [59] ALICE Collaboration, *The ALICE detector at LHC*, Nucl. Instrum. Meth. **A 344**, 27–38 (1994).
- [60] LHCb Collaboration, *LHCb Technical Proposal*, CERN-LHCC-98-04, 1998.
- [61] ATLAS collaboration, *The ATLAS Experiment at the CERN Large Hadron Collider*, JINST **3**, S08003 (2008).
- [62] T. Sjöstrand, *Monte Carlo Generators*, **arxiv:hep-ph/0611247** (2006).
- [63] M. Worek, *Monte Carlo Generators for the LHC*, talk given at the German Physical Society meeting in Munich (2009).
- [64] A. Doucet, N. de Freitas, N. Gordon, *Sequential Monte Carlo Methods in Practice*, Springer, 2001.
- [65] V.N. Gribov, L.N. Lipatov, Sov.J.Nucl.Phys. **15** (1972),
G. Altarelli and G. Parisi. Nucl. Phys. **B 126** (1977),
Yu. L. Dokshitzer. Sov. Phys. JETP, **46** (1977).
- [66] V. Sudakov, *Vertex parts at very high-energies in quantum electrodynamics*, Sov. Phys. JETP **3**, 65–71 (1956).
- [67] S. Catani, F. Krauss, R. Kuhn, B.R. Webber, *QCD matrix elements + Parton Showers*, JHEP **0111 063** (2001).
- [68] F. Krauss, *Matrix elements and Parton Showers in Hadronic Interactions*, JHEP **0208 015** (2002).
- [69] T. Gleisberg et al., *SHERPA 1.alpha., a proof-of-concept version*, JHEP **02 056 arxiv:hep-ph/0311263** (2004).
- [70] T. Gleisberg et al., *Event generation with SHERPA 1.1*, JHEP **0902 arxiv:hep-ph/0811.4622** (2009).
- [71] M. Moretti, *Matching Matrix Element and Parton Shower*, talk given at an INFN workshop in Frascati (2006).
- [72] ATLAS Collaboration, *ATLAS Computing Technical Design Report*, ATLAS-TDR-017, CERN-LHCC-2005-022 (2005).
- [73] J. Allison et al., *Geant4 Developments and Applications*, IEEE Transactions on Nuclear Science **53**, 270–278 (2006).

- [74] S. Agostinelli et al., *Geant4 - A Simulation Toolkit*, Nuclear Instruments and Methods A **506**, 250–303 (2003).
- [75] ATLAS Collaboration, *The ATLAS Simulation Infrastructure*, to be published in EPJC (2010).
- [76] A. Rimoldi et al., *The Simulation of the ATLAS Experiment: Present Status and Outlook*, **CERN-ATL-COM-SOFT-2004-006** (2004).
- [77] ATLAS Electromagnetic Liquid Argon Calorimeter Group, B. Aubert et al., Nucl. Inst. Meth. A **500**, 202–231 (2003).
- [78] ATLAS Electromagnetic Liquid Argon Calorimeter Group, B. Aubert et al., Nucl. Inst. Meth. A **500**, 178–201 (2003).
- [79] ATLAS Electromagnetic Liquid Argon Calorimeter Group, B. Aubert et al., Nucl. Inst. Meth. A **568**, 601–623 (2006).
- [80] E. Richter-Was, D. Froidevaux, L. Poggioli, *ATLFast 2.0 a fast simulation package for ATLAS*, **ATL-PHYS-98-131** (1998).
- [81] K. Edmonds et al., *The Fast ATLAS Track Simulation (FATRAS)*, **ATL-SOFT-PUB-2008-01** (2008).
- [82] M. Duehrssen, *Study of Higgs bosons in the WW final state and development of a fast calorimeter simulation for the ATLAS experiment*, Ph.D. thesis, Albert-Ludwigs-Universitaet Freiburg im Breisgau (2009).
- [83] E. Barberio et al., *The Geant4-Based ATLAS Fast Electromagnetic Shower Simulation*, **ATL-SOFT-CONF-2007-002** (2007).
- [84] M. Spira, *HIGLU: A Program for the Calculation of the Total Higgs Production Cross Section at Hadron Colliders via Gluon Fusion including QCD Corrections*, **arxiv:hep-ph/9510347** (1995).
- [85] C. Anders et al., *Discovery Potential of $A/H \rightarrow \tau\tau \rightarrow \ell h$ in ATLAS*, **ATLAS-PHYS-INT-2010-036** (2010).
- [86] A.D. Martin, R.G. Roberts, W.J. Stirling, R.S. Thorne, Eur. Phys. J. C **28**, 455–473 (2003).
- [87] A.D. Martin, R.G. Roberts, W.J. Stirling, R.S. Thorne, Phys. Lett. B **604**, 61–68 (2004).
- [88] T. Sjostrand et al., *High-energy-physics event generation with PYTHIA 6.1*, Comput. Phys. Commun. **135**, 238 (2001).
- [89] K. Melnikov and F. Petriello, Phys. Rev. Lett. **96**, 231803 (2006).
- [90] K. Melnikov and F. Petriello, Phys. Rev. D **74** 114017 (2006).
- [91] J.M. Butterworth, J.R. Forshaw, M.H. Seymour, *Multiparton interactions in photoproduction at HERA*, Z. Phys. C **72**, 637–646 (1996).

-
- [92] R. Bonciani, S. Catani, M. Mangano, *NLL resummation of the heavy-quark hadronproduction cross section*, Nucl. Phys. **B 529**, 424–450 (1998).
- [93] N. Kidonakis, R. Vogt, *Next-to-next-to-leading order soft gluon corrections in top quark hadroproduction*, Phys. Rev. **D 68**, 114014 (2003).
- [94] S. Frixione and B. R. Webber, *Matching NLO QCD computations and parton shower simulations*, JHEP **06**, 029 (2002), [arxiv:hep-ph/0204244](#),
S. Frixione, P. Nason, and B. R. Webber, *Matching NLO QCD and parton showers in heavy flavour production*, JHEP **08**, 007 (2003), [arxiv:hep-ph/0305252](#).
- [95] J. Campbell, F. Tramontano, *Understanding single-top-quark production and jets at hadron colliders*, Phys. Rev. **D 70**, 114012 (2004).
- [96] J. Campbell, F. Tramontano, *Next-to-leading order corrections to Wt production and decay*, Nucl. Phys. **B 726**, 109–130 (2005).
- [97] B.P. Kersevan and E. Richter-Was, *The Monte Carlo event generator AcerMC version 2.0 with interfaces to PYTHIA 6.2 and HERWIG 6.5*, [arxiv:hep-ph/0405247](#) (2004).
- [98] Th. Lagouri et al., IEEE Trans. Nucl. Sci. **51**, 3030–3033 (2004).
- [99] S. Hassini et al., NIM **A 572**, 77–79 (2007).
- [100] ATLAS Collaboration, *Cut-based Identification of Hadronic τ Decays in Early ATLAS Data*, **ATL-PHYS-PUB-2010-001** (2010).
- [101] A. Christov et al., *Performance of the tau reconstruction and identification algorithm with release 14.2.10*, **ATL-COM-PHYS-2008-122** (2008).
- [102] G.C. Blazey et al., Run II Jet Physics: Proceedings of the Run II QCD and Weak Boson Physics Workshop .
- [103] S. Catani, Y.L. Dokshitzer, B.R. Webber, Phys. Lett. **B 285**, 291–299 (1992).
- [104] S.D. Ellis, D.E. Soper, Phys. Rev. **D 48**, 3160–3166 (1993).
- [105] M. Cacciari, G.P. Salam, G. Soyez, *The anti-kt jet clustering algorithm*, JHEP **04**, 063 (2008).
- [106] G.P. Salam, G. Soyez, JHEP **05**, 086 (2007).
- [107] R.K. Ellis, I. Hinchliffe, M. Soldate and J.J. van der Bij, Nucl. Phys. **B 297**, 221 (1988).
- [108] J. Schaarschmidt, *A study of b -associated Higgs Production in the Decay Mode $b\bar{b} \rightarrow h/H/A \rightarrow \tau\tau \rightarrow 2\ell + 4\nu$ with ATLAS at LHC*, Diploma Thesis, TU Dresden (2007).
- [109] D. Cavalli, G. Negri, *Extension of the Study of $A/H \rightarrow \tau\tau \rightarrow \text{lepton} - \text{hadron}$ in the high M_A region*, **ATL-PHYS-2003-009** (2003).
-

- [110] I. Rottländer, *Studie zum Entdeckungspotenzial fuer ein Higgs-Boson aus Vektorbosonfusion mit leptonischem Zerfall fuer das ATLAS-Experiment am LHC*, Diploma thesis, Bonn University (2005).
- [111] CDF Collaboration, *Search for neutral MSSM Higgs bosons decaying to tau pairs in p-pbar collisions at $\sqrt{s} = 1.96$ TeV*, Phys. Rev. Lett. **96**, 011802 (2006).
- [112] ATLAS Collaboration, *Discovery Potential of $h/A/H \rightarrow \tau\tau \rightarrow 2\ell + 4\nu$* , **ATL-PHYS-PUB-2009-059** (2009).
- [113] ATLAS Collaboration, *Detector and Physics Performance. Technical Design Report. Volume I.*, CERN/LHC, 1999.
- [114] R. Barlow, *Systematic Errors: Facts and Fictions*, **arxiv:hep-ex/0207026v1** (2002).
- [115] M. Schmitz, *Studie zur Bestimmung des Untergrundes aus Daten und der Higgs-Boson-Masse in Vektorbosonfusion mit $H \rightarrow \tau\tau \rightarrow \mu\mu + 4\nu$ mit dem ATLAS-Detektor*, Diploma thesis, Bonn University (2006).
- [116] ATLAS Collaboration, *Measurement of the $Z \rightarrow \ell\ell$ production cross section in proton-proton collisions at $\sqrt{s} = 7$ TeV with the ATLAS detector*, **ATL-CONF-2010-076** (2010).
- [117] M. Simonyan, *The Standard Model W and Z boson production cross section and their uncertainties*, **ATL-COM-PHYS-2009-289** (2009).
- [118] K. Gottfried and J.D. Jackson, *On the Connection between production mechanism and decay of resonances at high-energies*, Nuovo Cim. **33**, 309–330 (1964).
- [119] K. Leonhardt, *Determination of $Z \rightarrow \tau\tau \rightarrow ee + 4\nu$ Background Shapes From Data in Context of the b-Quark Associated Higgs Boson Production with ATLAS at the LHC*, Diploma thesis, Dresden University (2008).
- [120] P. Czodrowski, *Improvement of a Data-Driven Method for the Simulation of the TauTau-Mass Shape in $Z \rightarrow \tau\tau \rightarrow ee + 4\nu$ for ATLAS at the LHC*, Diploma thesis, Dresden University (2009).
- [121] T. Vickey et al., *A Control Sample for $t\bar{t}$ +jets Backgrounds with One or More Leptons in the Final State*, **ATL-COM-PHYS-2008-145** (2008).
- [122] N. Möser, M. Schmitz, J. Kroseberg, M. Schumacher, N. Wermes, *Estimation of $Z \rightarrow \tau\tau$ Background in VBF $H \rightarrow \tau\tau$ Searches from $Z \rightarrow \mu\mu$ Data using an Embedding Technique*, **ATL-PHYS-INT-2009-109** (2009).
- [123] A. Ahmad et al., *Search for the Standard Model Higgs boson via Vector Boson Fusion production process in the di-tau channels with ATLAS*, **ATL-PHYS-INT-2009-053** (2009).
- [124] ATLAS Collaboration, *Discovery Potential of $A/H \rightarrow \tau\tau \rightarrow \ell h$ in ATLAS*, **ATLAS-PHYS-PUB-2010-011** (2010).
- [125] CDF Collaboration, *Measurement of the $t\bar{t}$ Production Cross Section in ppbar Collisions at $\sqrt{s} = 1.96$ TeV*, **arXiv:hep-ex/0606017v2** (2006).

-
- [126] ATLAS Collaboration, *Prospects for Higgs boson searches using the $H \rightarrow WW^*$ decay mode with the ATLAS detector at $\sqrt{s} = 10$ TeV*, **ATL-PHYS-PUB-2010-005** (2010).
- [127] A. Stuart, J.K. Ord and S. Arnold, *Kendall's Advanced Theory of Statistics*, Oxford Univ. Press, 1999.
- [128] S.S. Wilks, *The large-sample distribution of the likelihood ratio for testing composite hypotheses*, Ann. Math. Statist. **9**, 60–2 (1938).
- [129] G. Cowen, E. Gross, *Discovery significance with statistical uncertainty in the background estimate*, ATLAS Statistics Forum, support document (2008).
- [130] K. Cranmer, G. Schott, L. Moneta, W. Verkerke, *RooStats User's Guide*, document to appear (2010).
- [131] J. Thomas, *Study of heavy MSSM-Higgs-bosons A/H in hadronic τ -decays in ATLAS*, **ATL-COM-PHYS-2002-040** (2002).
- [132] CMS Collaboration, *The CMS physics reach for searches at 7 TeV*, **CMS-NOTE-2010/008** (2010).
- [133] R. Kinnunen and S. Lehti, *Search for the heavy neutral MSSM Higgs bosons with the $H/A \rightarrow \tau\tau \rightarrow e + \text{jet}$ decay mode*, **CMS-NOTE-2006/075** (2006).
- [134] A. Kalinowski et al, *Search for MSSM heavy neutral Higgs boson in $\tau\tau \rightarrow \mu + \text{jet}$ decay mode*, **CMS-NOTE-2006/105** (2006).
- [135] S. Lehti, *Study of MSSM $H/A \rightarrow \tau\tau \rightarrow e\mu + X$ in CMS*, **CMS-NOTE-2006/101** (2006).
- [136] ATLAS Collaboration, *ATLAS Sensitivity Prospects for Higgs Boson Production at the LHC Running at 7 TeV*, **ATL-PHYS-PUB-2010-009** (2010).
- [137] C. Anders et al., *ATLAS Sensitivity Prospects for the Neutral MSSM Higgs Bosons in the $H/A \rightarrow \tau\tau \rightarrow \ell h$ Decay Channel at $\sqrt{s} = 7$ TeV*, **ATL-COM-PHYS-2010-255** (2010).
- [138] ATLAS Collaboration, *Performance of the ATLAS Detector using First Collision Data*, accepted by EPJC, **arXiv:1005.5254v1** (2010).
- [139] ATLAS Collaboration, *Charged-particle multiplicities in pp interactions at $\sqrt{s} = 900$ GeV measured with the ATLAS detector at the LHC*, Phys. Lett. **B 688**, 21–42 (2010).
- [140] ATLAS Collaboration, *Measurement of the $W \rightarrow l\nu$ production cross-section and observation of $Z \rightarrow \ell\ell$ production in proton-proton collisions at $\sqrt{s} = 7$ TeV with the ATLAS detector*, **ATLAS-CONF-2010-051** (2010).
- [141] ATLAS Collaboration, *Search for top pair candidate events in ATLAS at $\sqrt{s}=7$ TeV*, **ATLAS-CONF-2010-063** (2010).
- [142] ATLAS Collaboration, *Properties of Jets and Inputs to Jet Reconstruction and Calibration with the ATLAS Detector Using Proton-Proton Collisions at $\sqrt{s} = 7$ TeV*, **ATLAS-CONF-2010-053** (2010).
-

- [143] ATLAS Collaboration, *Performance of the Missing Transverse Energy Reconstruction and Calibration in Proton-Proton Collisions at a Center-of-Mass Energy of $\sqrt{s} = 7$ TeV with the ATLAS Detector*, **ATLAS-CONF-2010-057** (2010).
- [144] ATLAS Collaboration, *Tau Reconstruction and Identification Performance in ATLAS*, **ATLAS-CONF-2010-086** (2010).
- [145] ATLAS Collaboration, *Tracking Studies for b -tagging with 7 TeV Collision Data with the ATLAS Detector*, **ATLAS-CONF-2010-070** (2010).
- [146] Y. Coadou et. al., *Event Display of $Z \rightarrow \tau\tau \rightarrow \mu + \text{had}$ in 7 TeV Collisions*, **ATL-COM-PHYS-2010-775** (2010).
- [147] H. Fu, O. Mencer and W. Luk, *Comparing floating-point and logarithmic number representations for reconfigurable acceleration*, IEEE Conference on Field Programmable Technology **10.1109/FPT.2006.270342**, 337–340 (2006).
- [148] J. Schaarschmidt, talk at HSG4 working group meeting, *Update on $t\bar{t}$ bar estimation in $bb h/A/H \rightarrow \tau\tau$* , <http://indico.cern.ch/conferenceDisplay.py?confId=66001>.

List of Figures

2.1.	Higgs potential V	10
2.2.	Global Standard Model fit ('green band plot')	13
2.3.	SM Higgs production processes	14
2.4.	SM Higgs boson branching ratios and production cross sections	15
2.5.	Atlas and CMS discovery potential for the SM Higgs boson	16
2.6.	Production graphs for MSSM Higgs bosons	24
2.7.	Masses of the neutral MSSM Higgs bosons as function of m_A	25
2.8.	Total width of the neutral MSSM Higgs bosons	26
2.9.	$\tau\tau$ branching ratio of the neutral MSSM Higgs bosons	26
2.10.	Production cross section for b-associated MSSM Higgs bosons	27
2.11.	Gluon fusion production cross sections of the neutral MSSM Higgs bosons	27
2.12.	Dependence of the cross sections for b-associated and direct production on $\tan\beta$	28
3.1.	LEP combination for the SM Higgs boson search	30
3.2.	Combined LEP search results for the neutral MSSM Higgs bosons	31
3.3.	Combined Tevatron results for the SM Higgs boson search	33
3.4.	Combined Tevatron results for the MSSM Higgs boson search	34
4.1.	Schematic view of the LHC	36
4.2.	ATLAS detector	37
4.3.	Coordinates used in ATLAS	39
4.4.	ATLAS inner detector	40
4.5.	ATLAS calorimeter systems	42
4.6.	Samplings of the electromagnetic calorimeter	43
4.7.	ATLAS muon system	46
4.8.	Schematic view of the ATLAS trigger system	49
5.1.	Cross section uncertainties for b-associated and direct production	57
5.2.	Feynman diagrams for background processes	60
5.3.	Feynman diagrams for single top production	60
6.1.	Distribution of χ^2 of combined muon candidates	67
6.2.	Tau reconstruction algorithm seeds	72
6.3.	B-tagging efficiency and light-jet rejection rate	76
6.4.	Refined final MET for signal and backgrounds	79
7.1.	Scheme of the collinear approximation	81

7.2. Angle between true tau and true electron/muon for Higgs boson events	82
7.3. Reconstructed collinear mass in the lepton-hadron channel	84
7.4. Reconstructed collinear mass broken down to lepton-hadron subchannels	85
7.5. Peak position of reconstructed $m_{\tau\tau}$ in the lepton-hadron channel	85
7.6. Width of reconstructed $m_{\tau\tau}$ in lepton-hadron channel	86
7.7. Distributions of $m_{\ell,h}$ and $x_1 \cdot x_2$ in the lepton-hadron channel	86
7.8. Distributions of x_1 and x_2 in the lepton-hadron channel	87
7.9. Distributions of $\Delta\Phi_{\ell h}$ and $p_{T,\text{Higgs}}$ in the lepton-hadron channel	87
7.10. Correlation of the $m_{\tau\tau}$ resolution with $\Delta\Phi_{\ell h}$	88
7.11. The correlation of the $m_{\tau\tau}$ resolution with $p_{T,\text{Higgs}}$	88
7.12. The correlation of the $m_{\tau\tau}$ resolution with $p_{T,\text{miss}}$	89
7.13. The correlation of the collinear mass with $x_1 \cdot x_2$	89
7.14. Relative efficiency of the collinear approximation	90
7.15. Reconstructed $m_{\tau\tau}$ in the dilepton channel	91
7.16. Peak position of $m_{\tau\tau}$ as a function of m_A in the lepton-lepton channel	91
7.17. Reconstructed width of $m_{\tau\tau}$ in the lepton-lepton channel	92
7.18. Distributions of $m_{\ell\ell}$ and $x_1 \cdot x_2$ in the dilepton channel	92
7.19. Distributions of $\Delta\Phi_{\ell\ell}$ and $p_{T,\text{Higgs}}$ in the dilepton channel	93
7.20. Distribution of x_1 and x_2 in the lepton-lepton channel	93
7.21. Correlations of $m_{\tau\tau}$ with $\Delta\Phi_{\ell\ell}$ and $p_{T,\text{Higgs}}$	94
7.22. Correlations of $m_{\tau\tau}$ with $p_{T,\text{miss}}$ and $x_1 \cdot x_2$	94
7.23. Efficiency of the collinear approximation in the lepton-lepton channel	95
7.24. Visible mass in the lepton-hadron channel for Higgs boson events	96
7.25. Peak position of the visible mass in the lepton-hadron channel	96
7.26. Width of the reconstructed visible mass in the lepton-hadron channel	97
7.27. Reconstructed visible mass in the dileptonic channel for Higgs boson events	97
7.28. Peak position of m_{visible} in the lepton-lepton channel	98
7.29. Width of the visible mass in the lepton-lepton channel	98
7.30. Distribution of ΣE_T and MET resolution in the lepton-hadron channel	99
7.31. Distribution of ΣE_T and MET resolution in the lepton-lepton channel	100
7.32. MET resolution in bins of ΣE_T for the lepton-hadron and lepton-lepton channels	100
7.33. Collinear mass in the lepton-hadron channel with true and reconstructed MET	101
8.1. Relative lepton isolation cut	105
8.2. Corrected b-tagging weight for Z+jets and Higgs boson events	107
8.3. Number of high- p_T jets and best cut value	107
8.4. MET distribution for signal and background processes and cut value	108
8.5. Distribution of $p_{T,\ell}$ for signal and background processes and cut value	109
8.6. Distribution of $m_{\ell\ell}$ for signal and background processes and cut value	110
8.7. $m_{\tau\tau}$ distributions after baseline selection in the dilepton analysis	114
8.8. Cut variables for $m_A = 110$ GeV in the dilepton analysis	117
8.9. Cut variables for $m_A = 130$ GeV in the dilepton analysis	118
8.10. Cut variables for $m_A = 160$ GeV in the dilepton analysis	119
8.11. Cut variables for $m_A = 200$ GeV in the dilepton analysis	120
8.12. Cut variables for $m_A = 300$ GeV in the dilepton analysis	121

8.13.	Cut variables for $m_A = 450$ GeV in the dilepton analysis	122
8.14.	Final $m_{\tau\tau}$ spectra for $m_A = 110$ GeV and $m_A = 130$ GeV in the dilepton analysis .	126
8.15.	Final $m_{\tau\tau}$ spectra for $m_A = 160$ GeV and $m_A = 200$ GeV in the dilepton analysis .	127
8.16.	Final $m_{\tau\tau}$ spectra for $m_A = 300$ GeV and $m_A = 450$ GeV in the dilepton analysis .	127
8.17.	m_{vis} for the events failing the collinear approximation	128
8.18.	Signal yield as function of $\tan\beta$ in the dilepton analysis	129
8.19.	Statistical significance as a function of cut on $\Delta\Phi_{\ell\ell}$	130
8.20.	Final $m_{\tau\tau}$ distributions for $\tan\beta = 10$ and $\tan\beta = 45$	130
8.21.	Distribution of $\cancel{E}_T^{\text{calo}}$ for $Z \rightarrow \tau\tau \rightarrow ee/\mu\mu + 4\nu$ events	135
8.22.	Cut variables for the $Z \rightarrow ee/\mu\mu$ control regions	136
8.23.	Event yield in the $Z \rightarrow ee/\mu\mu$ control regions as function of the integrated luminosity	137
8.24.	$Z \rightarrow \tau\tau \rightarrow \mu\mu + 4\nu$ reference histograms	138
8.25.	Comparison of masses for $Z \rightarrow \tau\tau \rightarrow \mu\mu + 4\nu$ events with reweighted $Z \rightarrow \mu\mu$ events	139
8.26.	Comparison of masses for $Z \rightarrow \tau\tau \rightarrow \mu\mu + 4\nu$ events with reweighted $Z \rightarrow \mu\mu$ events without b-tagging requirement	139
8.27.	Comparison of muon energies of $Z \rightarrow \tau\tau \rightarrow \mu\mu + 4\nu$ events with reweighted $Z \rightarrow \mu\mu$ events without b-tagging requirement	140
8.28.	Comparison of muon momentum components of $Z \rightarrow \tau\tau \rightarrow \mu\mu + 4\nu$ events with reweighted $Z \rightarrow \mu\mu$ events without b-tagging requirement	141
8.29.	Comparison of MET components of $Z \rightarrow \tau\tau \rightarrow \mu\mu + 4\nu$ events with reweighted $Z \rightarrow \mu\mu$ events without b-tagging requirement	142
8.30.	Comparison of MET and $\Delta\Phi_{\ell\ell}$ of $Z \rightarrow \tau\tau \rightarrow \mu\mu + 4\nu$ events with reweighted $Z \rightarrow \mu\mu$ events without b-tagging requirement	142
8.31.	$m_{\tau\tau}$ shape of $Z \rightarrow \tau\tau$ events for different subchannels	143
8.32.	Ratios of numbers of events for $Z \rightarrow \tau\tau$ and $Z \rightarrow \ell\ell$	145
8.33.	Double-ratios of numbers of events for $Z \rightarrow \tau\tau$ and $Z \rightarrow \ell\ell$	146
8.34.	2D distributions of lepton p_T for $Z \rightarrow \tau\tau$ and $Z \rightarrow \ell\ell$ events	147
8.35.	Results of binned normalization method as function of binsize	148
8.36.	Significances as functions of m_A for the dilepton analysis	154
8.37.	Significances as functions of $\tan\beta$ for the dilepton analysis	155
8.38.	5σ discovery contour in the lepton-lepton analysis	156
8.39.	95% exclusion contour in the lepton-lepton analysis	157
8.40.	Discovery and exclusion contours of the published dilepton analysis	158
8.41.	5σ contours for different integrated luminosities in the dilepton analysis	159
9.1.	Turn-on curves for e20 and mu20 trigger	162
9.2.	Lepton p_T and track isolation in the lepton-hadron analysis	163
9.3.	Distributions of $p_{T,h}$, LLH ratio and track multiplicity	164
9.4.	Distribution of m_T in the lepton-hadron analysis	166
9.5.	Distribution of MET in the non b-tagged analysis	167
9.6.	Distribution of $\Delta\Phi_{\ell h}$ in the non b-tagged analysis	168
9.7.	Distribution of $p_{T,h}$ in the non b-tagged analysis	169
9.8.	Distribution of the jet multiplicity	170

9.9. Distribution of MET in the b-tagged analysis	171
9.10. Distribution of $\Delta\Phi_{\ell h}$ in the b-tagged analysis	172
9.11. Distribution of $p_{T,h}$ in the b-tagged analysis	173
9.12. Distributions of $\Delta\Phi_{\ell h}$ in the b-tagged and non b-tagged analysis	175
9.13. Final $m_{\tau\tau}$ spectra for $m_A = 150/200/300$ GeV in the lepton-hadron analysis . . .	182
9.14. Final $m_{\tau\tau}$ spectra for $m_A = 450/600/800$ GeV in the lepton-hadron analysis . . .	183
9.15. Jet multiplicity distribution in the b-tagged analysis	185
9.16. Jet multiplicity in the control regions for $m_A = 150$ GeV and $m_A = 200$ GeV . . .	189
9.17. Jet multiplicity in the control regions for $m_A = 300$ GeV and $m_A = 450$ GeV . . .	190
9.18. Jet multiplicity distribution in the signal regions and results of $t\bar{t}$ estimation . . .	191
9.19. Illustration of Gaussian significance	206
9.20. Significance as a function of m_A in the lepton-hadron analysis	208
9.21. Significance as a function of $\tan\beta$ in the lepton-hadron analysis	209
9.22. Combined significance as a function of m_A	210
9.23. Combined 5σ discovery contour	211
9.24. Combined 95% CL. exclusion limits	212
9.25. Combined 5σ discovery contour for different luminosities	212
9.26. Distribution of $p_{T,h}$ for low and high m_A	214
9.27. Distribution of MET and SumET for the $\tau\tau$ subchannels	214
9.28. Former ATLAS results and CMS results for MSSM $h/A/H \rightarrow \tau\tau$	215
9.29. First data extrapolation of the results of this thesis	216
10.1. Event display of a $Z \rightarrow \tau\tau \rightarrow \mu + \text{had} + 3\nu$ decay candidate	218
A.1. Distributions of $\Delta\Phi_{\ell\ell}$ and $p_{T,\ell}$ in Rel. 12 and Rel. 14	223
A.2. Distributions of E_ℓ and MET in Rel. 12 and Rel. 14	224
A.3. Distributions of $m_{\ell\ell}$ and $m_{\tau\tau}$ in Rel. 12 and Rel. 14	224
C.1. m_{vis} spectra after baseline selection in the dilepton analysis	228
C.2. m_{vis} spectra after all cuts in the dilepton analysis	231
D.1. Ratios of $Z \rightarrow \tau\tau$ to $Z \rightarrow ee$ for increased systematic variations	233
D.2. Ratios for $Z \rightarrow \tau\tau$ and $Z \rightarrow ee$ for increased systematic variations	234
D.3. Double-ratios for $Z \rightarrow \tau\tau$ and $Z \rightarrow \ell\ell$ for increased systematic variations	235
E.1. Significance obtained by approximation compared to PLH result	238
G.1. Distribution of $m_{\tau\tau}$ for single top events	245
I.1. Combined significance when assuming $\Delta\sigma_{t\bar{t}} = 0$ in the dilepton analysis	254
I.2. Combined 5σ discovery contour when assuming $\Delta\sigma_{t\bar{t}} = 0$ in the dilepton analysis . . .	255
I.3. Combined 95% CL. exclusion limit when assuming $\Delta\sigma_{t\bar{t}} = 0$ in the dilepton analysis . . .	256

List of Tables

2.1. Leptons and quarks and their properties	3
2.2. Gauge bosons and their properties	4
2.3. Left and right chiral fermions and their quantum numbers	7
2.4. Field content of the MSSM	19
2.5. Couplings of the neutral MSSM Higgs bosons	21
2.6. Parameters of the benchmark scenarios	24
5.1. MC samples for b-associated Higgs boson production in Release 12	57
5.2. MC samples for b-associated Higgs boson production in Release 14	58
5.3. MC samples for Higgs boson production by gluon fusion in Release 14	58
5.4. QCD dijet MC samples and virtualities	59
5.5. MC samples for background processes in Release 12	61
5.6. MC samples for background processes in Release 14	62
6.1. Efficiencies of electron ID cuts for the lepton-lepton analysis	65
6.2. Efficiencies of electron ID cuts for the lepton-hadron analysis	66
6.3. Efficiencies of muon ID cuts for the lepton-lepton analysis	68
6.4. Efficiencies of muon ID cuts for the lepton-hadron analysis	69
6.5. Tau decay modes and branching fractions	70
6.6. Efficiencies of tau ID cuts for the lepton-hadron analysis	73
8.1. Trigger cut efficiencies in the lepton-lepton analysis	104
8.2. Lepton isolation cut efficiencies in the lepton-lepton analysis	106
8.3. Baseline selection cut flow for the lepton-lepton analysis	112
8.4. $m_{\tau\tau}$ window cuts for the baseline selection in the dilepton analysis	113
8.5. Number of events and statistical significance after baseline selection in the dilep- ton analysis	115
8.6. m_A -dependent cut values in the lepton-lepton analysis	116
8.7. Cut flow for the full selection in the dilepton analysis for $m_A = 110$ GeV	124
8.8. Cut flow for the full selection in the dilepton analysis for $m_A = 130$ GeV	124
8.9. Cut flow for the full selection in the dilepton analysis for $m_A = 160$ GeV	124
8.10. Cut flow for the full selection in the dilepton analysis for $m_A = 200$ GeV	125
8.11. Cut flow for the full selection in the dilepton analysis for $m_A = 300$ GeV	125
8.12. Cut flow for the full selection in the dilepton analysis for $m_A = 450$ GeV	125
8.13. $m_{\tau\tau}$ window cut for the optimized selection in the dilepton analysis	126
8.14. Numbers of events after full selection in the dilepton analysis	128

8.15. Statistical significance after full selection in the dilepton analysis	129
8.16. Experimental and theoretical systematics on $t\bar{t}$ in the dilepton analysis	133
8.17. Number of events in the $Z \rightarrow ee/\mu\mu$ control regions	136
8.18. Number of $Z \rightarrow \tau\tau$ events by data-driven normalization method	148
8.19. Uncertainties on $Z \rightarrow \tau\tau$ in the dilepton analysis	150
8.20. Summary of systematic uncertainties on background processes in the dilepton analysis	151
8.21. Summary of systematic uncertainties on the signal in the dilepton analysis	152
9.1. Tight cut values on the τ LLH ratio	165
9.2. m_A -dependent cuts in the non b-tagged analysis	166
9.3. m_A -dependent cuts in the b-tagged analysis	170
9.4. Mass window cut values in the lepton-hadron analysis	174
9.5. Results of single top estimation in the lepton-hadron analysis	175
9.6. Cut flow for $m_A = 150$ GeV in the lepton-hadron analysis	176
9.7. Cut flow for $m_A = 200$ GeV in the lepton-hadron analysis	177
9.8. Cut flow for $m_A = 300$ GeV in the lepton-hadron analysis	178
9.9. Cut flow for $m_A = 450$ GeV in the lepton-hadron analysis	179
9.10. Cut flow for $m_A = 600$ GeV in the lepton-hadron analysis	180
9.11. Cut flow for $m_A = 800$ GeV in the lepton-hadron analysis	181
9.12. m_A -dependent cut values for the $t\bar{t}$ control regions	186
9.13. Composition and purity of the $t\bar{t}$ control regions	187
9.14. Composition and purity of signal regions at high jet multiplicities	188
9.15. Results of $t\bar{t}$ estimation for $\tan\beta = 5$	192
9.16. Results of $t\bar{t}$ estimation for $\tan\beta = 20$	192
9.17. Results of $t\bar{t}$ estimation for $\tan\beta = 45$	193
9.18. $\tan\beta$ -dependent bias of the $t\bar{t}$ estimation	193
9.19. Impact of systematic variations on the purity of the $t\bar{t}$ control regions	194
9.20. Impact of systematic variations on the purity of the signal regions at high multi- plicities	195
9.21. Impact of systematic variations on the number of events in different kinematic regions for the $t\bar{t}$ estimation	197
9.22. Uncertainties on the extrapolation ratio for the $t\bar{t}$ estimation	199
9.23. Systematic uncertainties on the $Z \rightarrow \tau\tau$ background in the lepton-hadron analysis	200
9.24. Uncertainties on the extrapolation factor for the W+jets estimation	201
9.25. Summary of systematic uncertainties on the backgrounds in the lepton-hadron analysis	202
9.26. Cross section uncertainties on the signal in the lepton-hadron analysis	202
9.27. Experimental uncertainties on the signal in the non b-tagged analysis	203
9.28. Experimental uncertainties on the signal in the b-tagged analysis	204
9.29. Cross sections at 14 TeV and 7 TeV for various processes	216
B.1. B-tagging weight corrections in Rel. 12	225
C.1. Cut values for the m_{vis} window after the baseline selection in the dilepton analysis	227

C.2. Statistical significance when reconstructing m_{vis} after the baseline selection in the dilepton analysis	229
C.3. Numbers of events for the visible mass analysis after all cuts in the dilepton channel	230
C.4. Statistical significance for the visible mass analysis after all cuts in the dilepton channel	230
E.1. P-values and corresponding significance values.	237
E.2. Ratio of approximated significance to PLH result	238
F.1. Event weights for the tight lepton ID in the lepton-hadron analysis	239
F.2. Event weights for the tight τ ID in the lepton-hadron analysis for $b\bar{b}$ QCD samples	240
F.3. Event weights for the tight τ ID in the lepton-hadron analysis for QCD samples with multi lepton filter	241
F.4. Event weights for the tight τ ID in the lepton-hadron analysis for W+jets and Z+jets samples	242
G.1. Cut flow for single top events up to the loose τ ID cut	244
G.2. Cut flow for single top events up to the $m_{\tau\tau}$ window cut	244
G.3. Results of single top estimation in the lepton-hadron analysis	245
H.1. Systematic uncertainties of data-driven $t\bar{t}$ estimation for $m_A = 150$ GeV	248
H.2. Systematic uncertainties of data-driven $t\bar{t}$ estimation for $m_A = 200$ GeV	249
H.3. Systematic uncertainties of data-driven $t\bar{t}$ estimation for $m_A = 300$ GeV	250
H.4. Systematic uncertainties of data-driven $t\bar{t}$ estimation for $m_A = 450$ GeV	251

Acknowledgements

Now I would like to take the opportunity to express my gratitude to all the people who supported me during my phd studies.

I thank Prof. Michael Kobel for the possibility to work on this very interesting topic, for his scientific guidance, his trust in me and all his personal advices to me. I thank Wolfgang Mader for all his effort, his patience with me and his constant support. I thank all my colleagues from the IKTP for the enjoyable atmosphere and your help.

I thank very much Leandro Nisati and Louis Fayard for their immense support, the useful discussions and their fighting spirit during CSC. I am grateful to Prof. Karl Jakobs for his patience with my note. I thank Louis for his friendly advice and that you always had time for me and cheered me up when needed.

I was given the opportunity to spend more than one year at CERN, which was clearly the highlight of my phd studies. I thank the Munich crew at the fourth floor of B54 at CERN for their friendliness and for absorbing me into their group: Alessia, Daniela, Felix, Gabi, big Jörg, small Jörg, Jürgen, Steffen, Thomas and all the others. I thank Jörg Dubbert for his guided tour into the heart of ATLAS. I also thank them for the fun we had playing armagedron and especially for the great cheese fondues we had in the garage. I thank the Bonn crew at CERN for our wonderful cooking evenings and the attempts to climb the Reculet: Nico, Duc, Guilherme, Robindra, Götz, Klemens and everybody else. I wish I would have spent more time with you. I thank Kostas Nikolopoulos for being my friend and for our tea times at midnight. I thank Daniela Rebuzzi for all her kindness. While being at CERN it was a pleasure doing shifts at the Liquid Argon desk in the ATLAS control room and I enjoyed learning from the LAr crew, as for example Emmanuel Monnier, Martin Aleksa, Adam Gibson, Kathy Copic and Stephanie Majewski.

I thank ATLAS for the outstanding opportunity to give a talk at the SUSY conference in Seoul, South Korea, at a very early stage of my phd studies.

I thank the Graduiertenkolleg "Mass - Spectrum - Symmetry" for the financial support, the great workshops and for granting me the travel to the Higgs Hunting conference in Paris.

I thank Will Davey for his immense effort during our 14 TeV project and the fruitful discussions. I am indebted to Ketevi Assamagan and Bill Murray for supporting this project and their input.

I cannot thank enough Rainer Schwierz for administrating our computers, his patience and effort. I am also very grateful for the smooth operation of the ZIH computing cluster.

I thank Anne Glück and Uta Bilow for the friendly atmosphere in our office, the ladies' office. I enjoyed your company and your regard, and the green wall helped me focus.

I thank the IKTP Friday football group for the beer and the fun and for even sometimes passing the ball to me (...without smashing).

I thank very much everybody reading and improving the thesis manuscript: Jun.-Prof. Arno Strässner, Deepak Kar, Felix Friedrich, Frank Seifert, Marcus Morgenstern, Patrick Czodrowski, Philipp Anger, Sebastian Wahrmund and Wolfgang Mader. I especially thank Felix Thomas for his incredibly careful reading.

I thank my father for all his support and for not giving up when suddenly facing severe illness. I warmly thank everybody who offered to help and who expressed his or her sympathy to me, especially Prof. Markus Schumacher for his kind words and Michael Kobel for bringing me back on course with his countless encouragements. I am greatly indebted to Alexander 'Omol' Domula for his tremendous help, his friendship and courage.

Finally, I thank all my friends in Dresden for sharing your time with me and for all the good times we had during the studies.

Versicherung

Hiermit versichere ich, dass ich die vorliegende Arbeit ohne unzulässige Hilfe Dritter und ohne Benutzung anderer als der angegebenen Hilfsmittel angefertigt habe; die aus fremden Quellen direkt oder indirekt übernommenen Gedanken sind als solche kenntlich gemacht. Die Arbeit wurde bisher weder im Inland noch im Ausland in gleicher oder ähnlicher Form einer anderen Prüfungsbehörde vorgelegt.

Diese Arbeit wurde am Institut für Kern- und Teilchenphysik der Technischen Universität Dresden unter wissenschaftlicher Betreuung von Prof. Dr. Michael Kobel angefertigt.

Es haben keine früheren erfolglosen Promotionsverfahren stattgefunden.

Ich erkenne die Promotionsordnung der Fakultät Mathematik und Naturwissenschaften an der Technischen Universität Dresden vom 20. März 2000, in der Fassung der vom Fakultätsrat am 19.06.2002 und 12.07.2002 beschlossenen und mit Erlass des Sächsischen Staatsministeriums für Wissenschaft und Kunst vom 18.03.2003 genehmigten Änderungen gemäß Satzung vom 16.04.2003, an.

Dresden, den 04.10.2010

Jana Schaarschmidt

